LIDAR STUDIES OF THE MIDDLE ATMOSPHERE.

By

Philip Stephen Argall, B.Sc. (Hons)

A thesis presented for the degree of

DOCTOR OF PHILOSOPHY

at the

UNIVERSITY OF ADELAIDE

(Department of Physics and Mathematical Physics)

(October 1993)

Contents

Abstract

The work described in this thesis includes the design, construction, operation and data analysis for a stratospheric Rayleigh lidar (LIght Detection And Ranging) system.

This thesis first reviews the areas of atmospheric physics and light propagation in the earth's atmosphere. A review of the history and present state of lidar techniques is also given.

The present Lidar system was designed to operate as a Doppler lidar, however as the first stage of this project it has been set up to operate in a similar manner to a more conventional stratospheric Rayleigh lidar.

This lidar system has a number of unique design features. These include the use of a single 1 m diameter telescope for transmission of the laser pulse and reception of the backscattered light. Associated with this is a high speed rotating shutter system that switches the optical system from transmit to receive mode. A detailed description of the equipment is given. This includes details of the production of the telescope and of the operation of the lidar's electronic control system.

A problem encountered with fluorescence from optical components that are common to both the transmit and receive optical paths is discussed, along with a solution.

The methods used for the analysis of Rayleigh lidar data are discussed. Scattering ratio and temperature profiles are calculated for data collected during the period 10 March 1992 to 11 May 1993.

The scattering ratio profiles clearly show the reduction in the scattering from the stratospheric aerosol layer. This is due to the removal of the aerosol injected by the eruption of Mt. Pinatubo. The measured relative density profiles show very good agreement with the CIRA model densities. Agreement with the model of Fleming et al is not as good.

Calculated temperature profiles generally agree well with the model temperatures.

Statement

This thesis contains no material which has been accepted for the award of any other degree or diploma in any University and, to the best of the author's knowledge and belief, it contains no material previously published or written by another person except where due reference is made in the text.

I consent to this thesis being made available for photocopying and loan by the librarian of the University of Adelaide, subject to acceptance for the award of the degree.

Philip Stephen Argall, B.Sc. (Hons)

Acknowledgements

Firstly and most importantly I thank my wife Julia without whose support and encouragement I would not have been able to undertake this work.

The majority of the work described here was accomplished under the supervision of the late Dr. Fred Jacka, who initiated this project in the early 1980's. Dr. Jacka's determination and insight were responsible for overcoming some of the seemingly insurmountable problems encountered during the construction of the equipment. Working with Fred Jacka was a privilege from which I gained a great deal.

Dr. Wayne Hocking[1] played a vital role in the continuation of this work after the closure of the Mawson Institute for Antarctic Research, under whose auspices the lidar project was initiated. For this and all of his subsequent encouragement and advice I am thankful.

I also thank Dr. Robert Vincent, who jointly supervised my work, for his suggestions on this thesis.

I thank Mr. Donald Creighton, whose electronic and mechanical design skills bought many idea's to fruition. Discussions with Mr. Creighton shaped many aspects of the instrument, his experience in designing and constructing optical and electronic equipment was invaluable throughout this work.

I thank Mr. Daryl White for his work on this project, for his effort in organising so many things that were necessary to get the equipment running and for the numerous useful discussions.

I would like to thank the former staff and students of the former Mawson Institute for Antarctic Research. To Heather Duff, Fred Fone, Frank Koltai, Richard Ferguson, Norman Jones, Paul Wardill, Pene Greet, Mark Conde, Andre Phillips, Gina Price, Maria Deduge and John French, I thank you for the discussions about; and support you gave to this work.

---

[1]Now at The University of Western Ontario

LIDAR telescope protruding from the roof of the LIDAR building at the Buckland Park Research Station

1 The Atmosphere

1.1 Introduction

The changing moods of the atmosphere have always played an important role in the lives of people. Day to day weather often influences, and even govern mankind's activities. While the weather is primarily a function of the state of the troposphere, the regions above the troposphere are increasingly being recognised for the role they play in determining the conditions at the surface of planet Earth.

Until recent times atmospheric change, on a large scale, has been as a result of natural forces. Anthropogenic activities have only made a significant impact on the general nature of the atmosphere in the past few decades. A steady increase in the concentration of a number of pollutants (eg CO_2, SO_2, and CH_4) on a global scale has been measured in recent decades, (McEwan et al 1975, and Zander et al 1992). Over the past decade measurements have also shown an extreme decrease in springtime southern polar stratospheric ozone concentrations. These changes are directly attributable to anthropogenic activities and threaten to change the atmosphere to at least the extent that they will have an effect on people.

1.2 Atmospheric Structure

It is usual to divide the atmosphere into a number of altitude region based upon the temperature gradient, as in figure 1.1. Many properties of the atmosphere change abruptly at the boundaries of these sub-divisions while changing only slowly within each sub-division. This makes these sub-divisions extremely useful in any discussion of the atmosphere. Sub-divisions based on other parameters such as ionisation are also commonly used.

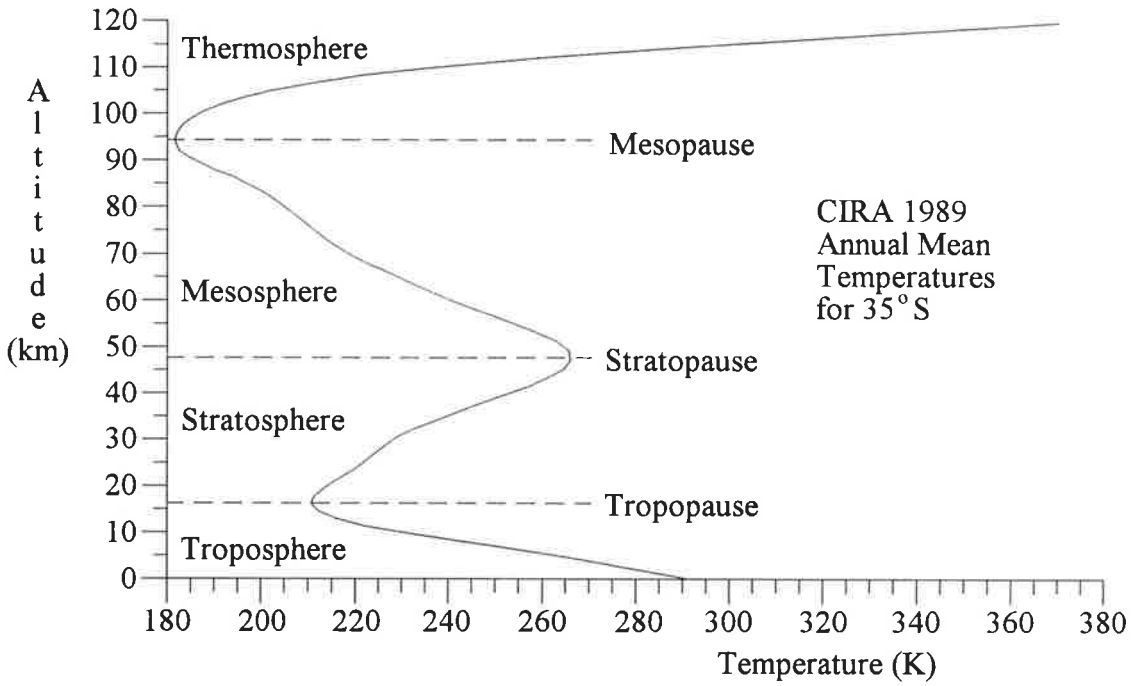

Figure 1.1 Atmospheric temperature profile. Annual mean temperatures for 35°S from the CIRA 1989 model (Rees et al 1990).

1.2.1 Composition

The major atmospheric species maintain a constant mixing ratio throughout the first 100 km of the atmosphere and exist in the concentrations as shown in Table 1.1. These data assume that any water vapour has first been removed. Above 100 km the dissociation of O_2 changes these mixing ratios.

Water vapour plays an important role in the structure and dynamics of the troposphere. However, the cold tropopause acts as a vapour trap, generally stopping water vapour being transported into higher regions of the atmosphere. In the regions above the tropopause water vapour concentrations are generally very low, and the water that is present

can generally be attributed to production via chemical reactions. Under some circumstances, moisture in the stratosphere can have significant effect on the chemistry of that region, eg the role of polar stratospheric clouds in ozone destruction.

Species	Concentration
N_2	7.8084×10^5
O_2	2.0946×10^5
Ar	9.34×10^3
CO_2	3.2×10^2
Sum of these four species	9.9996×10^5

Table 1.1 Concentrations of the 4 most abundant atmospheric species.

Many of the great variety of minor species that exist in the atmosphere have concentrations that vary in time and/or location. The concentration of these species generally depends on the chemical and photo-chemical reactions that produce or destroy them. Although minor in concentration some of these species play major roles in determining atmospheric properties.

1.2.2 Temperature Structure

In the absence of water vapour and species able to absorb or emit electro-magnetic radiation, the atmospheric temperature profile would consist simply of a decrease with altitude of 9.8 K km^{-1} . This is the dry adiabatic lapse rate (Γ_d), the rate at which a parcel of dry air will change temperature if displaced vertically, under adiabatic conditions. The actual temperature structure is, however, a result of the absorption of energy of both solar and terrestrial origins, as well as the transport of energy via atmospheric wave and tidal activity, combined with this lapse rate effect. The radiative transfer processes involve a number of ions, atomic and molecular species, both absorbing and emitting radiation over a wide band of the electro-magnetic spectrum, (see for example Andrews et al 1987 and Liou 1980).

Heating of the Earth's surface by the sun, ($\lambda \approx 0.3$ to 2.4 μm) causes it to warm and re-emit radiation, but at much longer wavelengths ($\lambda \approx 3$ to 50 μm). A number of atmospheric species, primarily H_2O and CO_2, and to a lesser extent O_3 and CH_4, absorb this radiation, causing the atmosphere to be warmed.

The average temperature of the Earth-atmosphere system is constant when averaged in time and space and as radiative processes are generally the only other means of transporting energy into or out of this system it must be in radiative equilibrium. Additionally, the very stable stratosphere allows little heat transfer with the troposphere via convective activity. As a consequence of this the Earth-troposphere system must be in radiative equilibrium as must the atmosphere above the tropopause, but there is a great deal of radiative interaction between these two systems.

Heating of the upper-thermosphere, the outer limit of the atmosphere, is due mainly to the absorption of energy through the ionisation of O_2, O, N_2 and NO. The absorption of radiation able to cause ionisation in the upper thermosphere leads to a reduction in the intensity of this radiation at lower levels of the thermosphere. This in turn leads to a reduction in the energy absorption and temperature in the lower thermosphere.

Throughout the mesosphere and stratosphere the production of ozone and its subsequent absorption of both solar ultra-violet and terrestrial infra-red radiation causes heating. This heating effect is maximised at the stratopause, even though the maximum mixing ratio for ozone occurs lower down. The combination of radiation levels increasing with altitude and O_3 concentration decreasing with altitude (above the middle stratosphere) leads to the heating due to O_3 maximising at the stratopause. Ozone contributes approximately 50% of the radiatively trapped energy input for the stratosphere, the other 50% is due to the absorption of IR by CO_2 and H_2O, (Shine, 1992). Cooling of the stratosphere is primarily due to IR emissions from CO_2 and H_2O, so that these two species serve to provide a net cooling to the stratosphere while O_3 provides a net heating.

The temperature structure of the troposphere is due to a combination of convective activity and the absorption of IR radiation by H_2O and CO_2. Convective activity is able to transport both heat and latent heat of water vapour. The IR radiation absorbed in the

troposphere is of both terrestrial and stratospheric origins. Thus the stratosphere has the effect of heating the troposphere.

The amount of H_2O in the troposphere is extremely variable and so is its effect on radiative processes. Clouds in particular play a very important role in tropospheric radiative transfer processes.

The lapse rate is defined as the negative rate of change of temperature with altitude and is positive for a temperature decrease with altitude. The lapse rate is an important parameter in defining the stability of the atmosphere.

1.2.3 Atmospheric Stability and Gravity Waves

As previously mentioned, in the absence of water vapour a parcel of rising air will cool at the dry adiabatic lapse rate (Γ_d). If this is greater than the actual lapse rate of the atmosphere (Γ), ie the risen parcel is warmer than the surrounding air mass, the parcel will continue to rise. This situation is unstable and is often referred to as convective instability. Under the same conditions a parcel of sinking air will continue to sink. If however the dry adiabatic lapse rate is less than the actual lapse rate then a vertically displaced parcel of air will return to its original altitude. In the presence of water (vapour, liquid or solid) a parcel of air displaced vertically will change temperature more slowly, assuming the water does not undergo a change of state.

In the troposphere where the lapse rate is normally in the range 3 to 10 K km^{-1} convectively unstable conditions often occur leading to large vertical mixing of the air. Stratospheric conditions are very different with lapse rates less than zero leading to a highly stable air mass.

Under stable atmospheric conditions a parcel displaced vertically will suffer a restoring force that will continue to act until the parcel has returned to its original altitude; at this time the parcel will have momentum in the direction opposite to that of the original displacement. As a result the parcel will oscillate about its original altitude with simple harmonic motion at a frequency N given by;

$$N^2 = \frac{g}{T}(\Gamma_d - \Gamma) \qquad \ldots (1.1)$$

Where g = acceleration due to gravity, and
T = thermodynamic temperature.

Andrews et al (1987), Holton (1975, 1992) and others have shown that under stable atmospheric conditions the flow of air over a sinusoidal mountain range can lead to the generation of gravity (or buoyancy) waves. These waves rely on the stability of the atmosphere to provide the restoring force after the initial displacement of the air parcel. The phase velocity of gravity waves is at right angles to the direction of oscillation of the air parcels, that is they are transverse waves. Under certain circumstance's gravity waves are able to propagate with a vertical component of the phase velocity.

The vertical propagation of gravity waves causes these waves to increase in amplitude, due to the decrease in atmospheric density with altitude. As gravity waves propagate vertically the perturbations caused by these waves increase in amplitude until they cause the atmosphere to become unstable and the waves begin to "break". This breaking causes the wave energy and momentum to be deposited throughout the altitude region where the breaking occurs. The transport of energy and momentum throughout the atmosphere by gravity waves has a significant effect on the dynamics of the middle and upper atmosphere.

Atmospheric features such as frontal structures, jet streams and larger scale convective instabilities may also result in the generation of gravity waves.

Rayleigh lidar has to ability to measure gravity wave parameters in the stratosphere and lower mesosphere on a routine basis, (Shibata et al, 1988, Gardner et al, 1989 and Wilson et al, 1990). Currently there is no other practical method available that is able to provide routine measurements in this region of the atmosphere with sufficient resolution to enable the determination of gravity wave parameters.

1.2.4 Dynamics

The synoptic and global scale motions that take place within the atmosphere are the result of the complex interaction of the temperature structure, the rotation of the earth, and the transport of energy by wave motions. Gravity waves, Rossby waves and Kelvin waves (Holton 1975, 1992 and Andrews et al 1987), all play an important role in determining the dynamics of the atmosphere. Large scale motions in the atmosphere are not only inherently important, they are also vital to the transport of energy and trace species.

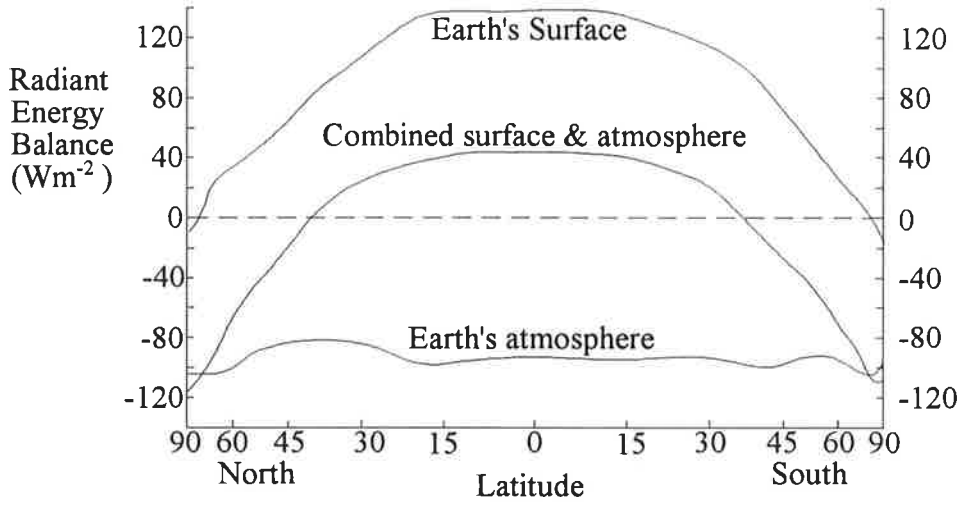

Figure 1.2 Variation in the radiation balance over the Earth's surface.
(After McIntosh et al, 1981.)

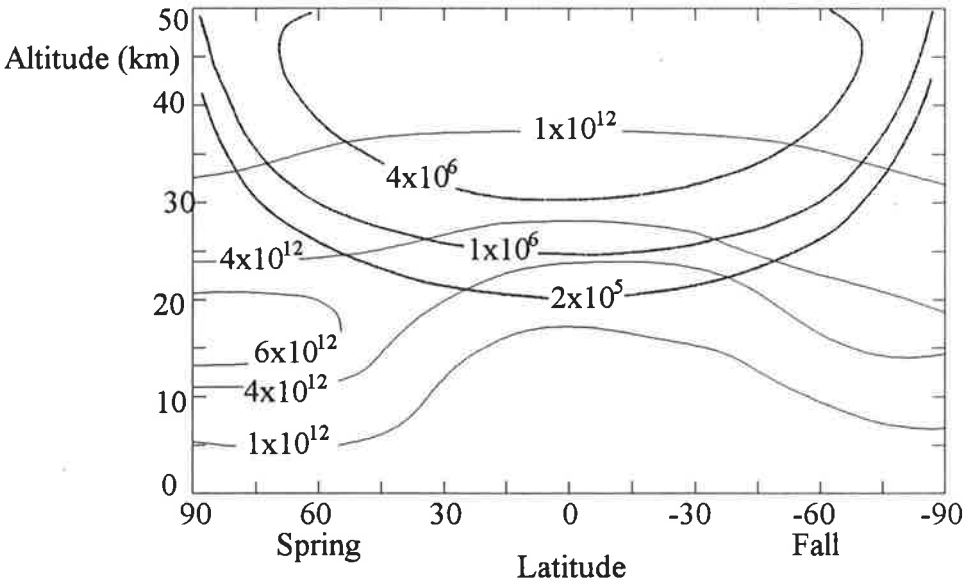

Figure 1.3 Regions of ozone production and residence. Zonal average ozone concentrations (thin lines) are shown in molecules·cm^{-3}. Zonal average production rates (thick lines) are given in molecules·cm^{-3}·s^{-1}. (After Chamberlain and Hunten, 1987.)

The theoretical description of the processes leading to the dynamic structure of the middle and upper atmosphere is found in texts such as Holton (1975, 1992) and Andrews at al (1987). Experimental results are summarised in model atmospheres such as CIRA '86.

Figure 1.2 gives the zonal mean heating rates due to radiative transfer processes for the earth-atmosphere system. This figure shows that these processes lead to excess heating at low latitudes and a cooling at latitudes higher than 40°. Atmospheric motion, and ocean currents equalise this imbalance by transporting heat energy from low to high latitudes.

Similarly figure 1.3 show the zonal distribution of ozone source and residence regions. The major production region for ozone is centred at approximately 40-45 km and equator ward of 70°, while the region of highest residence concentration is centred at approximately 18 km and pole ward of 55°. Again the apparent anomaly can be explained in termsof transport via atmospheric dynamics.

1.3 The Stratosphere

The stratosphere has its lower boundary at the tropopause, whose altitude varies from about 8 km over the poles to about 18 km at low latitudes. The upper boundary is the stratopause which occurs at approximately 50 km at most latitudes but rises to around 55 km at the winter pole.

Lidar (LIght Detection And Ranging) plays an important role in the measurement of stratospheric parameters. The middle and upper stratosphere and lower mesosphere (approximately 20-65 km) are ineffective at scattering radio waves and therefore this region has remained out of the range of radar techniques. Scattering of electromagnetic radiation requires refractive index perturbations with scales approaching the size of, or larger than, the wavelength of the incident radiation. Perturbation of sufficient scale and intensity do not exist in the 20-65 km range to enable radar techniques to be effective. The wavelength of light is such that individual atoms and molecules are effective in scattering enough light to enable the lidar technique to be effective in this altitude range.

Two of the outstanding and important features of the stratosphere are the aerosol and ozone layers.

1.3.1 The Stratospheric Aerosol Layer

Studies of the twilight by Gruner and Kleinert, (1927) suggested the existence of a dust layer in the lower stratosphere. The conformation of the existence of this layer came when Junge et al, (1961) used impactors mounted on balloon platforms to collect particle from the layer, between 10 and 25 km. This and much subsequent research (Whitten et al 1982, Inn et al 1982, Turco et al 1992) has shown that the layer consists of a number of different types of particles, (see figure 1.4).

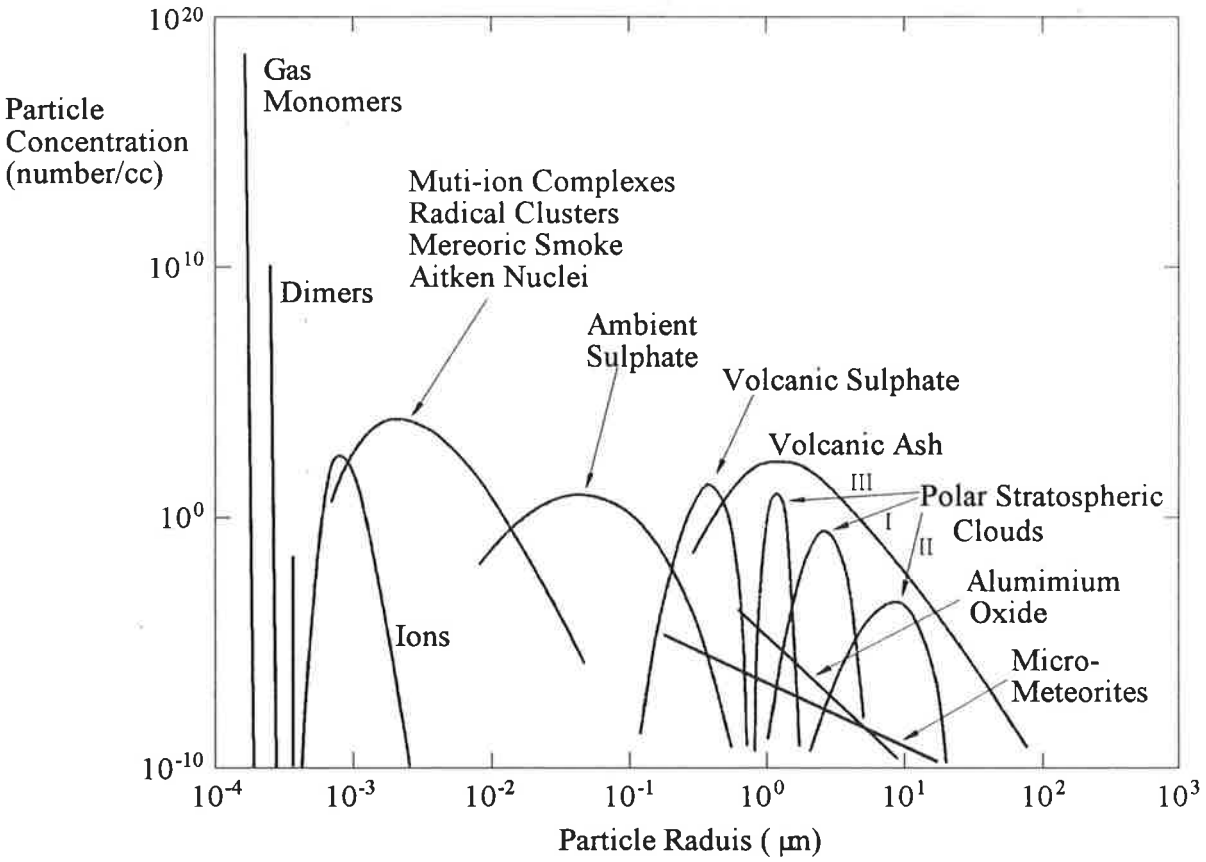

Figure 1.4 Spectrum of particles in the Earth's stratosphere. Shown are approximate size dispersions of particles of different composition and origin. The total number concentration of each type of particle is roughly indicated by the peak value on the vertical scale. (After Turco et al, 1992.)

Usually the major component of the stratospheric aerosol layer are sulphate aerosols, (see figure 1.4). These sulphate particles are principally in the form of a solution of H_2SO_4 in water with the ratio of H_2SO_4 to H_2O being approximately 3:1 by weight.

At mid-latitudes and after several years without major volcanic activity the aerosol layer is dominated by the presence of a background level of sulphate aerosols. These sulphate aerosols are produced in the stratosphere via chemical reactions involving sulphate vapours (SO_2 , OCS, CS_2) of tropospheric origin, Turco (1982). On a global scale an equilibrium level of the sulphate aerosol is maintained by the balance of production with the removal by sedimentation and wash-out. Large volcanic eruptions inject ash and SO_2 directly into the lower stratosphere. The oxidisation of this SO_2 to H_2SO_4 enhances the sulphate aerosol level. This enhancement decays over a period of a few years. The size distribution of the volcanic ash grains varies widely, (see figure 1.4), and thus so does the rate at which they settle out of the stratosphere. In general volcanic ash settles out over a period of a few months. In the case of the Mt. St. Helens eruption the settling rate increased due to the coating of the ash grains with sulphuric acid forming larger and heavier particles, (Farlow et al 1981).

Local geological conditions determines the amount of sulphur in the plume of a volcano and the explosive force of the volcano determines how much of this sulphur enters the stratosphere.

The stratospheric aerosol layer scatters and absorbs incoming solar radiation. This increases the heating throughout the aerosol layer and reduces the heating effect on the surface of the Earth. This leads to the possibility of abnormal cold weather conditions after major volcanic eruptions. In order for volcanic activity to cause climatic change the stratospheric aerosol layer would need to be greatly perturbed for an extended period of time. The settling period of the sulphate aerosol is a few years so that climatic change would require persistent and violent volcanic activity.

Many studies have tried to show a relationship between volcanic activity and abnormally cold weather conditions. Toon and Pollack (1982) summarise and comment on a number of these studies. These workers conclude that there is good evidence supporting such a relationship, however they put forward a number of points that tends to grey the evidence somewhat. Labitzke and van Loon (1992) have shown that the eruptions of Mt. Anung, 1963, El Chichon, 1982 and Mt. Pinatubo, 1991 preceded an unusually warm tropical stratosphere and an unusually strong Northern Hemispheric vortex.

Anthropogenic influences on the aerosol layer come about in a number of ways, (Turco et al, 1992). Probably the most significant of these is the injection of sulphur compounds into the atmosphere from the combustion of fossil fuels, especially coal and heavy oils.

1.3.2 The Ozone Layer

The ozone layer is a very tenuous but very important part of the stratosphere. The most common measure of ozone column abundance is the Dobson unit (DU), where one DU is equal to a layer of ozone 10 μm thick at standard temperature and pressure. Thus if all the ozone in an average atmospheric column of 300 DU was bought to the earths surface it would form a layer approximately 3 mm thick. This is what protects life on earth from the harmful effects of solar ultra-violet radiation and is also primarily responsible for the temperature inversion of the stratosphere.

Ozone is produced by the reactions described by (A) and (B) below,

$$O_2 + h\nu \rightarrow 2O \qquad (A)$$

$$O + O_2 + M \rightarrow O_3 + M \qquad (B)$$

Where M is any third body, usually N_2 or O_2.

The destruction of ozone molecules is primarily due to photo-dissociation by solar ultra-violet radiation. This is the mechanism for ozone's shielding of the earth from ultra-violet rays. The photo-dissociation reaction is described by (C) below,

$$O_3 + h\nu \rightarrow O + O_2 \qquad (C)$$

This leaves an O molecule free to undergo reaction (B) and again produce ozone. The solar energy input to this cycle, $h\nu$ in reaction (C), causes the products of this reaction to be in excited electronic states. This energy is subsequently converted to heat.

A number of other chemical reactions reduce the effectiveness of this cycle by reacting with and removing both O_3 and O; see for example McEwan and Phillips (1975) and Warneck (1988).

The destruction of ozone by chlorine atoms derived from chloro-fluro-carbons (CFC) has received much publicity recently. In this process chlorine is photo-dissociated from the

CFC's and then catalytically destroys ozone. Each chlorine atom has the ability to destroy a very large number of ozone molecules. See for example Turco et al (1992) and WMO (1992) for further discussion.

The concentration of ozone is variable in both space and time. Figure 1.5 shows a typical altitude profile of ozone concentration obtained with a LIDAR.

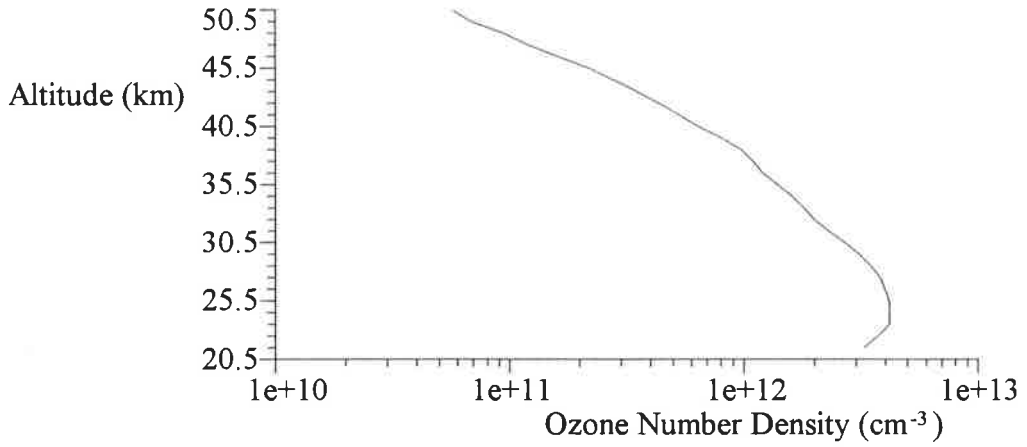

Figure 1.5 Ozone profile obtained by a Lidar. (After McDermid et al, 1990b.)

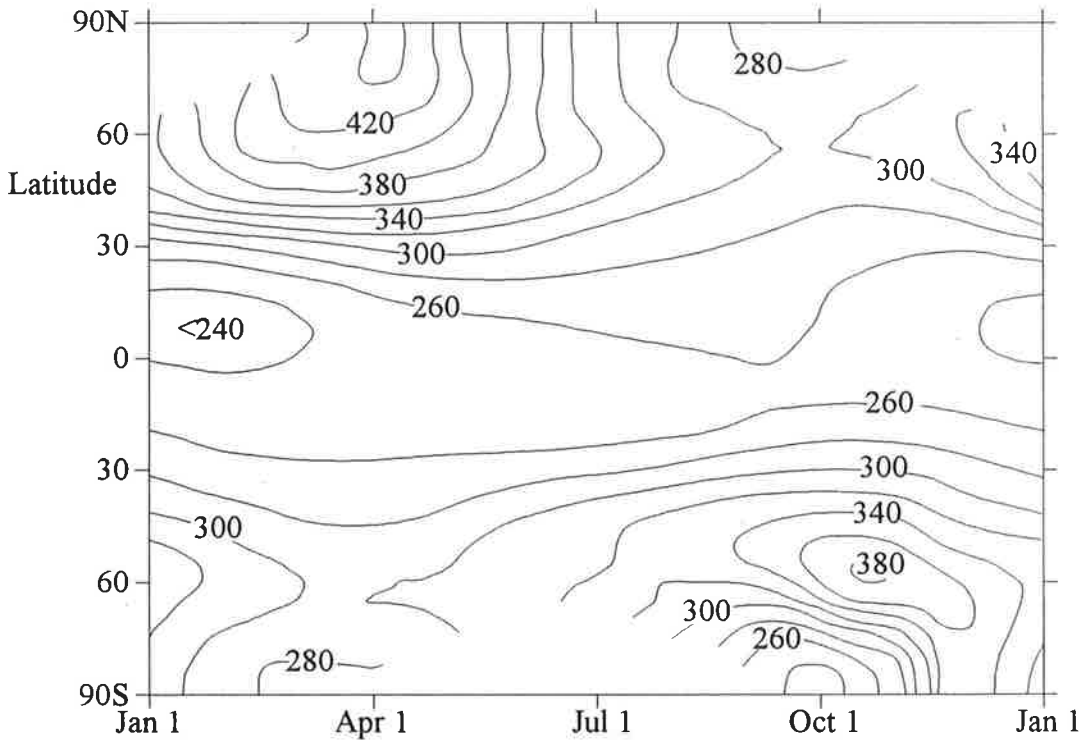

Figure 1.6 Time latitude section showing the seasonal variation of total ozone (Dobson units) based on data from the total ozone mapping spectrometer (TOMS). (After Holton, 1992.)

Satellite mounted instruments provide global scale measurements of ozone concentration. The best known of these is the Total Ozone Mapping Spectrometer (TOMS) instrument aboard the Nimbus 7 satellite. This instrument has provided the most compelling evidence of the existence of the Antarctic ozone hole. Figure 1.6 shows a time latitude section of total ozone distribution as measured by the TOMS instrument.

1.4 Conclusions

The radiative, chemical and dynamic structure of the middle and upper atmosphere influence the troposphere and biosphere in a number of ways. These include the protection of the biosphere from UV radiation provided by the ozone layer. Also of great importance is the radiation exchange between the troposphere and stratosphere that helps determine the temperature structure of both these regions. The dynamics of the stratosphere play an important role in transporting both heat energy and chemical species throughout this region.

2 Light Scattering and Absorption in the Atmosphere.

2.1 Introduction

The effects of light scattering in the Earth's atmosphere are easily observed. The blue sky, white clouds and red sunsets are all examples of the results of this effect.

Both molecules and aerosols cause light to be scattered as it propagates through the atmosphere. Molecular scattering takes place via a number of different processes and may be either elastic or inelastic, coherent or incoherent. It is possible to calculate, with at least a reasonable degree of accuracy the parameters that describe these molecular scattering processes.

The theory of light scattering and absorption by aerosols, usually called Mie theory is well understood but limited in its application. This is due to computational difficulties encountered when trying to solve atmospheric scattering problems where the variations in size, shape and refractive index of the particles can be enormous.

All of the scattering processes that take place in the atmosphere play a role in lidar remote sensing techniques. For this reason the present chapter gives an over-view of each of these scattering processes and the role they play in the various lidar techniques.

2.2 Atomic and Molecular Scattering

There are a variety of processes by which molecules scatter light, there is however an even greater variety of terms used to describe these processes. In addition to this the same terms have been applied to different processes by different workers. Most of the confusion has come about due to the use of the term Rayleigh scattering. This term has been used to identify at least three different spectral regions of the light scattered by molecules.

In an attempt to clear up this confusion Young (1980, 1981, 1982) discusses the history of the discovery of the various molecular scattering processes in an attempt to give each a unique name. Although many suggestions are made, some of the terminology-related problems remain unresolved. The suggestions given are used here. The term Rayleigh scattering is not used, but Rayleigh's name is used to identify the theory that he developed.

2.2.1 Rayleigh Theory

Rayleigh theory describes the scattering of light by particles that are small compared to the wavelength of the incident radiation. This theory was developed by Lord Rayleigh (1871 a, b) to explain the colour, intensity distribution, and polarisation of the sky in terms of scattering by atmospheric molecules.

In his original work on this subject Rayleigh used simple dimensional arguments to arrive at his well-known equation. In later years Rayleigh (1881, 1899) and more recently Stratton (1941), McCartney (1976), Kerker (1969) and Measures (1984) have replaced these dimensional arguments with a more rigorous mathematical derivation of the theory. The scattering equation can be derived by considering a dielectric sphere, of radius r, in a parallel beam of linearly polarised electro-magnetic radiation. The influence of this radiation causes the sphere to become an oscillating dipole that generates its own electro-magnetic field, the scattered radiation. It can be seen that for this derivation to hold the incident field must be almost uniform over the volume of the scattering centre, and this leads to the restriction of Rayleigh theory to scattering by particles that are small compared to the wavelength of the incident radiation. Pendorf (1962) has shown that when $r < 0.03\lambda$ the differences between results obtained with Rayleigh theory and the more general Mie theory are less than 1%.

Rayleigh theory gives an equation for the scattered intensity from a linearly polarised

beam by a single molecule as

$$I_m(\phi) = E_0^2 \frac{9\pi^2 \varepsilon_0 c}{2N^2\lambda^4}\left(\frac{n^2-1}{n^2+2}\right)^2 \sin^2\phi \quad \ldots (2.1)$$

and by a single particle, where a particle is a clump of molecules, as

$$I_p(\phi) = E_0^2 \frac{8\pi^4 \varepsilon_0 c r^6}{\lambda^4}\left(\frac{n^2-1}{n^2+2}\right)^2 \sin^2\phi \quad \ldots (2.2)$$

Where r = radius of the sphere,

n = relative refractive index of sphere to medium, $= \frac{n_{sphere}}{n_{medium}}$

ε_0 = the permittivity of free space,
c = the velocity of light in a vacuum,
N = the number density of the scattering centres,
λ = wavelength of the radiation in the medium,
ϕ = angle between the dipole axis and the scattering direction, and
E_0= maximum value of the electric field strength of the incident wave.
(McCartney, 1970 and Measures, 1984)

Both equations 2.1 and 2.2 show the intensity of the scattered light varies as λ^{-4}. However, as the refractive index may also have a small wavelength dependence the scattered intensity is in fact not exactly proportional to λ^{-4}. Midelton (1952) gives a figure of -4.08 for wavelengths in the visible, while Elterman (1968) shows that dispersion leads to a deviation of less than 3% from the λ^{-4} law.

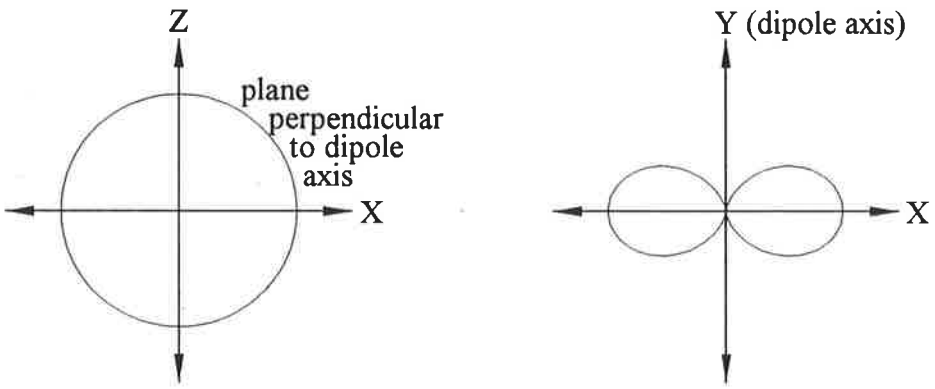

Figure 2.1 Intensity distribution patterns predicted by Rayleigh theory for scattering from a beam travelling in the +ve X direction and polarised in the Y direction.

Another point that should be considered from these equations is most easily seen with reference to figure 2.1. This figure shows that there is no light scattered in the direction of oscillation of the electric field of the incident beam.

A quantity that is found useful in a discussion of scattering is the angular scattering cross section (McCartney, 1976) which is also called the differential scattering cross section by Measures (1984). The terminology used by Measures will be followed here. The differential scattering cross section is the fraction of the power of the incident radiation that is scattered, per unit solid angle, in the direction of interest.

In mathematical terms the differential scattering cross section is defined by;

$$\frac{d\sigma_r(\phi)}{d\Omega} I_0 = I(\phi) \qquad \ldots (2.3)$$

The subscript $_r$ indicates Rayleigh theory.

Where $I_0 = \frac{1}{2} c \varepsilon_0 E_0^2$

= irradiance of the incident beam.

By substituting equations 2.1 and 2.2 into 2.3 it can be seen that for an individual molecule or particle illuminated by plane polarised light, the differential scattering cross section is given by,

$$\frac{d\sigma_{rm}(\phi)}{d\Omega} = \frac{9\pi^2}{N^2\lambda^4}\left(\frac{n^2-1}{n^2+2}\right)^2 \sin^2\phi \qquad \ldots (2.4)$$

$$\frac{d\sigma_{rp}(\phi)}{d\Omega} = \frac{16\pi^2 r^6}{\lambda^4}\left(\frac{n^2-1}{n^2+2}\right)^2 \sin^2\phi \qquad \ldots (2.5)$$

If it assumed that $n \approx 1$, (true for molecules but not necessarily for particles), then equation 2.4 can be approximated by:

$$\frac{d\sigma_{rm}(\phi)}{d\Omega} = \frac{\pi^2 (n^2-1)^2}{N^2\lambda^4} \sin^2\phi \qquad \ldots (2.6)$$

Born and Wolf (1970) show that for a gas, the term $(n^2 - 1)$ is approximately proportional to the number density N, which means that equation 2.6 has only a very slight dependence on N. The ratio $(n^2 - 1)/N$ varies less than 0.05 % for the range of N occurring between 0 and 65 km altitude.

Aerosols scatter light in the atmosphere, and in the lower troposphere this is usually the dominant form of scattering. However, most of this scattering is caused by particles that are too large for the application of Rayleigh theory. For this reason a discussion of aerosol scattering is left to the section on Mie scattering and only the equation relevant to molecular scattering is carried further here.

When Rayleigh theory is extended to include unpolarised light the angle ϕ no longer has any meaning. This is because the dipole axis may lie along any line in the plane perpendicular to the direction of propagation (ie the Y-Z plane). The only directions that can be uniquely defined are the direction of propagation of the incident beam and the direction in which the scattered radiation is being detected, and therefore θ is defined as the angle between these two directions.

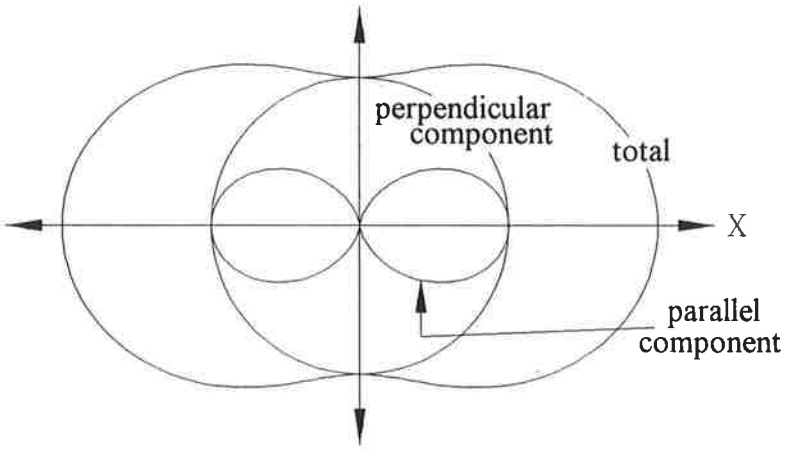

Figure 2.2 Intensity distribution pattern for Rayleigh scatter from an unpolarised beam travelling in the x direction. This is the sum of the two components given in figure 2.1. Perpendicular component refers to scattering of radiation with its electric vector perpendicular to the plane formed by the direction of propagation of the incident beam and the direction of observation.

The differential scattering cross section for an individual molecule which is illuminated by a parallel beam of unpolarised light is given by,

$$\frac{d\sigma_{rm}(\theta)}{d\Omega} = \frac{\pi^2 (n^2-1)^2}{2 N^2 \lambda^4} (1+\cos^2\theta)$$

... (2.7)

From figure 2.2 it can be seen that the intensity distribution pattern for Rayleigh scattered light from an unpolarised beam has peaks in the forward and backwards directions.

Rayleigh theory shows that light scattered at right angles to the incident beam is plane polarised. Because of the anisotropy of molecules, (which causes the dipole moment to be slightly out of alignment with the incident field), scattering by molecules causes some depolarisation of the scattered light. This results in some light with a polarisation parallel to the incident beam being detected at a scattering angle of 90 deg. The depolarisation ratio, δ_n^t is defined as,

$$\delta_n^t = \frac{I_=}{I_\perp}$$

... (2.8)

Where the perpendicular and parallel direction are taken with respect to the direction of the incident beam. The subscript n denotes natural or unpolarised incident light and the superscript t denotes total molecular scattering. The depolarisation is sometimes defined in terms of polarised incident light and/or for different spectral components of molecular scattering. Confusion about which is the correct depolarisation to use under different circumstances is sufficiently large that Measures (1984, p 46) sounds a warning about using the correct ratio and then goes on to use the wrong one.

Young (1980) gives a brief survey of depolarisation measurements for dry air and concludes that the effective value of δ_n^t is 0.0279.

To take account of the effects of depolarisation King (1923) calculates a correction factor, F_K^a, which will be called the King angular correction factor, by which the differential scattering cross section should be multiplied. The King angular correction factor is given by;

$$F_K^a(\theta) = \frac{1 + \delta_n^t + (1 - \delta_n^t)\cos^2\theta}{(1 - \frac{7}{6}\delta_n^t)(1 + \cos^2\theta)}$$

... (2.9)

Applying this correction to equation 2.7 gives,

$$\frac{d\sigma_{rm}(\theta)}{d\Omega} = \frac{\pi^2 (n^2 - 1)^2}{2 N^2 \lambda^4} \frac{1 + \delta_n^t + (1 - \delta_n^t) \cos^2\theta}{1 - \frac{7}{6}\delta_n^t}$$

... (2.10)

In most lidar applications, including the present case, it is the backscatter, $\theta = \pi$, which is of prime importance. The differential backscatter cross section per molecule for scattering from an unpolarised beam is given by;

$$\frac{d\sigma_{rm}(\theta = \pi)}{d\Omega} = \frac{\pi^2 (n^2 - 1)^2}{2 N^2 \lambda^4} \left(\frac{12}{6 - 7\delta_n^t} \right)$$

... (2.11)

The King-correction factor for backscatter is independent of the polarisation state of the incident beam (Kerker, 1969). This means that the correction factor and thus the backscatter cross section per molecule is independent of the polarisation characteristics of the laser used in a lidar that utilises only backscatter.

The Rayleigh molecular backscatter cross-section, without the King angular correction factor, for the atmosphere below 90 km is given by Kent and Wright (1970) as $4.60 \times 10^{-57} / \lambda^4$ $m^2 sr^{-1}$. When the King angular correction factor is applied, using $\delta_n^t = 0.0279$, this becomes,

$$\frac{d\sigma_{rm}(\theta = \pi)}{d\Omega} = \frac{4.75 \times 10^{-57}}{\lambda^4} \; m^2 sr^{-1}$$

... (2.12)

Collis et al (1976) give a value of the constant in equation (2.12) as 4.99×10^{-57} $m^6 sr^{-1}$. Using the refractive index of air, calculated from Kaye and Laby (1968) as 1.0002787 at $\lambda = 510$ nm for a dry atmosphere at 760 mm Hg and 15°C, and δ_n^t as above, the value of the constant is 4.88×10^{-57} $m^6 sr^{-1}$.

Fiocco (1984) gives equation 2.12 as

$$\frac{d\sigma_{rm}(\theta = \pi)}{d\Omega} = \frac{4.73 \times 10^{-57}}{\lambda^{4.09}} \; m^2 sr^{-1}$$

... (2.13)

Here the exponent of λ (4.09), takes account of the dispersion in air. The value of the constant used in equations 2.12 and 2.13 is applicable to the atmosphere at altitudes less than

90 km. Above this altitude the concentration of atomic oxygen becomes significant, and this change in composition causes a change in the refractive index. Thus the equation, as written, is no longer valid.

Equation 2.12 and 2.13 are used in the determination of the intensity of the backscatter from molecules expected for a particular lidar system.

2.2.2 Attenuation due to Molecular Scattering

In addition to backscatter it is important, for lidar studies, to consider the total amount of light scattered by a molecule or the total cross section σ_r. The total cross section allows the calculation of the degree of attenuation of a light beam as it propagates through the atmosphere. The total cross section is the ratio of scattered to incident power, so it is therefore equal to the integral of the differential scattering cross section over a sphere that is concentric with the scattering centre. Carrying out this integration on equation 2.10 gives;

$$\sigma_{rm} = \frac{8\,\pi^2\,(n^2 - 1)^2}{3\,N^2\,\lambda^4}\left(\frac{6 + 3\delta_n^t}{6 - 7\delta_n^t}\right) \qquad \ldots (2.14)$$

This is the total cross section per molecule. Again using a refractive index of 1.0002787 and a dry atmosphere at 760 mm Hg and 15°C, equation 2.14 becomes

$$\sigma_{rm} = \frac{4.18\text{x}10^{-56}}{\lambda^4}\ m^2 \qquad \ldots (2.15)$$

Then substituting λ = 510 nm and multiplying by N to obtain the volume total cross section, for the conditions stated above, gives

$$\beta_{rm}(\lambda = 510) = N\sigma_{rm}(\lambda = 510) = 1.57\text{x}10^{-5}\ m^{-1} \qquad \ldots (2.16)$$

This is the attenuation coefficient due to scattering from molecules under the atmospheric conditions stated above. With increasing altitude density decreases so that the attenuation coefficient decreases also.

Altitude (km)	Vertical Path	Vert. Return Path	45° Path	45° Return Path
1	0.015	0.030	0.021	0.042
2	0.028	0.055	0.040	0.081
5	0.060	0.117	0.085	0.165
10	0.094	0.178	0.133	0.252
20	0.118	0.222	0.167	0.314
50	0.12	0.23	0.17	0.33
100	0.12	0.23	0.17	0.33

Table 2.1 Molecular scattering attenuation for paths from sea level to the altitudes indicated.

Attenuation coefficients due to molecular scattering for a light beam (λ=510 nm) transmitted from the ground to various altitudes, are given in table 2.1. This table was calculated using a simple model for the density altitude profile and it was assumed that (n^2 - 1) is exactly proportional to N. From the table it can be seen that the attenuation coefficient due to molecular scatter for a vertically projected beam drops off rapidly with altitude. In the absence of aerosols a beam transmitted from the ground to 50 km and reflected back again would be attenuated by about 23% due to scattering by atmospheric molecules, most of this scattering occurring below 20 km.

Molecular absorption also serves to attenuate a light beam as it propagates through the atmosphere. However, when the wavelength of the beam is distant from the absorption lines of all atmospheric constituents then the absorption coefficient will be much less than the scattering attenuation coefficient. Under these circumstances the extinction coefficient, which is the sum of the scattering and absorption coefficients, ($Q_{ext} = Q_{sca} + Q_{abs}$) is given to a good approximation by the scattering attenuation coefficient, ie ($Q_{ext} \approx Q_{sca}$).

2.2.3 Raman Scattering

When monochromatic light, or light of sufficiently narrow spectral width, is scattered by a molecular gas or liquid the spectrum of the scattered light can be observed to contain

lines at wavelengths different from that of the incident radiation. This effect was first observed by Raman (1928), and is due to the interaction of the radiation with the quantised vibrational and rotational energy levels of the molecule. Raman scattering involves a transfer of energy between the scattered light and the molecule, it is therefore an inelastic process. The cross sections due to Raman scattering are included by the Rayleigh theory (Young, 1982) even though Raman spectroscopists use the term Rayleigh line to indicate only the unshifted central component of the scattered light.

Scattered radiation that loses energy during its interaction with a molecule, and so decreases in frequency, is said to have a Stokes shift, while radiation that gains energy and increases in frequency is said to have an anti-Stokes shift. In general the Stokes radiation is more intense than the anti-Stokes as the Stokes can always occur, subject to selection rules, while the anti-Stokes also requires the molecule to initially be in an excited state.

A number of models have been developed to help understand and explain the complex form of the Raman spectrum. The vibrating rotator model can be used to show how the molecular vibrational energy levels are split by a number of rotational levels, (Banwell 1983). Figure 2.3 shows part of the spectrum of a diatomic molecule.

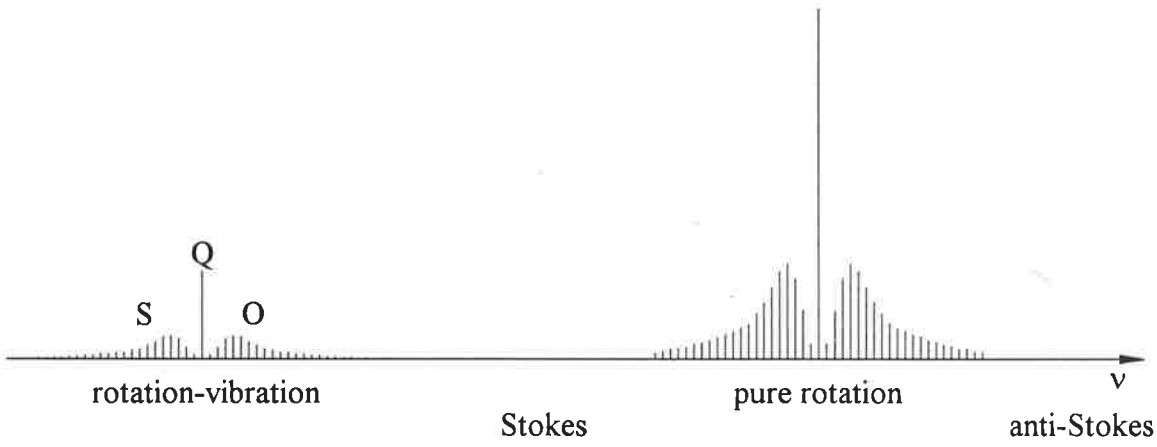

Figure 2.3 The Raman spectrum of a diatomic molecule. (After Banwell, 1983).

The most important aspect of Raman scattering is that the frequency shift of the scattered radiation is dependent on the structure of the scattering molecule. This allows molecules to be identified by the spectrum of the light that they scatter.

In discussing Raman scattering it is necessary to introduce the vibrational and rotational quantum numbers v and J respectfully. Transitions which involve a change in rotational quantum number are denoted by letter symbols as given below;

ΔJ	-2	-1	0	+1	+2
Branch	O	P	Q	R	S

The Q-branch contains a number of degenerate lines; this is the reason for the higher intensity of this branch.

The Q-branch frequency shifts for a number of molecules that can be found in the atmosphere are given in figure 2.4. Measures (1984) gives a more comprehensive list that includes differential cross sections.

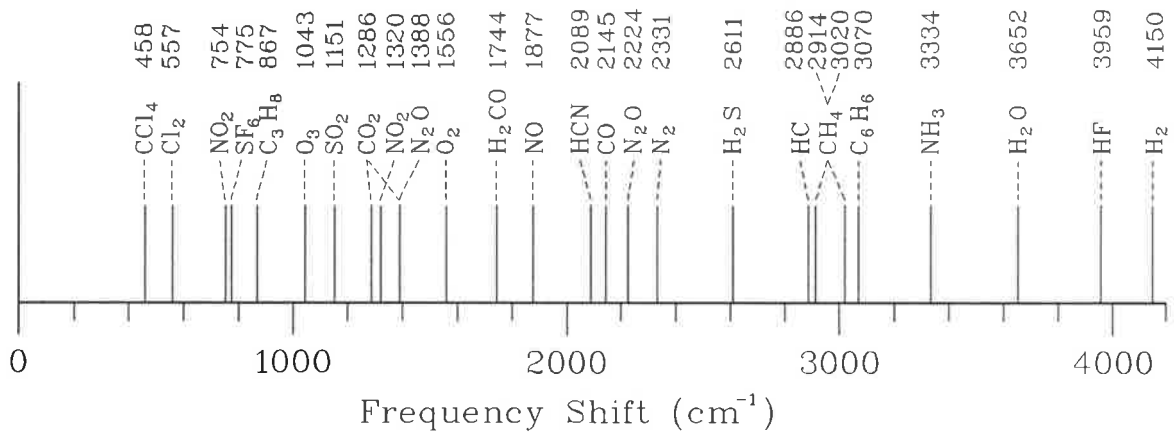

Figure 2.4 Q-branch frequency shift of the Raman spectrum of a number of molecules that are found in the atmosphere. (After Measures, 1984).

The pure rotational Raman spectrum (PRRS), which occurs when there is no vibrational transitional transition, ie $\Delta v = 0$, is more difficult to measure as the spectral shift of the lines is quite small. The separation of lines in the PRRS of N_2 is about 16 cm^{-2} while the vibrational transition $\Delta v = 1$ has a shift of about 2330 cm^{-2}.

The energy level diagram and resulting spectrum for the PRRS of a linear molecule is shown in figure 2.5. The intensities of the individual lines and the shape of the envelope of the lines are temperature dependant. This allows temperature determination from PRRS.

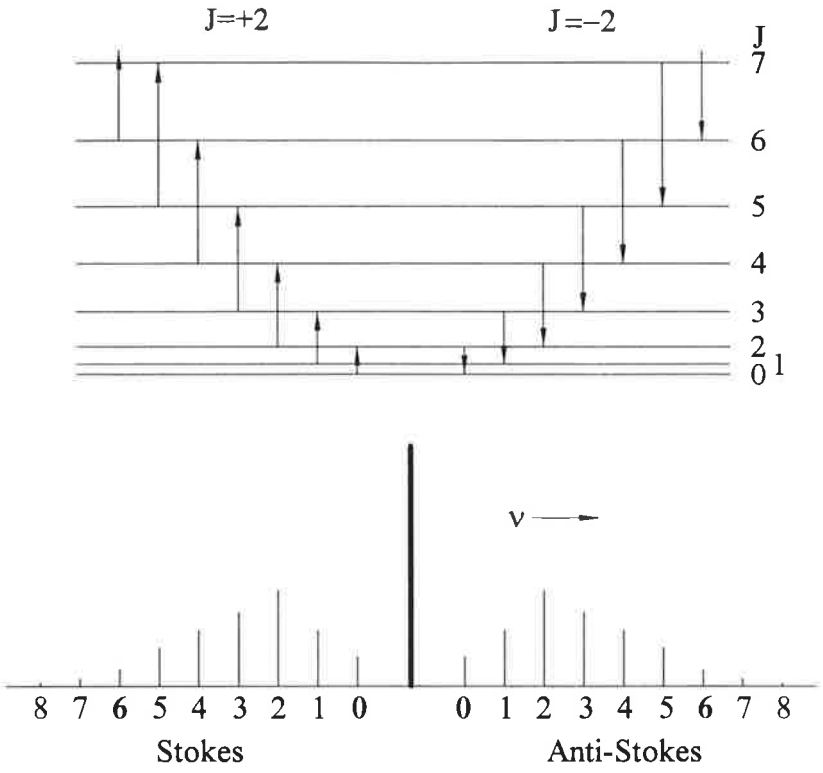

Figure 2.5 The rotational energy levels of a diatomic molecule and the rotational Raman spectrum arising from transitions between them. Note, spectral lines are numbered according to their lower J number. (After Banwell, 1983).

2.2.4 Brillouin Scattering

The shape of the central unshifted line in the Raman spectrum, called the Cabannes line by Young (1982), is dependent on the environment of the scattering molecules. When the scattering gas is at low density the motions of the molecules are independent of each other and dependent only on the temperature of the gas. This leads to the Cabannes line taking the familiar Gaussian shape (see section 2.2.5). As the density of the gas is increased the motion of the molecules becomes increasingly correlated. This leads to the Cabannes line splitting into three components.

The symmetrically frequency shifted Brillouin doublet is the result of scattering from acoustic phonons associated with propagating pressure fluctuations (sound waves) in the gas. Boley et al (1972) give a comparison of the shape of the Cabannes line, both theoretical and experimental, for hydrogen at three different values of the y parameter (equation 2.17). These data show a very good agreement between the theoretical and experimental results.

Central to the theory of Brillouin scattering is the y parameter, which is the ratio of collision frequency to the spatial frequency of scattering (Shimizu et al, 1983). This parameter is defined as;

$$y = 2.308 \frac{T + 110.4}{T^2} \frac{p\lambda}{\sin(\theta/2)} \quad \ldots (2.17)$$

There are two theories used to describe Brillouin scattering; each is applicable to a different range of the y parameter. The hydrodynamic description is applicable to gases with high densities, ie large y values. The kinetic or low density, low y value regime has a separate theory. The atmosphere has a relatively low y value even at surface level, and therefore comes within the kinetic regime.

The theory of Brillouin scattering in the kinetic regime has been developed (Yip et al, 1964; Sugawara, 1967; Boley, 1972 and Tenti, 1974) to the stage where theoretical and experimental results agree to within the accuracy required for the present purposes, (Schwiesow and Lading, 1981).

Using an early theory Fiocco et al (1971) gave estimates of the relative increase in width of the Cabannes line due to Brillouin scattering at 4 altitudes in the atmosphere, and these results are presented in table 2.2

Altitude (km)	Relative increase in width of Cabannes line when Brillouin scattering is included	Relative error in temperature
0	1.082	0.17
4	1.055	0.11
10	1.029	0.059
18	1.008	0.016

Table 2.2 Shows the relative increase in width of the Cabannes line when the effects of Brillouin scattering are included for four atmospheric altitudes (Fiocco et al, 1971).

From table 2.2 it can be seen that any method that relies on the measurement of the width of the Cabannes line for temperature determination in the lower atmosphere must take into account the effect of Brillouin scattering, [see for example Shipley et al (1983),

Schwiesow and Lading (1981) and Shimizu et al (1986)].

Schwiesow and Lading also point out that as the y parameter is temperature dependent an iterative procedure may be needed if accurate temperature measurements are to be made using the width of the Cabannes line.

2.2.5 Doppler Effects

In the following section only the Cabannes line is considered and Brillouin scattering is ignored.

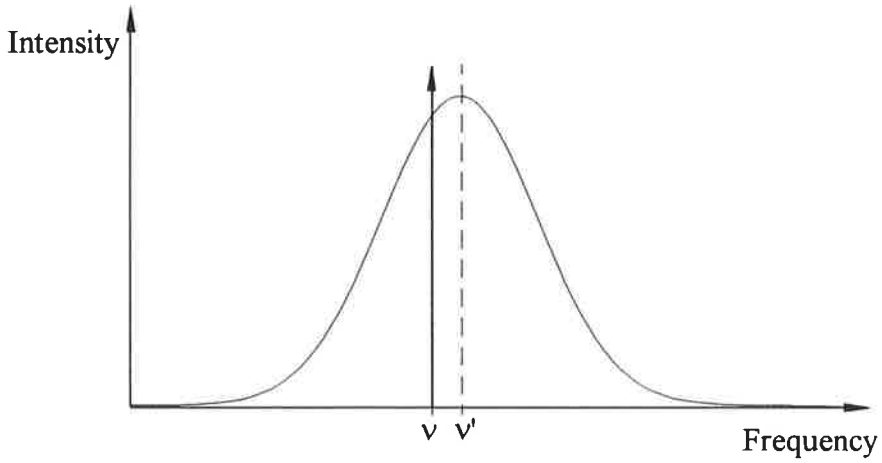

Figure 2.6 Shows the frequency distribution function for Rayleigh backscattering from a perfectly clean dry atmosphere, for monochromatic incident radiation of frequency ν. The broadening is due to random thermal motions and the shift is due to wind.

Both random thermal motions and wind contribute to the motion of air molecules. When light is scattered by atmospheric molecules it will generally suffer a change in frequency due to the Doppler effect, (see figure 2.6). Hyllerass (1970), amongst others, derived a formula for the change in frequency of a photon that is reflected from a mirror that is moving at a non-relativistic velocity, the same derivation and formula are also applicable to light scattered from a molecule. If we consider only the backscattered light and the component of velocity of the scattering centre in the direction of the scatter, then the change in frequency $\Delta\nu$ is given by,

$$\Delta\nu = \nu' - \nu \approx 2\,\nu\frac{v}{c} \qquad \ldots (2.18)$$

Where ν = frequency of the incident photon,

ν' = frequency of the scattered photon, and

v = the component of the velocity of the scattering centre in the direction of scatter (backscatter).

The random thermal motions of the air molecules cause backscattered light to be spectrally broadened, while wind causes an overall spectral shift.

The velocity distribution function for the molecules of a gas that is in thermal equilibrium is given by Maxwell's distribution. Kennard (1938) gives the function that describes the distribution of a component of the velocity, of such a gas, in a particular direction, ie.

$$P(v_x)\, dv_x = \left(\frac{M}{2\pi k T}\right)^{1/2} \exp\left(-\frac{M v_x^2}{2 k T}\right) \quad \ldots (2.19)$$

Where M = molecular weight,

k = Boltzmann constant,

T = Temperature in Kelvin, and

v_x = component of velocity in the x direction.

Using equation 2.18 and 2.19 it can be shown that when monochromatic light is backscattered by a gas the frequency distribution of the light is given by,

$$P(\nu')\, d\nu' = \frac{2}{\pi^{1/2}\,\Delta} \exp\left(-\frac{4\,(\nu' - \nu)^2}{\Delta}\right) \quad \ldots (2.20)$$

Where

$$\Delta = \frac{4\nu}{c}\left(\frac{2 k T}{M}\right)^{1/2} \quad \ldots (2.21)$$

So that $P(\nu')$ is a Gaussian or normal distribution with a full width at the 1/e points of Δ (fwhm = $(\ln 2)^{1/2}\Delta$).

The above formulas 2.19 to 2.21 are strictly true only if all the atoms or molecules of the gas have the same atomic or molecular weight. Air contains a number of molecular and atomic species, and therefore the frequency distribution function for Rayleigh backscattered

light $P_a(\nu')$ is the sum of a number of Gaussian functions, one for each gaseous constituent.

Species	M	Concentration (ppm)	$\frac{d\sigma_{rm}(\theta=\pi)}{d\Omega}$	Δ (Hz)	% contribution to total scattering (Gaussian height)
N_2	28.02	7.808×10^{5}	8.49×10^{-32}	1.904×10^{8}	80.958
O_2	32.00	2.095×10^{5}	7.07×10^{-32}	1.781×10^{8}	18.098
Ar	39.95	9.34×10^{3}	7.60×10^{-32}	1.594×10^{8}	0.867
CO_2	44.01	3.25×10^{2}	1.94×10^{-31}	1.579×10^{8}	0.077

Table 2.3 Data used to calculate frequency distribution function for Rayleigh backscatter from atmospheric gas.

In table 2.3 details are given of the four most abundant gaseous species in the atmosphere, which together make up more than 99.9% of the atmospheric molecules. The information in this table was used to form the frequency distribution function $P_a(\nu')$, where the subscript a indicates air. This function, $P_a(\nu')$, is the sum of the Gaussian function which describe the Doppler broadening due to each of the four atmospheric constituents listed in the table. This distribution was then compared to a single Gaussian that represented the frequency distribution for a gas with particles of M = 28.966 (mean molecular weight of air), $P_m(\nu')$, where the subscript m stands for mean of air. Figure 2.7 shows the ratio of these two distributions as a function of frequency. The main difference in the shape of the distributions is the rate at which they decrease in the wings, $P_a(\nu')$ falling off more slowly than $P_m(\nu')$.

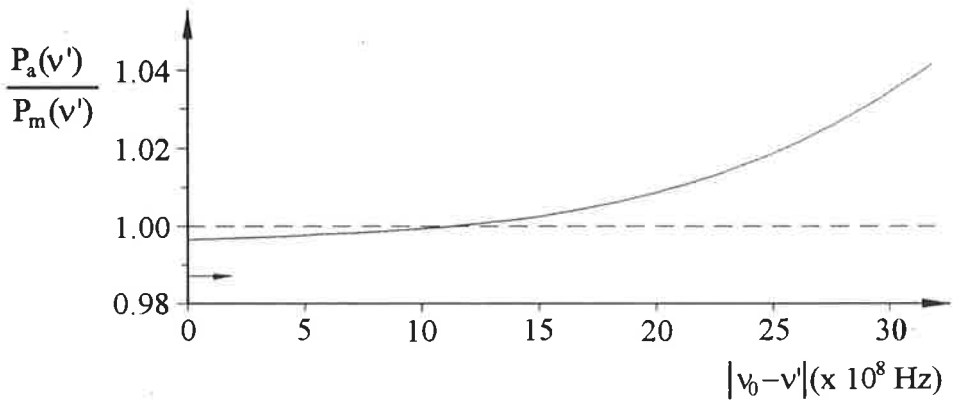

Figure 2.7 Ratio of frequency distribution functions $P_a(\nu')$ and $P_m(\nu')$. See text for explanation. The arrow indicates the 1/e half width of $P_m(\nu')$.

Using a weighted fitting procedure to fit a Gaussian to the function $P_a(\nu')$ it is possible to estimate the error in width, and thus temperature, caused by assuming that the actual frequency distribution is $P_m(\nu')$. It is found that for temperatures between 150 and 350 K (includes all temperatures likely to be found in the middle atmosphere) the error in width of the fitted Gaussian is less than 0.5% and the error in temperature is less than 1%. The particular fitting procedure used always gives a measured temperature greater than the actual temperature for the non-Gaussian function $P_a(\nu')$.

Wind, the gross motion of air, causes the distribution function to move in frequency while maintaining its shape. The frequency shift can be calculated directly from equation 2.18. This equation shows that the frequency shift is directly proportional to the component of the wind velocity in the direction of scattering, or the radial wind velocity.

2.2.6 Fluorescence and Resonant Scattering

The previous sections on scattering are concerned with the scattering of light that is distant from any absorption line of the scatterer. When the incident light is within an absorption line of the scatterer then it may be absorbed and re-emitted, either at the same or a lower frequency. For the case where the emitted photon is the same frequency as the absorbed photon, the process in called resonant scatter, whilst where the emitted photon has a lower frequency it is called fluorescence.

The absorption cross section is dependant on the transition probability and may be large. This leads to large values for both the resonant scatter and fluorescence cross sections. These cross sections may however be reduced by collisional quenching.

It is important to note that because each type of atom and molecule has a unique absorption (and hence resonant scatter) and fluorescence spectrum, these may be used to identify and measure the concentration of a particular species.

A good description of the theory of fluorescence and resonance can be found in both Chamberlain (1961) and Measures (1984).

2.3 Mie Scattering

The theory of scattering that was developed by Mie early this century is a general

solution that covers the scattering of electromagnetic radiation by a homogeneous sphere. Because it is a general solution to this problem it provides solutions for all wavelengths of radiation and spheres of all sizes. A parameter that is basic to the Mie theory is the size parameter α. This parameter is a measure of the relative size of the scattering particle to the wavelength of the radiation. It is defined as:

$$\alpha = \frac{2 \pi a}{\lambda} \qquad \ldots (2.22)$$

Where a = the radius of the scattering particle, and
λ = the wavelength of the incident radiation.

When the particle size is small compared to the wavelength of the incident radiation (ie. α small) Mie theory reduces to Rayleigh theory, this point is illustrated in figure 2.8. This figure shows the angular scattering pattern for particles of increasing α, and illustrates that as α increases the pattern deviates further from that of the Rayleigh theory.

Mie theory uses a large amount of complicated mathematics and because of this is not used in the ranges where either Rayleigh theory or geometrical optics apply. This has led to the common use of Mie scattering to mean scattering from particles larger than those to which Rayleigh theory applies and smaller than those to which geometrical optics applies.

Mie theory solves Maxwells equations for the boundary conditions imposed by a homogeneous sphere of refractive index different from that of the surrounding medium. Since Mie first provided the solution to this problem other workers have extended the calculations to include other shapes (eg infinite cylinders and paraboloids) and have provided methods for finding solutions for irregular shapes and non-homogenous particles, see for example Van De Hulst (1951), Bohren and Huffman (1983), Bayvel et al (1981) and Kerker (1969).

The atmosphere contains particles with a wide variety of shapes, sizes and refractive indices. There are many problems associated with the measurement of aerosol parameters arising mainly from their delicate nature and small size; see for example Davies (1987), Yaskovich (1986), Georgiyevskiy et al (1986) and McCartney (1976). The processes of evaporation, condensation, coagulation, adsorption, desorption and chemical reactions serve to change the atmospheric aerosol on a short time scale. These problems mean that it is difficult to determine the nature of the aerosols in the atmosphere.

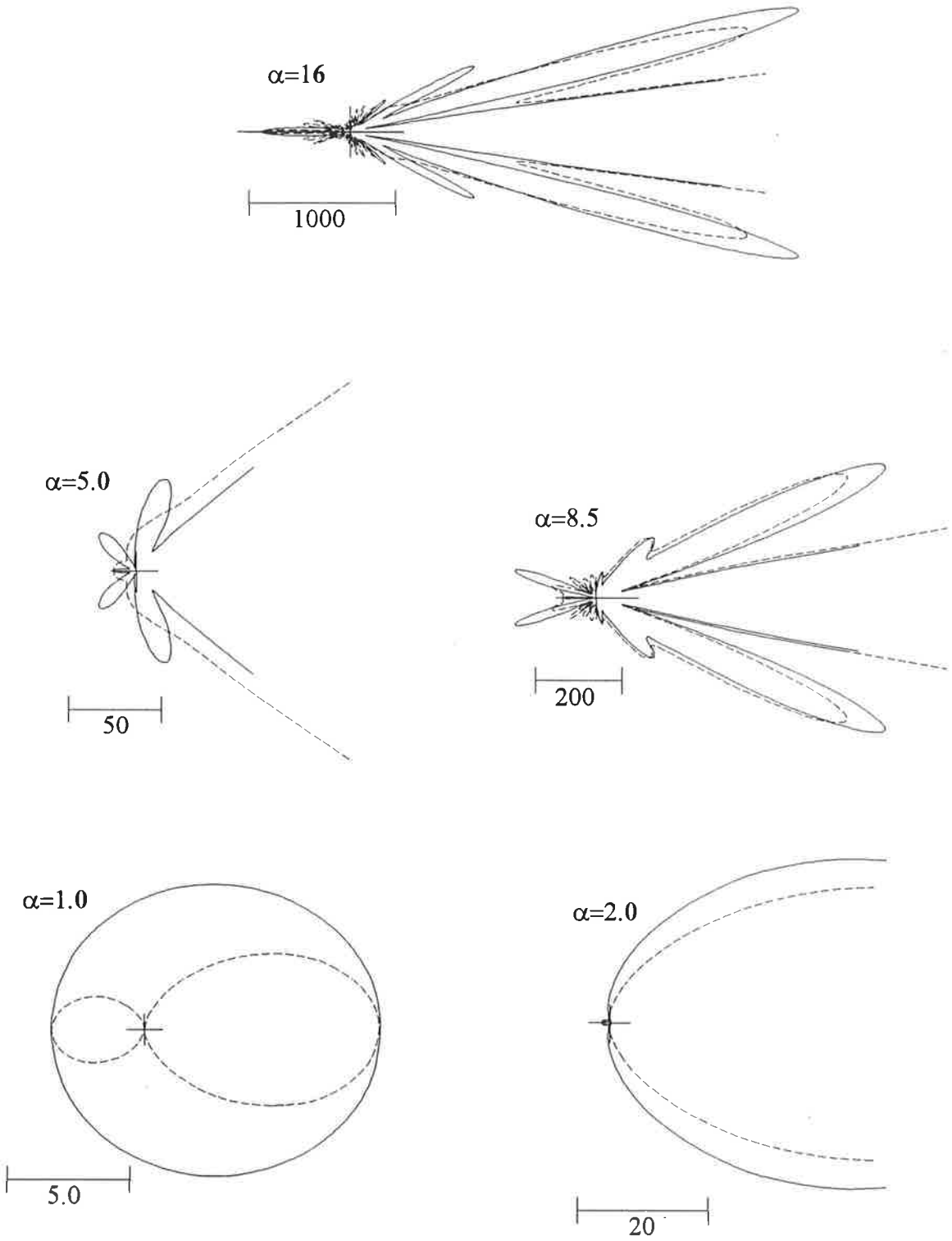

Figure 2.8 Shows the Mie intensity distribution patterns for particles with different size parameters. All patterns are calculated for refractive index of surrounding medium=1, refractive index of particle = 1.4+0i and for plane polarised incident light. The solid line represents the angular scattering cross-section for the plane perpendicular to the direction of polarisation of the incident beam. The dashed line represents the same quantity calculated for the plane defined by the direction of propagation of the incident beam and its direction of polarisation. Note change of scale in each diagram, scales are given only to indicate relative intensities.

In an attempt to gain some insight into the atmospheric aerosol scattering problem a number of simplifying assumptions can be made, the most common of these is to assume that the particles are all spherical and homogenous. This allows a solution to be found from Mie`s formulation.

Most lidar systems are able to measure only the intensity of the backscatter from the atmosphere. Even if the signal due to aerosols can be separated from that due to molecules, this information alone is not sufficient to determine anything further about the atmospheric aerosol. Given the intensity of light backscattered from an aerosol-distribution it is not possible, even for a non-absorbing particle, to determine the extinction of a beam due to aerosol scatter. The backscatter efficiency and the extinction due to scattering from a single homogenous sphere are only very loosely correlated. So, even for this extremely simplified case it is not possible to infer any more information on the aerosols given the backscattered intensity. Apart from this, variations in refractive index (both real and imaginary parts) affect the extinction and backscatter cross-sections differently.

Extinction Coefficients (km^{-1})							
	Molecular Extinction					Aerosol Extinction	
	Tropical	Mid-Latitude		Sub-Arctic			
Altitude km		Summer	Winter	Summer	Winter	Clear	Hazy
0	1.5e-2	1.5e-2	1.6e-2	1.5e-2	1.7e-2	1.8e-1	8.6e-1
0-1	1.4	1.4	1.5	1.5	1.6	1.1	5.4
1-2	1.3	1.3	1.4	1.3	1.4	5.2e-2	2.0
2-3	1.2	1.2	1.2	1.2	1.3	2.2	7.2e-2
3-4	1.0	1.0	1.1	1.1	1.1	1.0	2.6
4-5	9.5e-3	9.5e-3	9.8e-3	9.6e-3	9.9e-3	6.5e-3	9.6e-6
5-10	7.0	7.0	7.0	7.0	7.0	3.9	3.9
10-15	3.9	3.9	3.6	3.6	3.4	3.2	3.2
15-20	1.9	1.8	1.6	1.7	1.5	2.5	2.5
20-25	7.9e-4	8.2e-4	7.5e-4	8.0e-4	7.1e-4	8.7e-4	8.7e-4
25-30	3.7	3.9	3.6	3.9	3.4	2.7	2.7
30-40	1.2	1.3	1.2	1.3	1.1	4.9e-5	4.9e-5
40-50	3.0e-5	3.2e-5	2.5e-5	3.2e-5	2.3e-5	3.4e-6	3.4e-6
50-70	7.5e-6	8.2e-6	6.0e-6	8.5e-6	5.2e-6	1.3e-7	1.3e-7
70-100	<1e-6	<1e-6	<1e-6	<1e-6	<1e-6	4.4e-10	4.4e-10

Table 2.4 Molecular extinction coefficients for summer and winter in three latitude zones, and aerosol extinction coefficients for two model aerosol distributions, for λ=510 nm. Estimated from McClatchey et al (1978).

The extinction cross-section given by the Mie theory for size parameters corresponding to those of the atmospheric aerosols and visible light are much larger than those for molecular scattering. This means that in the lower parts of the atmosphere where the aerosol concentrations are high the extinction of a beam is much greater than that due solely to molecular scatter (as given in table 2.1). Due to the large range of aerosol types and the large range of concentrations in which they occur, previously measured extinction values can serve only as a guide to estimating atmospheric transmission. Using the information given by McClatchey et al (1978) total extinction coefficients, as a function of altitude, have been estimated for a wavelength of 510 nm. These estimates are presented in table 2.4 and they show the wide range of extinction coefficients that occur in the atmosphere under normal conditions, the possible effects of such things as clouds and fog are not included. Table 2.4 also shows the advantage of situating a stratospheric lidar at a high altitude site.

2.4 Conclusions

The theory of light scattering by atmospheric molecules is well understood. Calculation of backscattered intensity (of primary importance in LIDAR work) and attenuation coefficients due to the molecular that occurs in the atmosphere is straight forward.

While the theory of scattering from aerosol particles is well developed, the complex nature of these particles makes the application of the theory extremely difficult. Many generalisations and assumptions must be made before scattering and attenuation coefficients can be estimated.

3 LIDAR Systems, An Overview

3.1 Introduction

The LIDAR (LIght Detection And Ranging) technique provides a method of remote sensing of the atmosphere. It relies on the interactions (scattering and absorption) of a beam of light with the constituents of the atmosphere. A portion of the scattered light, usually that which is backscattered, is collected and analysed to provide information on the volume in which the scattering occurred. Depending on the design of the lidar a wide variety of parameters may be measured, these include molecular and aerosol densities, temperature, wind velocity and atomic or molecular species concentration.

3.2 Historical Overview

The method of determining atmospheric density by the detection of scattering from a beam of light projected into the atmosphere was first proposed by Synge (1930). He proposed the use of anti-aircraft searchlights as the source of the beam and, after collecting the scattered light with a large telescope, detection by photoelectric apparatus. With the source and detector separated by a large distance ≈10 km, the altitude of the scattering could be determined by geometry. This type of lidar, with source and detector separated by large distances has become known as bi-static lidar. To improve the signal level and thus increase the maximum altitude at which measurements could be made, Synge also suggested that not

one but a large array of several hundred searchlights could be used to illuminate the same region of the sky.

The first reported results obtained by using the principles of this method are those of Duclaux (1936) who made a photographic recording of the scattered light from a searchlight beam at a distance of 2.4 km with an F:1.5 lens and an exposure of 1.5 hours. The beam was visible on the photograph to an altitude of 3.4 km. These results were extended by Hulbert (1937) who photographed a beam to 28 km and made calculations of atmospheric densities from the photographs.

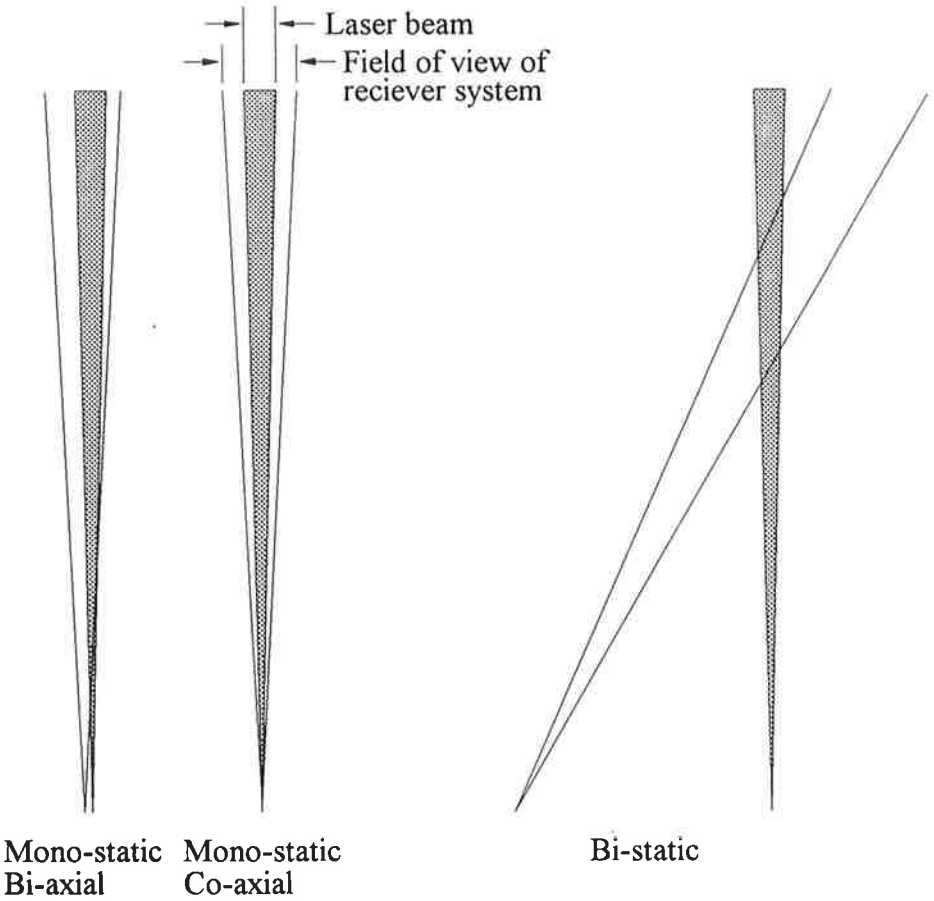

Figure 3.1 Lidar laser beam and detector optics field of view arrangements.

A mono-static lidar is a system which has its transmitter and receiver at the same location, (see figure 3.1). Mono-static systems can be subdivided into two categories; co-axial systems where the laser beam is transmitted coaxially with the field of view of the receiver, and bi-axial systems, where the transmitter and receiver are located adjacent to each other. The first recorded use of a mono-static system is that of Bureau (1946) in 1938, in

which case the system was used for the determination of cloud base altitudes. As is usual with a mono-static system the light source was pulsed, thereby enabling the range to be determined from the round trip time of the scattered light pulse.

With refinements of technique and improved instrumentation, including electrical recording of backscattered light intensity, Elterman (1953) was able to calculate density profiles up to 67.7 km. He used a bi-static system with a separation between transmitter and receiver of 20.5 km. From his density profiles Elterman was also able to calculate temperature profiles.

The use of a pulsed mono-static system for density determination was reported by Friedland et al (1956). In this paper the authors summarised the advantages of the mono-static system over the then more commonly used bi-static system. The major advantage they described was that for each pulse fired from a mono-static system a complete scattering profile can be recorded (≈500 μs), although commonly many such profiles are required to obtain useful information. A bi-static system, on the other hand, can only detect scattering from a small layer in the atmosphere and the detector must be moved many times in order to obtain a profile. The re-alignment of the detector can be difficult due to the large separations and the alignment requirements of the beam and the detector field of view.

A recent suggestion by Welsch and Gardner (1989) proposes the use of a detector array in a bi-static lidar system. This would allow the lidar to record the signal from many points along the laser's path for each pulse, overcoming, to some extent, the problems mentioned above. It may also allow very good altitude resolution to be obtained over small altitude ranges. This method of recording the lidar signal is in fact equivalent to the method used by Duclaux in 1936, his film being the analogue of the detector array.

3.3 Lasers in LIDAR

The invention of the laser in 1960 and the giant pulse laser in 1962 provided a powerful new tool which could be used to probe the atmosphere. Developments in the lidar technique have been closely linked to advances in laser technology.

Two properties of the laser, low beam divergence and extremely narrow spectral width, provide a number of advantages over white light as the light source for a lidar. Firstly,

as the laser beam has a low divergence it is not necessary to use a large reflector to transmit the beam into the atmosphere, a small telescope if any is all that is required. Secondly and more importantly, the laser has a narrow spectral width.

The narrow spectral width of the laser has been used to advantage in many different ways in different lidar systems. The first used and simplest advantage is that it allows the detection optics to spectrally filter the incoming light. A narrow-bandpass filter, which is tuned to the laser wavelength is placed in the detection optics. The filter will transmit a relatively large fraction of the collected scattered laser light while transmitting only a very small amount of the background white light. The first reported results obtained using a lidar that incorporated a laser and a narrow bandpass spectral filter are those of Fiocco and Smullin (1963). These workers used a ruby laser which fired pulses of 0.5 J at a wavelength of 694 nm and a spectral filter with a 0.2 nm bandpass in the detection optics.

3.4 Aerosol and Cloud LIDAR

Over the past 25 years a number of lidar systems have been built at many research establishments around the world which are designed to study the troposphere and lower stratosphere. In particular the stratospheric aerosol layer, and to a lesser extent clouds have beenstudied with these systems. In general these are relatively simple systems consisting of the following essential components:

1)a laser with a mean power of a few Watts, (a range of lasers have been used have been used for this purpose),

2)a telescope with a diameter of approximately 30 - 60 cm, (usually one which is readily available),

3)a narrow bandpass spectral filter with a bandpass of anything down to about 0.3 nm (this filter width makes the instrument suitable for night time use only; for daytime use the filter width must be reduced), and

4)a photomultiplier to suit the laser wavelength and the signal strength.

Recently more sophisticated systems have been used for cloud and aerosol studies. These include; high spectral resolution techniques (Grund and Eloranta, 1991 and She et al,

1992), multiple wavelength techniques (Sasano and Browell, 1989) and polarisation techniques (Sassen, 1991). A review of this type of work is presented in Reagan et al (1989).

In the last few years lidars have been used to study polar stratospheric clouds in order to determine their role in the Antarctic ozone depletion (Stefanutti et al 1992)

3.5 Modern Rayleigh LIDAR

The term Rayleigh lidar is used to describe a lidar system that is designed to collect the photons in the Cabannes line backscattered from altitudes above the aerosol layer and below about 100 km. The result of this type of measurement allows the calculation of a relative density profile, this in turn allows the determination of the absolute temperature profile, (see chapter 7). The measurement of the density and temperature profiles allow studies of the temporal variations in atmospheric structure caused by gravity waves, planetary waves and tides as well as seasonal and climatic changes.

The principle of operation of a Rayleigh lidar system is quite simple. A pulse of laser light is fired up into the atmosphere, and any photons that are backscattered and collected by the receiving system are counted as a function of range. After a correction for range the signal will be proportional to the atmospheric density profile. This technique assumes that atmospheric transmission throughout the region being studied is high enough not to have an affect on the experiment.

In order to give an idea of the "power" or effectiveness of a Rayleigh lidar system it is usual to calculate the power-aperture product, that is the mean power of the laser (watts) multiplied by the collecting area of the receiver system (m^2). With reference to section 3.10 it can be seen that the lidar signal strength is proportional to the power-aperture product. It can also be been seen that the signal strength is dependent on a number of other parameters. However, these tend to vary little from one system to another. This makes the power-aperture product a good measure of system performance.

To be effective a Rayleigh lidar should have a power-aperture product of more than about 3 and of course the higher the better. This means that the cost of the laser and the collecting telescope is quite high. So, even though the appropriate laser technology has existed for many years only relatively few of this type of lidar are in existence.

The choice of laser for use in a lidar depends on a number of factors, including cost. The best wavelengths for a Rayleigh lidar are in the mid visible region. If one goes into the infra-red the scattering cross-section is smaller so less light is scattered. In the other direction, the ultra-violet, the scattering cross-section is higher but the atmospheric transmission is much lower leading to an overall reduction in signal strength.

Most Rayleigh lidar systems use a frequency doubled neodymium YAG laser, which operates at 532 nm in the green. Another advantage of this type of laser is that it is a well-developed technology and in general provides a reliable light source. The designers of some systems have opted to use a XeF laser operating at about 352 nm, in the ultraviolet. The higher power available from this type of laser overcomes, to some degree, the atmospheric transmission problem. The technology of the XeF laser is relatively new and more complex when compared to the YAG systems and therefore cannot be considered to be as reliable. Nothing is more frustrating to a lidar worker than an unreliable laser, except perhaps cloudy skies, Personal Experience (1992,1993).

The French group from the Service d'Aeronomie du CNRS, France, has operated a Rayleigh lidar at the Observatory of Haute-Provence since 1979 (Hauchecorne and Chanin 1980, Chanin and Hauchecorne 1981, Chanin and Hauchecorne 1984, Chanin et al 1987). The data set collected by this group provides an excellent record of temperatures in the middle and upper stratosphere and in the lower mesosphere.

A Rayleigh lidar has been operated by a group from University College of Wales, Aberystwyth in the United Kingdom since December 1982. To the end of 1989, some 138 sounding session had been completed (Jenkins et al 1987, Mitchell et al 1990).

An Italian group has been operating a Rayleigh lidar since 1988 at Frascati, Italy, (Adriani et al, 1991). This group recorded sixty temperature profiles in the year starting November 1988.

Using a XeF laser, workers from Kyushu University, Fukuoka, Japan have reported observations of temperature and density in the period April 1985 to March 1986, (Shibata et al 1986 a,b). Shibata et al (1988) shows that this work continued up until at least April 1988, however lack of more recent publications makes it difficult to establish the current status of this research.

Workers from the Max Plank Institut fur Aeronomie in Germany have developed a mobile Rayleigh lidar system using a XeF laser, but the only results available from this system are those of Czechowsky et al (1990) and are for 15 nights in the period 21st January 1990 to 7th March 1990.

STATION	LASER	TELESCOPE	POWER-APERTURE PRODUCT
Aberystwyth Wales 52.4°N 4.1°E	Nd:YAG (doubled) PRF 10 Hz av. power 3W	1 m Diameter	2.4 Wm^2
Observatory Haute Provence, France 44°N 13°E	Nd:YAG (doubled) av. power 15W	≈0.75 m^2	11 Wm^2
Italy 42°N 13°E	Nd:YAG (doubled) PRF 10 Hz av. power 2.5W	5 m^2 mosaic	12.5 Wm^2
Fukuoka Japan 33.6°N 130.4°E	XeF (λ=351 & 353) PRF 80 Hz av. power 16W	0.5 m Diameter	3.1 Wm^2
Germany mobile system	XeF (λ=351) av. power 20W	0.8 m Diameter	10 W m^2
Arecibo Puerto Rico 18°N 67°W	Dye Laser (Na) λ=589 PRF=200 Hz av. power 5W	1.17 m^2	5.9 Wm^2
York Canada 43.8°N 79.0°W	Nd:YAG (doubled) PRF 20 Hz av. power 10W	0.25 m Diameter	1.9 Wm^2
London Canada 43.0°N 81.2°W	Nd:YAG (doubled) av. power 15W	2.7 m Diameter	86 Wm^2
Adelaide Australia 35°S 138°E	Cu Vapour PRF 2kHz av. power 4W	1 m Diameter	3.1 Wm^2

Table 3.1. A summary of Rayleigh lidar stations and their power aperture products.

Powerful sodium lidar systems used by workers at the University of Illinois at Urbana-Champaign are also used to measure Rayleigh scattering through the stratosphere. These measurements have been used to calculate gravity wave spectra, (Gardener et al, 1989 and Beatty et al, 1992).

There are two stratospheric lidar systems operating in Canada. One operated at York University is of modest power, (Carswell et al, 1991), while the other at The University of Western Ontario can claim to be the worlds most powerful, (Sica, 1992).

3.6 Differential Absorption LIDAR (DIAL)

In 1964 Scholand (1964) suggested the use of a lidar technique which has become known as differential absorption lidar or DIAL. Originally Scholand proposed, and obtained initial results with, a spectral lamp in place of a laser. This does not affect the way in which DIAL works.

The DIAL method relies on the sharp variation in atmospheric transmission near an absorption line of an atmospheric constituent. A differential absorption lidar operates on two closely spaced wavelengths. One of these wavelengths coincides with an absorption line of the constituent of interest while the other is in the wing of this absorption line. During transmission of these two wavelengths through the atmosphere the emission that is tuned to the absorption line of interest will suffer greater attenuation than the emission in the wing of the absorption line. The DIAL technique can use either a target or the scatter from air to provide the required backscatter. In the case that a target is utilised to provide the backscatter the measurements will be an average over the entire path from the transmitter/receiver to the target. Range resolved measurements can be achieved by utilising the backscatter from the atmosphere and range gateing the receiver. This technique is sometimes call differential absorption and scattering (DAS).

In both of these methods the difference in transmission over the atmospheric path can be determined from the amount of backscatter detected at each wavelength. Then, using this information a density profile or the path average density of the atomic or molecular species can be calculated.

If a target is used to scatter the laser pulse back to the lidar then the measurement will

be the path average density of the species, this method usually involves the use of an airborne lidar using the ground as a target.

Temperature measurement is possible with the DIAL method if the absorption line selected is temperature dependant, such as the oxygen A-band. (See for example Kalshoven et al, 1981 and Schwemmer et al, 1987).

The DIAL technique has been developed mainly for pollution monitoring, (Rothe et al 1974, Menyuk et al 1983, Uthe 1986 and Zanzottera 1990) in which case Mie or target scattering are responsible for the majority of the backscatter. This technique is very successful in the lower atmosphere providing accurate measurements with good time and spatial resolution for a number of species including NO_2, H_2O, O_3, HCl, SO_2 and CO_2.

Use of the DIAL technique in the middle atmosphere has been restricted mainly to the measurement of ozone profiles. Pelon et al (1986), Werner et al (1984), McDermid et al (1990a) and Bronwell (1989) have reported the use of the DIAL technique for the determination of ozone profiles up to 50 km, although integration times of at least a few hours are required to obtain useful accuracy at the upper altitude levels. These same lidar systems are able to obtain profiles up to 20 km in approximately 15 min due to the much higher concentration of ozone at the lower levels.

3.7 Raman LIDAR.

The term Raman lidar is generally used to refer to a lidar system which makes use of the Raman shifted component with $\Delta V = \pm 1$, that is a transition which involves a change in vibrational energy level. Pure rotational Raman lidar refers to a system which makes use of the pure rotation transitions of a molecule, ie $\Delta V = 0$

Two workers, Cooney (1968) and Leonard (1967), reported the use of lidar measurement of the Raman shifted component of N_2 at about the same time. Due to the very small spectral separation between the Raman signal and the unshifted central component of the backscatter, the Cabannes line, Raman lidar requires very carefully designed and operated equipment.

Table 3.2 gives details of the backscatter cross-sections for the Raman, pure rotational Raman and the Cabannes lines for four molecules that are found in the atmosphere.

This table shows that the backscatter cross-section for Raman scattering is about three orders of magnitude less than that for the Cabannes line. Careful spectral filtering is therefore required to adequately reject elastically backscattered photons, allowing the Raman shifted component to be measured.

Molecule	Raman	Pure-rotational Raman	Cabannes
N_2	$3.5x10^{-30}$	$1.1x10^{-28}$	$3.9x10^{-27}$
O_2	$4.6x10^{-30}$	$2.0x10^{-28}$	$3.3x10^{-27}$
CO_2	$4.2x10^{-30}$	$8.3x10^{-28}$	$9.0x10^{-27}$
CH_4	$2.1x10^{-29}$	0	$8.6x10^{-27}$

Table 3.2. Gives the Raman, Pure-rotational Raman and Cabannes line backscatter cross-sections for 4 atmospheric molecules, at λ=510 nm. (After Measures, 1984.)

The Raman lidar technique has been applied to the measurement of a number of atmospheric molecules including N_2 , O_2 , and H_2O, (see for example Cooney, 1970,1972b, Cooney et al, 1985 and Melfi, 1972). The use of Raman lidar is restricted to the more abundant species in the atmosphere, due to the small backscatter cross-section involved. The DIAL technique has proved to be much more efficient for the measurement of trace gases in the atmosphere.

Measurement of the intensity of the Raman component of N_2 , which is free from aerosol scattering contamination, allows the extension of the Rayleigh lidar method down below the aerosol layer, (Keckhut et al, 1990).

Temperature measurement based on the shape of the pure rotation Raman spectrum (PRRS), was first proposed by Cooney (1972a). This method utilises the variation in population of the rotational levels of a molecule with temperature; the greater the temperature the greater the probability of a higher level being populated. Figure 3.2 shows the envelope of the PRRS lines of a nitrogen molecule at three temperatures. It can be seen from this diagram how temperature measurements could be made by measuring the intensity of some or all of the PRRS lines.

The first reported use of this method was by Cooney and co-workers, Cohen et al

(1976), Cooney et al (1976) and Gill et al (1979). Since this time, very few other results have been published, Arshinov et al (1983). Separation of the Cabannes line from the PRRS has proved to be very difficult, even though the backscatter cross-section for PRRS in much greater than that for vibrational rotational Raman scattering, (see table 3.2). The spectral separation of the PRRS and the Cabannes line is quite small and this leads to technical difficulties while trying to separate these two signals.

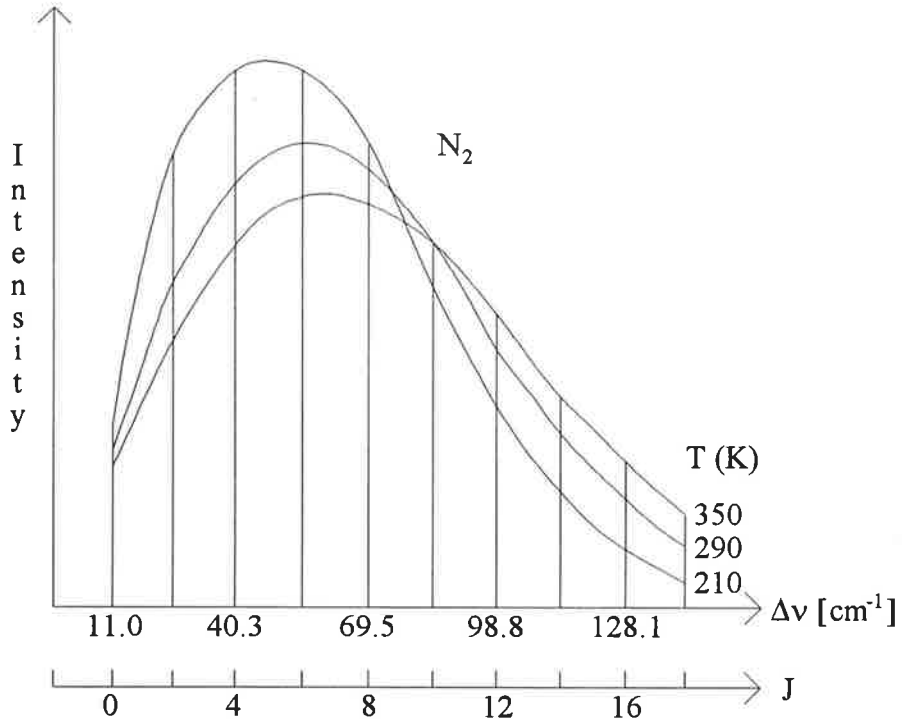

Figure 3.2 Intensity distribution for PRRS of N_2 at three temperatures. (After Arshinovo et al, 1983.)

3.8 Resonance LIDAR

A layer of sodium which exists in the earths atmosphere between about 80 and 100 km has been probed by many workers using resonant scattering lidar. The first reported use of a resonance lidar to study the Na layer is by Bowman et al (1969). Tunable dye lasers are used to provide light of the required wavelength, the Na D-line in this case.

The backscatter cross section for resonant scatter from the Na layer is about $3\text{x}10^{-16}$ m^{2}sr^{-1}, (Fricke et al, 1985). This value is sixteen orders of magnitude greater than the backscatter cross section for molecules calculated using Rayleigh theory for the same

wavelength. The large value of this cross section allows measurements to be made on the Na layer even though the density of the Na is relatively low and the layer is relatively high, at about 95 km altitude.

A method for the measurement of temperature utilising resonant scatter from the sodium layer has been developed. Studies of the Na layer, using the Resonance lidar technique have been reported by von Zahn et al (1987), Kirchhoff et al (1986), Fricke et al (1984), Gardner et al (1986), Gardner (1989), Nomura et al (1987), Bills et al (1991) and She et al (1992) amongst others.

Neutral and ionised calcium have been observed in the atmosphere by resonance lidar along with potassium and lithium. Thomas (1987) provides a review of this work. More recently Bills and Gardner (1990) have used a resonance lidar to study atmospheric iron.

3.9 High Spectral Resolution LIDAR

The term high spectral resolution lidar (hsrl) is generally used to describe a lidar system that uses the spectral shape and/or position of the Cabannes line to determine atmospheric parameters. A number of methods have been devised to achieve these measurements.

Fiocco et al (1968) presented a reasonably comprehensive discussion of the results that should be obtainable by scanning the Cabannes line using a Fabry-Perot interferometer. Details of the measurement of temperature, wind speed and aerosol-to-molecule scattering ratio are given. This paper also includes some initial laboratory results in which a comparison is made between the spectral width of the return from air and that from a target, the target simulating aerosol scattering. Further results of the work of this group are found in Fiocco et al (1971), Benedetti-Michelangelli et al (1972,1974) and Congeduti et al (1981).

Chanin et al (1989) describes a method whereby a pair of interferometers is used to measure the intensity of the backscatter on either side of the centre of the Cabannes line. By comparing the signal in each of the channels the shift of the Cabannes line and thus the wind velocity can be determined. This particular lidar system is effective in measuring velocities at altitudes up to 50 km.

Another method for the measurement of wind velocity is described by Abreu et al

(1992), which involves the measurement of the shift of the peak of the aerosol scattering signal with an imaging Fabry-Perot interferometer.

3.10 The LIDAR Equation

The basic lidar equation is straight forward to derive. It covers all forms of scattering and can be used to calculate the signal strength for a variety of forms of lidar.

Let

$N(\lambda)$ = the number of photons emitted by the laser in the wavelength interval λ to $\lambda + d\lambda$, in a single laser pulse, and

$T_t(\lambda)$ = the transmission coefficient of the transmitter optics for wavelength λ.

Then the total number of photons to be transmitted into the atmosphere by a single laser pulse, is given by;

$$\int_{\Delta\lambda} N(\lambda)\, T_t(\lambda)\, d\lambda \qquad \ldots (3.1)$$

Where $\Delta\lambda$ is a wavelength range which includes the entire wavelength range of the laser emission.

The number of photons available to be scattered at each level in the atmosphere is given by;

$$\int_{\Delta\lambda} N(\lambda)\, T_t(\lambda)\, T_a(r,\lambda)\, d\lambda \qquad \ldots (3.2)$$

Where r = the range at which the scattering occurs, and

$T_a(r,\lambda)$ = transmission of the atmosphere along the laser path from the lidar to the scattering altitude r, at wavelength λ.

The total number of photons backscattered, per unit solid angle, from the range interval R_1 to R_2, is

$$\int_{\Delta\lambda_1} NS(\lambda)\, T_t(\lambda) \int_{R_1}^{R_2} T_a(r,\lambda) \sum_i \rho_i(\lambda)\, \eta_i(r)\, dr\, d\lambda \qquad \ldots (3.3)$$

Note: To make range resolution possible it is necessary that the length of the laser pulse be much less than the length of the scattering volume, $R_2 - R_1$.

Where $\rho_i(\lambda)$ = scattering coefficient, for scattering of type i, at wavelength λ,

$\eta_i(r)$ = number density of scattering centres, which cause scattering of type i, at range r,

$NS(\lambda)$ = the convolution of $N(\lambda)$ and $S(\lambda)$, where $S(\lambda)$ is a function which takes into account any wavelength shift of the scattered light. This includes Doppler and Raman shifts, and

$\delta\lambda_1$ = wavelength range for which $NS(\lambda)$ is non zero; this range may be much larger than $\Delta\lambda$ as it may also takes into account Raman shifted scatter.

The number of photons incident on the telescope or collecting lens of the lidar is;

$$A\int_{\Delta\lambda_1} NS(\lambda)\, T_t(\lambda) \int_{R_1}^{R_2} \xi(r)\, T_a(r,\lambda)^2 \frac{1}{r^2} \sum_i \rho_i(\lambda)\, \eta_i(r)\, dr\, d\lambda \qquad \ldots (3.4)$$

Where A = the area of the telescope.

$\xi(r)$ = overlap factor, which takes into account the intensity distribution across the laser beam and the physical overlap of the transmitted laser beam and the field of view of the receiver optics at the scattering range.

The term $1/r^2$ arises due to the decreasing illuminance of the telescope by the scattered light as r increases.

The number of photons detected as pulses at the photomultiplier output, per laser pulse is;

$$A\int_{\Delta\lambda_1} NS(\lambda)\, T_t(\lambda)\, T_r(\lambda)\, Q(\lambda) \int_{R_1}^{R_2} \xi(r)\, T_a(r,\lambda)^2 \frac{1}{r^2} \sum_i \rho_i(\lambda)\, \eta_i(r)\, dr\, d\lambda \qquad \ldots (3.5)$$

Where $T_r(\lambda)$ = transmission coefficient of the reception optics of the lidar at wavelength λ, and

$Q(\lambda)$ = quantum efficiency of the photomultiplier at wavelength λ.

In many cases approximations allow the simplification of equation 3.5. If the range R is much greater than the length of the scattering volume, $R_2 - R_1$, and the atmospheric transmission $T_a(r,\lambda)$ and number density $\eta_i(r)$ do not change greatly over the scattering volume, then the range integral may be removed. ie.

$$A\int_{\Delta\lambda_1} NS(\lambda)\, T_t(\lambda)\, T_r(\lambda)\, Q(\lambda)\, \xi(R)\, T_a(R,\lambda)^2 \frac{1}{R^2} \sum_i \rho_i(\lambda)\, \eta_i(R)\, \delta R\, d\lambda \quad \ldots (3.6)$$

Where R = the range of the centre of the scattering volume,

$\xi(R)$ = the average overlap factor for the range,

$T_a(\lambda,R)$ = the transmission of the atmosphere, from the lidar to the centre of the scattering volume,

$\eta_i(R)$ = the average number density of scattering centres over the scattering volume, and

δR = length of the scattering volume

$= R_2 - R_1$.

If only elastic scattering (ie the molecular scattering Cabannes line and Mie scattering) is important then the function $S(\lambda)$ has a width consistent with the mass and temperature of the scatters $S_d(\lambda)$. this allows the range of the wavelength integral to be reduced to $\Delta\lambda_2$ which should include all wavelengths where $NS_d(\lambda)$ is non zero. Then, if all the wavelength dependant terms in equation (3.6), except $NS_d(\lambda)$, do not vary greatly over $\Delta\lambda_2$ the wavelength integral may also be removed. ie

$$A\, N_0\, T_t\, T_r\, Q\, \xi(R)\, T_a^2(R)\, \frac{1}{R^2} \sum_i \rho_i\, \eta_i(R)\, \delta R \quad \ldots (3.7)$$

If λ_0 = wavelength of the laser, then

N_0= the total no of photons emitted from the laser,

T_t = transmission coefficient of the transmitter system at $\lambda = \lambda_0 = T_t(\lambda_0)$,

T_r = transmission coefficient of the receiver system at $\lambda = \lambda_0 = T_r(\lambda_0)$,

$T_a(R)$ = transmission coefficient of the atmosphere over the path from the laser to the scattering volume at $\lambda = \lambda_0 = T_a(\lambda_0,R)$,

Q = quantum efficiency of the photomultiplier at $\lambda = \lambda_0 = Q(\lambda_0)$,

ρ_i = backscattering coefficient for scattering of type i at $\lambda = \lambda_0 = \rho_i(\lambda_0)$,

This form of the lidar equation can be used to calculate the signal strength for a Rayleigh lidar sensing the middle atmosphere, so long as it does not incorporate any filter with a spectral width of the same order or smaller than the width of the laser output or the Doppler broadening function.

For HSRL when such a narrow spectral width filter or spectrometer is used, Equation

3.6 may be required to calculate the intensity of the backscattered light. If a scanning spectrometer is used computer simulation of the instrument may be required to provide an estimate of the accuracy of results.

3.11 Conclusions

The term LIDAR is used to describe a remote sensing instrument that emits a beam of light and then collects some of the light scattered from that beam. The purpose being to determine something about the medium in which the beam has propagated or the medium in which it has been scattered. This covers a variety of instruments from those designed to measure pollutants over small areas, to those designed to measure temperatures and winds in the stratosphere and mesosphere.

4 Equipment

4.1 Introduction

The following chapter describes the lidar system used in this work. This description outlines the principles of operation of the equipment; it is not intended to be a technical reference. Emphasis is placed on parts of the equipment that are considered to be unique, unusual or special in some way.

4.2 Laser

The laser used in this lidar system is a copper vapour laser (CVL). The basis for the selection of this type of laser was that it provides a good power level at a relatively low cost. The copper vapour laser emits two laser lines simultaneously, one at 510 nm (green) and the other at 578 nm (yellow). The power obtainable from the green line is about twice that obtainable from the yellow line, depending on operating conditions. In this work only the green line was utilised. The laser used in this work proved to be extremely unreliable and its failure abruptly halted many observing sessions. This type of laser also has the disadvantage of a long warm-up time, approximately 45 min to lase and a further hour or so to reach full power.

4.2.2 Laser Specifications

Wavelength	510.6 nm
Pulse Repetition Frequency	2 kHz
Energy per pulse	3 mJ
Average Power	6 W (typical) 9 W (max)
Pulse duration	<50 ns
Line width	<6 GHz
Beam diameter	34 mm
Beam divergence (unstable resonator)	<2 mRad

4.2.3 Laser Pulse Repetition Frequency Considerations

The pulse repetition frequency (PRF) of a laser used in a stratospheric lidar is not critical. Current systems tend to use a PRF of about 10 Hz. In this case a PRF of 2 kHz was used, meaning that photons backscattered from 75 km reached the telescope as the next pulse was fired. A lower PRF is required in order to make measurements at higher altitudes. The laser used operates most efficiently at 10-12 kHz, with the average power output dropping off as the PRF is reduced, (see figure 4.1). A PRF of 2 kHz was chosen as a compromise between a decrease in average laser power and maximum observable height.

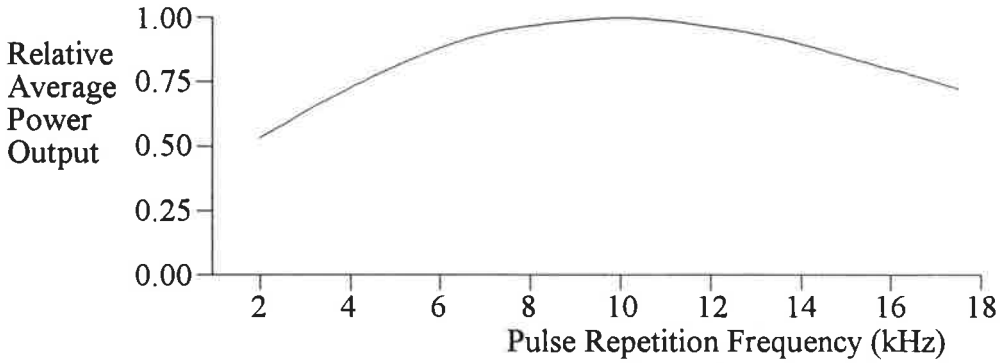

Figure 4.1 Laser average power output (510.6nm) plotted as a function of pulse repetition frequency. (Manufactures data.)

As the PRF of a Lidar system is increased the signal level will remain the same, assuming that the average power of the laser remains the same. However, the background signal, due to photo-multiplier dark counts and sky background, will increase linearly with the PRF.

The live time per channel is defined as the actual time for which a storage channel (corresponding to one altitude region) is active. For an altitude range of 1 km this will be 6.6667×10^{-6} seconds per laser pulse, (2 x height range / speed of light), or 6.6667×10^{-6} x PRF (seconds).

If the PRF of a lidar system is increased by a factor of 10 then the live time per channel will increase by the same amount

PRF	Observing time for a 1km altitude interval per pulse (s)	Observing time for a 1km altitude interval per second (s) (or live time per channel)
10	6.6667×10^{-6}	6.6667×10^{-5}
100	6.6667×10^{-6}	6.6667×10^{-4}
1000	6.6667×10^{-6}	6.6667×10^{-3}

Table 4.1 Shows the relationship between PRF and actual observing time per channel per second.

The background signal for any height range is proportional to the total observing time for that height range, ie. the live time. Thus, the background signal is directly proportional to the PRF. At PRF's of 10 Hz the background signal becomes very low, assuming a narrow bandpass filter and a reasonable quality, cooled photo-multiplier are being used.

The lower altitude limit for Rayleigh lidar observations is usually set by the ability of the photo-multiplier to adequately handle the large number of photons backscattered from the lower levels. The intensity of backscatter from each altitude region is proportional to the pulse energy of the laser. By increasing the PRF of the laser, while maintaining the same average power, the energy in each pulse is reduced and the intensity of backscatter per pulse is reduced, but the average power and signal level remain the same. This allows observations lower down in the atmosphere.

4.2.4 Theory of the Copper Vapour Laser

The CVL employs electron impact to excite ground state copper atoms, in the gaseous phase, to the lowest resonance level (^2P). This is an allowed transition and so the atom quickly returns to the ground state emitting a photon in the process. If the density of copper atoms is high enough it is likely that this emitted photon will be absorbed by another copper atom causing it to be excited to the (^2P) level. This process is known as radiation trapping and its efficiency is dependant on the size of the laser tube, the number density of copper atoms and the ratio of copper atoms in the ground state to those in the (^2P) level. The energy level diagram in figure 4.2 shows that the laser action of the CVL relies on the transition from ($3d^{10}$ 4p ^2P) to ($3d^9$ $4s^2$ ^2D), this lower level being a metastable level.

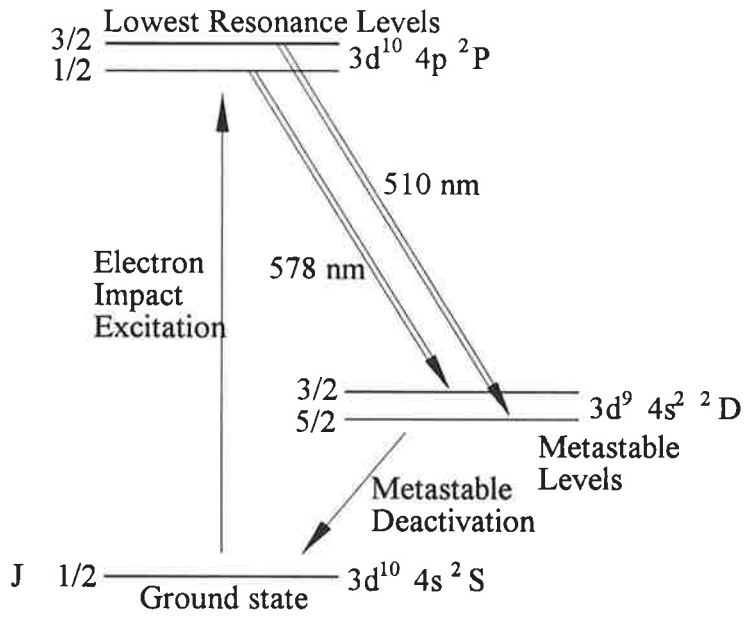

Figure 4.2 Energy level diagram for copper, showing the transitions occurring during the operation of the laser.

To initiate a pulse from a CVL a high voltage (12 kV) high current (1 kA) discharge is created in the tube, switching on as quickly as possible. This discharge causes the population inversion required for lasing. The lasing action quickly destroys the population inversion and leaves a large population of the copper atoms in the metastable states. A buffer gas of neon in the tube causes collision deactivation of these excited atoms on a time scale of about 25 ms, leaving the tube ready to fire again. The energy from the discharge also keeps the tube at a temperature high enough to maintain the density of copper atoms in the gaseous phase.

4.3 Optics

4.3.1 Introduction

A basic Rayleigh Lidar system requires few optical components. A Doppler lidar requires much more careful design and many more optical components. In this case, where the same steerable telescope is used for transmission and reception the optical design becomes more complex and the number of optical components becomes quite large.

4.3.2 Design Requirements

As a Doppler lidar determines line-of-sight velocity it needs to be able to probe the sky in a number of directions to enable the determination of wind velocity. A number of schemes have been used by other workers to achieve this. These include multiple telescopes, and the use of steerable, large flat mirrors in front on the telescope. Here a single telescope is used for both transmission of the laser pulse and reception of the backscattered light and to make the lidar steerable.

To enable a single telescope to be used for transmission of the laser pulse and reception of the backscattered light a fast optical switch must be incorporated, allowing the switching of the telescope between these two modes.

4.3.3 Optical System

The following section provides a description of the function of the optical system of the lidar and should be read in conjunction with figure 4.3.

A pulse of light from the laser is incident on the dichroic beam splitter where the 510 nm emission is reflected at the same time the 578 nm emission is transmitted and absorbed by a blackened surface, thereby playing no further part in the operation of the instrument. The reflected light (510 nm) is then focused to a point by D1 and passes through a cut-out in the laser shutter. The beam is then re-collimated by D2 and again focused to a point by D3, passing through a cut-out in the mirror shutter about three quarters of the way from the lens to the focus. From here the light is re-collimated by D4 and passed through the beam steering prisms P1 and P2. These beam steering prisms connect the stationary part of

the optics to the moveable telescope. From the beam steering prisms the beam is focused to a point by D5 and then transmitted into the atmosphere by the telescope.

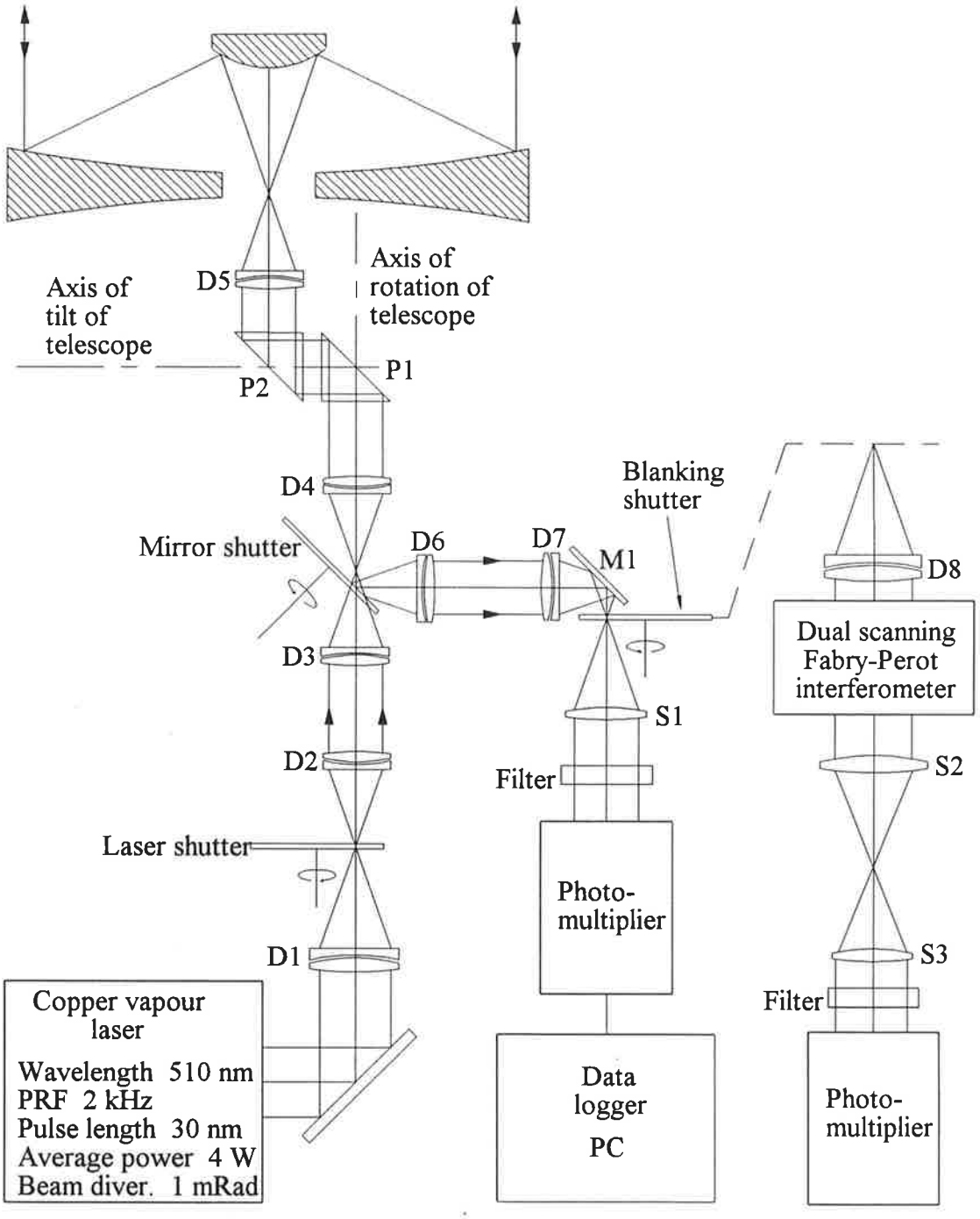

Figure 4.3 Optical schematic of the LIDAR system.

Light backscattered from the atmosphere and collected by the telescope passes through D5, P2, P1, D4 and is then reflected by the mirror shutter onto D6 which collimates the beam. D7 focuses the beam so that it can pass through the aperture switched by the blanking shutter. The mirror M1 is used to change the direction of the beam only so that the

optical system can be contained within the support structure of the lidar. From the blanking shutter S1 collimates the light for filtering by a narrow band interference filter. The light transmitted by this filter is incident on the photomultiplier.

Future modifications to the equipment involve the use of a dual scanning Fabry-Perot interferometer (FPI). This will be installed between the blanking shutter and the interference filter allowing daytime and Doppler measurements.

The function of the laser shutter is to stop after-glow from the laser being scattered into the detector during the time that light backscattered from the atmosphere is detected.

The blanking shutter stops scattered light reaching the photo multiplier during the time that the laser is firing.

The primary function of the mirror shutter is to switch the system from transmit to receive mode. A secondary function of the mirror shutter is to provide attenuation of the signal from between 5 km and 18 km so that the photomultiplier is not overloaded. The attenuation provided by the mirror shutter decreases with time so that for a range of 5 km the attenuation is close to 1 while for a range of 18 km the attenuation is close to 0. This attenuation function essentially requires that the shutter operates slowly; which is achieved not by slowing the shutter but by increasing the aperture over which it operates. So, instead of placing the mirror shutter at the focus of D3 where it would chop the small diameter of the beam very quickly, it is placed three quarters of the way to the focus, where the beam diameter is larger.

An image of the exit pupil of the laser is produced between the beam steering prisms P1 and P2 and again at the surface of the telescope primary mirror. For the receive system the primary mirror, which forms the entrance pupil of the system, is imaged between P1 and P2 (of course) and again at the interference filter. When the Fabry-Perot Interferometer is installed the primary mirror will also be imaged mid-way between the etalons. This setup allows the best possible use of expensive optical components.

4.3.4 Optical Components

In order to operate the system in the day time and with the FPI it is necessary to ensure that the system field of view is quite small, and this means that the quality of the

lenses should be such that they do not degrade the quality of the beam. To achieve this it is necessary to use doublets for correction of spherical aberration. The doublets were designed specifically for this instrument and each element was coated on both sides with an anti reflection "V" coating optimised for 510 nm. The doublets were air spaced rather than conventional cemented doublets because the cement was considered likely to fluoresce. The matter of fluorescence will be further discussed in chapter 6, but it should be noted here that while initially all doublets were manufactured from BK7/LF7, D4 and D5 were replaced with silica/silica doublets due to problems with fluorescence. The silica/silica doublets had essentially the same optical performance as the BK7/LF7 combination

The beam steering prisms had 20 x 20 mm entry and exit faces that have anti-reflection "V" coatings. Fused silica is the substrate for these prisms.

Production of the mirror shutter surface posed a special problem for the precision optician. The shutter is only 0.5 mm thick across most of its area and is machined from aluminium, thus being a "flexible" piece. In operation the mirror shutter must act as a flat mirror so that the light reflected by it does not change direction as the mirror rotates. Another common problem that occurs when a soft material is ground and polished is a turned down edge (bevel), and it is desirable that this effect be minimised on the edges of the cut-outs in the mirror shutter. The mirror shutter was polished to the required flatness and with minimal turn down on the edged due to the ingenuity and care of the precision optician. After polishing the mirror shutter was coated with a multi-layer reflection enhancement coating optimised for 510 nm.

Testing the mirror shutter at low speed (spun by hand) showed that the axis of rotation of the shutter was not parallel to the normal of the mirror surface. This is to say that if a laser were directed onto the mirror shutter and it is spun slowly around, the reflected light mapped out a cone. Measurements showed that the angle between the axis of rotation and the normal to the mirror surface was 1.2 mRad. However when the shutter was spun at its working speed the alignment improves significantly, and the error reduced by a factor of 10.

4.4 Telescope

A major part of the construction of the equipment used in this project was the

production of the telescope. For this reason a separate chapter has been devoted to describing its design and construction.

There were two main factors to consider in selecting the design for the telescope. Firstly the physical length of the telescope had to be short, thus keeping the moment of inertia low and thereby making rotating the telescope easier. Secondly the optical connection between the telescope and the rest of the optical system is simplified if the light collected by the telescope is directed out of the back of the telescope and along its optical axis. The Cassegrain design fulfils these two requirements.

4.5 Shutter System

In order that the same telescope be used to transmit the laser pulse and also to act as the collector for the detection system an optical switch must be incorporated in the system. The optical switch must be able to open and close very quickly ($3x10^{-5}$ s). It must also provide very positive switching. Transmission along the 'on' path must be very high, while transmission along the 'off' path and between switched paths must be very low. This requirement led to the use of rotating metal shutters to provide the switching.

4.5.1 Mirror Shutter

The mirror shutter provides the main switching function for the telescope. Figure 4.4 shows the mirror shutter and how it operates. The mirror shutter is an aluminium disk with 5 identical cut-outs. This shutter has a mirrored front surface. The mirror shutter performs its switching function in the following way; a pulse of light fired from the laser passes through a cut-out in the shutter and through the telescope out into the atmosphere. In the time taken for this laser pulse to be backscattered from the altitudes of interest the shutter has rotated. The backscattered light is then reflected off the mirrored surface of the shutter and into the detection system.

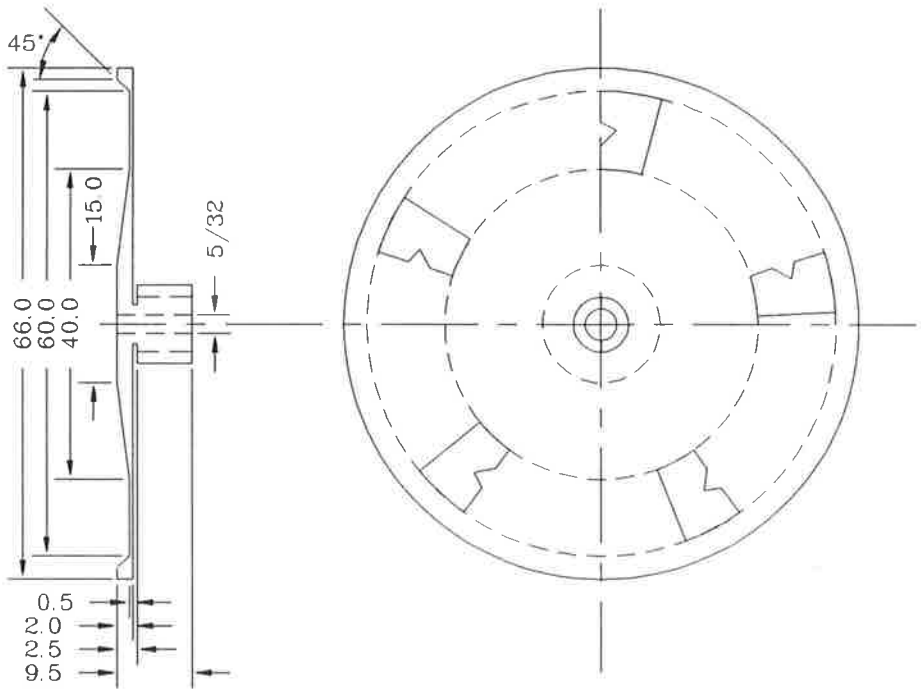

MIRROR SHUTTER

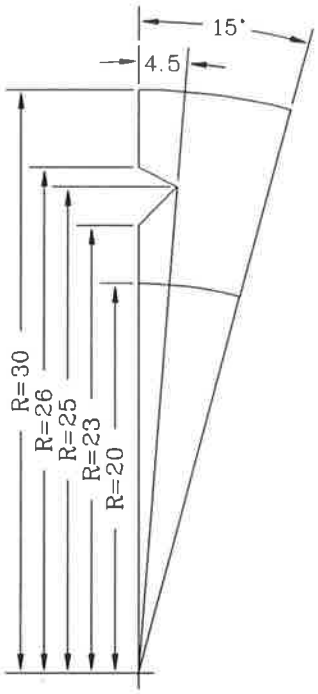

DETAIL OF
HOLE SHAPE

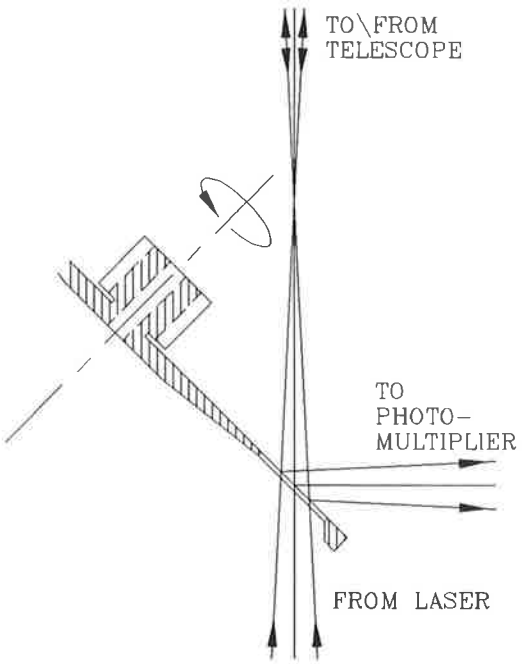

MIRROR SHUTTER OPERATION

Figure 4.4 Mirror shutter, dimensions and operation.

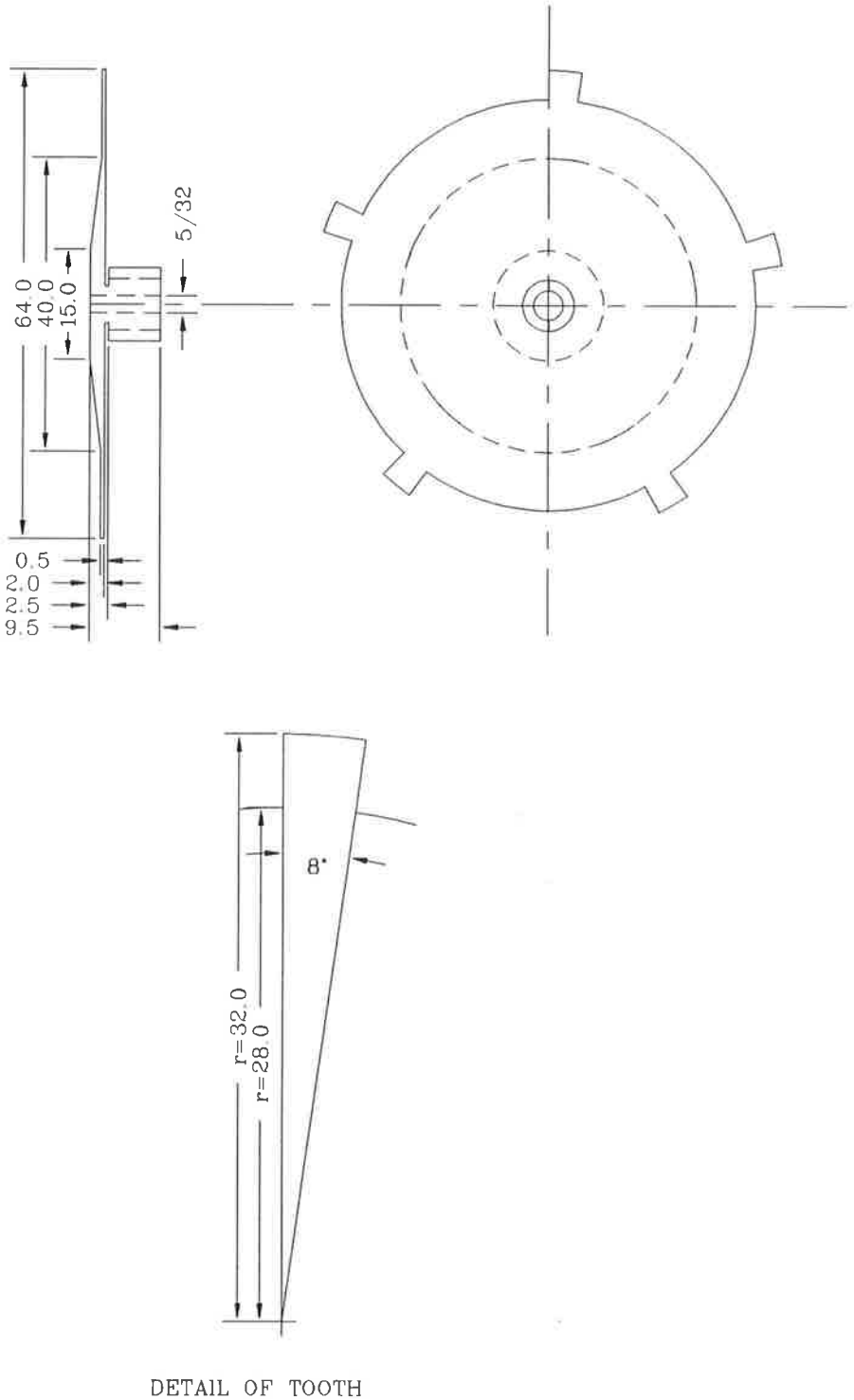

Figure 4.5 Blanking shutter.

4.5.2 Blanking Shutter

To avoid temporarily affecting or permanently damaging the photomultiplier it is necessary to ensure that the optical path to the photomultiplier is blocked when the laser is firing. Even a very small fraction of the laser light being scattered into the detection system could cause a problem. The blanking shutter provides protection for the photomultiplier from

internally scattered laser light. The blanking shutter is a thin aluminium disk with 5 small teeth on its edge, see figure 4.5. During the time that the laser is firing the blanking shutter is positioned so that one off its teeth blocks the optical path to, and thus protects, the photomultiplier, see figure 4.6.

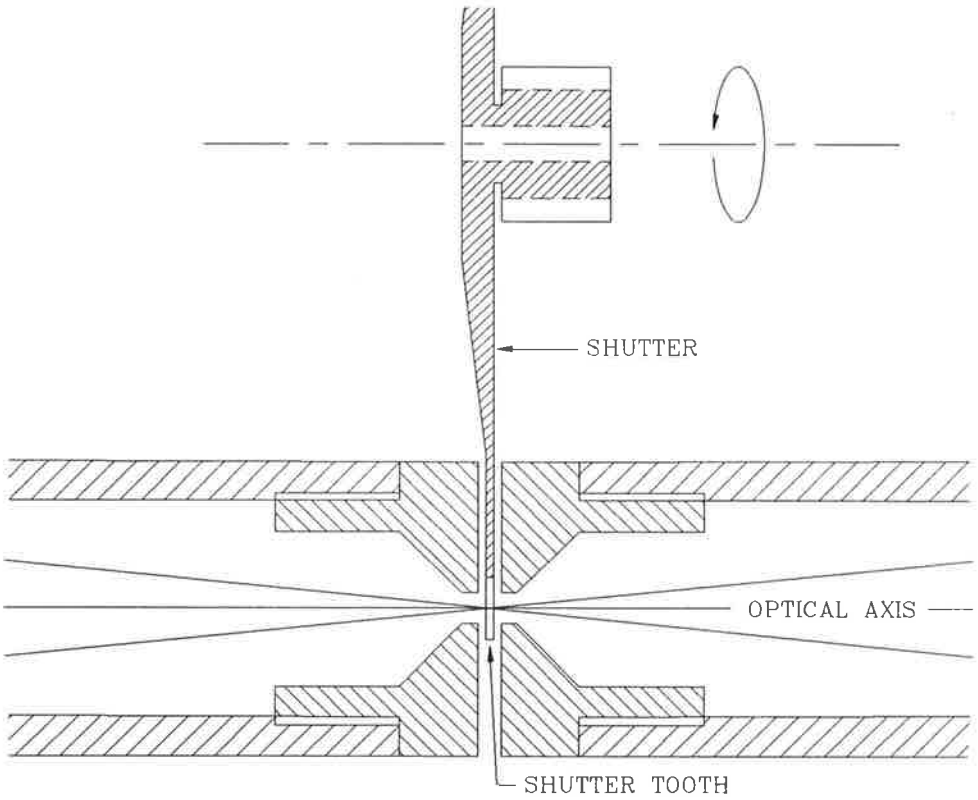

Figure 4.6 Blanking shutter and laser shutter operation.

4.5.3 Laser Shutter

After the laser has fired it continues to emit light at the working wavelength. This light is scattered within the lidar system and a small, but significant, amount finds its was to the photomultiplier. This is obviously undesirable and to eliminate this problem a third high speed rotating shutter is used, the laser shutter. This shutter is a disk with 5 small notches cut into its periphery, (see figure 4.7). The laser pulse fires through one of the notches in the laser shutter, the optical path from the laser is then closed until the laser is ready to fire again. This stops any laser after-glow reaching the detection system and causing a problem.

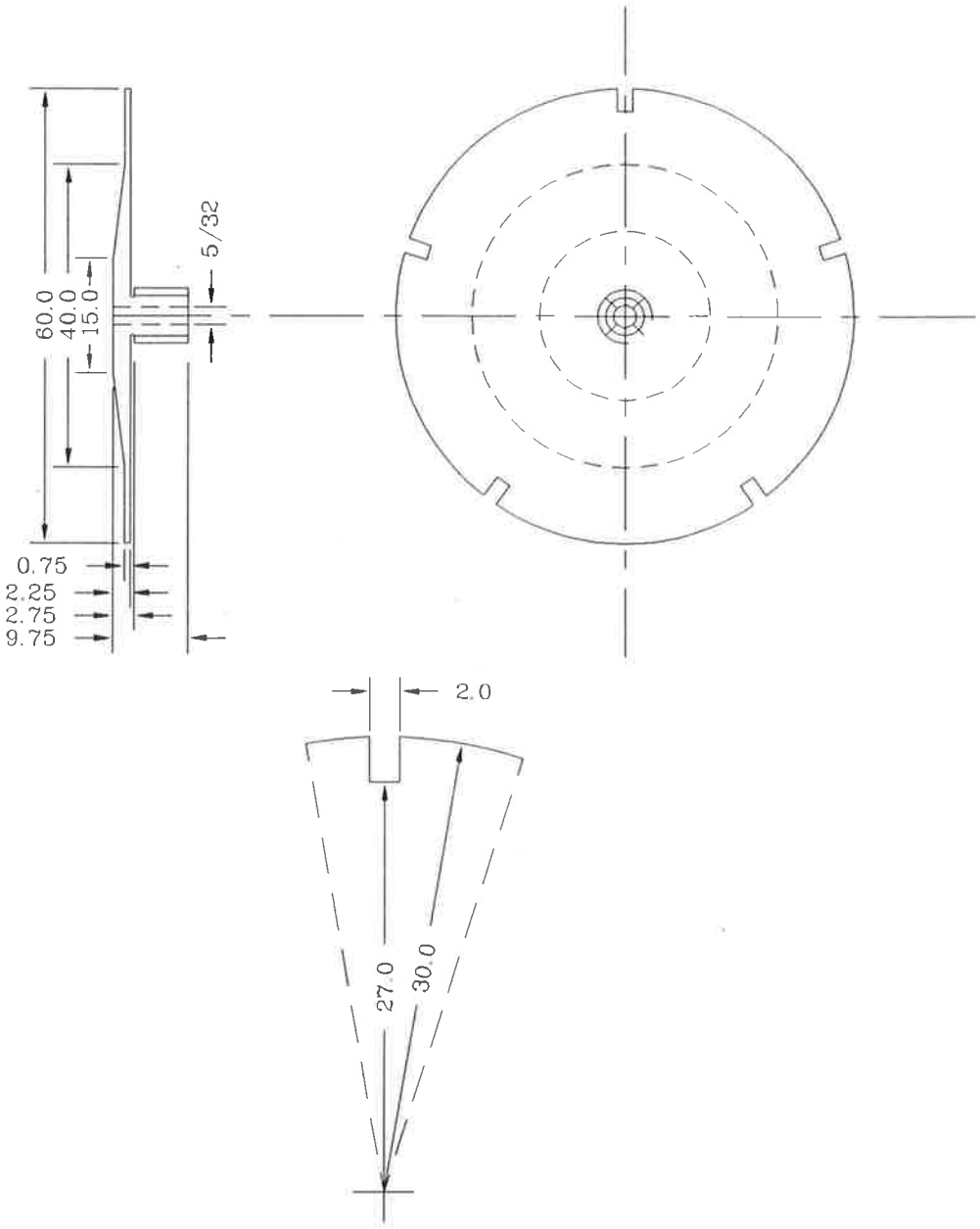

Figure 4.7 Laser shutter.

4.5.4 Shutter Switching Speed

The switching speed of the shutters is proportional to both the rotational velocity of the shutter and its diameter. Both of these variables are ultimately limited by the motor used to drive the shutter. The power of the motor determines the maximum size of the shutter that it will drive. Larger shutters will have greater aerodynamic drag so that greater power will be required to drive them. A larger shutter can be driven by a motor if the shutter is run

in a chamber at reduced pressure. This reduced the aerodynamic drag of the shutter.

An acceptable switching speed was achieved with the use of small synchronous motors (Globe B-2002, 18A1003-2) running at 24,000 rpm. These are quite low power motors, but they will drive a thin disk of up to 66 mm in diameter up to full speed in air. The switching speed achievable by running the shutters at normal air pressure was found to be adequate for the present purposes.

The speed at which the shutters are able to switch from fully open to fully closed is also dependent on the size of the aperture that is being blocked or opened. In the case of the laser shutter the aperture is 1 mm in diameter and this will open or close in 14 μs. The other two shutters open and close larger apertures and therefore take longer to perform their functions.

The switching speed of the mirror shutter from transmit to receive is deliberately slowed by the shaped leading edge of the mirrored segment of the shutter, (see figure 4.4). The reason for this is as follows: the amount of light backscattered by the atmosphere at heights below about 18 km is too large for the photomultiplier. However if the system is able to attenuate this signal to a level safe for the photomultiplier then the system will be able to collect data at the lower altitudes. The mirror shutter starts to open the detection system when backscattered light is received from 5 km. When light backscattered from above 18 km is received the mirror shutter transmits all of this received light into the detection system. Between 5 km and 18 km the attenuation of the received signal is such that the intensity of light reaching the photomultiplier remains at safe and useable levels.

The passing frequency of the teeth/cut-outs in the shutters must have very little jitter, so if the tooth/cut-out is more than 0.1 mm from its required position (phase) the control system will try to correct this error. Therefore it is necessary to produce the shutters with the teeth/cut-outs machined to a positional accuracy much better than 0.1 mm. A complicating factor is that the shutters are as thin as 0.5 mm making them quite fragile. The tooth forms of all three shutters were cut using wire discharge machining. This process exerts very little force on the work piece and can achieve very accurate results, of the order of a few microns, this is also important for the dynamic balance of the shutter.

4.6 Electronic Control System

In order that the lidar system operates correctly the three high speed rotating shutters must have their relative positions (phases) maintained to a high degree of accuracy. As well as this the laser and data collection systems must be triggered if and only if these phases are correct.

A digital electronic control system (the controller) was constructed, "in house", to achieve these requirement. The controller constantly monitors the phase of the rotating shutters and provides correction as necessary. If the rotating shutters have the correct phase relationship then the control system will trigger the laser and data collection system. A schematic showing the components and interconnection of the control system is presented in figure 4.8.

Due to the electromagnetic radiation emanating from the laser when it is pulsed it has been necessary to provide protection from interference for the electronic control system. This is achieved by the use of optical fibres to provide signal connections between individual components. The use of individual transformers to provide power to each position sensor and the photo-multiplier pre-amplifier provides further protection for these components.

Optical reflective sensors monitor the phase of the rotating shutters. This is the type of device used in bar code wands; it consists of an LED and a photo-diode in a single package. A pair of moulded lenses form the front of the package. The arrangement of these lenses is such that the LED and photo-diode are both imaged to the same point, (about 4.5 mm in front of the package). A mirror positioned at the focus of the sensor reflects the emitted light back onto the detector. The position of the shutter is such that when rotated its teeth chop the path between the sensor and the mirror, thus alternately allowing and disallowing illumination of the photo-diode. The signal from the photo-diode is discriminated, amplified and then a pulse sent to the controller. This is the shutter phase signal. The components used allow the detection of the phase of the shutter with jitter less than that caused by the small machining errors in the shape of the shutters.

The process of shutter phase comparison and correction is completely digital, including the phase of the supply to the motors. A TTL square wave is filtered to give a sine wave and then amplified to provide the power for the high speed motors.

Control over the phase of the shutters is maintained in the following way. The control system generates a correction window within which the shutter position signal should lie.

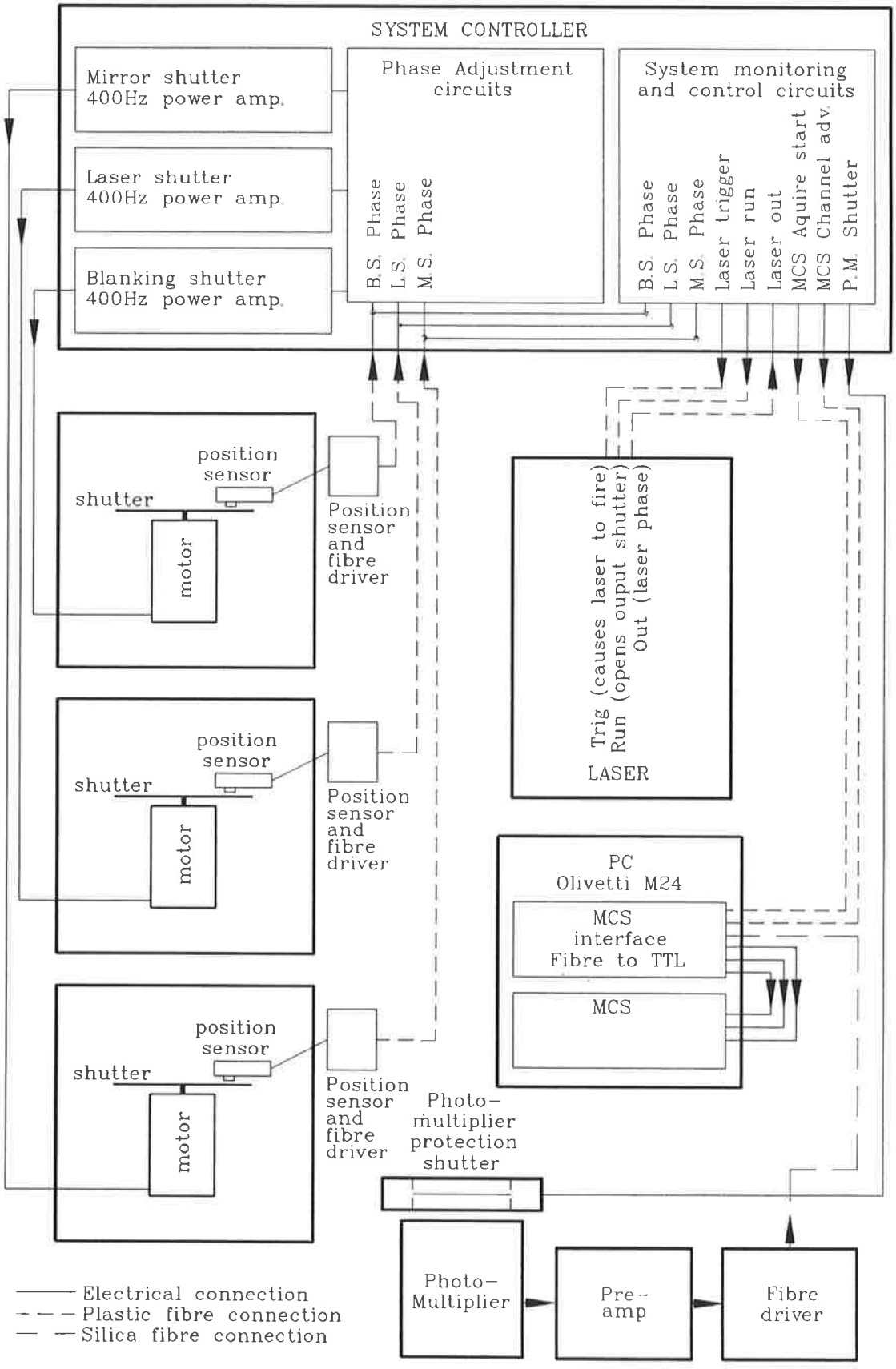

Figure 4.8 Schematic of the lidar control system.

The phase of the 400 Hz supply to the motor is adjusted if the shutter position is outside the correction window. The phase adjustment occurs in small steps by adding or subtracting pulses from the frequency divider chain that generates the 400 Hz. This correction process occurs at the 1 MHz point in the divider chain resulting in shutter phase steps of 0.144^{o}. Adjusting the rate at which the supply phase steps also adjusts the rate at which the shutter phase changes. Thumb wheel switches permit changing the correction window, and hence the shutter position, over a small range.

A variety of time-base frequencies are derived from a quartz crystal oscillator. These are used to determine the timing of the correction windows for the shutter phase comparisons. Current timing values have been determined empirically. The width of the correction windows is 3.4 μs; in which time the shutters will move about 0.2 mm. This gives an idea of the control needed to enable the system to operate - each of the three shutters spinning at 24,000 rpm should be within ±0.1 mm of a specified position 2000 times each second. During operation corrections are made to the phase of the 400 Hz supply at 1 Hz.

Two signals generated by the controller synchronise and control the output of the laser. One signal, called **trig**, triggers the laser allowing synchronisation of the laser with the shutter system. The **trig** signal consists of a continuous 2 kHz pulse train, and is operating whenever the controller is on. Without this signal the laser will operate at a slightly lower frequency provided the laser output shutter remains closed. The laser output shutter is a simple solenoid operated shutter that is able to block the laser output. The other signal, called **run**, controls whether the laser should emit light. If the controller detects a problem (in the phase of one of the shutters or the laser) it is important that the laser does not emit any further pulse of light until the problem is corrected. When a fault occurs the **run** signal is removed from the laser, thereby causing the laser to stop firing and the laser output shutter to close. Once the laser output shutter has closed the laser starts to fire again. On restoration of the **run** signal the laser output shutter opens. The reasons for this mode of operation are as follows: the laser operates much better if it is firing continuously (this maintains the tube temperature), and firing the laser while the laser output shutter is closed allows the controller to check the phase of the laser before the system restarts after a fault.

To protect the photomultiplier and other parts of the system, separate circuitry

monitors the timing of the laser pulse and the position signals from the three rotating shutters. If these do not fall within specified time windows (called run windows) the system run signal is removed. This in turn removes the laser **run** signal, halts data acquisition and closes the photomultiplier protection shutter. Once the system regains synchronisation and after a further delay of one second, for settling down, the system run signal is restored. An EPROM and counter circuitry determine the relative positions of the run windows. This allows easy adjustment of the of system timing. The run windows for the shutters are wider than their correction windows. The blanking shutter and mirror shutter run windows are set at 8 us, that for the laser shutter at 15 us and the laser run window at 6 us. The reason for the laser shutter run window being longer than the other two is that the timing of the laser shutter is not as critical to the operation of the instrument.

The figures quoted above show that the run windows are wider than the correction windows, this allows the correction system to attempt to correct any problems before a synchronisation error occurs and the system shuts down.

4.7 Data Collection System

The addition of the signal obtained from the firing of many laser pulses is require in order that a useful signal to noise ratio be achieved. A Multi-Channel Scaling board (Nuclear Data FMS board) collects and sums the data. This FMS board is installed in an expansion slot of an IBM compatible computer (Olivetti M24). The board is self-contained and can be setup via software.

A cooled photomultiplier detects the backscattered light. Initially the photomultiplier was an EMI 9558B, in case of an accident. Installation of an EMI 9659 followed a period of testing.

Single photo-electron pulses are amplified and discriminated by circuitry mounted adjacent to the photomultipliers refrigerated chamber. The discriminator rejects low level noise pulses improving the signal to noise ratio. Transmission of the output pulse of the discriminator is via an optical fibre to an interface board in the Personal Computer. This interface board provides a TTL signal that is compatible with the input of the MCS board.

The maximum pulse pair resolution of the data collection system is 40 ηs.

Two other signals control the operation of the FMS board, both of which are generated by the electronic control system. The first of these is the acquire start signal which determines when the FMS board should start a scan. The other signal is a channel advance signal which tells the FMS board to advance to the next acquisition channel. In order to simplify data analysis, collection of data occurs for a height resolution of 1/3 km, this is equivalent to a dwell time of $2^2/_9$ ms. An external channel advance signal is required to achieve this dwell time.

A program running on the Personal Computer controls Data collection and the FMS board. This program writes data collected by the FMS board to the hard disk at programmed intervals. Further data analysis is carried out on a separate Personal Computer.

Generally data are collected using the following parameters:

Altitude at which data collection system starts 0 km,
Altitude at which data collection system stops $66^2/_3$ km
Number of altitude intervals 200,
Dwell time in each channel $2^2/_9$ ms (equivalent to $^1/_3$ km range),
Time for each record 30 s (approx 60000 scans),
Data saved to disk every 30 s (1 record) or 5 min (sum of 10 records).

The laser PRF and the speed of the shutters determine the maximum height for data collection. The laser PRF of 2 kHz gives 500 ms between pulses, this being equivalent to a range of 75 km. Allowing time for the shutters to move into their correct positions for the laser to fire means that the reception system is effective only up to about 60 km

4.8 Conclusions

The optical system of this lidar, in particular the use of a single telescope for transmission and reception, is unique. Many problems associated with the use of a single telescope were encountered during the development of the system. However these have been overcome and the system performs well.

The shutters and the associated electronic control system required a great deal of thought, design and experiment before a working solution was established, this being due to the very high tolerances on the phase and speed of the shutters.

5 Telescope Production

5.1 Introduction

This chapter gives details of the production of the telescope used in this lidar system. This includes the manufacture of a 1 metre diameter aluminium parabolic mirror used as the primary mirror of the telescope. The emphasis of this chapter is on the shaping, polishing and testing of the mirror surface. Suggestions are given to aid in the design and construction of this type of telescope.

5.2 Design Requirements

A feature of this particular lidar system is that it should be able to make measurements at any azimuth angle and at zenith angles up to 45 deg. To achieve this requirement the same telescope is to be used to transmit the laser pulse as well as receive the backscattered light. A very high speed optical switch is used to take the system from transmit mode to receive mode. To enable the system to observe different areas of the sky the telescope is tilted about a horizontal axis and rotated about a vertical axis. The support structure and drive system for the telescope is simplified if the weight of the telescope is kept to a minimum.

Another feature of this lidar system is that it has been designed to be used in the daytime; this is not usually attempted because of the very high level of background light. The

use of a dual scanning Fabry Perot interferometer as a narrow band pass filter will allow effective rejection of the daytime background, although the level is still high. The level of background light detected by the system is proportional to the area of sky viewed, ie the field of view of the receiving system. To enable all backscattered photons that are incident on the telescope to reach the photo-multiplier the field of view of the receiving system must be at least twice the divergence angle of the transmitted beam. As the divergence of the transmitted beam is limited by the quality of the telescope (unless the telescope is of very high quality) it is necessary for effective daytime use, that the quality of the telescope be as high as practicable. Numerical simulations indicate satisfactory performance with a surface accuracy of 2.5×10^{-5} Rad. That is, the actual slope of the optical surfaces should not deviate from the ideal slope by more than 2.5×10^{-5} Rad.

Most existing lidar systems use either conventional glass astronomical telescopes (where the investigators have been able to obtain one) or reflectors of the type used in large searchlights. Neither of these solutions is appropriate in the present case. The conventional glass mirror would be too heavy and far too expensive while the large searchlight type reflector is of insufficient quality to allow daytime observations. Therefore we have opted to undertake the construction of a short focal length aluminium primary mirror "in house". This constituted a major undertaking and the first few years of this work were dedicated almost exclusively to the production of the mirror.

5.3 Telescope Specifications

The telescopes optical design is classical Cassegrain, that is a parabolic primary mirror with a hyperbolic secondary mirror. This arrangement is illustrated in figure 5.1. The telescope has a diameter of 1.025 meters and a focal length of 10 meters. A significant advantage of the Cassegrain design is that it allows the physical length of the telescope structure to be significantly shorter than its focal length, in this case about 2 m and 10 m respectively. Having a short physical length reduces the moment of inertia of the telescope structure when it is tilted off vertical and rotated about the zenith.

Tables 5.1 and 5.2 give the specifications of the primary and secondary mirrors used to form the telescope.

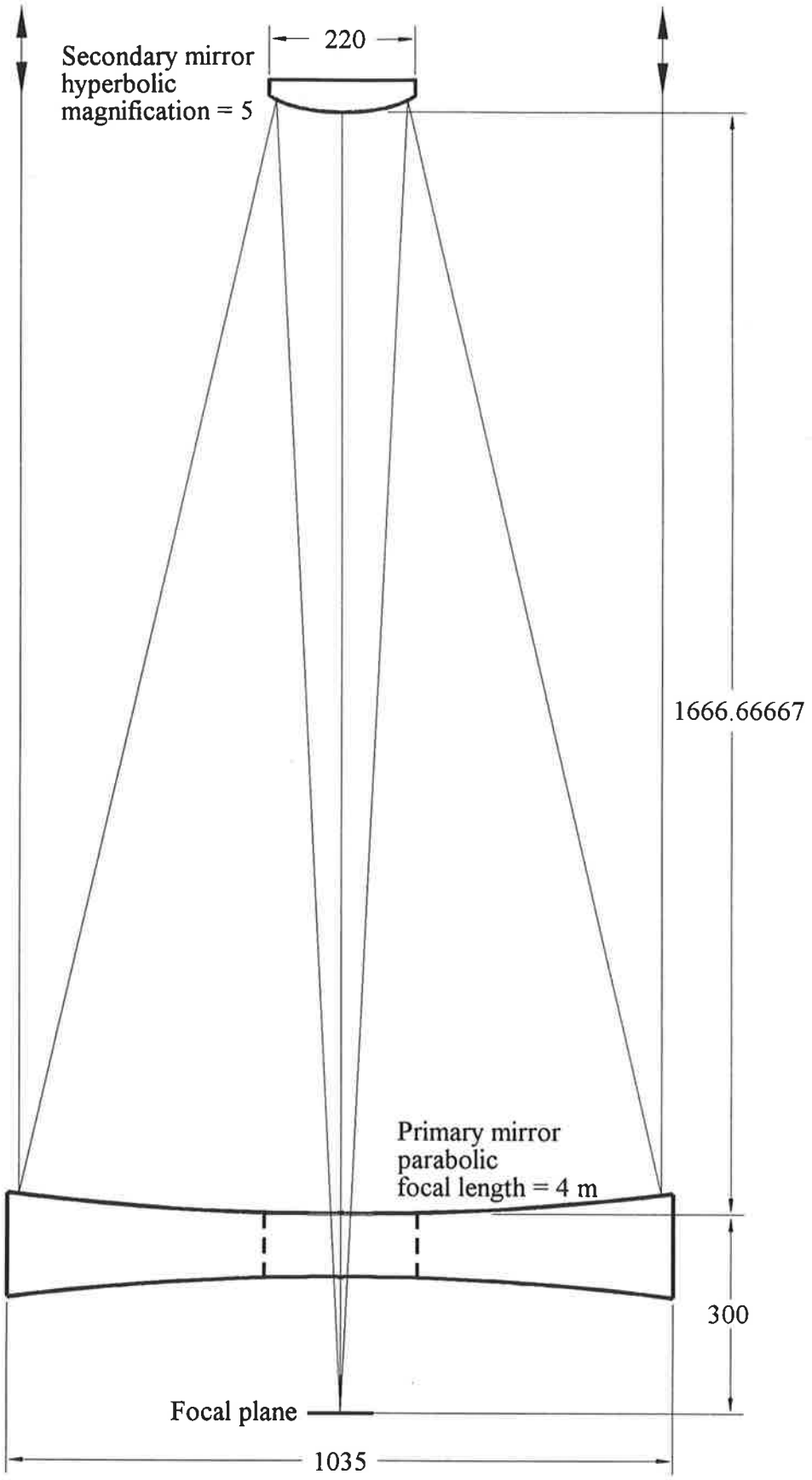

Figure 5.1 Schematic of telescope.

PRIMARY MIRROR SPECIFICATIONS.	
Shape	Parabolic
Focal length	2.00 m
Diameter: actual : working	1035 mm 1025 mm
Surface Accuracy Reqd: Max deviation of surface slope from theoretical	2.5×10^{-5} Rad.
Material: Working plate : Backing plate	AP703 (aluminium) AP601 (aluminium)
Mechanical Structure	see figure 5.2.

Table 5.1 Primary mirror specifications.

SECONDARY MIRROR SPECIFICATION	
Shape	Hyperbolic
Focal length: f1 : f2	383.33 mm 1916.67 mm
Diameter: actual : working	220 mm 200 mm
Material	L111 (aluminium)

Table 5.1 Secondary mirror specifications.

5.4 Classification of Errors

In order to discuss the errors in the shape of the mirror they have been classified into two categories. The first type of errors will be referred to as axi-symmetric errors; these are errors in the shape of the mirror when an average in taken around the optical axis. A common example of such an error is a turned down edge.

The second type of errors are those which show no axi-symmetry. These will be referred to simply as asymmetric errors. This type of error appears as high and low areas, rather than axi-symmetric rings.

5.5 Primary Mirror Manufacture

The mechanical design and production of the primary mirror blank were carried out at the Defence Science and Technology Organisation (DSTO) at Salisbury in South Australia.

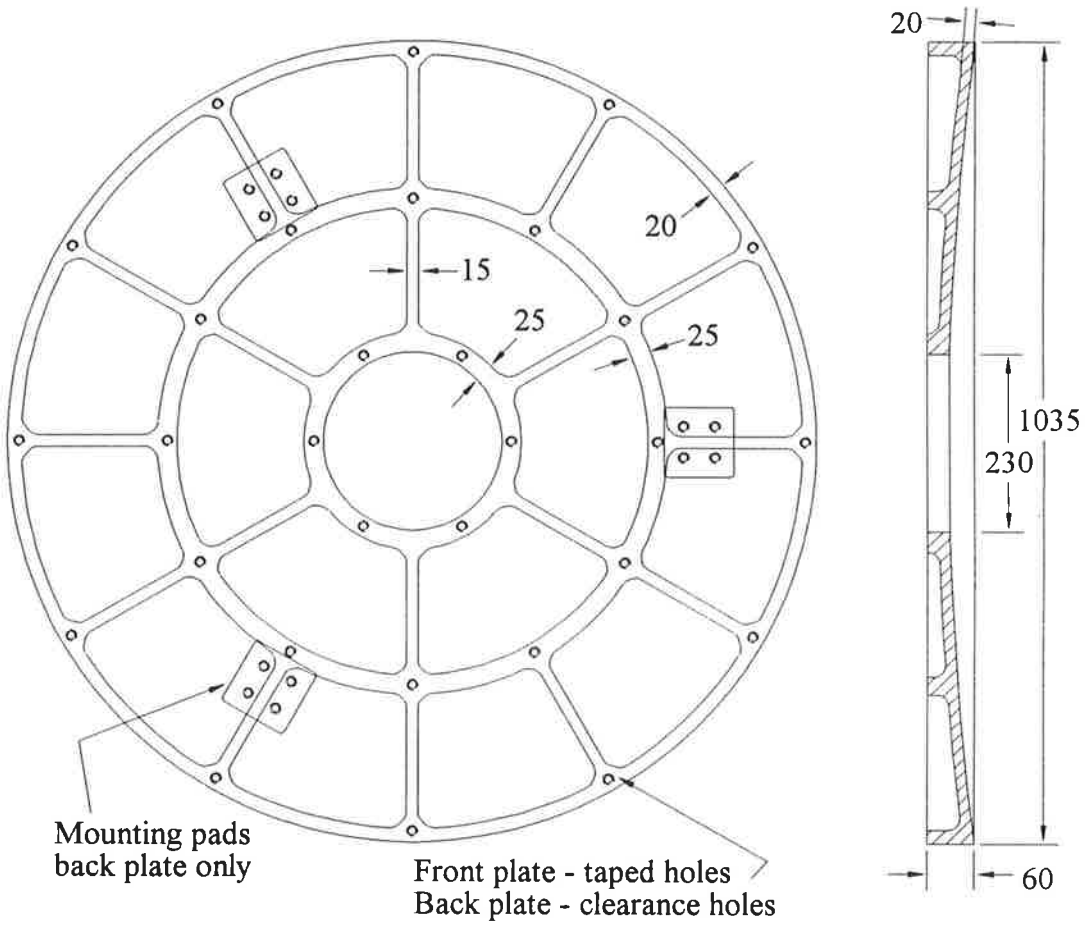

Figure 5.2 Mechanical structure of primary mirror.

The selection of the most appropriate material was assessed by casting a number of samples of different Al alloys and polishing their surfaces in order to find a material that produced a good quality finish.

During the initial stage of the project DSTO cast and heat-treated the two plates that make up the mirror blank. These were then assembled and the front surface was cut on a copying lathe to be as close as possible to the required parabolic shape. The shape was defined by a template consisting of a steel plate with one edge milled to the required parabolic form. These two components were then delivered to The University of Adelaide.

After some initial polishing and testing, the shape of the blank was found to deviate further from the required shape than had been expected. The blank was then machined again on a large computer-controlled lathe operated by a local company. This was done to improve the shape but met with only limited success.

It should be noted that it is not possible to do any optical testing on a component that has machining lines that are visible to the naked eye. These lines cause a regular scattering

pattern that makes testing impossible. If the surface has similar sized, but un-correlated, marks then optical testing is much more likely to be successful.

Both axi-symmetric and asymmetric errors were found to be present in the shape of the mirror after the second machining. The reason for the asymmetric errors is not clear, but two possible sources are as follows. Firstly the mirror may have been stressed while being held in the lathe, although steps were taken to avoid this by bolting the mirror to a large thick steel plate and holding this plate in the chuck. The second possible cause of the asymmetric errors is wear in the bearings of the lathe. The peak amplitude of these asymmetric errors was approximately 70 μm.

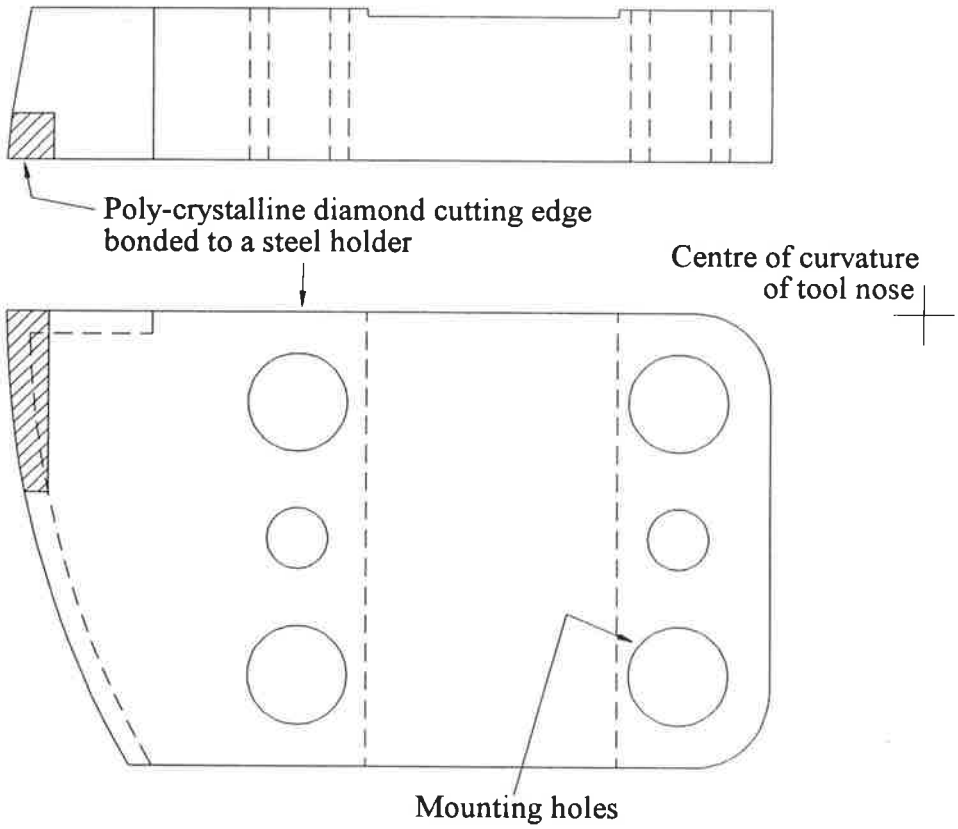

Scale 2:1

Figure 5.3 Poly crystalline diamond tool used to machine the primary mirror.

The lathe used to machine the mirror was not located in a controlled environment and was subject to considerable temperature fluctuation; this can lead to dimensional instability in the machine and cause errors in the shape of the work. To minimise the chance of this

happening it was necessary to make each cut of the mirror in as little time as possible. A special tool was manufactured for machining this mirror; it was made from poly crystalline diamond (PCD). PCD was selected because of its hardness, so that it would not wear significantly during a cut. A small piece of PCD was bonded to a steel holder and then ground to give a tool nose radius of 60 mm, (see figure 5.3). The use of such a large tool nose radius meant that the tool could move across the surface of the mirror relatively quickly without producing deep tool marks. In this way it was possible to make a cut in a relatively small time (20 mins) while still producing a high quality finish.

The special tool worked well, however its large nose radius caused a completely unexpected problem. Machines of this type are required to automatically take into account the tool nose-radius when calculating machining coordinates. It appears that this did not occur in the present case. Axi-symmetric errors consistent with the machine not having allowed for the nose-radius of the tool were discovered after the mirror had been taken back to the university. It would appear that the tool post actually moved through the parabolic arc required as the shape of the mirror, but the large tool nose-radius meant that the cut was actually about 0.5 mm too shallow in the centre. This error diminished smoothly towards the outside.

Due to difficulties in getting the telescope back onto the lathe and because of the presence of asymmetric errors it was decided to grind the mirror by hand with a large tool.

5.6 The Polishing Machine

A special purpose machine was produced to aid in the grinding, polishing, and testing of the mirror. Although it was used in all three functions it will generally be referred to here as the "polishing machine". This machine consisted of a steel frame that carried a large bearing on which the telescope and its mounting frame were supported, as in figure 5.4. A variable speed motor was used to rotate the mirror about its optical axis at up to 5 rpm.

In order to undertake optical testing of the mirror it was necessary to have the mirror standing vertically, that is with its optical axis horizontal. This restriction was imposed by the ceiling height of the laboratory being insufficient to allow testing of the mirror while supported horizontally. The radius of curvature of the mirror is 4 m, in order to test from the

centre of curvature one needs to be 4 m away from the mirror along its optical axis. The polishing machine incorporated a winch and a vertical frame that enabled the mirror to be swung up and locked into a vertical position.

For practical reasons the polishing machine also had a drip tray that caught any lubricating fluid, slurry or rinsing fluid and drained this into a bucket.

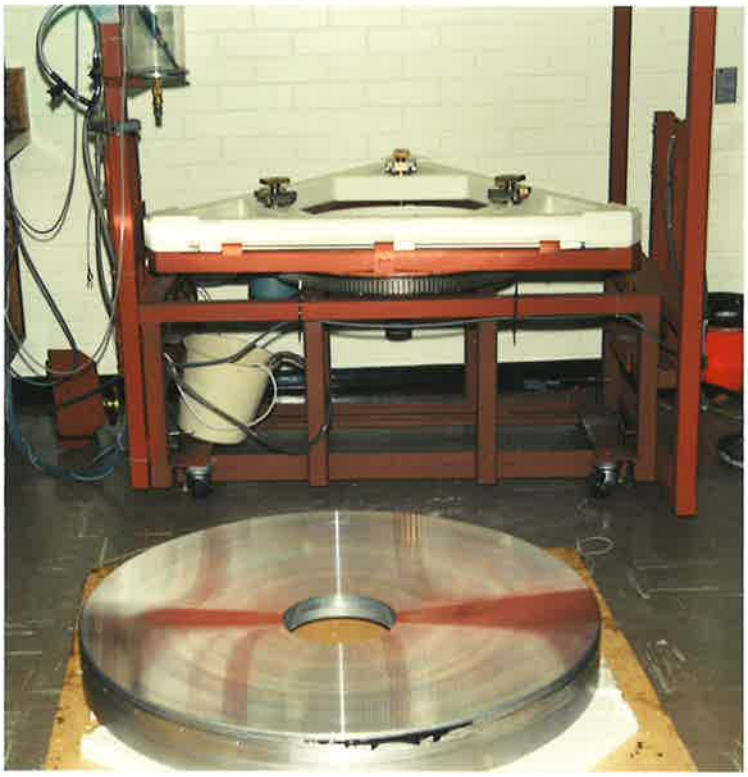

Figure 5.4 Polishing machine in the background with the primary mirror in the foreground.

5.7 The Tool

The tool used to grind the mirror was a 750 mm diameter aluminium disk machined to a radius of curvature of 4020 mm, which is in the mid-range of the radii of curvature of the mirror. The tool was machined on a computer controlled lathe using a standard cutting tool. A metal hoop was attached to the back of the tool with a number of small legs to produce a handle, this can be seen in figure 5.5.

As the mirror was required to be parabolic the exact axi-symmetric shape of the tool was not critical. It is not possible to grind the tool to the required parabolic shape and then grind the mirror to the exact shape of the tool. This process is only possible for spherical components.

In order to remove asymmetric errors from the tool it was ground against the mirror.

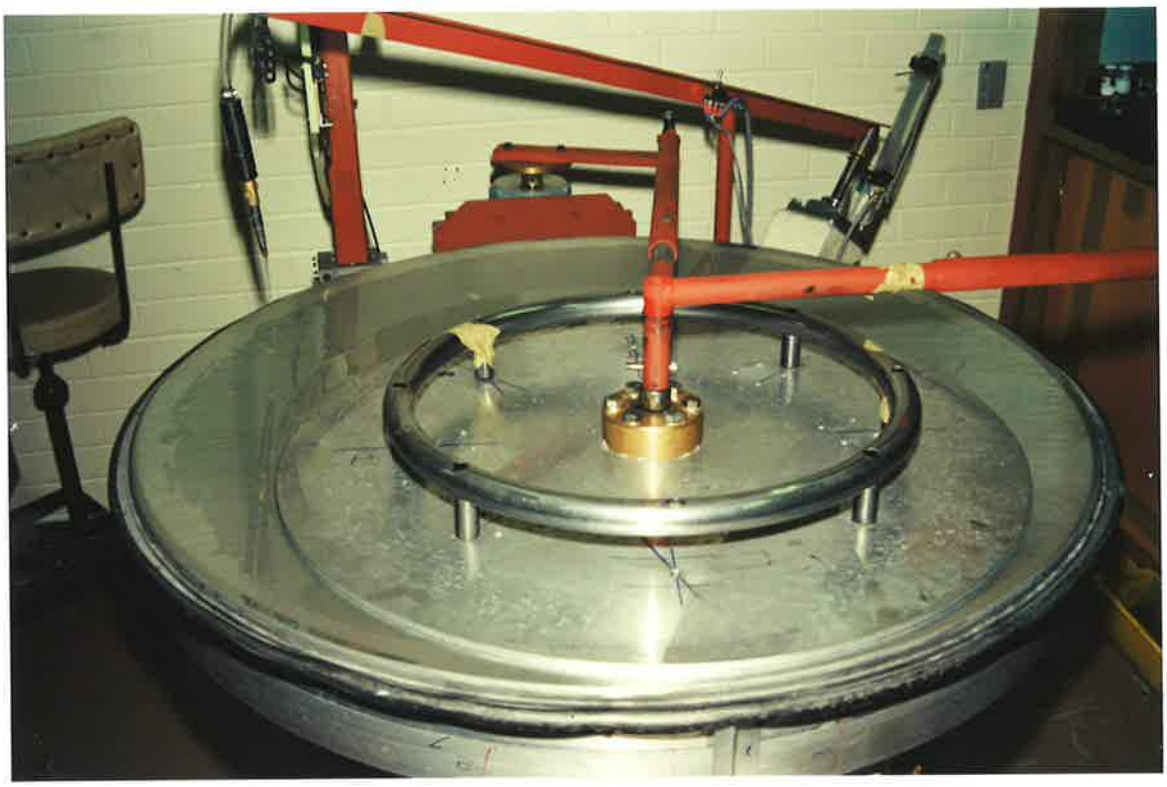

Figure 5.5 Polishing tool on top of the mirror, showing the handle used for manual work and drive mechanism for power assisted work.

5.7.1 Grinding the Tool

The most effective form of grinding was found to be with the use of self adhesive silicon carbide grinding pads. These pads are used in the ophthalmics industry for the production of plastic spectacle lenses and are readily available.

In order to grind the tool 320 grit pads were stuck to the mirror. To obtain good adhesion the surface must be very clean and completely dry. After pressing the grinding pads in place a small amount of water was sprayed over the pads, just sufficient to dampen them. If too much water is used the pads will come unstuck and tear against each other causing

large scratches in the surface of the mirror and tool. The tool was then placed on top of the mirror and the mirror rotation is started. The tool was worked back and forth across the surface by hand in a motion that is suitable to adjust the shape of the surface to that required. In order to grind the tool into an axi-symmetric shape it must be continually rotated as it is worked across the surface.

5.7.2 Testing the Tool

The shape of the tool was checked using a spherometer which measured over a distance of approximately 250 mm. Large errors could be detected by observing the pattern in the grinding marks on the surface being worked and also in the feel of the tool as it was worked. A symmetric surface provided the same resistance to the motion of the tool for all orientations of the tool, while an asymmetric surface provided differing resistances to the motion of the tool depending on its orientation.

5.8 Grinding the Primary Mirror

Grinding the tool and grinding the mirror are essentially the same process except that to grind the mirror the pads are stuck to the tool.

The first stage in grinding the mirror was to remove the large axi-symmetric error generated during the machining. This took approximately 60 hours of actual grinding time plus an approximately equal amount of time in tool preparation and cleanup.

Tool preparation involved removal of worn grinding pads, the thorough cleaning of the surface and application of new pads. Great care was taken when new pads were first used; they were firmly pressed onto the surface to aid adhesion. The first few minutes of work were undertaken with only a little water, (used as a lubricating fluid) and as gently as possible. This minimises the risk of dislodging or tearing the pads and subsequent damage to the surface being ground. After the first few minutes of working the adhesion of the pads improved (due to the pressure and heat generated by the grinding process) and the risk of dislodging the pads was minimal. At this stage a larger amount of water could be added. In contrast to the situation just after new pads were added, it was found that once the pads had reached the stage where they need to be replaced they adhered to the surface so strongly that

they were difficult to remove. When grinding aluminium a set of pads lasted a few hours before they need replacing. Section 5.11 describes subsequent work on the mirror requiring an electroless nickel coating. This coating is very hard and wore out a set of grinding pads in only 10 - 15 minutes.

5.9 Primary Mirror Testing - Mechanical

During the initial grinding stage the shape of the mirror was checked against the template using feeler gauges. The smallest error detectable with this method was about 10 μm, the thickness of the thinnest available feeler gauge. This method of testing measured the relative height of the surface across any diameter but did not relate one diameter to another, so that it did not provide conclusive information on asymmetric errors.

An attempt was made to produce a contour map of the surface using mechanical measurements. The mirror template was suspended just above the mirror surface and the gap between the template and mirror was measured with a linearly variable differential transformer. As the mirror could be rotated under the template it was possible to map the entire surface. However, the bearing on which the mirror was supported was not of sufficient quality to enable the tests to be effective, as the mirror was rotated it would also move vertically.

Once the limit of accuracy of the template feeler gauge tests had been reached optical tests were employed.

5.10 Primary Mirror Testing - Optical

The standard optical tests used by astronomical mirror makers are the Foucault and Ronchi tests. These tests were found to be unsuitable in this case due to the mirror having a f-number of only 2; most astronomical telescopes have an f-number of about 10. These methods are also very sensitive and provide a jumble of information unless the mirror is close to required shape and at least axi-symmetric.

In order to optically test a mirror it is necessary to reflect light from its surface; therefore the surface must be polished prior to testing. The size of the errors in the shape of the surface generally determine the quality of the polish required for testing. A poorly

polished mirror will have a large number of fine scratches in its surface. The effect of these scratches is to produce a blur of light rather than a sharp point at the focus. If there are large errors in the mirror then these can be measured by estimating the centre of the blur. However as the shape of the mirror improves so the quality of the polish required for effective testing must also improve.

Diamond paste was used to produce a quick polish for testing. The diamond paste used was Metadi II; this was placed very sparingly onto polishing pads (C-Brite II) and Metadi extender fluid used as a lubricant. This particular brand of diamond paste comes in a variety of grit sizes from 15 μm down to 0.2 μm. Initial optical tests required polishing with only 15 μm diamond but as higher accuracy was required at later stages, so smaller grit sizes were used.

In general the most effective way to test an optical system or component is to arrange that if the system is perfect, all of the output rays from the system should come to a single point. By measuring the size of the focal spot that occurs and determining the position of various rays within the focal spot it is possible to determine the correction required to the component under test.

If a point source of light is placed at the centre of curvature of a spherical mirror so that the entire surface of that mirror is illuminated, then all the reflected light will come back to exactly the same point, at the source. However, if the spherical mirror is replaced with a parabolic one, then only the light from the central zone of the mirror will come back to the source. Light reflected from zones away from the central region of the mirror will be imaged at a point behind the source, this is illustrated in figure 5.6.

If it were possible to produce a collimated beam of light equal to the diameter of the primary mirror then it would be possible to reflect this light off the mirror and it would, ideally, be focused at a point. However the facilities to produce a 1m diameter collimated beam did not exist locally. As a testing setup able to produce a sharp focal point for the entire aperture of the mirror was unavailable an indirect method of determining the shape was used. Two optical tests were employed, one to determine axi-symmetric errors and the other asymmetric errors.

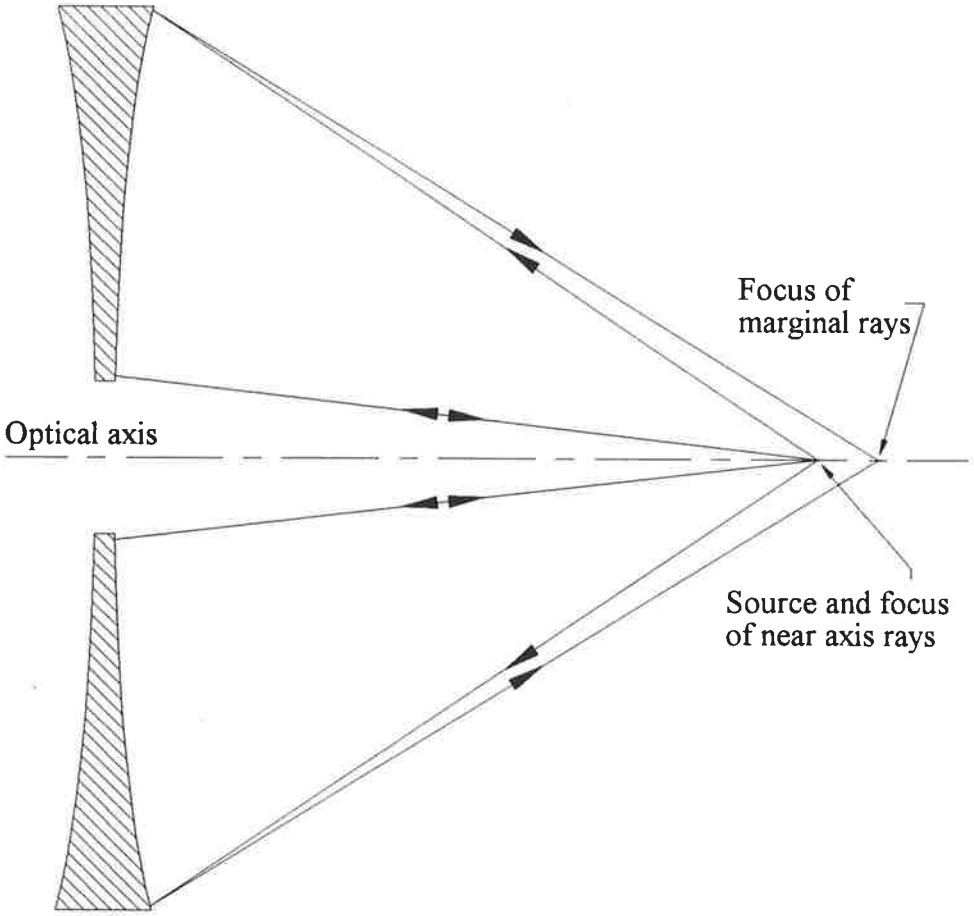

Figure 5.6 Ray trace for a parabola with point source illumination.

To test the mirror for asymmetric errors a mask was placed over the mirror so that only a thin annular ring of the mirror was exposed. This approximates a section of a sphere and the light from the centre of curvature of this annular ring should be reflected back onto itself. In practice the point source was a small HeNe laser expanded with a (x40) microscope objective. This point source was displaced slightly sideways from the centre of curvature of the mirror in order that the image could be easily observed at an equal displacement on the other side of the centre of curvature. This displacement causes a change in the size and shape of the focal spot and one must ensure, by prior calculation, that this effect will not be significant.

By moving a small screen through the focal spot of the mirror one can observe the ring of light (this should be a circular) that comes together at the focus. By noting the shape of this ring, and the size and shape of the focal spot it is possible to determine the size and scale of asymmetric errors.

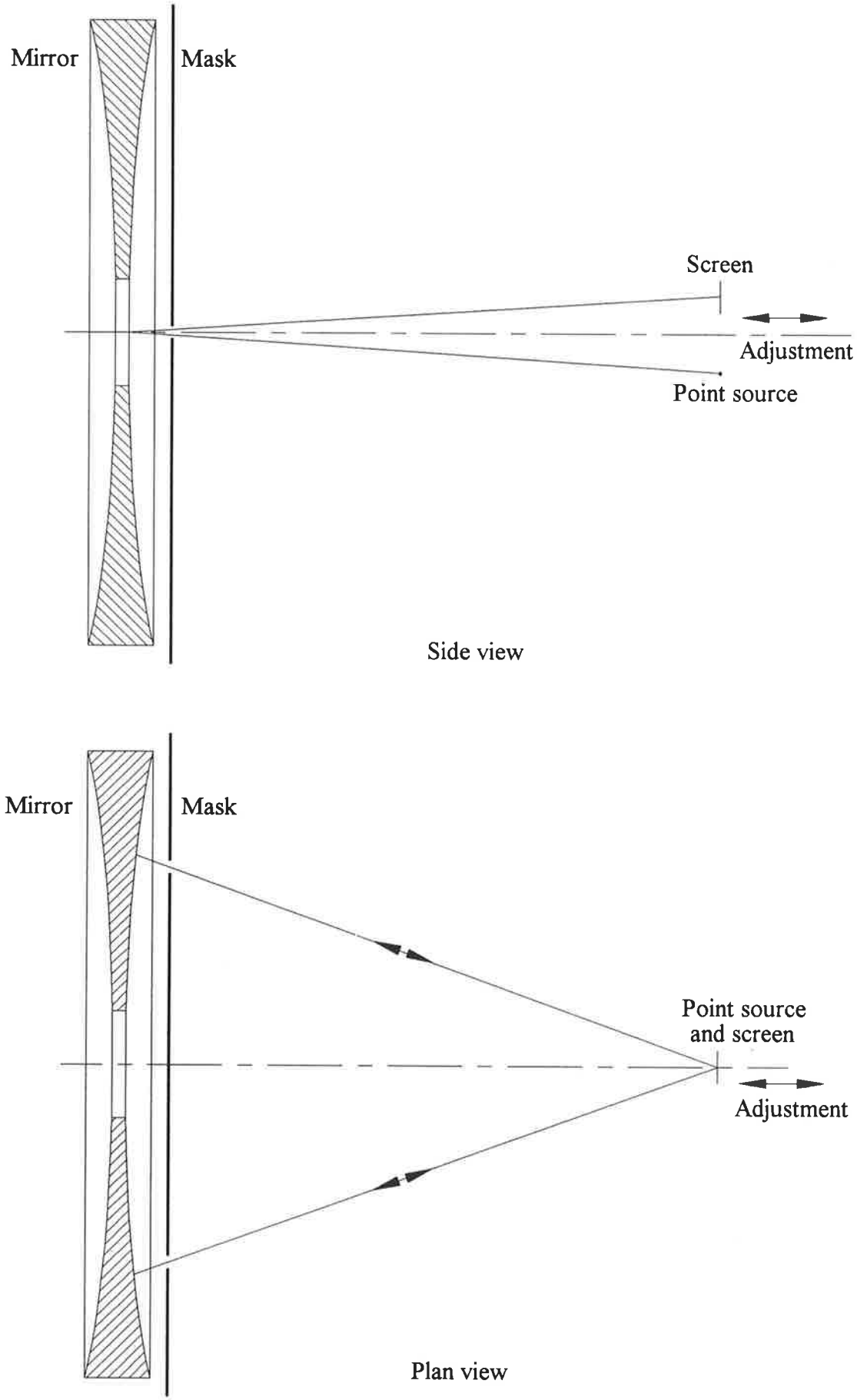

Figure 5.7 Schematic of testing procedure for primary mirror, see text for explanation.

Testing of the shape of the mirror across a diameter was achieved by placing a mask on the mirror which exposed two small areas on a diameter, equally spaced from the centre, as in figure 5.7. The point source was mounted on an optical bench so that it could be moved along the optical axis of the mirror. A screen was mounted at right angles to the optical axis in line with the point source. This screen was mounted so that it moved with the point source. When testing along a vertical axis the point source and its image were arranged in a horizontal plane and vis versa, this eliminates any problems with off-axis aberrations.

To test the shape of the mirror the point source and screen were moved along the optical axis until the light reflected from the two exposed windows came to a point on the screen. The distance from the screen to the mirror was then measured. By repeating this typeof measurement for a number of pairs of points along the same diameter it was possible to calculate the average shape of the mirror across that diameter.

5.11 Electroless Nickel Plating

When the shape of the mirror was approaching that required, so that a fairly good polish was required for testing, it was noticed that the surface of the aluminium was full of many very fine casting pits. These pits had typical dimensions of 100 to 200 μm and in places accounted for up to 50 % of the area of the mirror. It is estimated that in total these casting pits accounted for 10 % to 20 % of the total area of the mirror. Apart from the loss of area these pits also caused a great deal of scattering from the surface; this would be a problem for daytime observation where sky light would be scattered into the instrument.

In order to overcome the problem of the casting pits an Electroless nickel coating was applied to the mirror. Electroless nickel is used commonly in the production of metal mirrors as it provides a very hard surface. The coating was applied by the Electrofabrication and Coating Technology section of DSTO. The application of this coating was completely successful in bridging the casting pits and producing a good hard surface suitable for polishing.

Although the electroless nickel coating solved the problem of the casting pits, during its application the mirror casting was significantly deformed. The coating process takes place at approximately 90°C and it is believed that at this temperature the epoxy resin that was

used to hold the two castings together softened. This allowed the castings to deform. The shape of the mirror as it came back from being coated is shown in figure 5.8. The scale of this error is of the same order of size as the tool, thus it would be very difficult to remove this error by grinding. To add to this, as the nickel coating is very hard and a great deal of work is required to remove even a small amount. The thickness of nickel coating applied to the mirror was about 175 μm and trying to remove the error by grinding would almost certainly cause the coating to be completely removed in places.

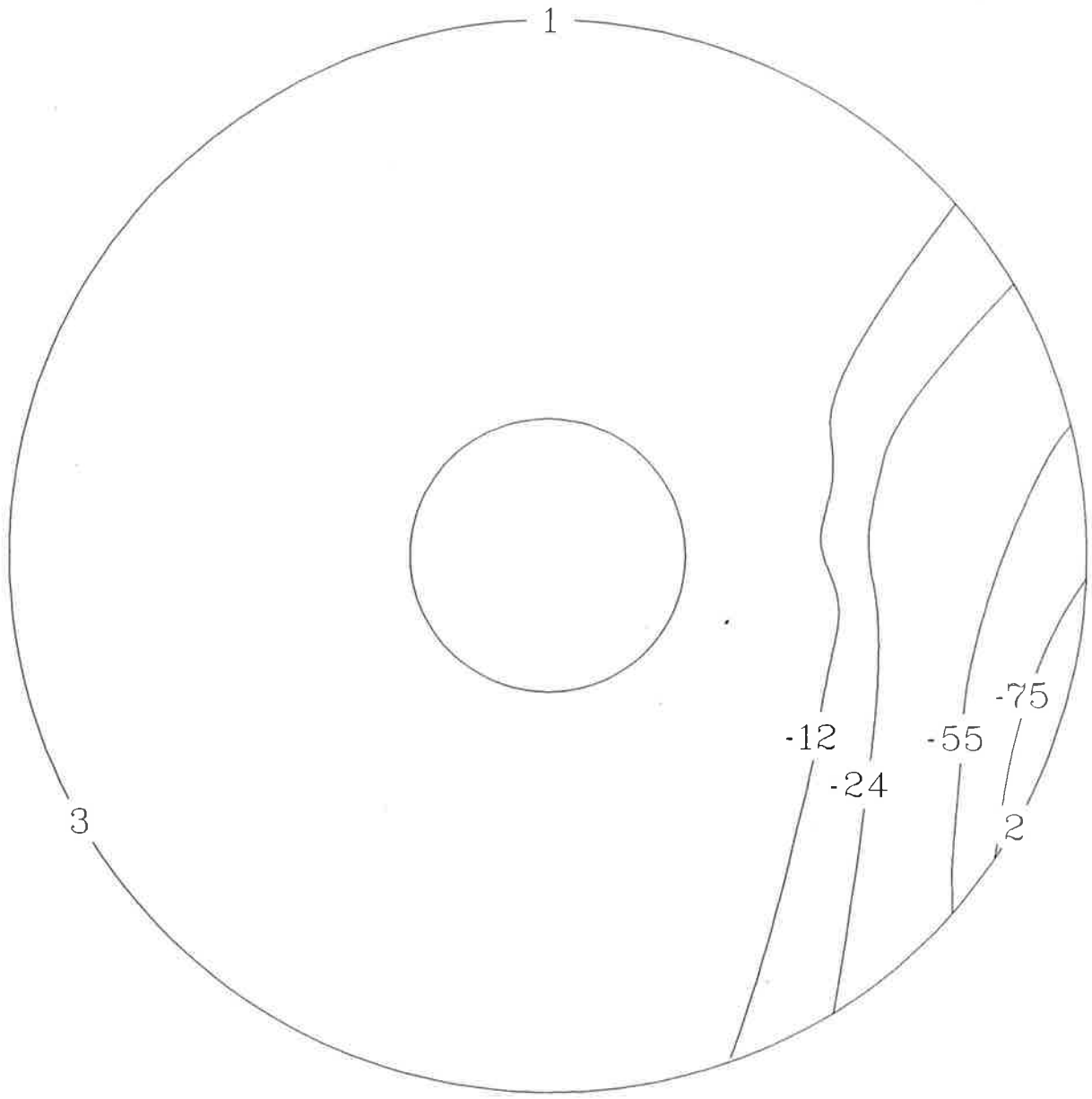

Figure 5.8 Contour plot of surface of primary mirror after electroless nickel coating, errors are in micrometers. Numbers on the outside diameter are for orientation reference

5.12 Further Shape Correction

As it was thought that it was not possible to correct the shape of the mirror by grinding it was decided to split the two castings and try to correct the front surface. The castings were split and the epoxy resin removed. Then the telescope was reassembled with some of the bolts that had previously been holding the plates together being replaced with bolts that pushed them apart. By using optical tests and adjusting the direction and magnitude of the force exerted by each bolt the shape of the mirror was improved; at least most of the larger scale errors were removed. The optical testing in this case was limited by the localised stress patterns in the surface caused by the individual bolts, (see figure 5.9). After this adjustment had been completed epoxy resin was injected into the spaces between the ribs in the mirror structure, in order to hold the hold the shape of the front surface.

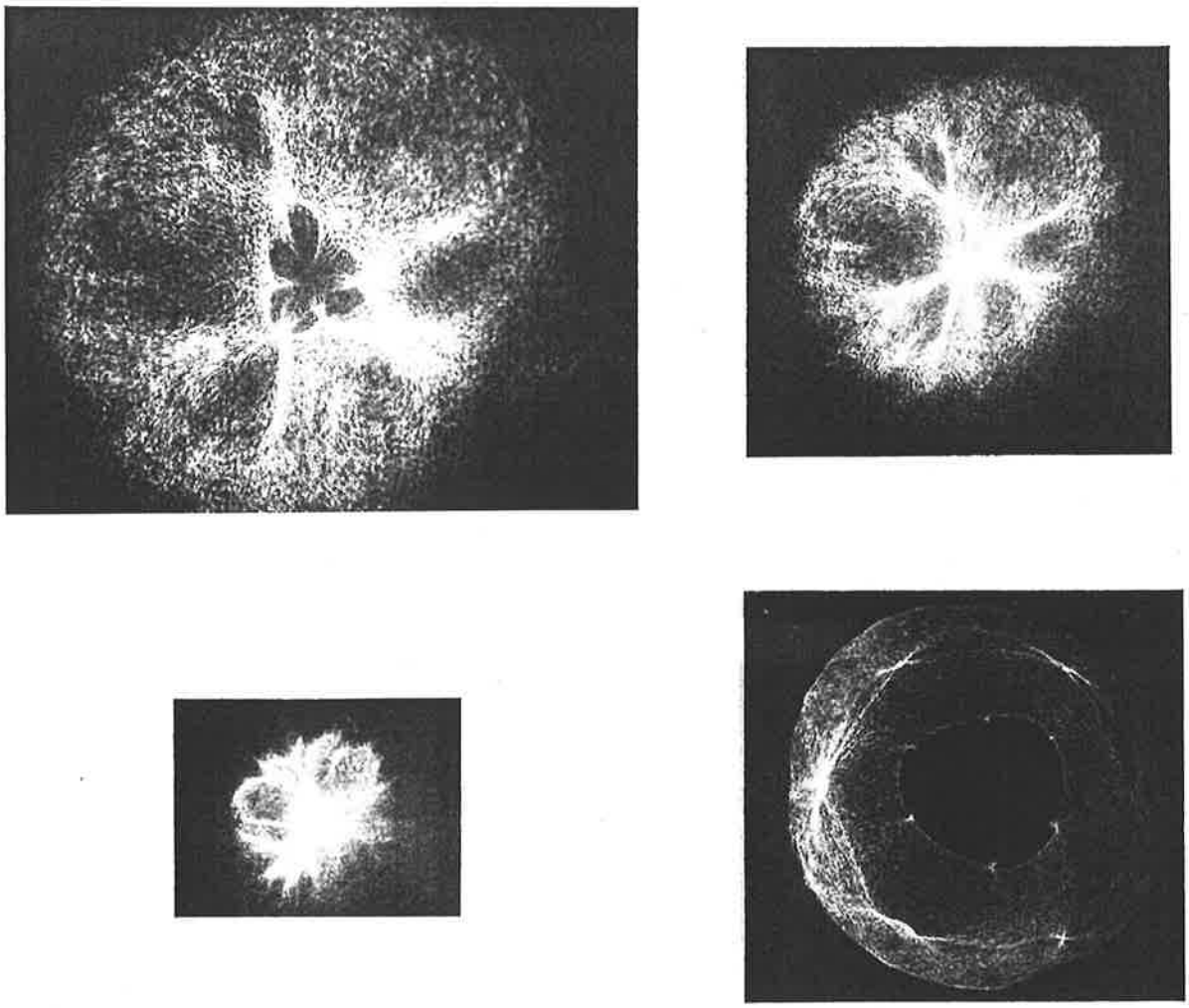

Figure 5.9 Photographs of the image produced by the primary mirror near its focus showing the effects of the stress patterns in the surface of the mirror caused by the bolts.

The process of grinding and testing the shape continued to the point where the mirror was of sufficient quality to be used for night time observations, with a focal spot size for the primary mirror < 0.6 mm in diameter.

Before the lidar can be used for daytime measurements or with the interferometer, further work must be done to improve the shape of the mirror. The final stages of testing may require a different testing technique as the techniques described here may not have the required resolution.

5.13 Secondary Mirror

The hyperbolic secondary mirror was machined on AWA Defence Industries (South Australia) single-point diamond lathe. The shape of this component is very difficult to test as it is a convex mirror and will thus cause a collimated beam that is reflected from it to diverge. Ideally a large parabolic mirror, like the primary, is required to test such a component.

As an alternative a test rig was manufactured which allows the secondary mirror to be tested across a diameter. This test rig is essentially a swinging arm that simulates the primary mirror, see figure 5.10.

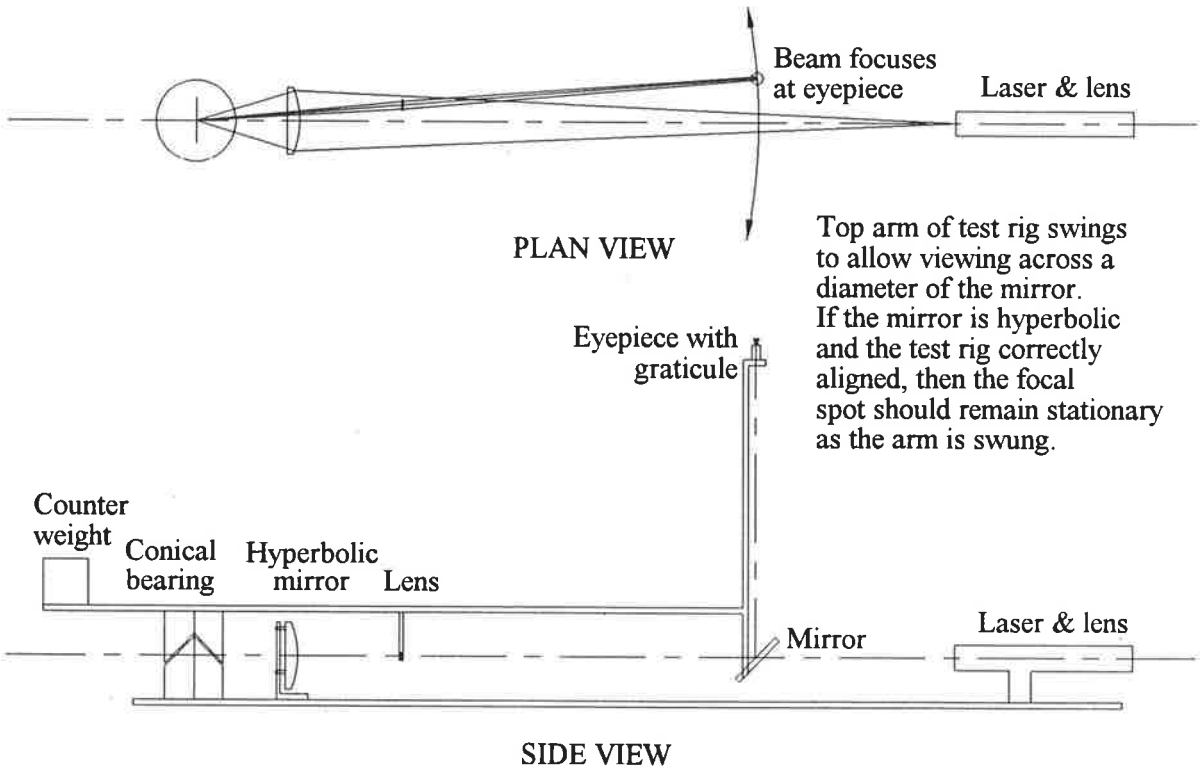

Figure 5.10 Schematic of secondary mirror test rig.

Machining marks in the surface of the mirror caused significant scattering of incident light. In order to reduce the amount of scattering the mirror was electroless nickel coated and then polished. It was important to coat the aluminium mirror with electroless nickel before polishing as this greatly reduces the risk of changing the shape of the component during polishing, as the nickel is so hard.

Testing of the secondary mirror showed that errors were smaller than the detection limit of the testing apparatus, as was expected from the capabilities of the single point diamond lathe.

5.14 Conclusions

When designing a large metal telescope, consideration should be given to producing all non-spherical components on a single-point diamond lathe. The primary mirror should be made spherical if possible (see below). Consideration should also be given to making the structure stable to at least 100°C to enable electroless nickel coating; this is seen as essential.

The base material and casting technique should produce a blank which has a minimum porosity. After the blank has been ground to the required shape electroless nickel should be applied to provide a tough, continuous, easily polished surface.

With a bit of practice, care and thought the actual process of grinding is relatively straight forward, but it is hard work. The more difficult problem encountered during the production of this telescope was the testing of the primary mirror. It makes grinding much easier if the shape of the mirror is well known and can be followed from one grinding session to another; this requires effective testing techniques.

If another instrument of this type should be required, consideration should be given to using a spherical primary mirror and an appropriately corrected secondary mirror. A spherical primary of this size should be much easier to test and therefore produce. The secondary mirror could be easily generated on a single point diamond lathe. The off-axis performance of this design is inferior to that of the classical Cassegrain design. However this may not be an important or significant factor; it will depend on the use to which the telescope is to be put.

6 Fluorescence From Optical Components

6.1 Introduction

Luminescence is the emission of electromagnetic radiation in excess of thermal radiation. This usually occurs in the visible. Fluorescence is the name given to the radiation emitted after the removal of the excitation that caused the luminescence. The intensity of the fluorescence reduces exponentially with time, the rate of decay being independent of excitation intensity and temperature, (Williams, 1966).

As previously described in section 4.3 this lidar system has some optical components that are common to both the transmission and reception optical paths. If the intense laser pulse were to cause these components to fluoresce at wavelengths observable by the detection system, this could contaminate and possibly over-whelm the atmospheric backscatter signal.

6.2 Available Information

This fluorescence problem was recognised at the design stage of the instrument. However data on the fluorescence of various glass types under the conditions of operation of the lidar were not obtainable. A literature search showed that the fluorescent properties of optical materials have been, and continue to be studied, (Rothschild, 1993), but information that may have been helpful in the selection of glass type was not found. Glass manufactures

were unable to provide quantitative information to help in the glass selection. Generally the fluorescence properties of glass are classified by illuminating the sample with UV light and measuring the emissions at longer wavelengths. From this information it is possible to guess which glasses might cause the least problem, but it is not possible to calculate the effect that using these materials would have on the lidar data. It therefore became necessary to test various optical materials in order find one or more that were not going to cause a fluorescence problem.

6.3 Fluorescence Testing

The ideal apparatus to undertake these fluorescence tests was the lower section of the lidar: that is the section up to and including the mirror shutter, as illustrated in figure 6.1. This part of the system was constructed; a description of its operation can be found in

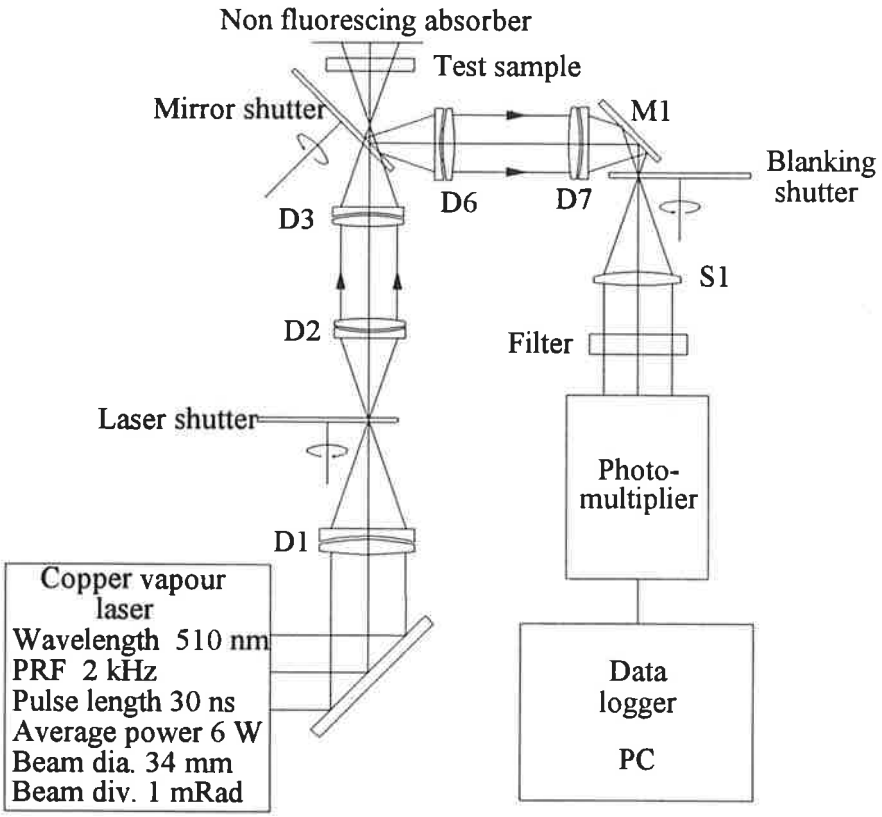

Figure 6.1 Schematic of equipment use for fluorescence testing of optical materials. This is the lower part of the lidar system.

chapter 5. Single samples of optical materials were placed in the optical path above the mirrored shutter, that is in both the transmission and reception paths. An absorbing, non-fluorescing surface placed above the test sample absorbed the light transmitted by the sample. Clean copper was found to be suitable for this purpose. This setup enabled measurement of fluorescence from the individual samples.

Initially the lenses for the entire system comprised BK7/LF7 air spaced doublets. Using air spaced doublets alleviates the need for an optical adhesive. Such adhesives are organic compounds and can therefore be considered a prime candidate to cause fluorescing, although the volume of any adhesive would be very small.

The samples tested for fluorescence were samples that were readily available both from our store of components and some samples from a precision optician. These samples varied in thickness and shape. To a first order approximation the fluorescence signal is proportional to the illuminated volume of the sample allowing a comparison of the fluorescence of the materials, even though tests were conducted on samples of different size.

6.4 Results

Testing of both BK7 and LF7 showed them both to be unsuitable for use in the common transmission-reception path of the lidar due to their fluorescence properties. Figures 6.2 and 6.3 show the measured fluorescence signal for these two materials respectively. The data presented in these figures has had the background removed and is scaled to give the signal equivalent to that from a one cubic centimetre sample. The intensity scales on these two graphs are in the same arbitrary units, enabling a direct comparison of the materials. Each of these figures contains data from approximately 600,000 laser pulses (5 minutes). The background, photo-multiplier dark counts, for this collection period correspond to approximately 48 on the arbitrary intensity scale, so it is possible to see an indication of the magnitude of the problem caused by the fluorescence of these materials. The BK7 sample tested had an illuminated volume of 0.44 cm^{-3} and that of the LF7 sample was 0.20 cm^{-3}.

The decay rates of the fluorescence signal from the samples of BK7 and LF7 have been obtained by fitting an exponential function to the data and calculating the decay rate

from the fitting parameters. The half life of the fluorescence from BK7 is 199±1 μs while that from LF7 is 248±8 μs.

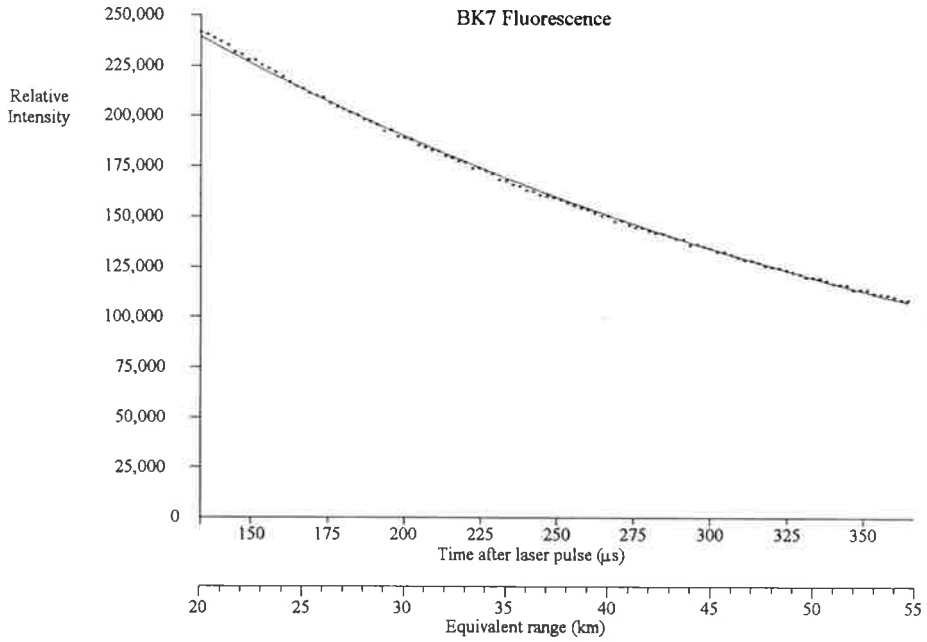

Figure 6.2 Shows the fluorescence signal of a sample of BK7 glass. The small crosses represent the experimental data and the solid line is a fitted exponential decay. The data plotted starts $133^{1}/_{3}$ μs after the laser had fired. Before this time the operation of the shutters reduces the signal level. See text for further explanation.

Testing of large samples, (3.0 cm^{-3}) of a fused silica showed no evidence of fluorescence. Subsequent testing with all optical components above the mirror shutter made of silica also showed no evidence of fluorescence.

Testing for the detection of fluorescence from components D2 and D3 was also undertaken. These two components are in the transmission path but not in the reception path as shown in figure 6.1. However fluorescent light emitted from these components and scattered inside the mirror shutter box is detectable at the photo-multiplier. Figure 6.4 shows the signal detected by the system with D2 and D3 as BK7/LF7 doublets and silica/silica doublets. Laser light passing through the mirror shutter was absorbed by a non fluorescing surface. The photo-multiplier dark counts have not been removed from the data presented in figure 6.4, but their level is indicated on the graph. This figure shows that the use of BK7/LF7 doublets at position D2 and D3 leads to a higher system background.

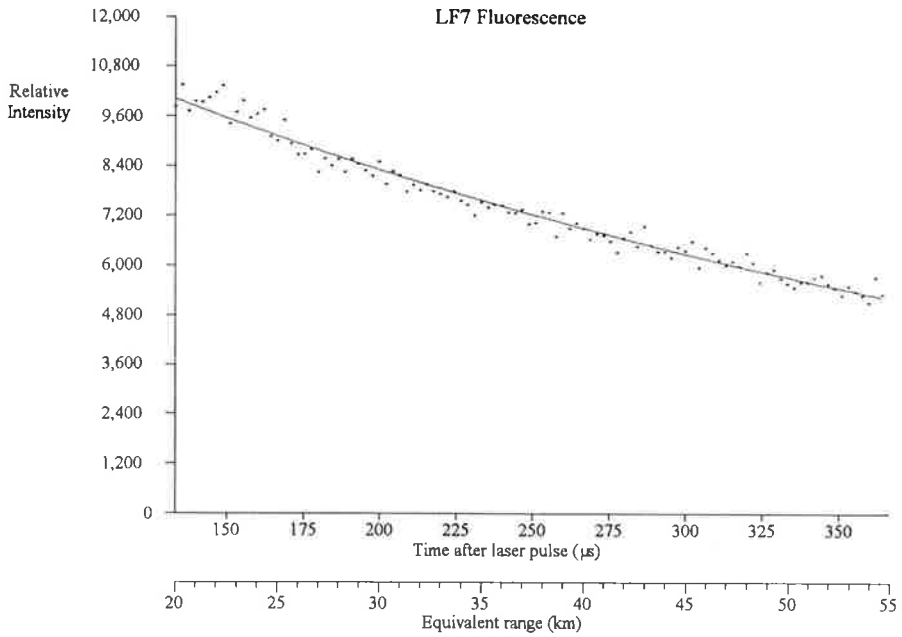

Figure 6.3 Shows the fluorescence signal of a sample of LF7 glass. The small crosses represent the experimental data and the solid line is a fitted exponential decay. The plotted data starts $133^1/_3$ μs after the laser had fired. Before this time the operation of the shutters reduces the signal level. See text for further explanation.

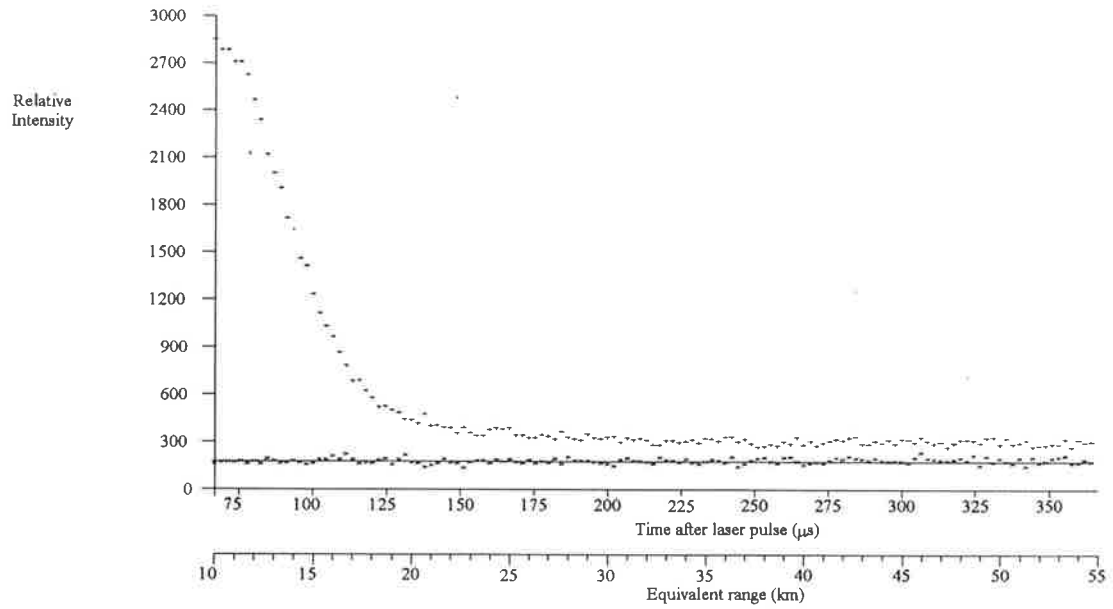

Figure 6.4 Shows the signal recorded with lenses D2 and D3 as BK7/LF7 doublets (top plot) and silica/silica doublets (bottom plot). The solid line represents the photo-multiplier dark-count level. Data in each plot is the sum of that taken for approximately 2.4 million laser pulses or 20 minutes collection time. During the time up to approximately 150 μs after the laser fired the reduction in signal level of the BK7/LF7 plot is primarily due to the operation of the mirror shutter. After this time the reducing intensity is due to the decay of the fluorescence emission.

Two samples of silica, both Dynasil 4000, were obtained from different sources, and it is believed that they could not have been produced as part of the same batch. Neither of these samples showed any evidence of fluorescence.

6.5 Modifications to Optics

In light of the problems associated with the use of BK7 and LF7 in the optical system of the lidar the critical lenses were redesigned and manufacture from silica. In order to maintain the optical quality of the system it was necessary to use silica/silica doublets. This use of doublets allowed the correction of spherical aberration so that the performance of the silica/silica doublets was very similar to the BK7/LF7 doublets they replaced. Two important differences remain between the two types of doublets. The first is that the BK7/LF7 doublets were designed to operate at 510 and 578 nm while the silica/silica doublets were optimised for operation at 510 nm. A doublet with components of the same material cannot have chromatic correction and must therefore be optimised for operation at a single wavelength. The other significant difference being the location of the principle planes of the doublet with respect to the physical optical components, this required slight modification to the lens mounts in order to adjust the position of the lenses.

6.6 Conclusions

The selection of optical material for the components of this type of lidar system, with combined transmitting and reception optics, is critical. The lidar would not operate correctly if BK7, the most common optical glass, were used for these components.

Silica, Dynasil 4000, was found to be suitable for use as the material for these components. It is likely that any good quality silica would be suitable for this purpose, but the only way to be sure it to test the material.

7 Data Analysis Techniques

7.1 Introduction

The basic data analysis for a Rayleigh Lidar involves the calculation of altitude profiles of scattering ratio, molecular density and temperature. The following chapter gives a detailed explanation of the methods used to analyse the data collected with the present instrument and discusses the methods used by other workers.

7.2 Raw Data

The raw data collected by a Rayleigh lidar consists of two signals: the light backscattered from the laser pulse and a constant background signal. Equation 3.7 shows that the number of backscattered laser photons detected (N_{blp}) is proportional to the atmospheric molecular density (ρ_{atm}) and inversely proportional to the square of the range (R), ie.

$$N_{blp}(R) \propto \frac{\rho_{atm}(R)}{R^2} \quad \ldots (7.1)$$

Equation 7.1 is true only if the following three assumptions are valid for the region of the atmosphere under study:

1) scattering from aerosols is insignificant (usually true above 35 km altitude),

2) the optical transmission is high enough that attenuation of the laser pulse and backscattered light can be ignored (usually true above 35 km altitude), and
3) the overlap function, $\xi(R)$ (defined after equation 3.4), is equal to one (achievable via experimental setup).

It can be seen from equation 7.1 that $N_{blp}(R)$ falls off quickly with range due, not only to its $1/R^2$ dependence but also the exponential decrease of $\rho_{atm}(R)$ with altitude. It should be noted that for a lidar located at sea level and operating vertically, as in the present case, range and altitude are equivalent. Under these operating conditions the value of $N_{blp}(R= 30$ km) is 230 times the value of $N_{blp}(R= 60$ km).

The second component of the lidar signal, the background, results from a number of sources; these are photomultiplier dark counts, scattered moon light and scattered light from other sources such as airglow and man made sources.

It is possible to reduce the background from man made sources by appropriate selection of site, and from airglow by appropriate spectral filtering. Background due to moonlight (or other white light sources) is a function of both the PRF of the lidar and the spectral width of the optical filter in the reception system. Reducing the spectral width of a filter decreases the fraction of the white light that it will transmit. However the cost of suitable filters increases as the filter width decreases and in general the peak transmission of the filter will be less for narrower filters.

Section 4.2.3 explains the dependence of the background on the PRF of a lidar system, in particular it shows that background is directly proportional to the PRF. In the case of the present instrument the background level becomes significantly higher on nights within several days of full moon, (see chapter 8).

Figure 7.1 show a raw data profile represented by a series of crosses. The crosses on this graph represent the number of photons detected in sequential time intervals of $2^2/_9$ μs (equivalent to a range of $^1/_3$ km) after the emission of the laser pulse. The data for each individual altitude region is stored as a single integer. For historical reasons concerning the way in which this type of data was collected and stored, an individual altitude region is often referred to as a channel. An explanation of the various features of this data profile follows.

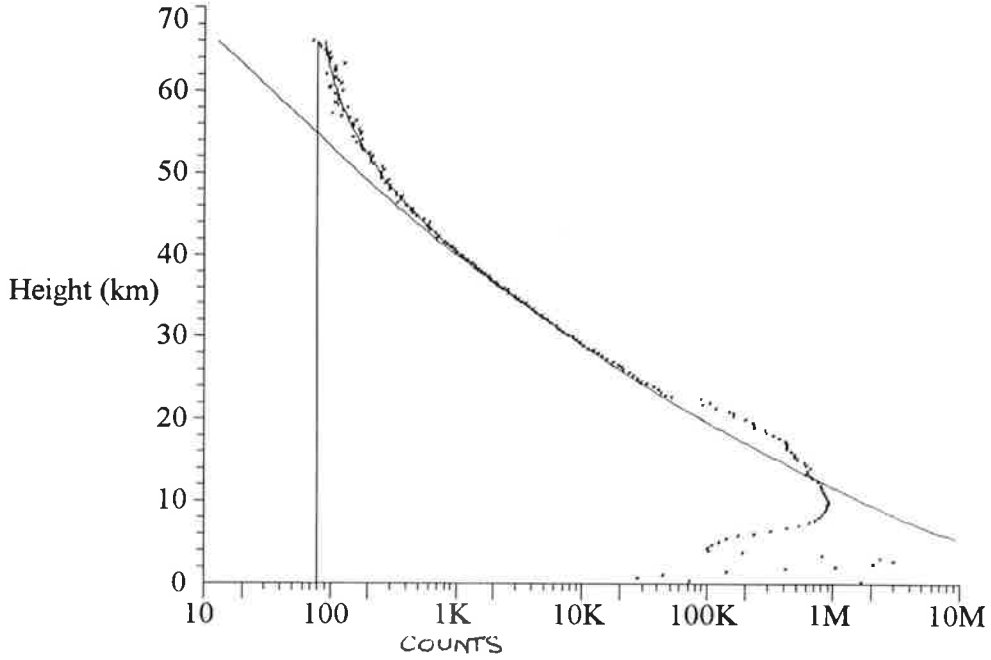

Figure 7.1 Shows a raw data profile (number of photoelectron pulses out of a photomultiplier tube as a function of range) represented by crosses, fitted background (vertical line) and expected molecular scattering level(slightly curved diagonal line). The third line (curved diagonal line) is the sum of the fitted background and expected molecular scattering signals.

In the region below 4 km altitude the signal is due to two factors; the first is electrical interference for the laser firing and the second is a small amount of light leakage around the shutters. This leakage allows a small fraction of the backscattered laser light to reach the photo-multiplier tube. The signal recorded for this altitude range is of no value and will not be discussed further.

The signal from the altitude range 18 to 64 km is due to a combination of backscattered laser light and background. Figure 7.1 also shows 3 lines plotted along with the experimental data. These lines represent the background (vertical line), the expected molecular backscatter signal (slightly curved diagonal line) and the sum of these two components (curved diagonal line). Section 7.3 gives a detailed discussion of the method used to determine the fitting of these profiles.

In the altitude region below approximately 25 km the experimental data has a higher magnitude than is expected from the sum of the background and molecular scatter signal. This enhancement in the level of the recorded data is due to Mie scattering from the aerosols

that form the stratospheric aerosol layer. The magnitude and altitude range of this enhancement vary with changes of the aerosol layer.

The signal level from the regions above 63 km and below 18 km suffers attenuation by the action of the shutter system, (see section 4.5.4). Appropriate calibration of the shutter system allows the correction of data from these regions. Section 8.2 discusses this point further.

In the case of a photon counting lidar the statistical distribution of the number of photons detected in any altitude region is described by a Poisson distribution, (Bevington 1969). A Poisson distribution has its standard deviation equal to the square root of the mean, and this fact allows an estimation of the uncertainty in the number of photons detected in each channel. Assuming that the number of photons counted is an approximation to the mean of the distribution from which it is taken, then the standard deviation of the distribution can then be taken as the square root of the measured value.

7.3 Separation of Background and Molecular Scattering Signals

It is important for subsequent data analysis to be able to determine the contributions of the background and molecular scattering to the recorded data profile. In the present case the following method has been used to separate these signals.

It is first necessary to determine an altitude region for which molecular scattering and background are the only sources of signal and for which the response of the lidar system remains constant. For convenience this altitude region will be referred to as "the clean signal region".

Variations in the response of a lidar system occur as a result of the operation of shutters and as a result of variations in the overlap factor $\xi(R)$, (see section 3.10). For a correctly aligned and focused monostatic co-axial lidar system $\xi(R)$ is equal to 1 for all R greater than a few kilometres, where this minimum range is dependent on the individual optical system of the instrument.

In the present case, the upper limit of the clean signal region is set by the range at which the shutter system begins to attenuate the signal, just above 60 km. The lower limit is determined by the altitude of the top of the aerosol layer, which is usually below 35 km.

Hence the clean signal region selected for the present work is 35 to 60 km. In some cases the top of the aerosol layer is much lower than 35 km and in these cases the clean signal range is extended down to 30 km.

By an extension of equation 7.1 it can be seen that the signal level recorded throughout the clean signal region, $N(R_{csr})$, is given by

$$N(R_{csr}) = B + k\frac{\rho_{atm}(R_{csr})}{R_{csr}^2} \quad \ldots (7.2)$$

where B = the background level,
R_{csr} = range (within the clean signal region), and
k = is the constant of proportionality.

Using an atmospheric model and assuming that on an average taken over the entire clean signal region the model provides a good approximation to the actual density profile, then $\rho_{model}(R)$ can be substituted for $\rho_{act}(R)$ in equation 7.2. This then allows the determination of the background (B) and the constant of proportionality (k).

The CIRA 1986 model and the model of Fleming et al are compared to the measured data in chapter 8. These comparisons show that the CIRA 1986 model provides a significantly better approximation to the measured data than the model of Fleming et al, hence the CIRA model was selected as the most appropriate to use in the following calculations. Subsequently $\rho_{cira}(R)$ is used in place of $\rho_{model}(R)$.

A weighted least squares fitting procedure was used to fit the fitting profile, $N_f(R_{csr})$, described by the equation 7.3, to the measured profile, $N(R_{csr})$, by appropriate adjustment of the parameters B and k. The calculation of this fitting uses **all** data points that lie within the clean signal region.

$$N_f(R_{csr}) = B + k\frac{\rho_{cira}(R_{csr})}{R_{csr}^2} \quad \ldots (7.3)$$

A least squares fitting procedure calculates the difference between two functions (in this case $N_f(R_{csr})$ and $N(R_{csr})$) for each value of the independent variable (in this case R_{csr}). These differences are then squared and their sum taken. The fitting is achieved by varying the fitting parameters (in this case B and k) in order to minimise the value of this sum. If for

some reason it is expected that the fit of the two functions will be better for some values of the independent variable than for others the fitting procedure should be weighted to take this into account. Weighting involves multiplying the square of the difference between the two functions by a value, the weight. These weights represent the expected goodness of fit of the two functions and are calculated for each value of the independent variable. Then χ^2, the goodness of fit parameter, is defined as,

$$\chi^2 = \sum \left[W(R_{csr}) \left(N(R_{csr}) - N_f(R_{csr}) \right)^2 \right] \quad \ldots (7.4)$$

Where $W(R_{csr})$ is the weighting factor at range R (within the clean signal region)

As the weights are required to reflect the expected goodness of fit of the two functions at each value of the independent variable they can be set equal to the reciprocal of the square of the expected uncertainty in the fit, that is,

$$W(R_{csr}) = \frac{1}{\left(\text{uncertainty in fit} \left(R_{csr} \right) \right)^2} \quad \ldots (7.5)$$

It is essential for the correct fitting of $N_f(R_{csr})$ to $N(R_{csr})$ that the weights applied in the fitting procedure be carefully considered. While still considering only the clean signal region, there are two reasons why the function $N_f(R_{csr})$ will not be exactly equal to $N(R_{csr})$. The first of these is the statistical fluctuations in the recorded signal level $N(R_{csr})$, while the second reason is that $\rho_{cira}(R_{csr})$ will not be exactly equal to $\rho_{atm}(R_{csr})$. The weighting function used in the fitting procedure should take into account both of these uncertainties.

If we first consider the statistical fluctuations of the recorded signal level, section 7.1 shows that the uncertainty in the number of photons detected in any channel is approximated by the square root of the number of photons detected. The square of the uncertainty is then just the of number photons detected, $N(R_{csr})$.

Using the information in Labitzke (1990) and the present data set it is estimated that variations between the actual density profile and the densities calculated from the CIRA model are usually less than 2% throughout the clean signal region. This gives an uncertainty of $(0.02\ k\ \rho_{cira}(R_{csr}))$ in the fitting of the two functions. Here the parameter k scales this

uncertainty to an equivalent number of photons detected, in order to combine it with the uncertainty due to the statistical fluctuations.

Combining both of these uncertainties allows the weighting function to be defined as,

$$W(R_{csr}) = \frac{1}{N(R_{csr}) + \left(0.02\, k\, \rho_{cira}(R_{csr})\right)^2} \quad \ldots (7.6)$$

Testing of the above method, for the separation of background and backscattered laser light signals, has been carried out using simulated data. The simulated data was calculated by combining appropriately scaled signals representing the background (a constant) and the atmospheric backscatter signal (calculated using an atmospheric model), the effects of aerosol scattering were not included. The signal level for each altitude range that is calculated in this way represents the mean signal for the altitude range. These mean signal levels were then used to calculate a Poisson deviate from the mean for each altitude range. These Poisson deviates were then used as the simulated data.

The testing of the method for the separation of the background and backscattered laser light signals has been undertaken for a range of background and backscattered laser light levels and in all cases where the CIRA model approximates the actual density profile, this procedure is effective in separating the signals.

In order to make comparisons between profiles a measure of the background level and the backscattered laser light level are used. The background level is the number of background counts per second of detector live time. The backscattered laser light level is the number of backscattered laser counts detected from 50 km ($^1/_3$ km range) per second of detector live time. Both of these quantities are measured in counts per second (cts/s).

In summary, the separation of the background and backscattered laser light signals was achieved by fitting a constant and an atmospheric density model to the experimental data such that χ^2, defined in equation 7.4, is minimised. The weighting function $W(R_{CSR})$ used in equation 7.4 being defined by equation 7.6.

7.4 Scattering Ratios

The scattering ratio, S(R) is defined as the number of laser photons backscattered from aerosols and molecules divided by the number backscattered from molecules alone (Fiocco 1984); that is,

$$S(R) = \frac{N_{mol}(R) + N_{aer}(R)}{N_{mol}(R)} \quad \ldots (7.7)$$

The number of backscattered laser photons detected is the sum of the number of backscattered laser photons detected from both molecular, $N_{mol}(R)$, and aerosol scattering, $N_{aer}(R)$, that is,

$$N_{blp}(R) = N_{mol}(R) + N_{aer}(R) \quad \ldots (7.8)$$

As it is not possible to determine whether an individual photon was scattered by a molecule or an aerosol particle it becomes necessary to estimate $N_{mol}(R)$ in order to determine the scattering ratio. The number of backscattered laser photons expected on the basis of molecular scattering is calculated using the CIRA model. Due to large uncertainties in the efficiency of both the transmission and reception systems of a lidar system and in the optical transmission of the lower atmosphere it is not possible to directly calculate this expected signal. That is, it is not possible to calculate from first principles the value of k in the above equations. From section 7.2 it can be seen that the expected signal from purely molecular scattering, $N_{em}(R)$ is to a very good approximation,

$$N_{em}(R) = k\frac{\rho_{cira}(R)}{R^2} \approx N_{mol}(R) \quad \ldots (7.9)$$

By substitution of equations 7.8 and 7.9 into 7.7 we obtain a practical formulation of the scattering ratio,

$$S(R) = \frac{N_{blp}(R)}{N_{em}(R)} \quad \ldots (7.10)$$

Throughout the clean signal range $N_{aer}(R) = 0$ (by definition of the clean signal range) and therefore,

$$S(R_{csr}) = \frac{N_{mol}(R_{csr})}{N_{em}(R_{csr})}$$

$$= \frac{\rho_{atm}(R_{csr})}{\rho_{cira}(R_{csr})} \quad \ldots (7.11)$$

and as $\rho_{atm}(R_{csr}) \approx \rho_{cira}(R_{csr})$,

$$S(R_{csr}) \approx 1 \quad \ldots (7.12)$$

The present data set shows that the scattering ratio calculated at altitudes in the clean signal region (35 to 60 km) and based upon the CIRA model atmosphere is usually in the range 0.98 to 1.02. This is illustrated in figure 7.2, by the figures in appendix B and those figures in appendix C calculated using the CIRA model. Figure 7.2 shows a scattering ratio profile calculated from the data collected during the night of 19 March 1993. The variations in the scattering ratio from a value of unity within the clean signal region for these data are due to two reasons. The first is variations between the model density and the measured density profiles (ie at 42 km altitude) and the second is statistical noise in the measured density profile (at the higher altitudes shown on the graph). Further discussion of the scattering ratio profiles calculated from the measured data is given in the following chapter.

In the lower stratosphere the aerosol layer causes significant scattering of the laser light and the term $N_{aer}(R)$ in equation 7.7 becomes greater than zero causing the scattering ratio to becomes significantly greater than unity . At this stage it should be noted that the amount of backscatter from molecules and that from aerosols varies with wavelength, furthermore the wavelength variation is different for these different forms of scattering, (see chapter 2). This implies that S(R) is also a function of λ, ie $S(R,\lambda)$. As it is not possible to calculate the wavelength dependence of aerosol scattering accurately no "standard" wavelength has been established for the presentation and inter-comparison of scattering ratio data. Instead, scattering ratios are calculated at the wavelength of operation of the lidar and this wavelength is presented along with the scattering ratio profiles.

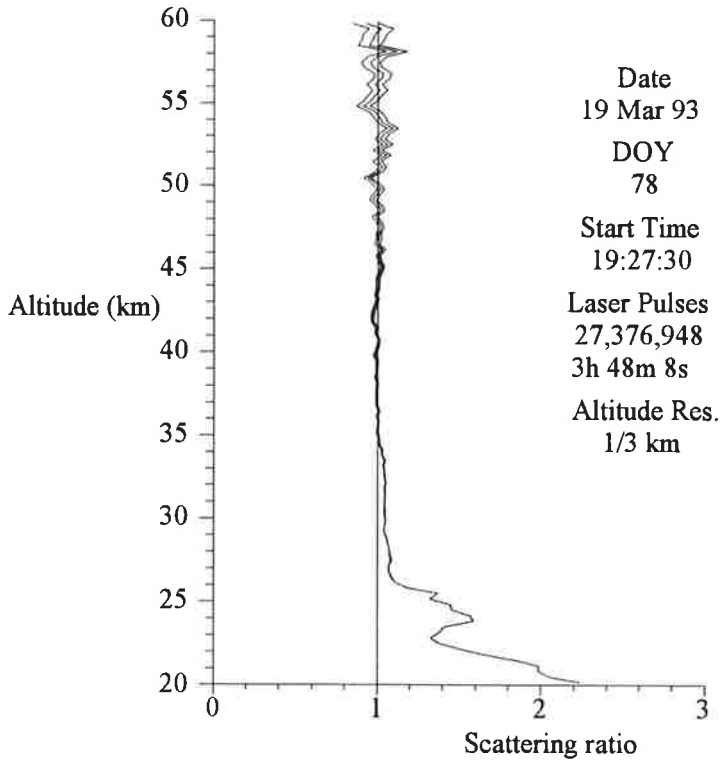

Figure 7.2 A typical scattering ratio profile calculated from data collected during the night of 19 March 1993. It should be noted that there can be large variations in this profile in the lower altitude region, below about 35 km due to variations in the stratospheric aerosol layer.

7.5 Density

The relationship between the actual atmospheric molecular density, $\rho_{atm}(R)$ and the recorded Rayleigh lidar data is given by equation 7.2. As described in section 7.3 it is not possible to independently calculate the value of k in this equation so that the calculation of an absolute density profile relies on fitting the CIRA model data to the recorded data as described above. This implies that the calculated density profile may be affected by the method used to fit the CIRA data to the recorded data and also by how well the CIRA data models the recorded data.

The method of fitting described in section 7.4 fits the CIRA model to the recorded data over the maximum possible altitude region, (the clean signal region). It also allows for the statistical uncertainties in the individual measurements and the uncertainty in the fit of the CIRA profile to the recorded data.

Detailed descriptions of the methods used by other workers for the removal of background and the scaling of the density profiles do not appear in the literature. The only information that can be found is provide by;

a) Chanin et al (1980,1981), who fit the experimental data with the CIRA model between 35 and 40 km (1980 paper) and 30 and 35 km (1981 paper),

b) Shibata et al (1986a, 1986b), who fit the experimental data with the CIRA model at 39 km, and

c) Adriani et al (1991), who fit the CIRA model to the data at the lowest available level, this ranged from 34 to 40 km for the presented data.

None of these authors gives any justification for the selection of the method used to fit the CIRA model to the experimental data.

There are two further points that should be taken into account when selecting the method and range or the CIRA fitting. The analysis of data with time resolutions small enough so that the effects of gravity waves are not averaged will mean that the fitting procedure should be biased to the lower levels, as the relative density perturbations caused by gravity waves are smaller at the lower altitudes. Events such as sudden stratospheric warmings may cause significant differences between the actual density and the CIRA model. These effects should be considered when selecting the fitting method.

All of the lidar systems mentioned above have PRF's of approximately 10 Hz, giving background levels about 200 times lower than those of the present instrument, (see section 4.2.3). No explanation of the method used to remove the background has been given by these authors. It should be noted that independent measurement of background levels is difficult, if not impossible to achieve due the changes that occur in the dark-count level of a photomultiplier tube for a short time after exposure to light.

The method of fitting or scaling of the measured density profiles to the CIRA model leads to small uncertainties in the absolute values of density obtained in this way. This type of density profile is best thought of as a relative density profile whose absolute calibration is not quite as well established. The absolute calibration depends on how well the monthly averaged CIRA models approximate the experimental data. In the case of the present data the CIRA model provides a good fit to the experimental data, (see chapter 8)

7.6 Temperature

It is possible to calculate an absolute temperature profile by using the density profile and assuming that the atmosphere is in hydrostatic equilibrium and obeys the ideal gas law. This method also requires calibration at the highest altitude used in the calculations, although the effect of this calibration on the calculated temperatures diminishes fairly quickly with altitude.

The physical basis for the calculation of temperature profiles is described below. Given the atmospheric density at some altitude and using model data (or data from some other source) to provide an estimate of either the temperature or pressure at this level, then the ideal gas law (equation 7.13) allows a complete description of the thermodynamic state of that region of the atmosphere.

$$P(z) = \rho(z)\ R\ T(z) \qquad \ldots (7.13)$$

Where $P(z)$ = pressure,
$\rho(z)$ = density,
R = specific gas constant for dry air = 287.03,
$T(z)$ = thermodynamic temperature, and
z = altitude.

Using this and the measured density profile it is possible to calculate a pressure profile by integrating downward from the initial level. This is achieved by assuming hydrostatic equilibrium, that is by using,

$$\frac{dP(z)}{dz} = - g(z)\ \rho(z) \qquad \ldots (7.14)$$

Where $g(z)$ = acceleration due to gravity.

With both density and pressure profile's known, equation 7.13 allows the calculation of the temperature profile.

Chanin et al (1980) and Shibata et al (1986a) both provide algorithms for the calculation of temperature profiles from density profiles based on the above method. Although differing in detail both of these algorithms give results of similar accuracy. This is shown in figure 7.3. This figure shows the CIRA temperature profile for January at 35°S along with temperature profiles calculated, using the density profile from the same model,

with each of these algorithms. When real data are used these algorithms will give slightly different results because of the different ways in which they use the data, but the results are well within the range of uncertainties expected when real data is used.

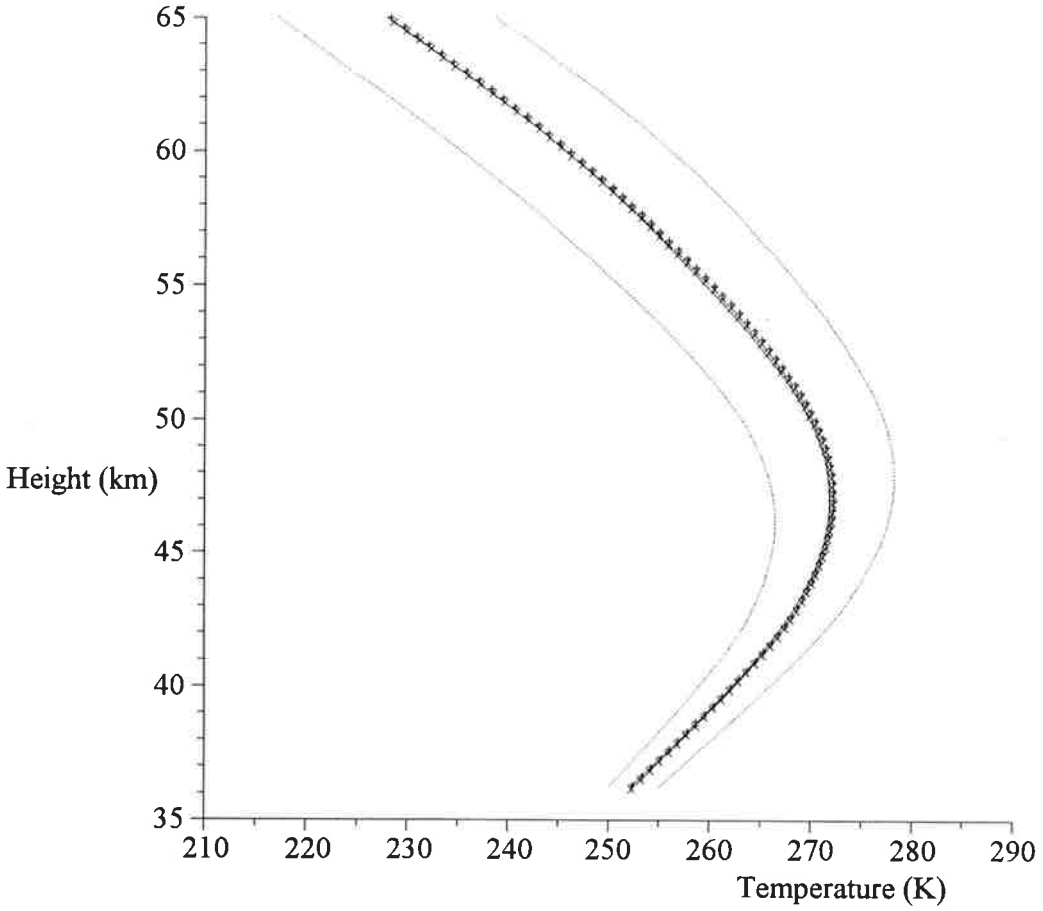

Figure 7.3 Shows temperature profiles calculated using CIRA model data for January at 35°S. The solid line represents the CIRA model temperature profile, the x's represent temperatures calculated using the algorithm of Shibata et al (1986a) and the +'s using the algorithm of Chanin et al (1980). The dashed lines represent the uncertainties expected on the basis of backscattered laser level from 50 km of 100 cts/s, background of 100 cts/s, 3 hours integration time and 1/3 km height resolution.

The algorithm used by Chanin et al explicitly calculates the pressure at each altitude level and fits this to a model at the uppermost altitude. The calculation of the pressure profile is achieved by the application of equation 7.14 and requires that the measured molecular density profile be scaled reasonably well to an absolute profile.

The algorithm suggested by Shibata et al uses as its starting point a temperature from a model, it never explicitly calculates pressures, and works for a relative density profile.

There is no requirement to scale the measured density profile to an absolute profile in order to use this algorithm.

As the current data set shows all density profiles fit the CIRA model well (section 8.4), so that both of these temperature calculation algorithms are expected to work well for this data set. The calculation of temperature profiles that follow are based on the algorithm suggested by Chanin et al.

The algorithm described by Chanin et al (1980) calculates a temperature profile from a density profile in the following way.

Let $P_m(z_n + \Delta z / 2)$ be the atmospheric pressure, taken from a model of the atmosphere for an altitude of $z_n + \Delta z / 2$.

where z_n is the altitude of the centre of the uppermost (n^{th}) channel of the density measurement, and

Δz is the altitude range corresponding to a density measurement channel,

so that $z_n + \Delta z / 2$ is the maximum altitude at which density measurements have been made.

Assuming that the region of the atmosphere under study is in hydrostatic equilibrium then the pressure at the top and bottom of the i^{th} layer then can be calculated using:

$$P(z_i + \Delta z / 2) = \sum_{j=i+1}^{n} \rho(z_j)\, g(z_j)\, \Delta z + P_m(z_n + \Delta z / 2) \qquad \ldots (7.15)$$

$$P(z_i - \Delta z / 2) = P(z_i + \Delta z / 2) + \rho(z_i)\, g(z_i)\, \Delta z \qquad \ldots (7.16)$$

The average temperature for the i^{th} altitude region $z_i - \Delta z / 2$ to $z_i + \Delta z / 2$ can then be calculated using,

$$T(z_i) = \frac{g(z_i)\, \Delta z}{R \log \left| P(z_i - \Delta z / 2) \;/\; P(z_i + \Delta z / 2) \right|} \qquad \ldots (7.17)$$

Chanin et al (1980) also give a summary of the calculation of the uncertainties in the temperature profile calculated using the above algorithm.

7.7 Uncertainties in Temperature Profiles

There are two main causes for the uncertainties in the calculated temperature profiles. The first of these is the uncertainty resulting from the statistical fluctuations in the number of photons detected, as described in section 7.2. The second is the uncertainty resulting from the use of model (or some other) data to provide a starting point for the temperature calculation algorithm.

The statistical fluctuations in the number of photons detected in each channel leads to an uncertainty in the relative density profile.

$$\frac{\Delta\rho_r(R_{csr})}{\rho_r(R_{csr})} = \frac{\Delta N(R_{csr})}{N(R_{csr})} \qquad \ldots (7.18)$$

Where $\rho_r(R_{csr})$ = Relative density.

While considering only the clean signal region, the number of backscattered laser photons is equal to the total signal minus the background, that is,

$$N_{blp}(R_{csr}) = N(R_{csr}) - B \qquad \ldots (7.19)$$

The uncertainty in $N(R_{csr})$ is simply $[N(R_{csr})]^{1/2}$. As B is determined by fitting over a large number of channels it can be considered as being well known, ie. $\Delta B \approx 0$. Hence,

$$\frac{\Delta\rho_r(R_{csr})}{\rho_r(R_{csr})} = \frac{[N_{tot}(R_{csr})]^{1/2}}{N_{tot}(R_{csr}) - B} \qquad \ldots (7.20)$$

Chanin et al (1980) gives details of the calculation of the uncertainties in a calculated temperature profile given the uncertainties in the density profile, and this will not be repeated here. Figures 7.4 and 7.5 show the uncertainties in a calculated temperature profile for different backscattered laser light and background levels. These plots were produced using simulated data and represent the mean of the uncertainties expected.

Remembering that the background is directly proportional to the system PRF, these figures show that it is desirable, for this type of temperature measurement, to have a PRF as low as possible. There are of course other factors that limit the useful range of PRF's.

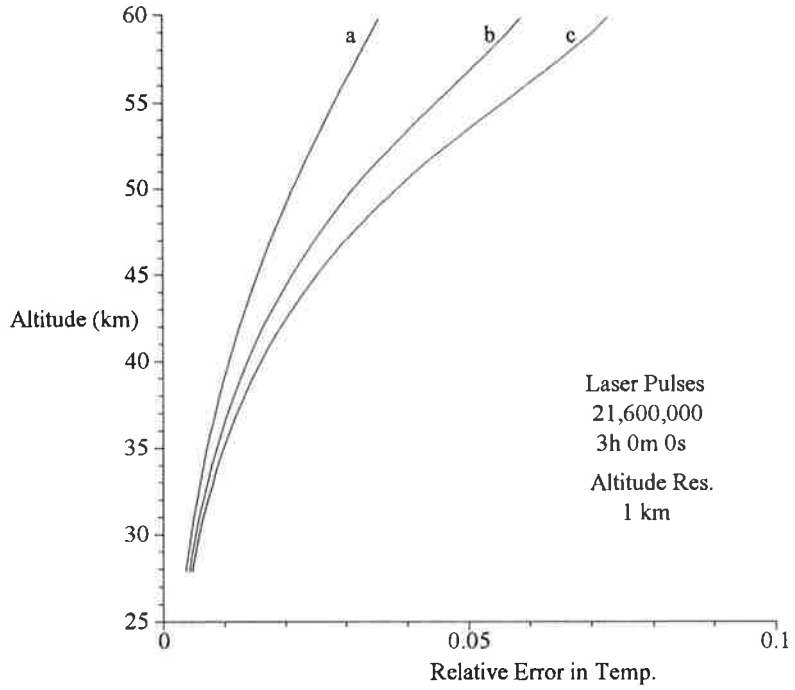

Figure 7.4 Shows the relative errors in temperatures calculated for a backscattered laser signal from 50 km of 100 cts/s and three background levels, (a) 0, (b) 100 and (c) 200 cts/s. (Simulated data used had height resolution of 1 km and collection time of 3 hrs at PRF = 2 kHz.)

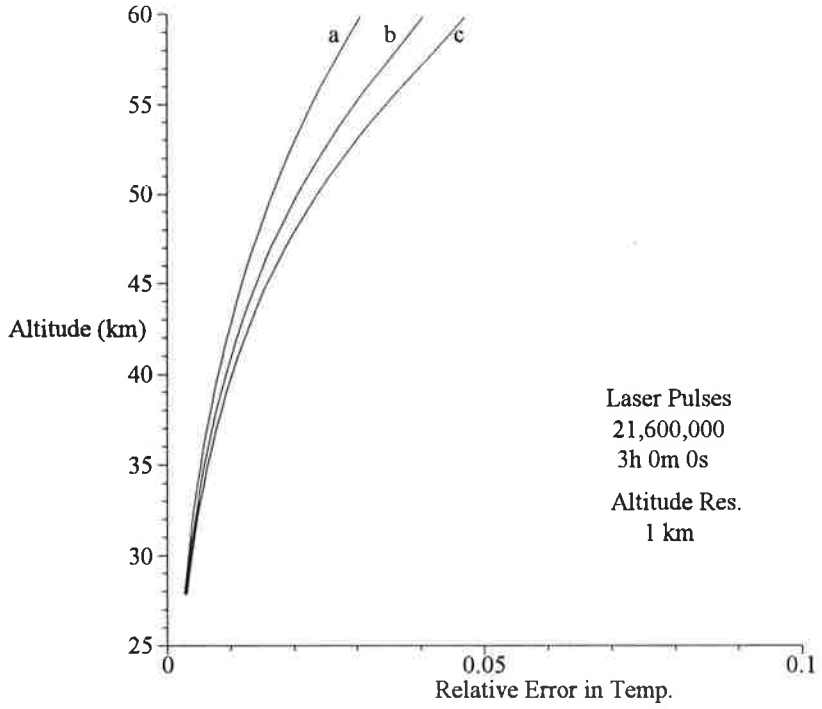

Figure 7.5 Shows the relative errors in temperatures calculated for a backscattered laser signal from 50 km of 200 cts/s and three background levels, (a) 0, (b) 100 and (c)200 cts/s. (Simulated data used had height resolution of 1 km and collection time of 3 hrs at PRF = 2 kHz.)

The uncertainties resulting from the use of a model pressure to initiate the algorithm reduce quickly as the algorithm proceeds. In other words the influence of the model data used as a starting point decreases with altitude. Figure 7.6 shows the relative uncertainties due to this fitting for three values of uncertainly in the initial fitting.

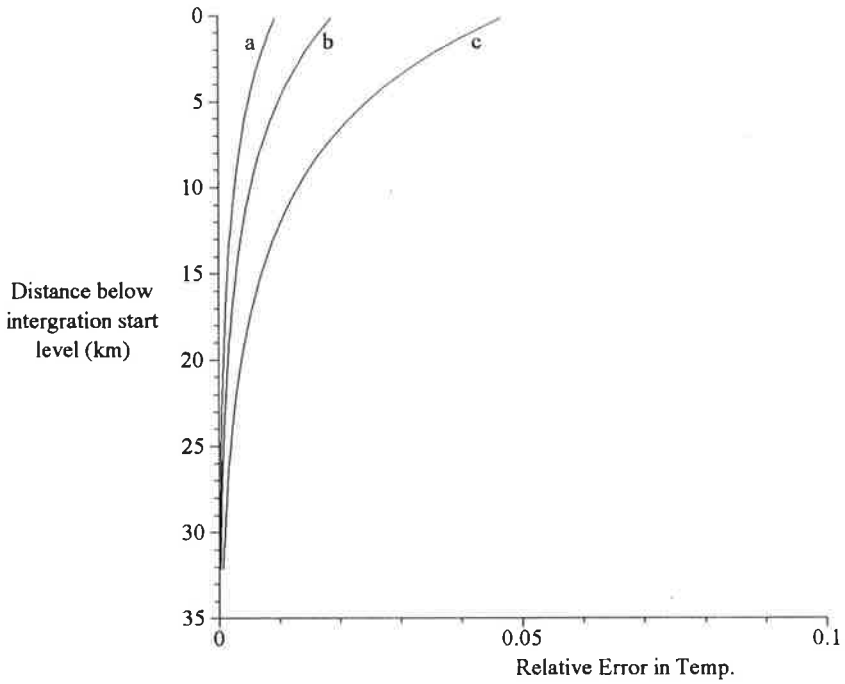

Figure 7.6 Shows the contribution to the relative uncertainty in temperature due to the uncertainty in the fitting of the data to a model at the upper level. Three cases are plotted for uncertainty in fitting to the model of (a) 1%, (b) 2% and (c) 5%. The uncertainties in the temperature profile due to the fitting of the data to a model at the upper level are independent of height resolution used in the calculations.

It is possible to combine the recorded signals from a number of adjacent range intervals in order to reduce the uncertainty in the calculated temperatures. Figure 7.7 shows the uncertainties in the temperatures for the same simulated data having differing height resolutions.

A short discussion of errors arising in Rayleigh lidar temperature profiles due to effects including multiple scattering and residual aerosols is given by Uchino et al (1986). If temperature profile calculations are extended down below the top of the aerosol layer then the effective increase in the measured density at these levels leads to calculated temperatures being lower than the actual temperatures.

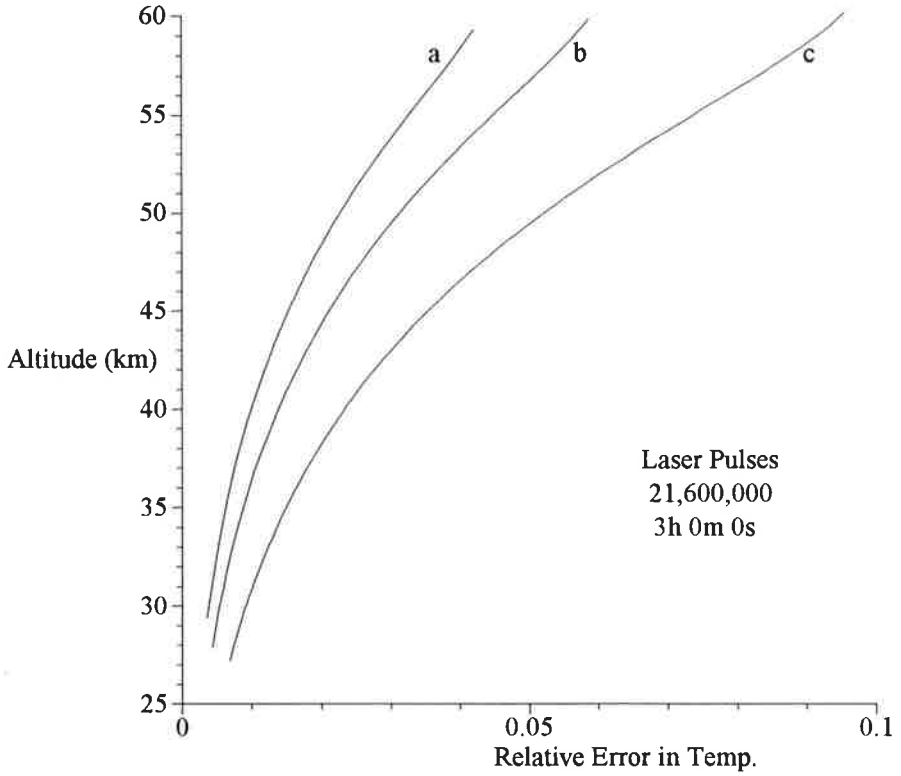

Figure 7.7 Shows the effect of changes in the height resolution on the uncertainty in the temperatures. Three cases are plotted, for height resolutions of (a) 1/3 km, (b) 1 km and (c) 2 km. (Simulated data used had backscattered laser signal from 50 km of 100 cts/s and background of 100 cts/s and collection time of 3 hrs at PRF = 2 kHz.)

7.8 Conclusions

The present data set varies from other Rayleigh lidar data in that in has a much higher background level (of the order of 200 times) due to the much higher PRF of the system. This has required that careful consideration be given to the separation of the background and the backscattered laser light. The method used to achieve this is effective, and allows standard techniques to be used for the calculation of scattering ratio and temperature profiles.

8 Data Analysis

8.1 Preliminary Examination

As data were collected they were written to the hard disk of the controlling computer along with a header containing information describing the circumstances under which the observations were made. At the conclusion of each observing session the data file was written to a floppy disk using a compression program and taken away for analysis.

The header for each data file contains the following information:

a) date and time for the start of data collection[1],
b) duration of observation,
c) shutter phase settings,
d) total number of laser pulses fired,
d) sum of all data channels,
e) profile code, and
f) azimuth and zenith angles.

Profile codes are numbers used to identify the different types of profiles. These include the different types of calibration profiles, atmospheric backscatter profiles, rejected profiles and sum profiles.

Initially the data were inspected visually by displaying the raw data profiles on a computer screen. This allowed any profiles that had obvious errors to be rejected and the

[1]All times are Central Australian Standard Time (CST), CST = GMT + 9 1/2 hours.

profile codes to be edited. Once this was complete sum profiles were added to the end of the data file. For each profile type a sum of all profiles of that type was taken, these became the sum profiles. In most subsequent data analysis only the sum profiles were used as the signal to noise ratio of individual profiles was too low to be useful.

8.2 Shutter calibration

The operation of the shutter system causes attenuation of the signal backscattered from the altitude range of about 5 to 20 km. Chapter 4 gives a description of the operation of the shutter system. Calibration of the shutter system would allow the signal to be corrected and the minimum data collection range would be reduced to about 5 km. This would not have any effect on the calculation of temperature profiles as the minimum altitude for temperature calculations is limited by the stratospheric aerosol layer. It would however allow scattering ratio profiles to be calculated down to 5 km. This would allow more extensive monitoring of the aerosol loading of the atmosphere.

The shutter system can be thought of as acting like a single shutter opening and closing an aperture. It starts to open the aperture when light backscattered from 5 km reaches the instrument and has fully opened the aperture when light backscattered from 20 km is received back at the instrument. A calibration of the shutter system requires a knowledge of what fraction of the light incident on the aperture is transmitted as a function of time (or range). This would be a simple task if the aperture were evenly illuminated, but this is not the case. If the entire field of view of the receiving system were evenly illuminated then the aperture would also be evenly illuminated. However the transmitted laser beam does not fill the field of view of the receiver system (this would cause a loss of signal). Added to this, aberrations in the optical system combined with the intensity distribution across the laser beam and the optical effects of the atmosphere cause the transmitted beam to non-uniformly illuminate the field of view of the receive system.

Although the backscattered laser light does not evenly illuminate the aperture any background light will do so, provided that it evenly illuminates the field of view of the receiver system. Hence a different calibration will apply to the backscattered laser light and to any background light. However as the backscattered laser light levels between 5 and 20 km

are many orders of magnitude greater that background levels (see figure 7.1) this difference can be ignored.

The signal level recorded by the lidar is a function of both the amount of backscattered light and the attenuation by the shutter system. The amount of light backscattered is a function of altitude while attenuation by the shutter system is a function of range. This allows these two effects to be separated by recording profiles at different zenith angles.

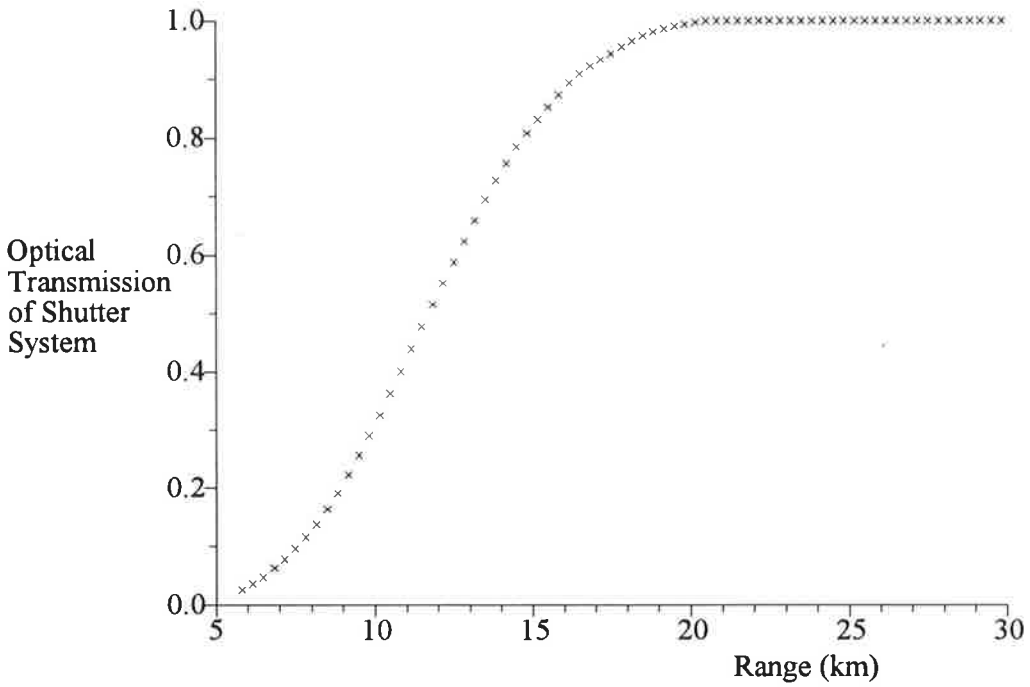

Figure 8.1 Shutter calibration function calculated from data collected between 20:35:00 and 21:18:00 (CST, Central Australian Standard Time) on 16 February 1993.

If profiles are recorded for two zenith angles, say 0° and 45°, and the shutter system attenuates the signal level of the vertical profile up to an altitude of 20 km, then the profile taken at 45° will suffer attenuation due to the shutter system up to a range of 20 km, which corresponds to an altitude of 20 sin(45°) or 14.2 km. The off vertical profile thus allows the measurement of backscattered intensity in the altitude range 14.2 to 20 km unaffected by the shutter system. This information combined with the attenuated signal from the vertical profile allows the calibration of the shutter system for ranges from 14.2 to 20 km. Once this calibration has been calculated and applied to the off vertical profile (corresponding to an altitude range of 14.2 km down to 10.0 km) the calibration function for the next range

interval can be calculated. After a few iterations of this process a complete calibration function of the shutter system can be determined.

While almost all data were taken with the telescope pointing vertically, data collected during the night of 16 February 1993 included some profiles taken with a zenith angle of 43°. This has allowed the calculation of a shutter calibration function from the data collected during this night. Figure 8.1 shows this shutter calibration function plotted as the optical transmission of the shutter system as a function of the lidar range.

The scattering ratios calculated down to 6 km by making use of this calibration are presented in figure 8.2. This scattering ratio profile shows the general features expected on the basis of a model (McClatchey et al 1978). That is a peak in the scattering ratio at approximately 18 to 22 km, a minimum at approximately tropopause altitudes and an increase below this level.

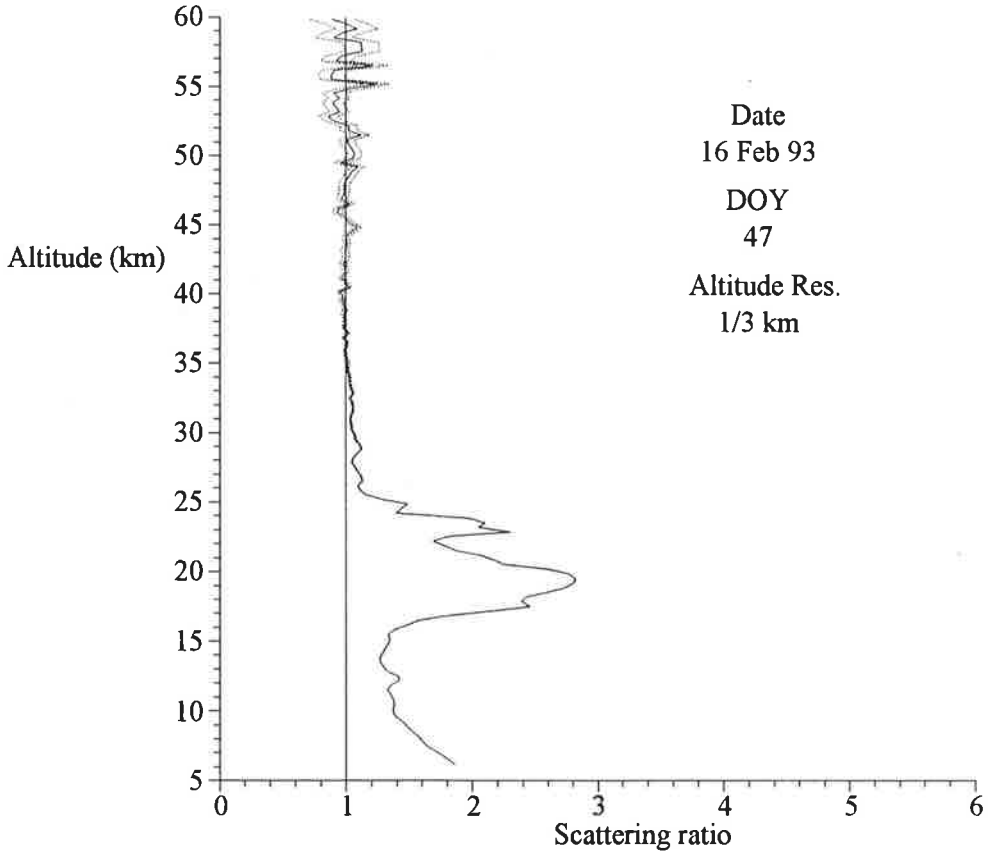

Figure 8.2 Scattering ratio profile calculated using data calibrated down to 6 km. The calibration was calculated using 15 minutes of data taken in the vertical and 15 min at a zenith angle of 45°. The data presented is the 15 min of vertical data with the calibration applied. No correction has been made for multiple scattering or attenuation of the beam in the lower atmosphere.

Data recorded at off vertical zenith angles require the telescope to be tilted. As this operation is not yet mechanised and is difficult to achieve manually, the only off vertical profiles were collected on the night of 16 February 1993.

A relative measure of the shutter system transmission function can be achieved by providing a reproducible illumination pattern over the system aperture. A small incandescent light was placed above the telescope primary mirror in order to provide this illumination and the receiver system was then run as usual (with the laser switched off). The relative transmission of the system determined in this way allowed the transmission function to be monitored throughout observing sessions and between sessions without the need for telescope re-positioning.

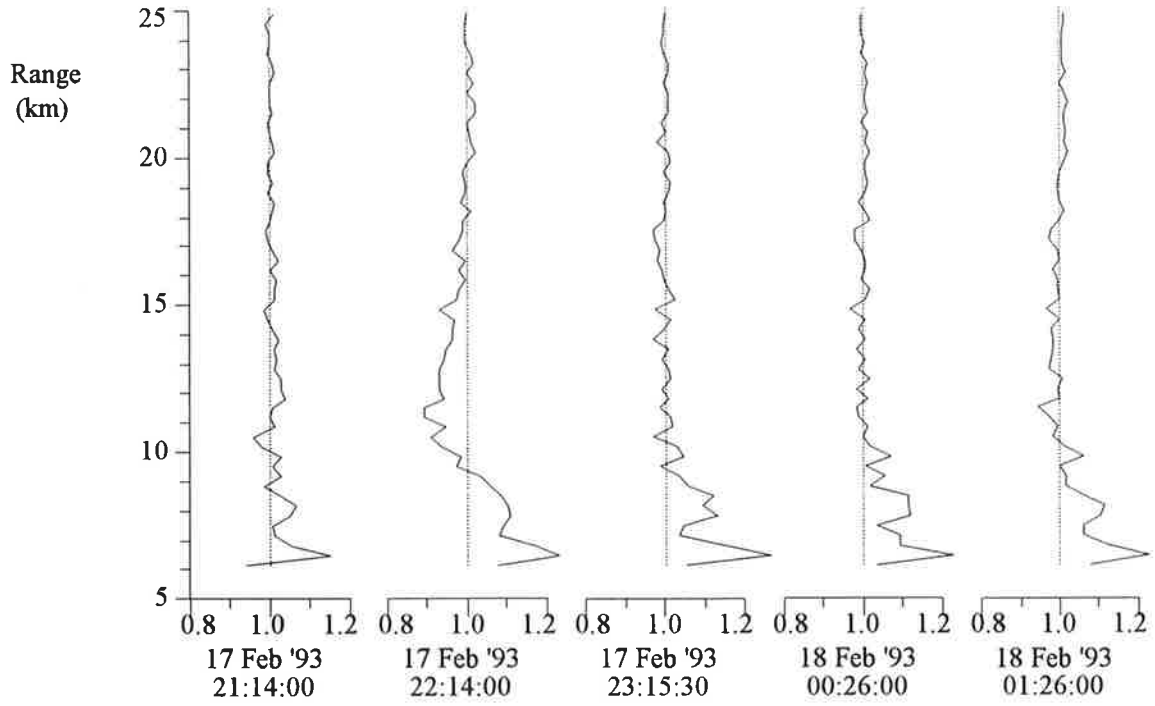

Figure 8.3 Shows the relative change in the shutter transmission function over a period of 5 hours. The change in the shutter transmission function is with respect to the transmission function measured at 20:13:30 (CST) on 17 Feb '93. Each of these transmission functions was calculated from approximately 5 minutes of data. The shutter transmission functions used in this figure are determined using an incandescent source, see text for explanation.

Figure 8.3 shows the changes that occurred in this relative transmission function throughout the night of 17 February 1993, and figure 8.4 shows the changes that occurred in

the relative transmission function between the nights of 17 February and 3 March 1993. These two figures show that the shutter transmission function can change by around 20% on a time scale of the order of an hour. Hence any calibration function is applicable only to data collected around the time of the calibration function.

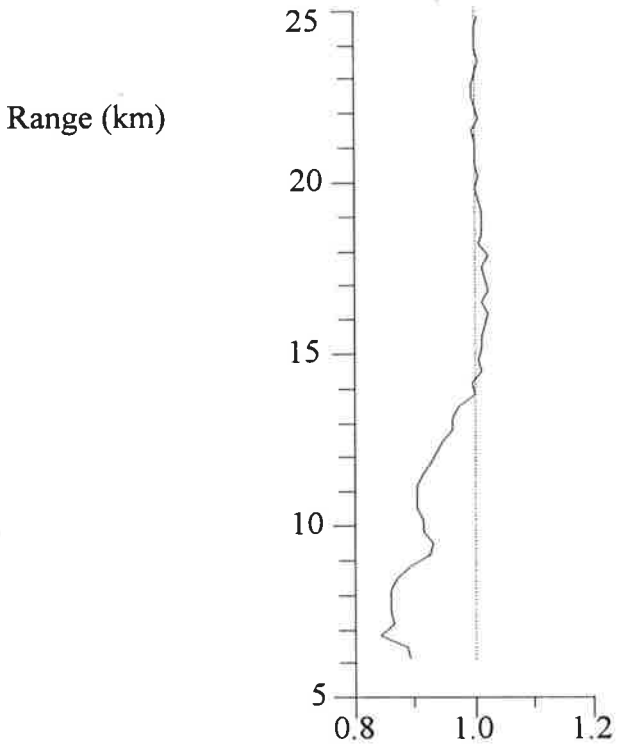

Figure 8.4 Shows the relative change in the shutter transmission function from 17 February 1993 to 3 March 1993. The shutter transmission functions used in this figure are determined using an incandescent source, see text for explanation.

The shutter function is dependent on the operation of both the mirror shutter and the photomultiplier shutter so that an increase in the transmission at one altitude does not necessarily mean an increase at all altitudes, (see figure 8.3, data for 22:14:00). The cause of these changes in the calibration function may be due to fluctuations in the phase of the shutters. The electronic control system maintains strict control over the phase of the shutters, but it is possible to account for the variations by assuming that the shutters' phases vary from one end of the control range to the other. In practice it is observed that the phase of the shutters varies quickly throughout their control ranges and so it could be expected that for data collected over periods of greater than about one minute the effects of shutter phase jitter would be averaged out.

Another possible cause of changes in the calibration function is changes in the illumination pattern of the aperture. This could be caused by changes in the shape of the telescope or changes in the alignment of other optical components due to thermal effects. Adjustments to the optical system may cause large changes in the shutter calibration function.

8.3 Background and Backscattered Laser Light Levels

The fitting procedure described in section 7.3 allows the background and backscattered laser light signals to be determined for individual profiles. The method used to quantify the background and backscattered laser light signals is given near the end of section 7.3.

Backscattered laser light and background levels are given, as a function of time, in figure 8.5. This figure shows that the backscattered laser light level increases rapidly during the first 40 min of data collection, then falls rapidly over about the next hour, remains fairly constant for nearly 3 hours then starts to fall off again. This behaviour is even more surprising when the intensity of the laser light transmitted into the sky and the efficiency of the receiver system over this period are considered, (see figure 8.6).

The intensity of the laser light transmitted into the sky was measured by a PIN diode (active area 1 cm^2) place in the transmitted laser beam about 1 m above the surface of the primary mirror. The efficiency of the receiver system was measured by illuminating the telescope with a small incandescent light bulb connected to a regulated power supply (necessary to ensure constant intensity). With the laser output turned off and the receiver system operating the detected signal allowed monitoring of the system efficiency.

Figure 8.6 shows that when the intensity of backscattered laser light is corrected for the laser power transmitted it falls during most of the period of observation. This is not an isolated incident; indeed all data for which laser power records were taken show a similar effect, (see figures 8.7 and 8.8). Observation on most nights commenced approximately 1 hour after sunset and these data all show a similar trend in the backscattered laser signal to that displayed in figure 8.5.

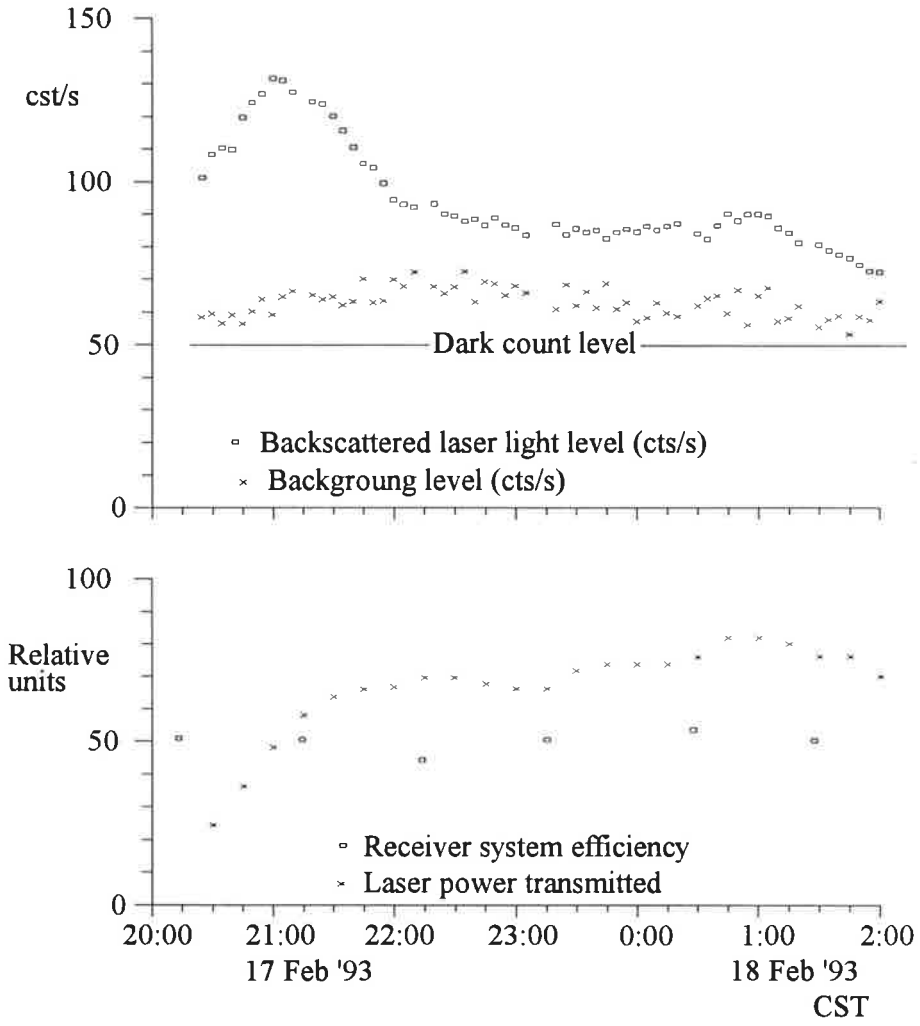

Figure 8.5 Top: Shows the backscattered laser light level (from 50 km) and background level as a function of time for data collected during the night of 17 February 1993. Each point is the average for 5 min of data. Bottom: Shows the intensity of the laser light transmitted into the atmosphere and the efficiency of the lidar receiver system (these two quantities are relative measures). The time scale for the two graphs is the same.

The monitoring of the intensity of the laser light transmitted into the sky and the efficiency of the reception system seem to indicate that the reduction in backscattered signal level is not due to changes in the operation of the instrument. Another possible instrumental cause of this reduction in signal level is changes in the alignment of the transmitted laser beam and the field of view of the receiver system. However due to the rigid mounting of the optical components that determine the alignment, this possibility has been discounted.

The reduction in signal level could be explained by diurnal changes in the optical transmission of the lower troposphere. A mechanism for these changes can be proposed based on the location of the instrument and local weather conditions.

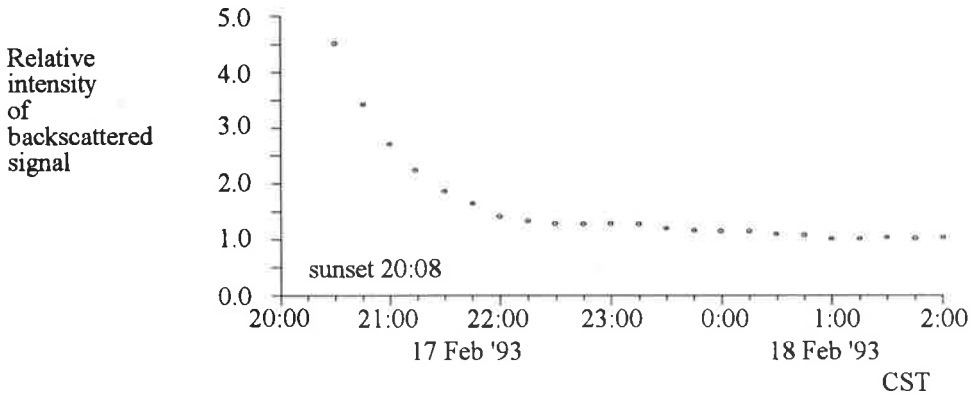

Figure 8.6 Shows the backscattered laser light level (from 50 km) corrected for transmitted laser power, as a function of time for data collected during the night of 17 February 1993. Each point is the average for 15 min of data.

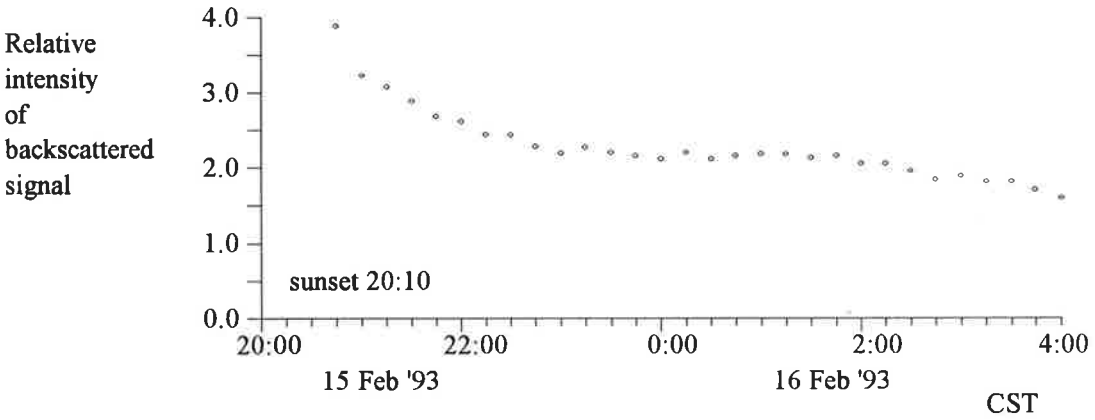

Figure 8.7 Shows the backscattered laser light level (from 50 km) corrected for transmitted laser power, as a function of time for data collected during the night of 15 February 1993. Each point is the average for 15 min of data.

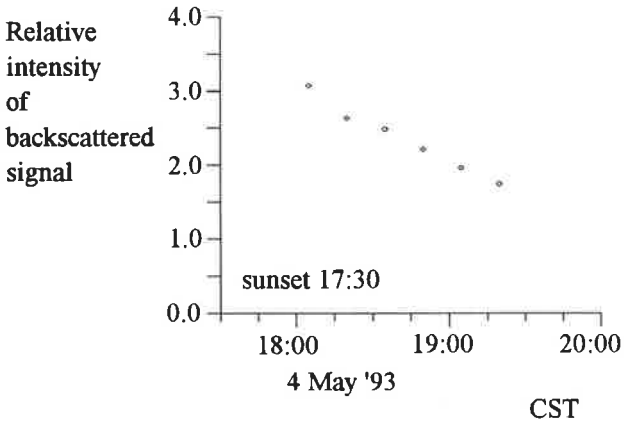

Figure 8.8 Shows the backscattered laser light level (from 50 km) corrected for transmitted laser power, as a function of time for data collected during the night of 4 May 1993. Each point is the average for 15 min of data.

The lidar system is located on a coastal plain approximately 1 km from the Gulf of Saint Vincent, on all observing nights the sky was cloud free (or very close to) and winds were light to very light. The clear skies and light winds give rise to radiative cooling which could cause the condensation of water vapour giving an optically thin mist. This conjecture is supported by the observation of condensation on the outside of the buildings, usually quite heavy. An optically thin mist of this type would be difficult to detect by eye at night due to the inability of the eye to detect slow changes in intensity. The effect on the backscattered signal is increased as the light must traverse this mist on both transmission and reception. The effect of this type of mist on the lidar would be the removal of light due to scattering. Scattering from small water droplets would be predominantly in the forward direction (see chapter 2) but even a small deviation in the path of a photon could remove it from the narrow field of view of the lidar system.

Figure 8.9 shows the variation of the background level with the phase of the moon. It is clear from this figure that the background level is significantly higher for several days around full moon. Generally data collected around new moon have the background level dominated by the photomultiplier dark counts. Two photomultipliers were used over the period that these data were collected, and these had dark count levels of approximately 35 and 48 cts/s at the temperature at which they were operated. The effect of the background level in the uncertainty in temperature profile calculations is demonstrated by figure 7.5.

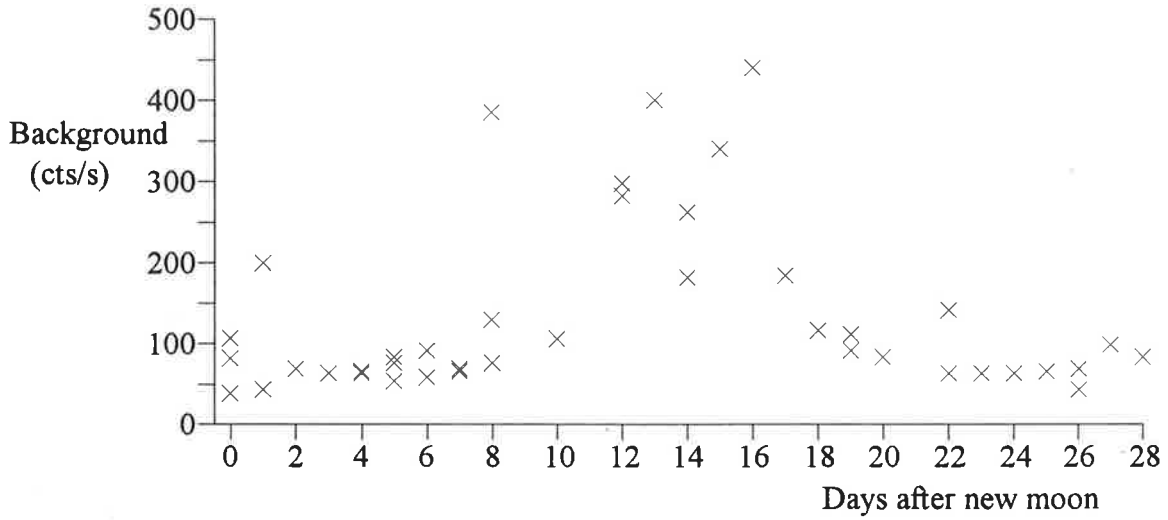

Figure 8.9 Shows the background level as a function of the phase of the moon. Each cross on the graph represents the average background level for an observing session. The background is also a function of the elevation of the moon leading to variations in the background level as the start time and length of observing session vary

8.4 Scattering Ratio Profiles

Scattering ratio profiles are useful for comparing the fit of the model to the experimental data, for determining the minimum altitude for temperature calculation, and also to monitor changes in the stratospheric aerosol layer. The scattering ratio profiles presented in appendix B (see for example figure 8.10) show the mean scattering ratios for each observing session calculated using the CIRA model. The scattering ratio profiles presented in appendix C (see for example figure 8.11) show the scattering ratios calculated from the sum of each months data using the model of Fleming et al along with those calculated using the CIRA model.

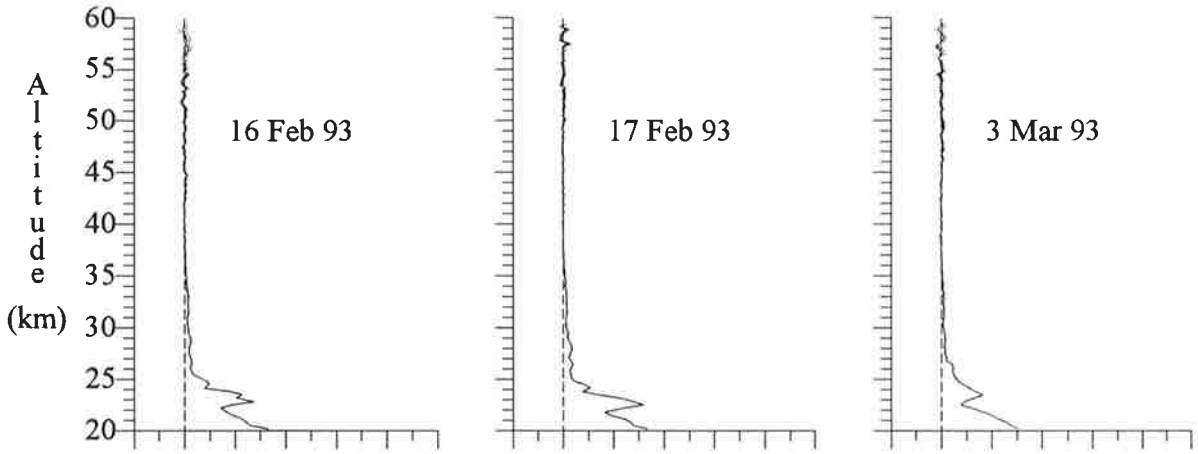

Figure 8.10 Scattering ratio profiles calculated from the data collected during the nights of 16 Feb, 17 Feb, and 3 Mar 1993. These scattering ratio profiles were calculated using the CIRA model. (Reproduced from appendix B.)

In the altitude region above the stratospheric aerosol layer variations in the scattering ratio from unity indicate variations between the model and experimental data. The scattering ratio profiles shown in appendix C clearly show that the CIRA model approximates the experimental data very well. The model of Fleming et al does not fit the experimental data nearly as well as the CIRA model. As an example of the agreement between the CIRA model and the measured density figure 8.11 shows the scattering ratio profile calculated using both the CIRA and Fleming at al models. Throughout the clean signal region the measured relative density profile fits the CIRA model density (for 35°S and the month of March) very well, while there are variations between the experimental data and the model of Fleming et al especially at the upper levels, above 45 km.

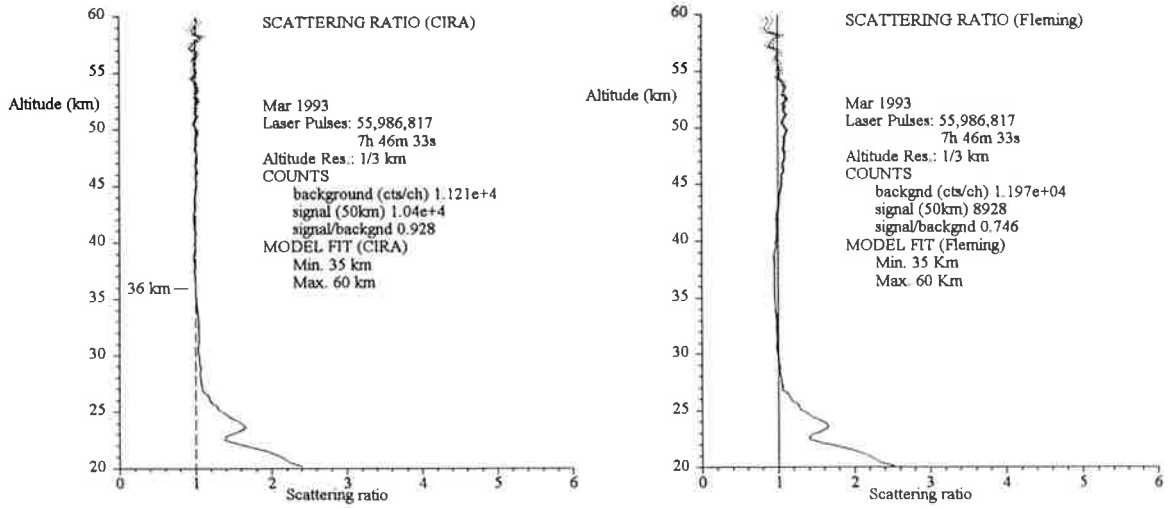

Figure 8.11 Shows the scattering ratio profiles for calculated from data collected during March 1993 using (a) the CIRA model and (b) the model of Fleming et al. (Reproduced from appendix C.)

The scattering ratio profiles presented in appendix B (see for example figure 8.10) show very good agreement with the CIRA model even though the experimental data used to calculate these scattering ratio profiles were recorded over periods ranging from 15 minutes to 7 1/2 hours and the CIRA model represents monthly averaged data.

The data presented in appendix C shows that except for the months of May '92, September '92 and May '93, the Fleming model densities are lower than the measured values in the altitude region ≈ 45 to 55 km. Between 57 and 60 km the Fleming model gives higher densities than the measured data. It should be noted that the data from the three months excluded from this general trend have larger uncertainties making it more difficult to determine whether this trend exists in these data also.

The CIRA model gives data for every 5° of latitude while the model of Fleming et al gives data only at every 10° of latitude. As the lidar is located at approximately 34° 40'S the most appropriate model data from the CIRA model are those for the latitude of 35°S. These data are not available in the model of Fleming et al, the closest data provided by this model are at 30°S and 40°S. Therefore all data from the model of Fleming et al used in this work are the average of those given for 30°S and 40°S and are referred to as the Fleming et al model (for 35°S).

The scattering ratio profiles presented in appendix C show that generally the measured relative density profile fits the CIRA model density very well. For all of the data

presented in appendix C the CIRA model provides an equally good, but in most cases substantially better fit to the measured relative density profile than the Fleming et al model. In order to quantify the relative goodness of fit of the these two models to the experimental data Figure 8.12 shows the ratio of the goodness of fit parameters for the fitting of the two models to the monthly summed data. The method used to calculate the goodness of fit parameter (χ^2) is given in chapter 7, and a more general definition can be found in many statistics texts, see for example Bevington (1969). The caption of Figure 8.12 shows how the ratios of the χ^2 values have been calculated. From this it can be seen that the smaller the value of this ratio the better the fit of the CIRA model to the data when compared to the fit of the Fleming et al model to the same data. Figure 8.12 shows that for all months data the CIRA model fits the experimental data better than the model of Fleming et al.

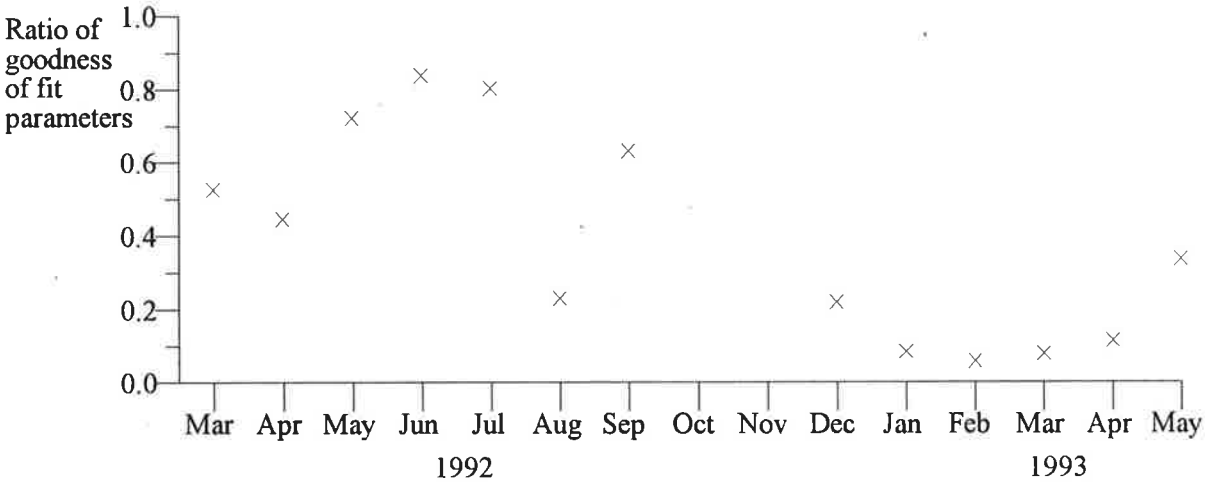

Figure 8.12 Shows the ratio of the goodness of fit parameters (χ^2) for fitting of the CIRA and Fleming models to the sum of each months data. A good fit is indicated by a low χ^2 value.

$$\text{Ratio of goodness of fit parameters} = \frac{\chi^2_{CIRA}}{\chi^2_{Fleming}}$$

Two functions that closely approximate each other lead to a goodness of fit parameter approaching zero while statistical fluctuation in the experimental data increases the value of the goodness of fit parameter. This has the effect of shifting the ratio of the goodness of fit parameters toward a value of one, and in fact the ratios presented in figure 8.12 are largest (closest to one) for the months with the largest statistical fluctuations in the

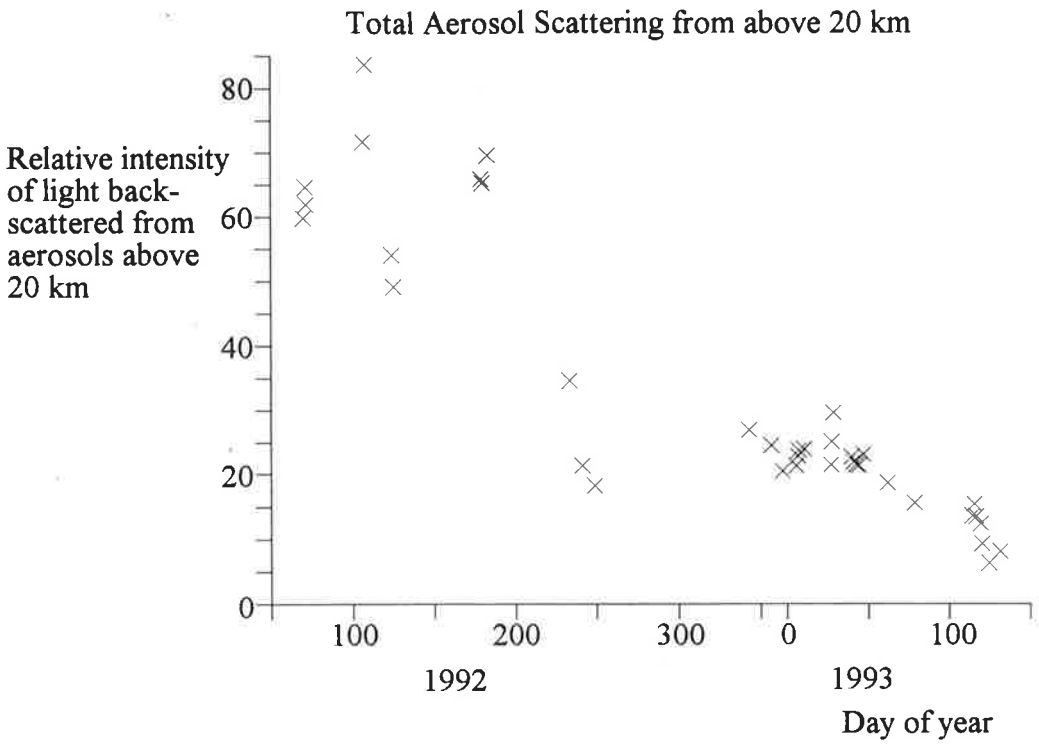

Figure 8.13 Total aerosol scattering from above 20 km for the average of each nights data as a function of time.

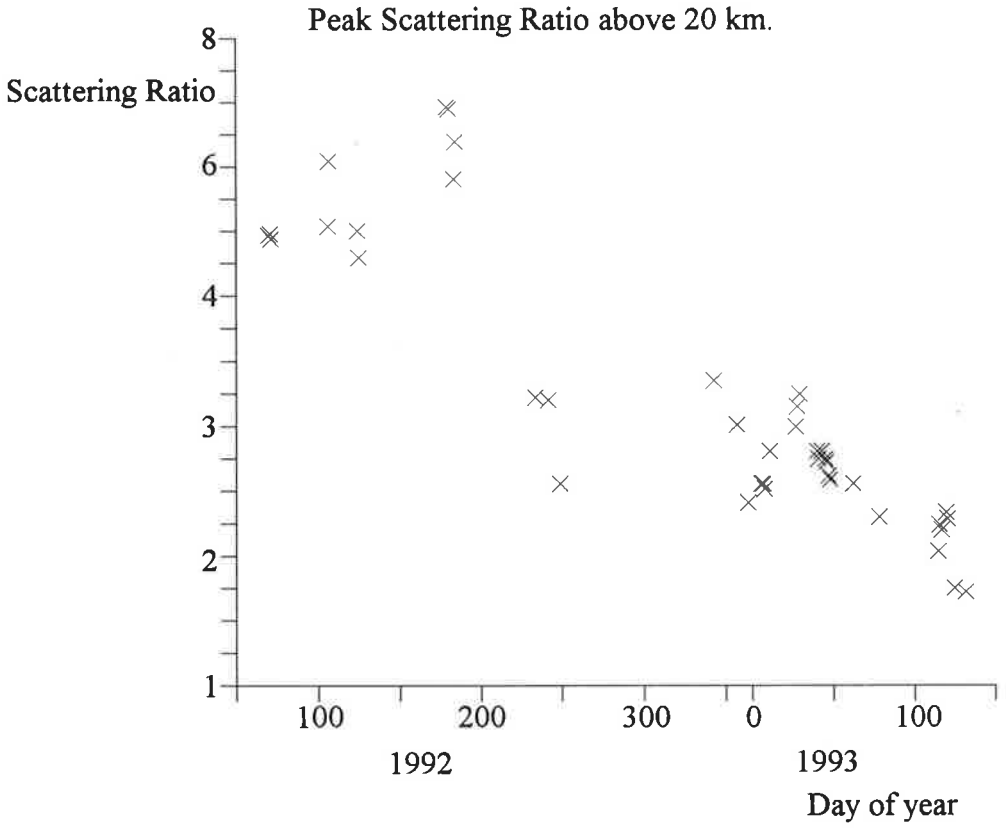

Figure 8.14 Maximum value of the scattering ratio measured above 20 km for the average of each nights data as a function of time.

data. Even though the data presented in figure 8.12 is influenced by the statistical fluctuation in the experimental data this figure shows that ratio of the goodness of fit parameter is consistently less than one. Thus the CIRA model provides a better fit to the experimental data than the Fleming et al model for all months in which data were taken.

Figure 8.13 shows a relative measure of the total aerosol scattering from above 20 km. Calculation of this relative measure of the total aerosol scattering above 20 km has been achieved by the application of equation 8.1.

$$\text{Relative total aerosol scattering} = \int_{20\,\text{km}}^{40\text{km}} (\text{Scattering ratio}(h) - 1)\, dh \qquad \ldots (8.1)$$

Figure 8.14 shows the peak scattering ratio measured at or above 20 km for all nights on which data were taken. Both figures 8.13 and 8.14, along with the scattering ratio profiles in appendices B and C reveal a substantial decrease in aerosol scattering from this region of the atmosphere over time period that data were taken (10 March 1992 to 11 May 1993). This general decrease in the amount of aerosol scattering can be attributed to the removal of the aerosol injected by the eruption of Mt. Pinatubo. Short term fluctuations in the scattering ratio can be attributed to the transport, both horizontal and vertical, of the aerosol. It should be noted that the majority of the stratospheric aerosol scattering occurs at altitudes below 20 km, (see figure 8.2).

It is interesting to note the structure of the aerosol layer and observe the changes that occur over periods as short as 24 hours (eg. 27 and 28 June 1992) as the aerosol "cloud" is transported through the region of the atmosphere monitored with the lidar.

The minimum altitude for temperature profile calculation is selected as the maximum altitude at which the aerosol layer contributes to the backscattered signal. This can be determined from graphs such as those in appendix C (see for example figure 8.10). The calculation of temperature below the top of the aerosol layer leads to underestimates of the temperature. The signal from the aerosol scattering gives an overestimate of the density and thus an underestimate of the temperature. Figure 8.15 shows the altitude of the top of the stratospheric aerosol layer for each night on which data were taken.

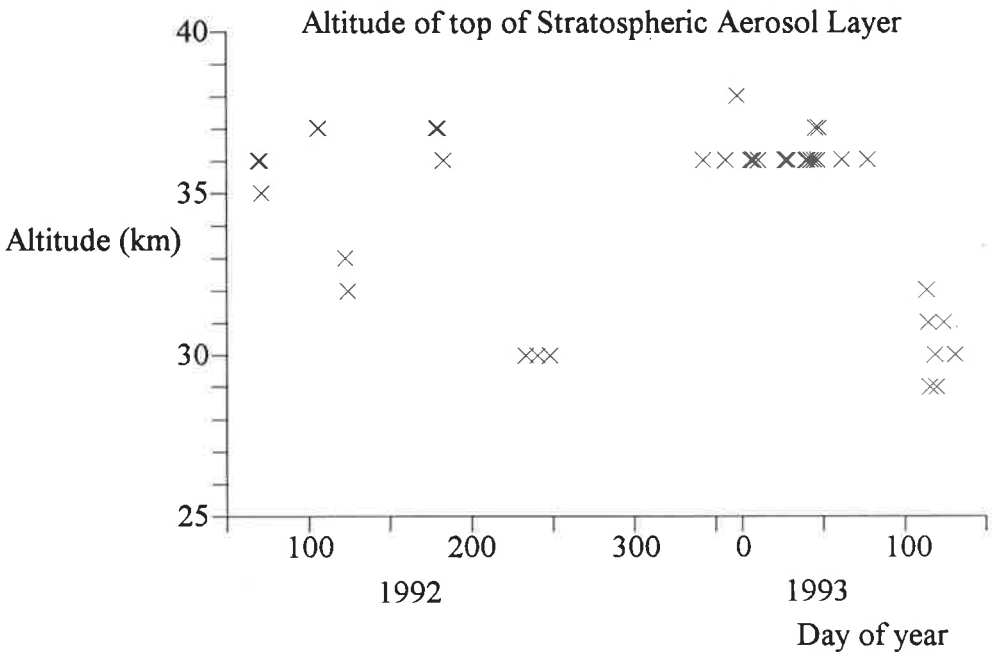

Figure 8.15 Altitude of the top of the stratospheric aerosol layer. Data presented in this figure is determined from the scattering ratio profiles presented in appendix B. The uncertainty in each data point varies, but is generally about ± 0.5 km.

8.5 Temperature profiles

Temperature profiles calculated for months with sufficient data are presented in appendix D (see for an example figure 8.16). Along with these temperature profiles are the temperatures from the CIRA model and the model of Fleming et al for the appropriate month.

All temperature profile calculations were initiated at an altitude of 60 km and are presented for altitudes below 55 km. This is due to the dependence of the calculated temperature on the model fitting over the first several kilometres of calculation, (see chapter 7). The minimum altitudes selected for the temperature profile calculation, for the monthly summed data, are given on the scattering ratio profiles in appendix C.

In appendix D, and figure 8.16, each graph has the CIRA model Temperature for 35°S and the appropriate month (dashed line); the model of Fleming et al for 35°S and the appropriate month (dotted line), plotted with the measured data (crosses) and the uncertainties in these measured values.

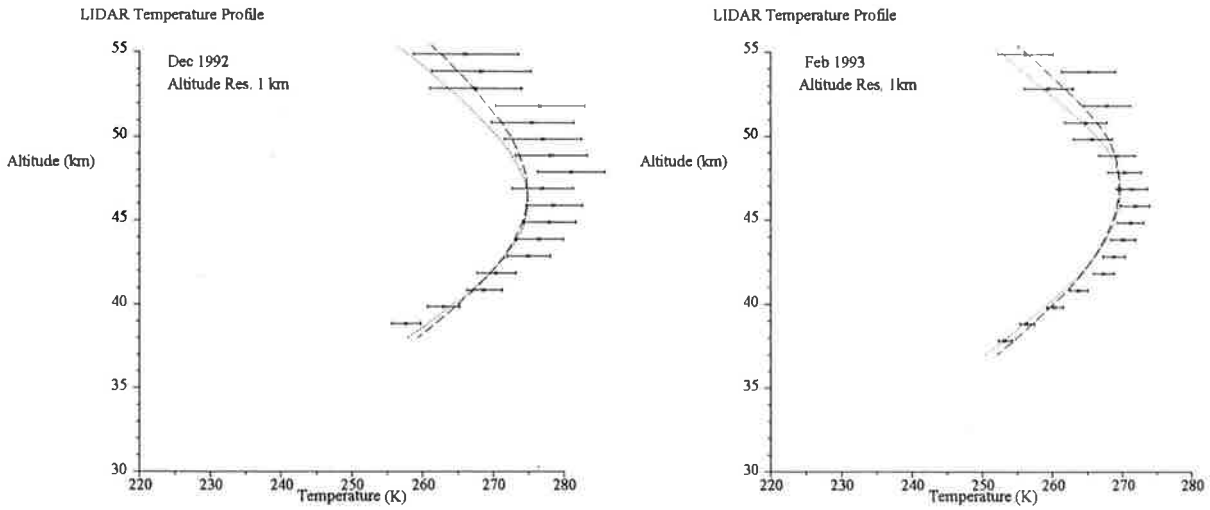

Figure 8.16 Temperature profiles calculated from the data collected during the months of (a) December 1992 and (b) February 1993. The dashed line represents the CIRA model temperatures for 35°S and the appropriate month. The dotted line represents the model of Fleming et al for 35°S and the appropriate month. (Reproduced from appendix D.)

The measured temperatures are not strictly an average for the month due to the sporadic nature in which the data were taken, (see appendix A) but still there is good agreement between the model and experimental data.

It has been established in section 8.4 that the CIRA model fits the measured density data better than the model of Fleming et al. Because of this, and due to the much greater relative uncertainty in the temperature measurements than in the density measurements no statistical analysis of the fit of the two models to the measure temperature data has been undertaken.

There were no independent measurements of temperature in the upper stratosphere available with which the lidar temperatures could be compared. Radiosonde data from Adelaide airport (Approx. 35 km south of the lidar station) were available from The Australian Bureau of Meteorology, however the maximum altitude to which these measurements extend (typically 22 to 25 km) is usually well below the minimum altitude of the lidar measurements.

The largest difference between the measured and model data occurred for the month of August 1992, where the measured temperatures between 32 and 38 km are significantly greater (up to 8°C) than both the CIRA and Fleming et al models. In the altitude region 45 to

52 km the lidar temperatures for this month are significantly less than those given in the two models. However the data used to determine the monthly temperatures for August 1992 includes data from only two nights, the 21st and the 28th It can be seen from figure 8.17 that this monthly temperature has been greatly influenced by the measurements taken during a single night, being the 21st.

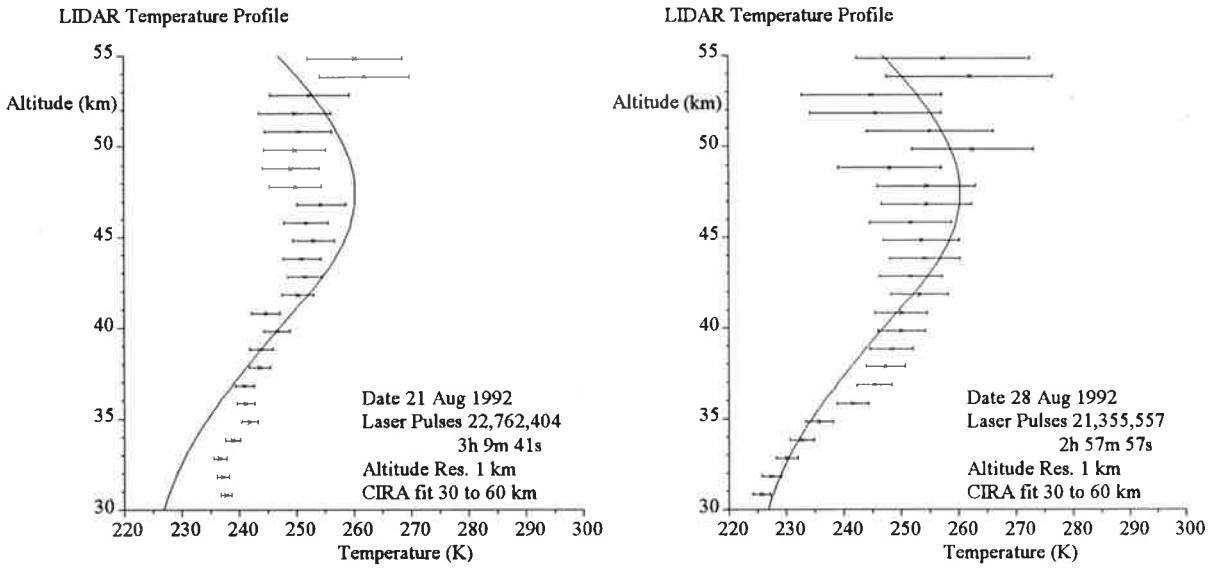

Figure 8.17 Lidar temperature profiles for the nights of 21 and 28 August 1992. (Reproduced from appendix E.)

Lidar temperatures for all other months generally compare fairly well with the models with most measurements being close to or within the calculated uncertainty in the measured temperatures.

Lidar temperatures calculated for individual nights are presented in appendix E (see for example figures 8.17 and 8.18). The temperature profiles presented in appendix E are those for all the nights where the data was of sufficient quality to enabled the calculation of temperature profiles with reasonable uncertainty levels. All of the available data for these observing sessions has been used to calculated the temperature profiles. As the observing session varied in length, and the laser power varied between observing sessions, the data quality also varies from session to session. This has lead to varying time resolutions used in the temperature profile calculations and varying uncertainty levels for results obtained on different nights. In cases where uncertainty levels are unacceptably large for temperatures calculated with an altitude resolution of 1 km the altitude resolution has be reduced to 2 km.

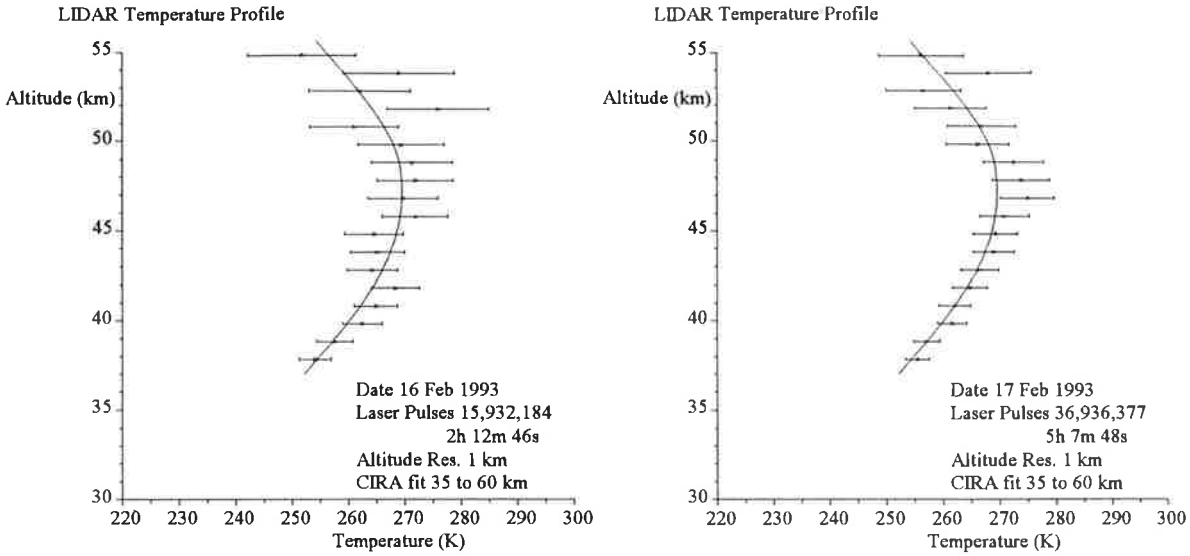

Figure 8.18 Lidar temperature profiles for the nights of 16 and 17 February 1993. (Reproduced from appendix E.)

The measured nightly temperature profiles generally show good agreement with the CIRA model even though the model gives monthly average temperatures. The only nightly temperature profile to show large variations from the CIRA model is from 21 August 1992. Radiosonde data for this night extends to an altitude of only 24 km and so is not useful in the validation of these data. The measured temperatures for 27 and 28 January 1993 show the atmosphere between 37 and 40 km to be about 5 K cooler than the temperatures given by the model. The generally good agreement between the nightly lidar temperature profiles and the month averaged model temperatures demonstrates the stability of the upper stratosphere and lower mesosphere throughout the period of these observations.

8.6 Conclusions

The calibration of the shutter system is more complex than was originally expected, but can be achieved for short time scales. This problem should not affect the determination of Doppler winds in the region 5 to 20 km when the interferometer in installed. This is due to the small time scales used for the scanning the interferometer.

The measured scattering ratio profiles clearly show a decrease in the amount of aerosol scattering from above 20 km over the period of the observations. This is due to the removal of the aerosol injected into the stratosphere by the eruption of Mt. Pinatubo. It is

expected that the aerosol levels were approaching the background level by the end of the period of observations.

Measured density and temperature profiles generally show good agreement with the CIRA model giving confidence in the operation of the lidar system and the data analysis techniques. In particular the monthly density profiles show excellent agreement with the CIRA model densities

The CIRA model densities provide a significantly better fit to the lidar data than those given by the model of Fleming et al.

9 Summary and Future Work

9.1 Summary

The work described in this thesis constitutes only the first phase of the construction and operation of this lidar system. That is the construction of the system to the point where it is able to operate as a stratospheric Rayleigh lidar and the subsequent analysis of the data obtained during operation in this mode. The complete design of the system includes a dual scanning Fabry-Perot spectrometer to enable Doppler wind and temperature measurements to be made. The complete system is expected to be assembled and operational by mid 1994. The dual scanning Fabry-Perot interferometer is being constructed 'in house' and is a refinement of previous instruments built within the Mawson Institute for Antarctic Research.

Design and construction of the equipment making up the first phase of the instrument accounted for the majority of the author's time while undertaking the work described in this thesis. In particular the grinding, polishing and testing of the telescope, (see chapter 5) required a large amount of time. The development and testing of the shutter system (see chapter 4) also required a substantial amount of time. Data analysis programs were developed mainly during the period over which the data were taken.

Atmospheric backscatter data were collected over a period of slightly more than one year (10 March 1992 to 11 May 1993). During this time the system was also undergoing debugging and testing resulting in much of the earlier data being rejected due to equipment

malfunctions, (mainly shutter phase errors). However a substantial amount of useful data were obtained during this period. These data have been used to monitor the upper part of the stratospheric aerosol layer. This monitoring has shown a substantial decrease in the amount of scattering from aerosols in the region above 20 km as the aerosol injected by the eruption of Mt. Pinatubo has been removed from the atmosphere.

The calculation of scattering ratio profiles allowed the comparison of the measured relative density profiles to the density profiles predicted by the CIRA and Fleming et al models. These comparisons have shown that the CIRA model fits the measured data very well, while the model of Fleming et al shows differs significantly from the measured data.

Temperature profiles calculated from the measured data show good agreement with the model data.

Data obtained with this lidar differ from that obtained by other workers using Rayleigh lidar systems in that the background levels for this system are about one hundred times higher due to the higher PRF of the equipment. This required very careful analysis to separate the background from the backscattered light signal.

The agreement between the experimental data and the CIRA model give confidence in the operation of the equipment and the method used to analysis the data.

9.2 Future Work

As the system has been designed primarily as a Doppler lidar system it has not been optimised for Rayleigh lidar operation. This has lead to less than optimal signal levels obtained when running in this mode. The major difference between the two types of systems is the number of optical components in each. A Doppler system will generally have many more optical components than a Rayleigh system. This is due to two factors, the first is the optics required to steer the beam around the sky. The second factor is the necessity to maintain good beam quality in order to measure the spectrum of the backscattered light.

The current system could make substantially improved Rayleigh measurement if optimised for such measurements. Relatively simple and inexpensive modifications to the equipment would allow the system to operate much more effectively in the Rayleigh mode without affecting its operation in the Doppler mode. These modifications include provision to

enable the laser pulse to be transmitted into the atmosphere directly (or via simple collimating optics if necessary). The system would not operate in both the Rayleigh and Doppler modes simultaneously, but would need to be switched between them.

For operation in Doppler mode it is proposed to replace the existing laser with a frequency doubled Nd:YAG laser. This type of laser offers a number of advantages over the current copper vapour laser, including

a) improved power level,

b) improved reliability,

c) lower PRF (resulting in lower background levels) and

d) much narrower spectral width.

The installation of the FPI and a new laser will give the instrument the ability to routinely measure temperatures and winds in the lower and middle stratosphere. The lidar techniques provide the most promising methods of providing routine measurement of the state of the middle atmosphere, (Chanin et al 1984,1987 and Chanin 1984). This makes the present instrument a potentially important source of stratospheric data especially due to the sparsity of such data in the southern hemisphere.

The improvements to the system may also allow the measurement of the Raman component of the backscattered light allowing it to be used to determine altitude profiles of the concentration of individual molecular species. The useful altitude range of these profiles would be determined by a number of instrumental parameters as well as the concentration of, and Raman differential scattering cross section for, the molecular species under study. Profiles of molecular nitrogen density would allow the extension of temperature measurements down below the top of the aerosol layer using the standard Rayleigh lidar techniques.

Once complete it is proposed to install this lidar system at Davis (an Australian Antarctic station) alongside a number of other instruments used for determining middle and upper atmospheric parameters that are located, or to be located, at this station. It is intended that the system should be operated at this site for several years in order to build up a picture of the climatology of the Antarctic middle atmosphere.

Appendix A

Data Summary

The table below gives a summary of data collected with the lidar system from 10 March 1992, when the first atmospheric backscatter profiles were taken. The following information is given for the data recorded in each observing session:

Start Date: The local date on which recording of the first profile of the session commenced
Data stored in file: The name of the computer file in which the recorded data were stored
Start Time (CST[1]): The time at which observing commenced (Central Aust. Standard Time)
End Time (CST): The time at which observing ceased (Central Aust. Standard Time)
Data Profiles: The number of data profiles recorded (vary from 30 to 300s integration time)
Data Collection Time: The actual time spent collecting data
Calib. Profiles: The number of calibration profiles recorded
Calib. Collection Time: The actual time spent collecting calibration profiles
Rejected Profiles: The number of profiles (data and calibration) that were subsequently rejected for one reason or another.
Rejected Collection Time: The actual time spent collection profiles that were subsequently rejected.
Background (cts/s): The average background count rate for the observing session.
Signal 50 km (cts/s): The average rate of detection of photons backscattered from 50 km for the observing session.

---

[1]CST = GMT + 9 1/2 hours

Start date	Data stored in file:	Start Time (CST)	End Time (CST)	# Data Profiles	Data Collection Time	# Calib. Profiles	Calib. Collection Time	# Rejected Profiles	Rejected Collection Time	Back-ground (cts/s)	Signal 50 km (cts/s)
10 Mar 92	92D070E.DAT	21:33:00	00:30:00	11	30:00	3	15:00	7	29:00	59.24	16.51
11 Mar 92	92D071E.DAT	22:05:00	00:15:00	4	20:00	0		18	1:30:00	67.55	56.18
12 Mar 92	92D072E.DAT	21:20:00	22:55:00	12	1:00:00	0		5	25:00	74.91	39.55
8 Apr 92	92D099E.DAT	19:40:00	01:30:00	27	2:15:00	3	6:00	16	1:15:30	54.09	18.47
15 Apr 92	92D106E.DAT	20:10:00	01:45:00	47	3:55:00	1	5:00	15	1:15:00	282.4	42.98
16 Apr 92	92D107E.DAT	20:25:00	23:55:00	27	2:15:00	3	15:00	12	1:00:00	400.1	29.49
17 Apr 92	92D108E.DAT	20:32:00	21:50:00	0		0		30	1:18:00	0.00	0.00
29 Apr 92	92D120E.DAT	20:00:00	22:50:00	0		0		34	2:50:00	0.00	0.00
3 May 92	92D124E.DAT	19:10:00	00:00:00	42	3:30:00	0		14	1:10:00	39.72	20.23
4 May 92	92D125E.DAT	20:00:00	00:15:00	31	2:35:00	0		17	1:25:00	43.53	21.61
25 May 92	92D146E.DAT	12:11:30	16:47:30	0		87	43:30	3	1:30	0.00	0.00
19 Jun 92	92D171E.DAT	17:50:00	17:58:30	0		0		17	8:30	0.00	0.00
27 Jun 92	92D179E.DAT	19:17:30	21:00:00	22	1:09:30	0		6	30:00	47.09	21.98
28 Jun 92	92D180E.DAT	18:26:30	23:05:00	43	3:12:30	1	30	10	50:00	102.6	23.53
30 Jun 92	92D182E.DAT	20:10:00	22:25:00	22	1:18:30	0		12	51:00	83.18	13.52
1 Jul 92	92D183E.DAT	19:00:00	22:45:00	31	2:35:00	0		14	1:10:00	206.6	26.45
9 Jul 84	92D189E.DAT	14:15:00	15:05:00	0		10	50:00	0		0.00	0.00
15 Jul 92	92D197E.DAT	19:34:00	23:42:00	0		0		228	3:48:00	0.00	0.00
16 Jul 92	92D198E.DAT	18:40:00	19:09:00	0		0		28	24:30	0.00	0.00
21 Aug 92	92D234E.DAT	18:39:00	23:30:00	96	3:36:00	0		0		144.0	170.4

28 Aug 92	92D241E.DAT	17:45:00	00:30:00	36	3:00:00	12	12:00	38	2:58:00	107.2	68.33
5 Sep 92	92D249E.DAT	18:18:00	22:54:00	48	3:19:30	28	14:00	13	51:30	385.9	48.69
18 Nov 92	92D323E.DAT	12:45:00	13:19:00	0		44	22:00	2	1:00	0.00	0.00
20 Nov 92	92D325E.DAT	11:50:00	13:47:30	0		162	1:21:00	5	2:30	0.00	0.00
8 Dec 92	92D343E.DAT	20:12:00	23:09:30	332	2:46:00	3	1:30	4	2:00	182.9	85.89
22 Dec 92	92D357E.DAT	20:08:30	22:15:00	159	1:19:30	3	1:30	16	8:00	84.84	83.02
29 Dec 92	92D364E.DAT	20:17:00	04:08:00	916	7:38:00	0		2	1:00	77.76	67.57
6 Jan 93	93D006E.DAT	20:22:00	23:30:30	373	3:06:30	0		0		263.3	123.2
7 Jan 93	93D007E.DAT	20:20:00	23:30:00	369	3:04:30	0		0		341.3	128.9
8 Jan 93	93D008E.DAT	20:20:00	21:30:30	132	1:06:00	1	30	0		440.0	163.2
11 Jan 93	93D011E.DAT	20:26:30	23:18:00	343	2:51:30	0		0		114.0	96.76
27 Jan 93	93D027E.DAT	20:28:00	23:20:00	333	2:46:30	4	2:00	0		68.70	122.1
28 Jan 93	93D028E.DAT	20:21:30	22:11:30	191	1:35:30	0		1	30	85.63	178.7
29 Jan 93	93D029E.DAT	20:09:00	23:10:00	320	2:40:00	25	12:30	1	30	92.40	130.1
9 Feb 93	93D040E.DAT	20:35:30	00:15:30	426	3:33:00	4	2:00	1	30	184.1	95.71
10 Feb 93	93D041E.DAT	20:07:00	00:25:30	515	4:17:30	0		2	1:00	117.3	124.5
12 Feb 93	93D043E.DAT	20:01:30	00:00:00	475	3:57:30	0		2	1:00	84.64	97.89
14 Feb 93	93D045E.DAT	20:36:30	00:30:30	466	3:53:00	0		2	1:00	65.10	106.2
15 Feb 93	93D046E.DAT	20:19:00	04:35:30	948	7:54:00	35	17:30	1	30	66.13	75.86
16 Feb 93	93D047E.DAT	20:15:30	23:51:00	268	2:14:00		0	2	1:00	65.81	105.3
17 Feb 93	93D048E.DAT	20:11:30	02:07:00	618	5:09:00	70	35:00	2	1:00	63.66	92.02
3 Mar 93	93D062E.DAT	19:58:00	00:27:00	483	4:01:30	23	11:30	0		108.7	96.28
19 Mar 93	93D078E.DAT	19:27:30	23:32:30	462	3:51:00	0		28	14:00	70.65	70.43

24 Apr 93	93D114E.DAT	18:35:30	22:15:30	432	3:36:00	2	1:00	5	2:30	64.78	84.81
25 Apr 93	93D115E.DAT	18:38:30	22:37:30	441	3:40:30	27	13:30	4	2:00	60.56	98.48
26 Apr 93	93D116E.DAT	18:55:00	19:16:30	33	16:30	9	4:30	0		58.98	144.3
29 Apr 93	93D119E.DAT	21:32:30	22:55:00	152	1:16:00	0		0		84.06	70.60
30 Apr 93	93D120E.DAT	18:59:30	20:55:00	190	1:35:00	0		0		129.6	111.6
4 May 93	93D124E.DAT	18:33:30	19:55:00	162	1:21:00	0		1	30	298.0	93.38
11 May 93	93D131E.DAT	18:09:00	18:58:00	98	49:00	0		0		93.77	92.17
24 May 93	93D144E.DAT	11:01:00	14:33:00	0		132	1:06:00	0		0.00	0.00
26 May 93	93D146E.DAT	10:43:00	11:59:30	0		40	20:00	0		0.00	0.00

Appendix B

Nightly Scattering Ratio Profiles

The scattering ratio profiles presented in this appendix were calculated from all of the data available for each night on which observations were taken.

Uncertainties in the plotted scattering ratios are indicated by the dotted lines. The maximum altitude for each plot is limited to 60 km or by the altitude at which the uncertainty reaches $\pm$ 30 %, which ever is lower.

Appendix A, which gives a summary of the data, shows the times for which the data were collected as well as the average background and backscattered signal levels for each observing session.

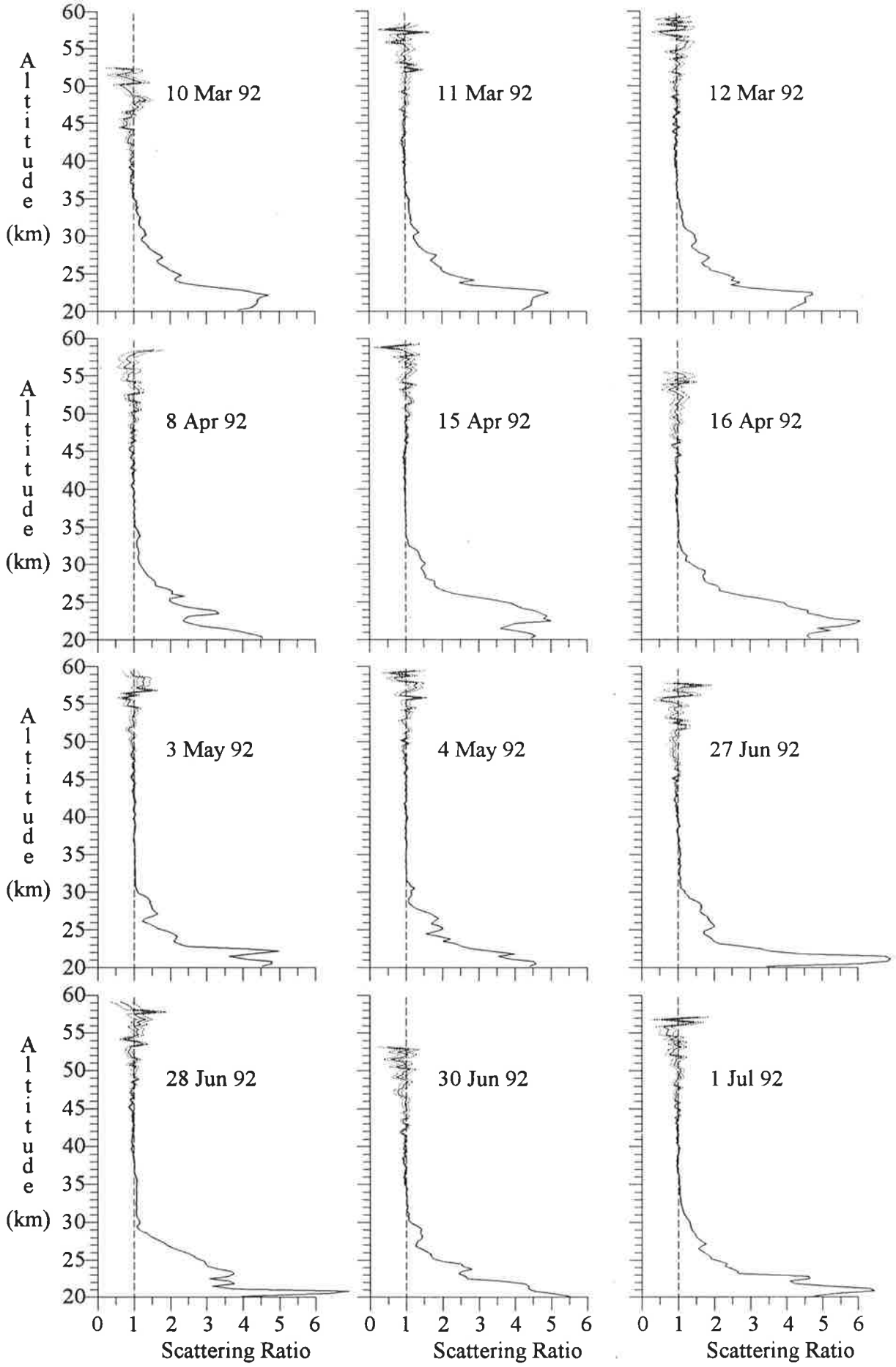
Altitude (km)
60
55
50
45
40
35
30
25
20
10 Mar 92
11 Mar 92
12 Mar 92
8 Apr 92
15 Apr 92
16 Apr 92
3 May 92
4 May 92
27 Jun 92
28 Jun 92
30 Jun 92
1 Jul 92
0 1 2 3 4 5 6
Scattering Ratio

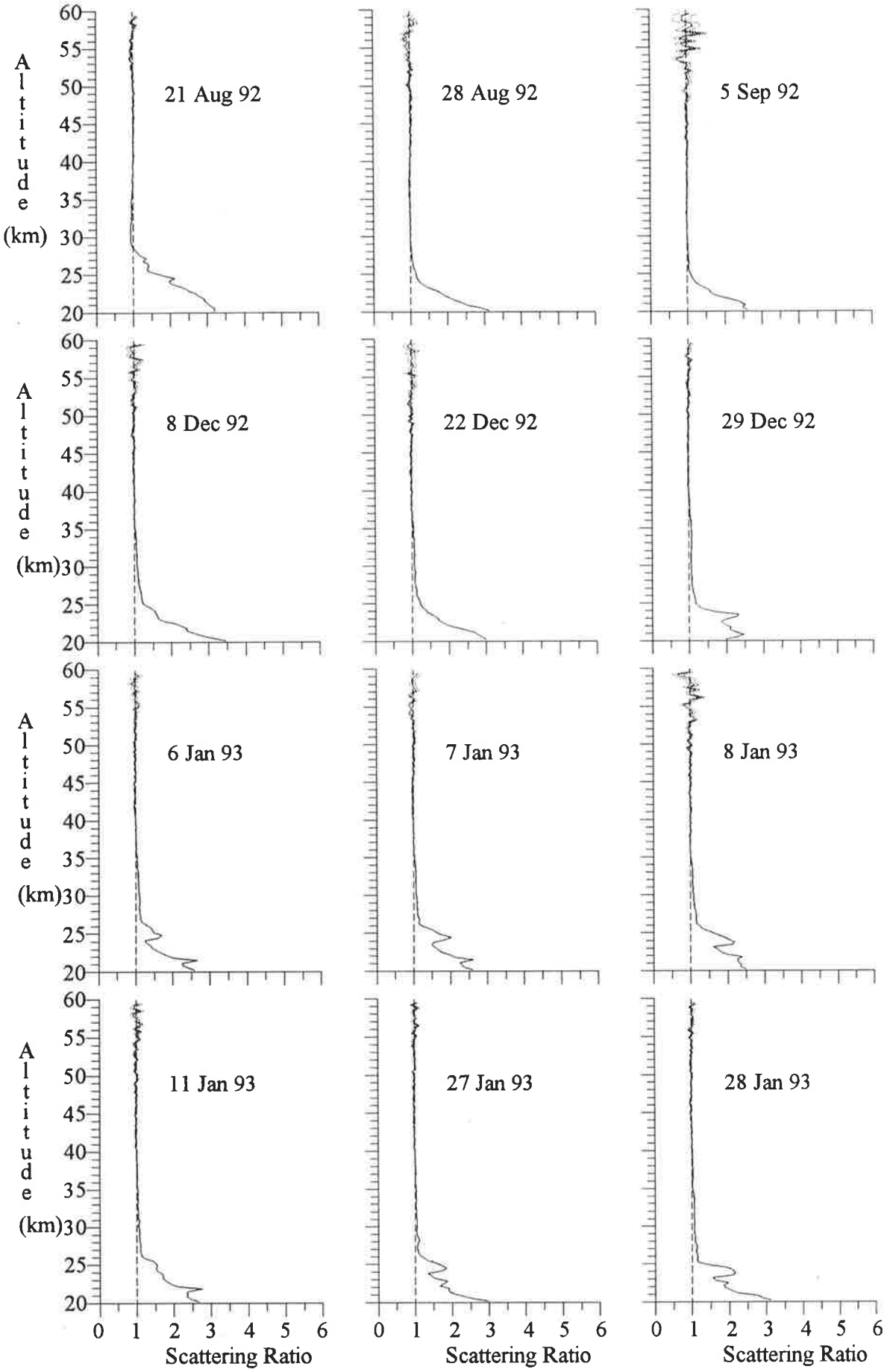
Altitude (km)
21 Aug 92
28 Aug 92
5 Sep 92
8 Dec 92
22 Dec 92
29 Dec 92
6 Jan 93
7 Jan 93
8 Jan 93
11 Jan 93
27 Jan 93
28 Jan 93
60
55
50
45
40
35
30
25
20
0 1 2 3 4 5 6
Scattering Ratio

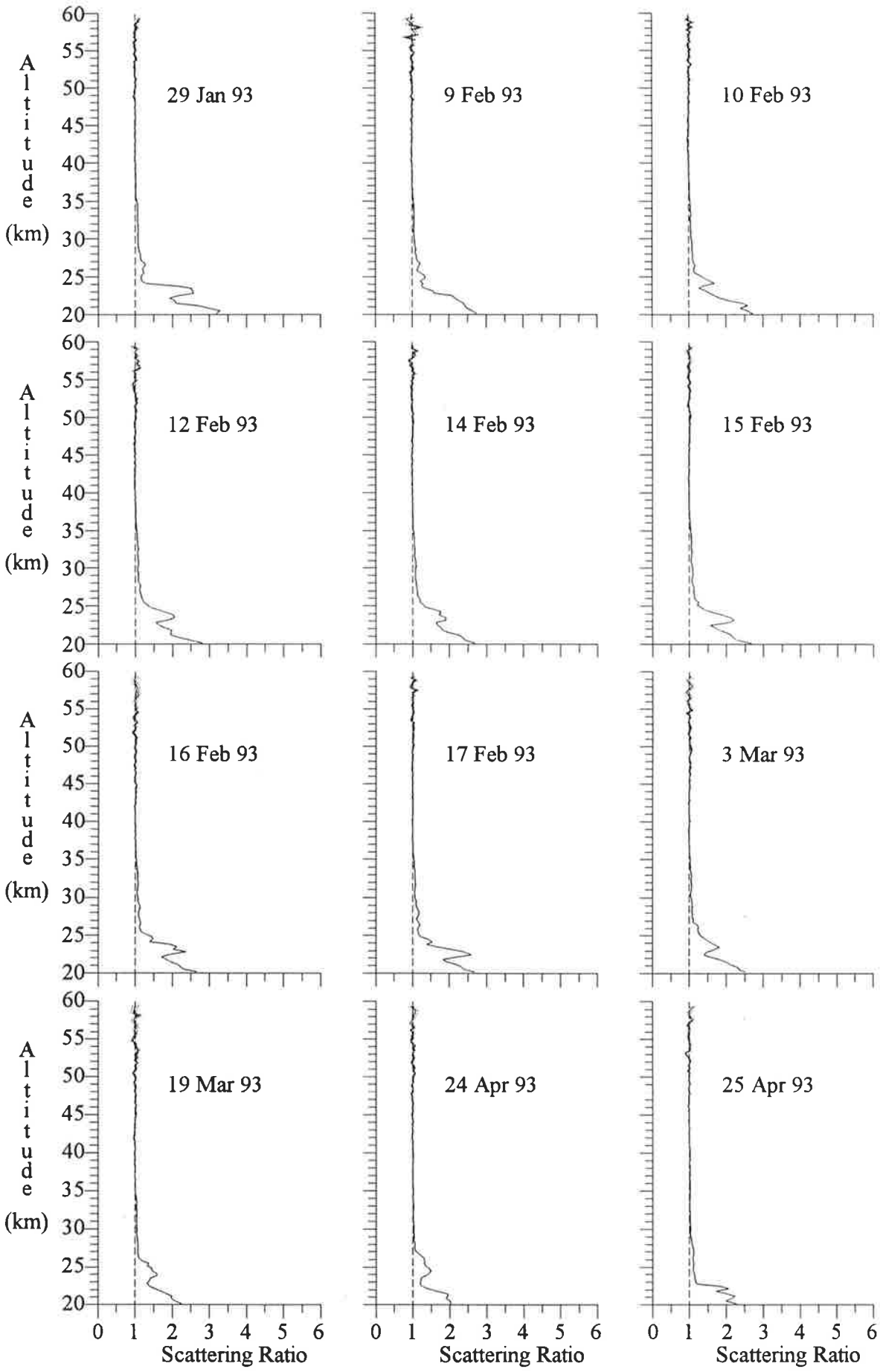
29 Jan 93
9 Feb 93
10 Feb 93
12 Feb 93
14 Feb 93
15 Feb 93
16 Feb 93
17 Feb 93
3 Mar 93
19 Mar 93
24 Apr 93
25 Apr 93
Altitude (km)
Scattering Ratio
20
25
30
35
40
45
50
55
60
0
1
2
3
4
5
6

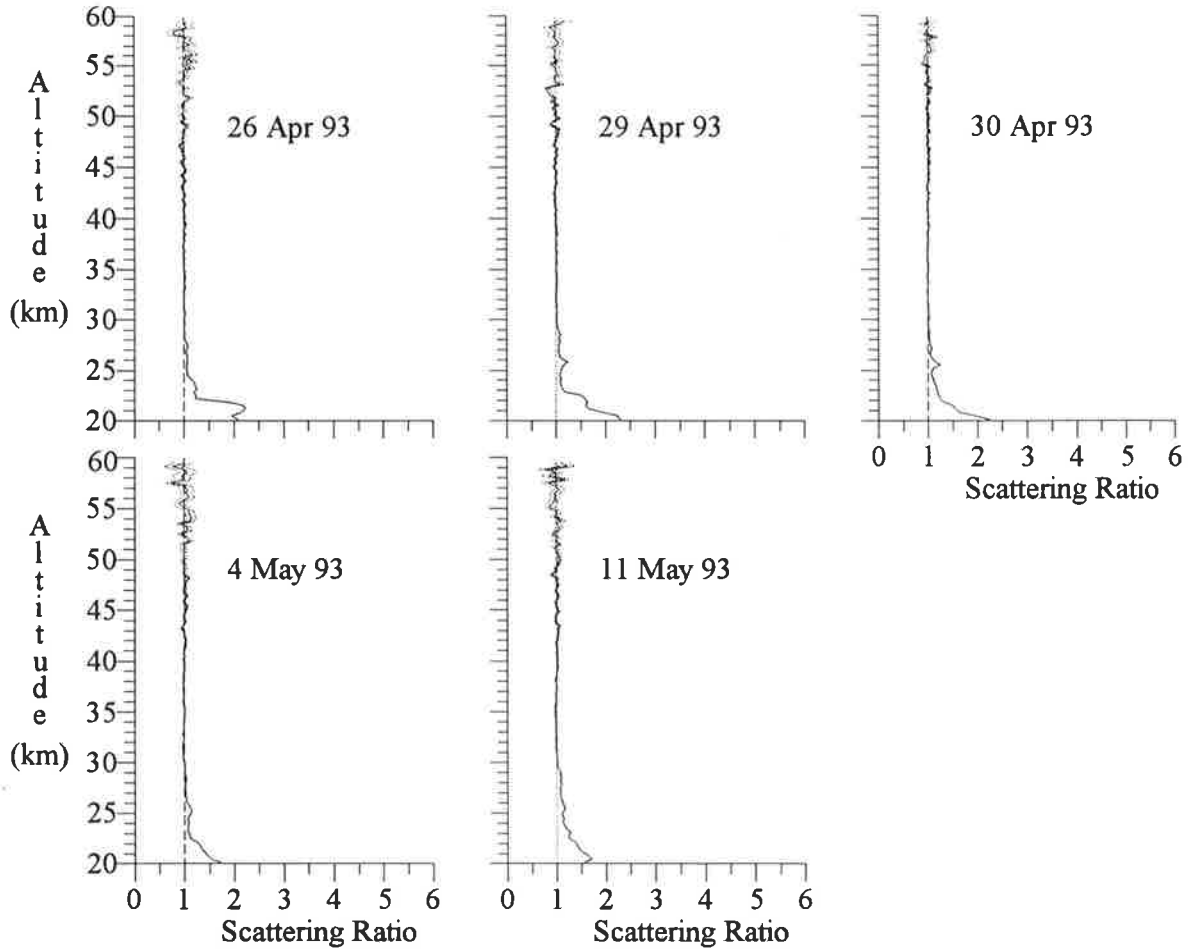
Altitude (km)
60
55
50
45
40
35
30
25
20
26 Apr 93
29 Apr 93
30 Apr 93
4 May 93
11 May 93
0 1 2 3 4 5 6
Scattering Ratio

Appendix C

Monthly Scattering Ratio Profiles

The scattering ratio profiles presented in this appendix were calculated from all of the data available for each month. Data are presented only for the months in which the signal to noise ratio is sufficient to be able to calculate a temperature profile with reasonable accuracy. Appendix A, which gives a summary of the data shows the nights and times for which the data used here were collected.

Each page has the scattering ratio calculated using the CIRA model (top) and the model of Fleming et al (bottom). Included with each plot, under the heading MODEL FIT, is the maximum and minimum altitudes used to fit the model and the background level to the experimental data, (see chapter 8).

Also indicated on the top (CIRA) graph is the altitude selected as the minimum for temperature calculation, this is the maximum altitude at which scattering from the stratospheric aerosol layer can be detected.

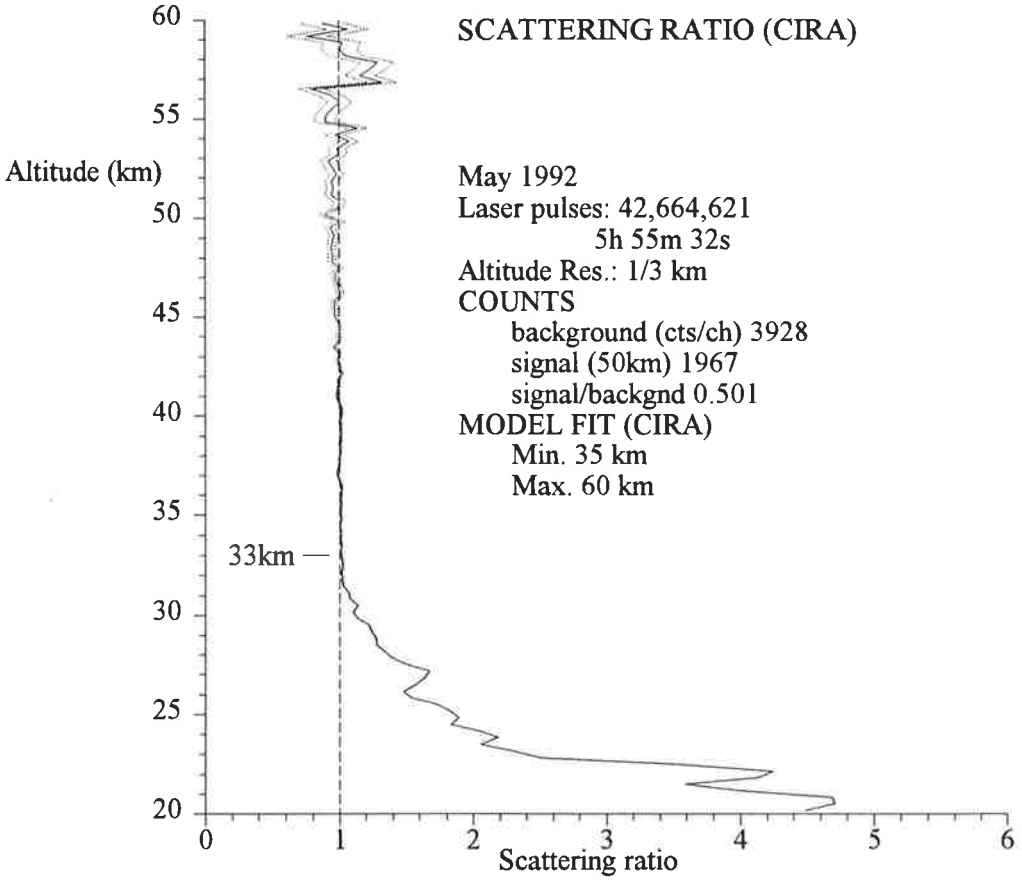
SCATTERING RATIO (CIRA)
May 1992
Laser pulses: 42,664,621
5h 55m 32s
Altitude Res.: 1/3 km
COUNTS
background (cts/ch) 3928
signal (50km) 1967
signal/backgnd 0.501
MODEL FIT (CIRA)
Min. 35 km
Max. 60 km
Altitude (km)
33km
Scattering ratio

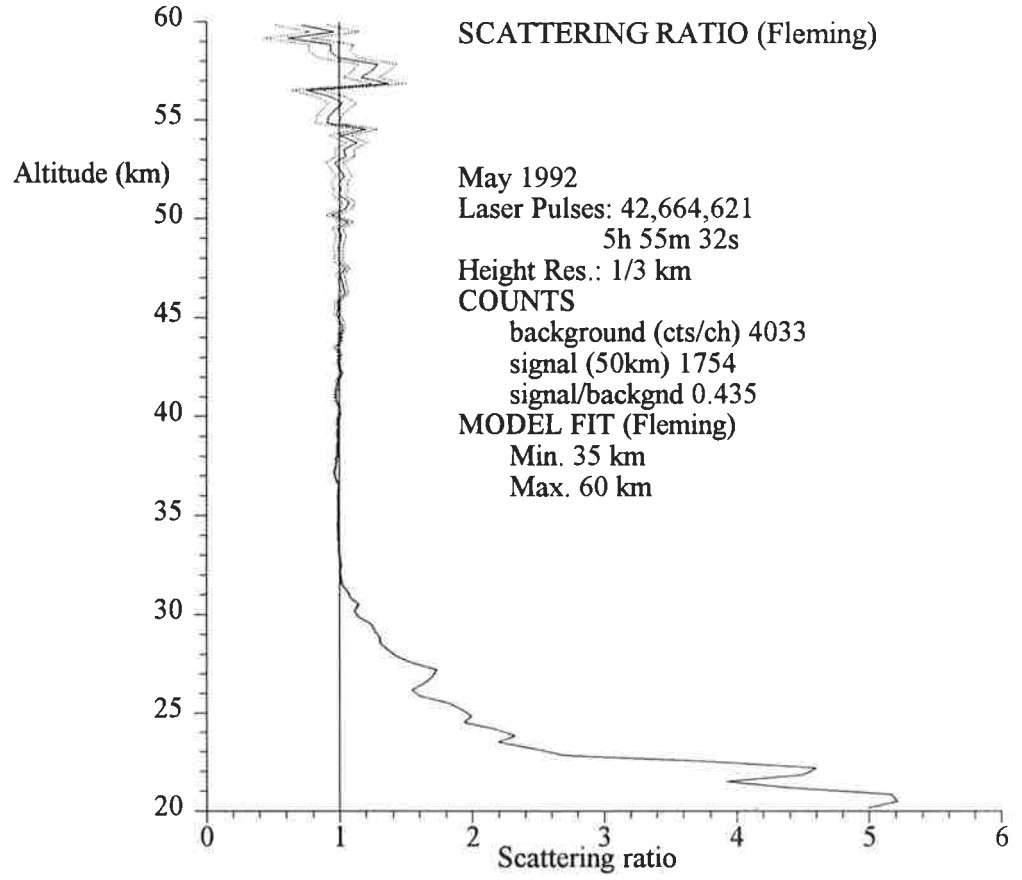
SCATTERING RATIO (Fleming)
May 1992
Laser Pulses: 42,664,621
5h 55m 32s
Height Res.: 1/3 km
COUNTS
background (cts/ch) 4033
signal (50km) 1754
signal/backgnd 0.435
MODEL FIT (Fleming)
Min. 35 km
Max. 60 km
Altitude (km)
Scattering ratio

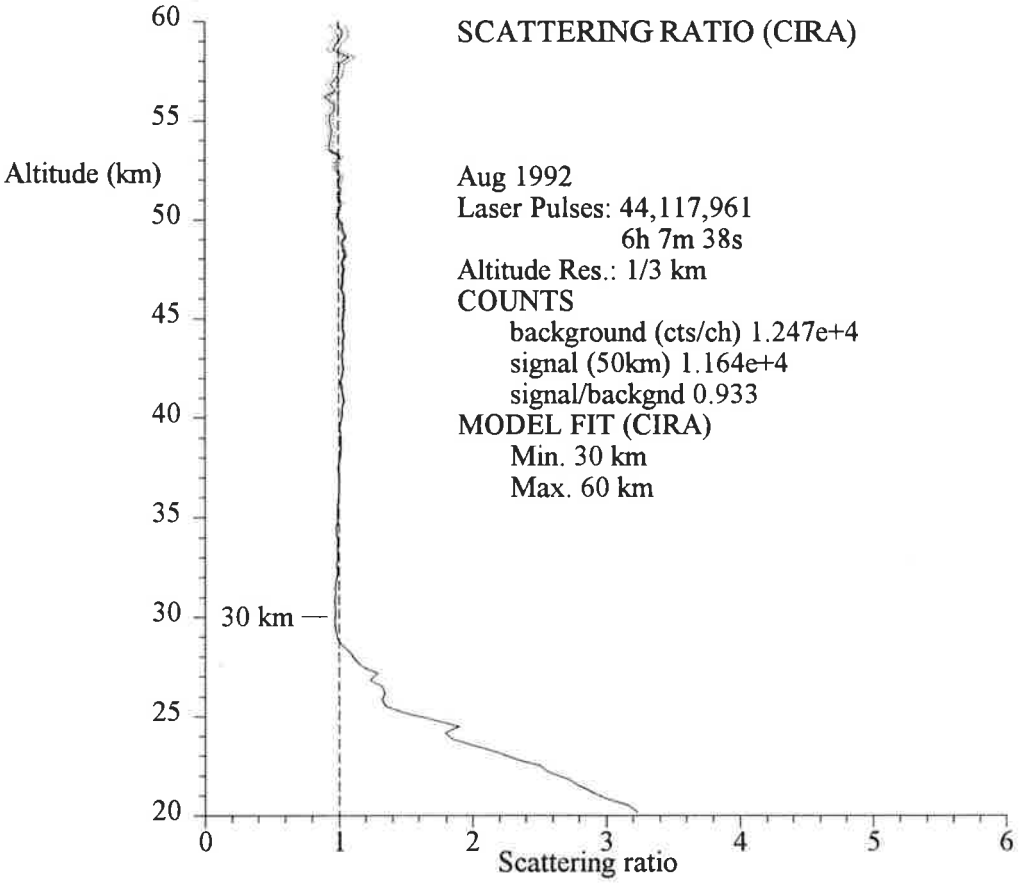
SCATTERING RATIO (CIRA)
Aug 1992
Laser Pulses: 44,117,961
6h 7m 38s
Altitude Res.: 1/3 km
COUNTS
background (cts/ch) 1.247e+4
signal (50km) 1.164e+4
signal/backgnd 0.933
MODEL FIT (CIRA)
Min. 30 km
Max. 60 km
Altitude (km)
60
55
50
45
40
35
30
25
20
30 km
0
1
2
3
4
5
6
Scattering ratio

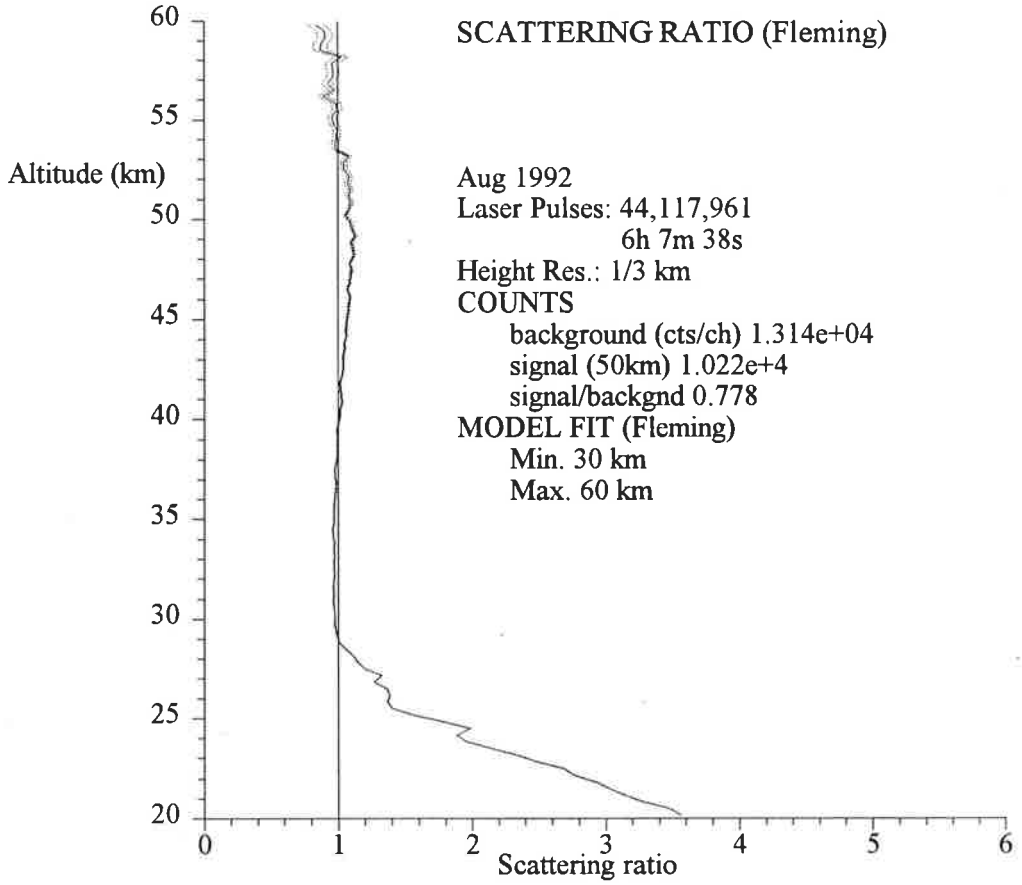
SCATTERING RATIO (Fleming)
Aug 1992
Laser Pulses: 44,117,961
6h 7m 38s
Height Res.: 1/3 km
COUNTS
background (cts/ch) 1.314e+04
signal (50km) 1.022e+4
signal/backgnd 0.778
MODEL FIT (Fleming)
Min. 30 km
Max. 60 km
Altitude (km)
60
55
50
45
40
35
30
25
20
0
1
2
3
4
5
6
Scattering ratio

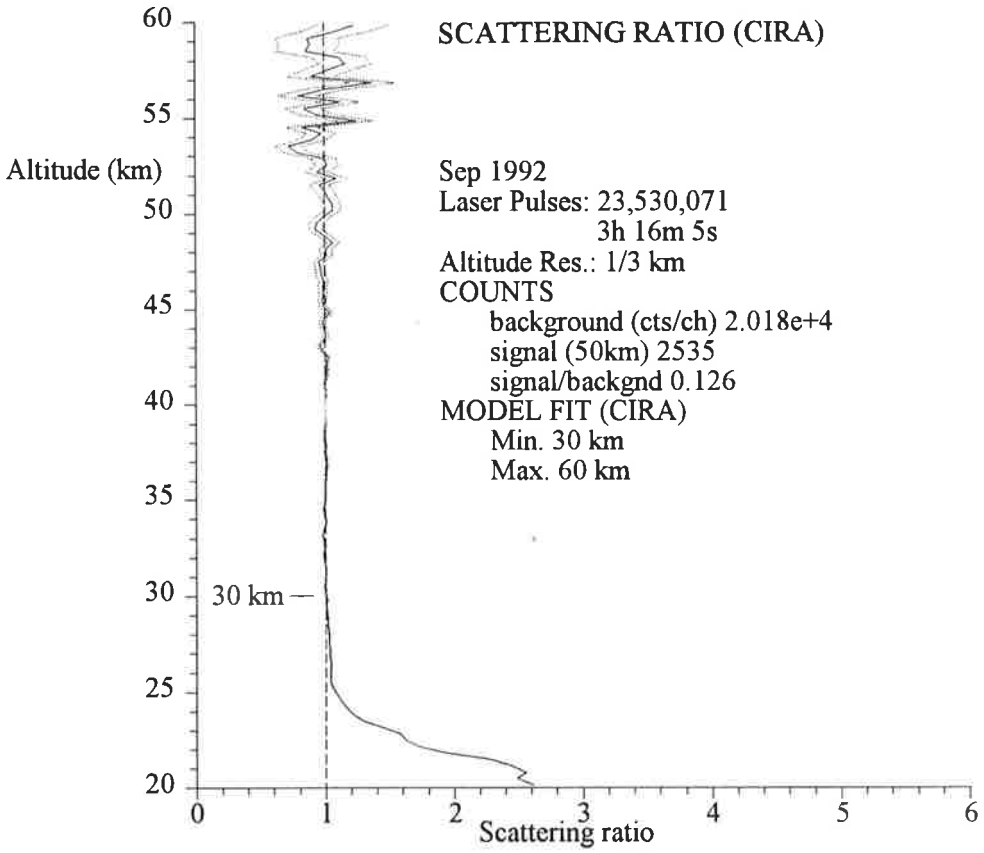
SCATTERING RATIO (CIRA)
Sep 1992
Laser Pulses: 23,530,071
3h 16m 5s
Altitude Res.: 1/3 km
COUNTS
background (cts/ch) 2.018e+4
signal (50km) 2535
signal/backgnd 0.126
MODEL FIT (CIRA)
Min. 30 km
Max. 60 km
Altitude (km)
30 km
Scattering ratio

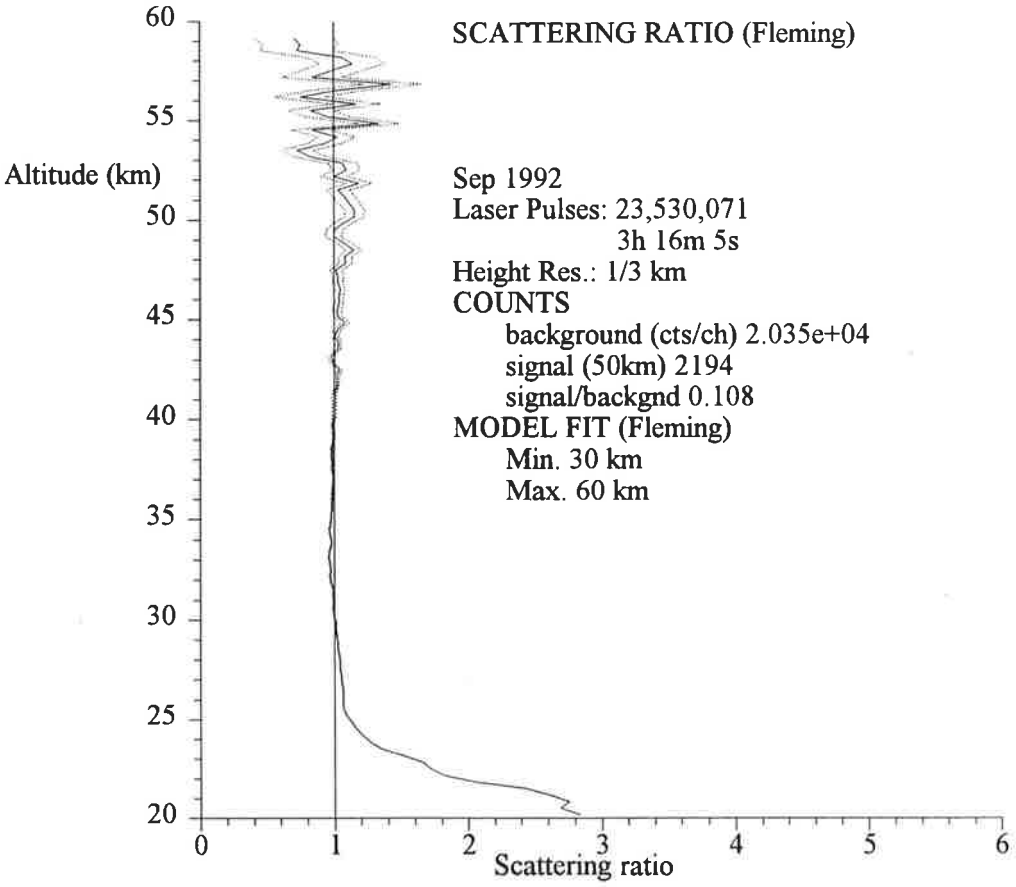
SCATTERING RATIO (Fleming)
Sep 1992
Laser Pulses: 23,530,071
3h 16m 5s
Height Res.: 1/3 km
COUNTS
background (cts/ch) 2.035e+04
signal (50km) 2194
signal/backgnd 0.108
MODEL FIT (Fleming)
Min. 30 km
Max. 60 km
Altitude (km)
Scattering ratio

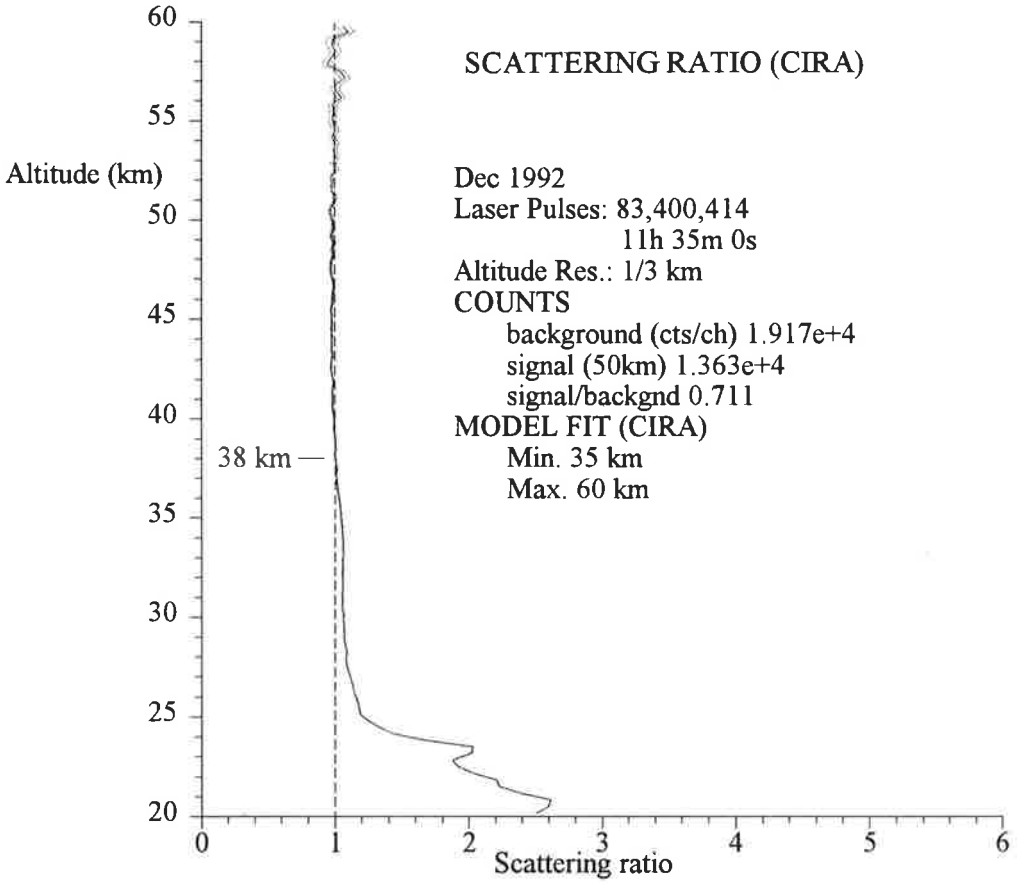
SCATTERING RATIO (CIRA)
Altitude (km)
60
55
50
45
40
35
30
25
20
38 km
Dec 1992
Laser Pulses: 83,400,414
11h 35m 0s
Altitude Res.: 1/3 km
COUNTS
background (cts/ch) 1.917e+4
signal (50km) 1.363e+4
signal/backgnd 0.711
MODEL FIT (CIRA)
Min. 35 km
Max. 60 km
0
1
2
3
4
5
6
Scattering ratio

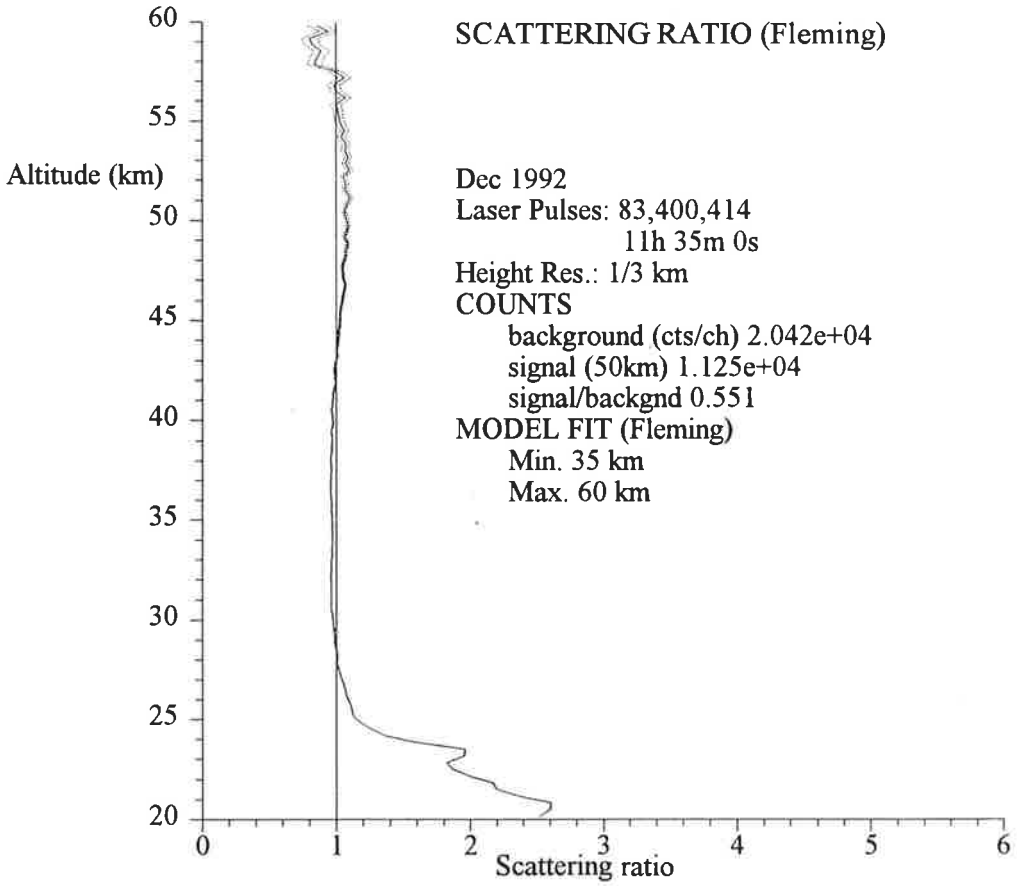
SCATTERING RATIO (Fleming)
Altitude (km)
60
55
50
45
40
35
30
25
20
Dec 1992
Laser Pulses: 83,400,414
11h 35m 0s
Height Res.: 1/3 km
COUNTS
background (cts/ch) 2.042e+04
signal (50km) 1.125e+04
signal/backgnd 0.551
MODEL FIT (Fleming)
Min. 35 km
Max. 60 km
0
1
2
3
4
5
6
Scattering ratio

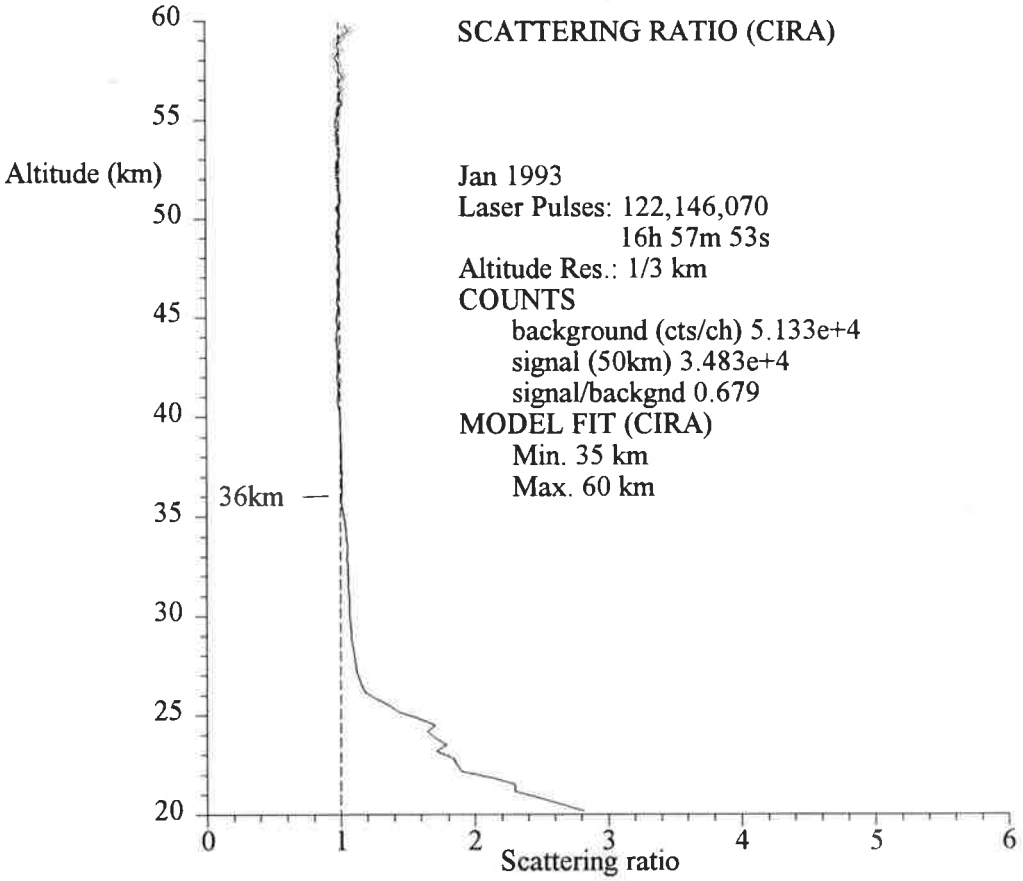
SCATTERING RATIO (CIRA)
Jan 1993
Laser Pulses: 122,146,070
16h 57m 53s
Altitude Res.: 1/3 km
COUNTS
background (cts/ch) 5.133e+4
signal (50km) 3.483e+4
signal/backgnd 0.679
MODEL FIT (CIRA)
Min. 35 km
Max. 60 km
Altitude (km)
36km
Scattering ratio

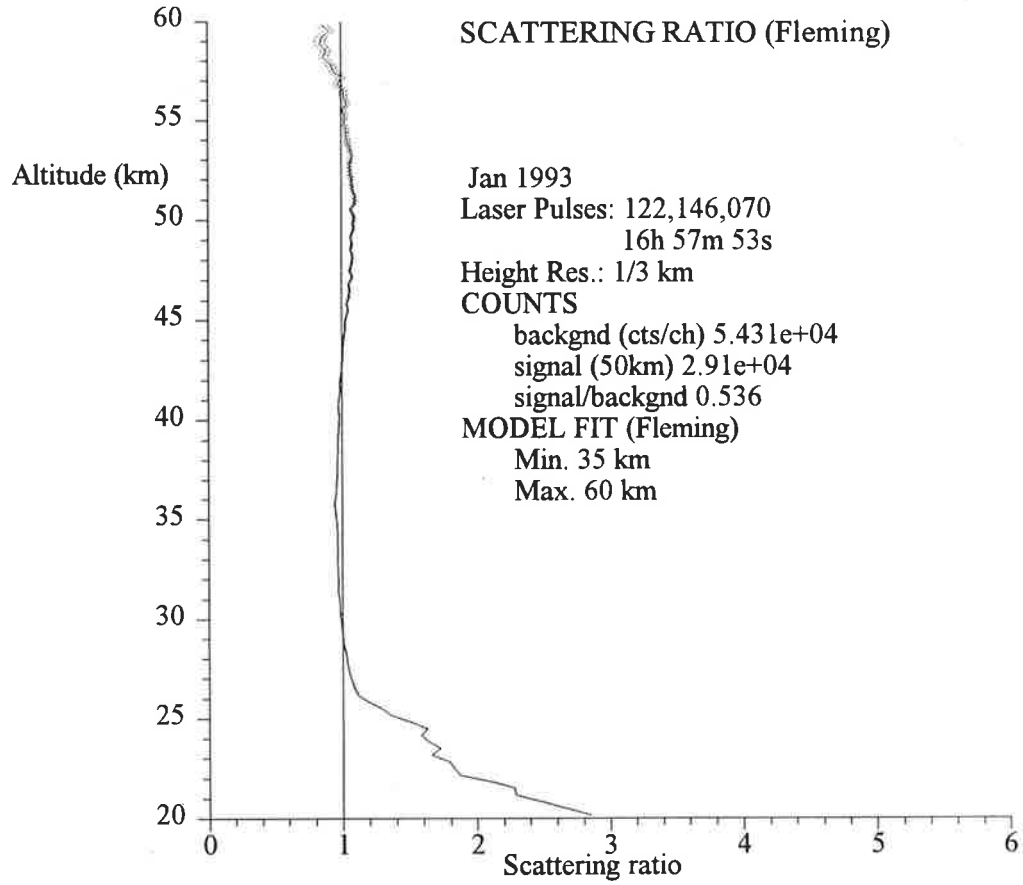
SCATTERING RATIO (Fleming)
Jan 1993
Laser Pulses: 122,146,070
16h 57m 53s
Height Res.: 1/3 km
COUNTS
backgnd (cts/ch) 5.431e+04
signal (50km) 2.91e+04
signal/backgnd 0.536
MODEL FIT (Fleming)
Min. 35 km
Max. 60 km
Altitude (km)
Scattering ratio

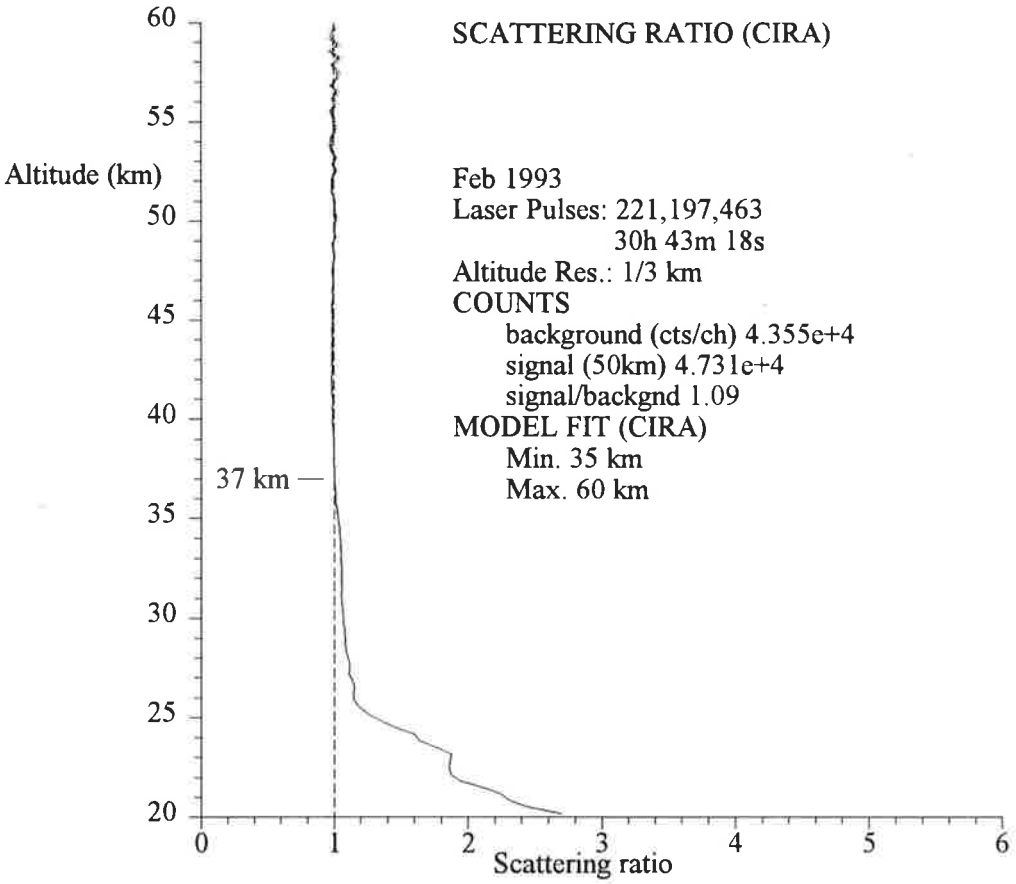
SCATTERING RATIO (CIRA)
Feb 1993
Laser Pulses: 221,197,463
30h 43m 18s
Altitude Res.: 1/3 km
COUNTS
background (cts/ch) 4.355e+4
signal (50km) 4.731e+4
signal/backgnd 1.09
MODEL FIT (CIRA)
Min. 35 km
Max. 60 km
Altitude (km)
37 km
Scattering ratio

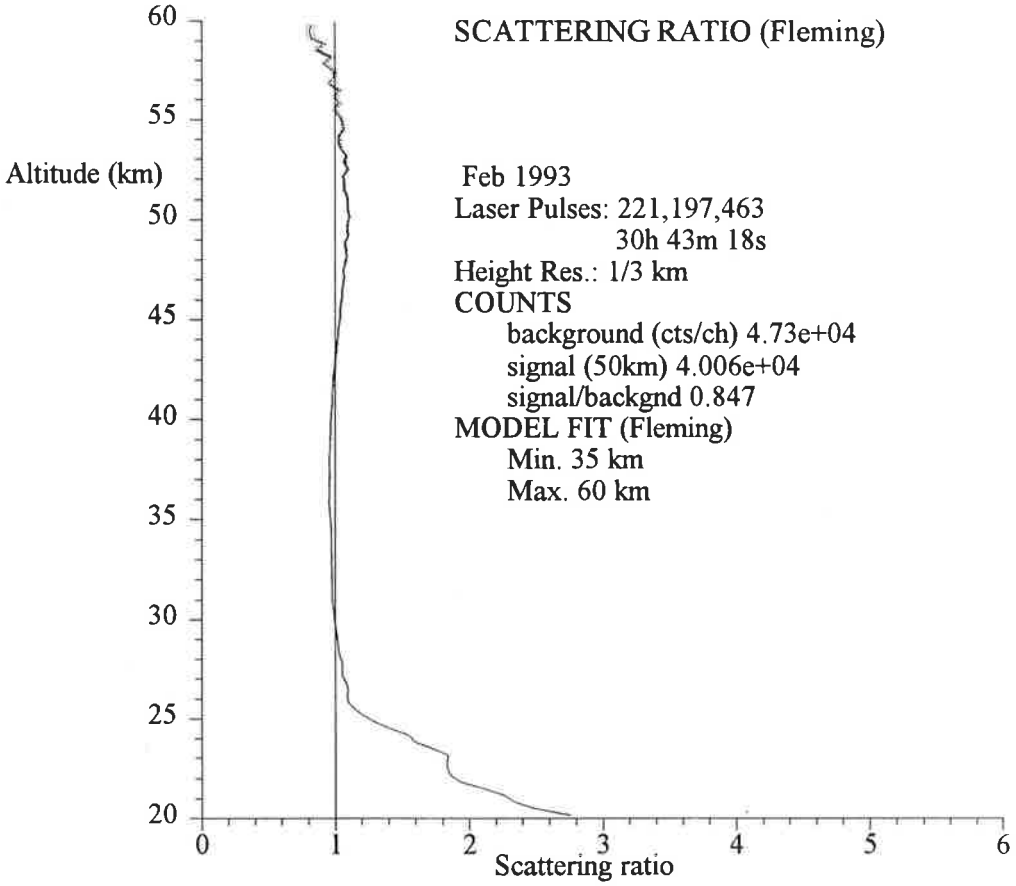
SCATTERING RATIO (Fleming)
Feb 1993
Laser Pulses: 221,197,463
30h 43m 18s
Height Res.: 1/3 km
COUNTS
background (cts/ch) 4.73e+04
signal (50km) 4.006e+04
signal/backgnd 0.847
MODEL FIT (Fleming)
Min. 35 km
Max. 60 km
Altitude (km)
Scattering ratio

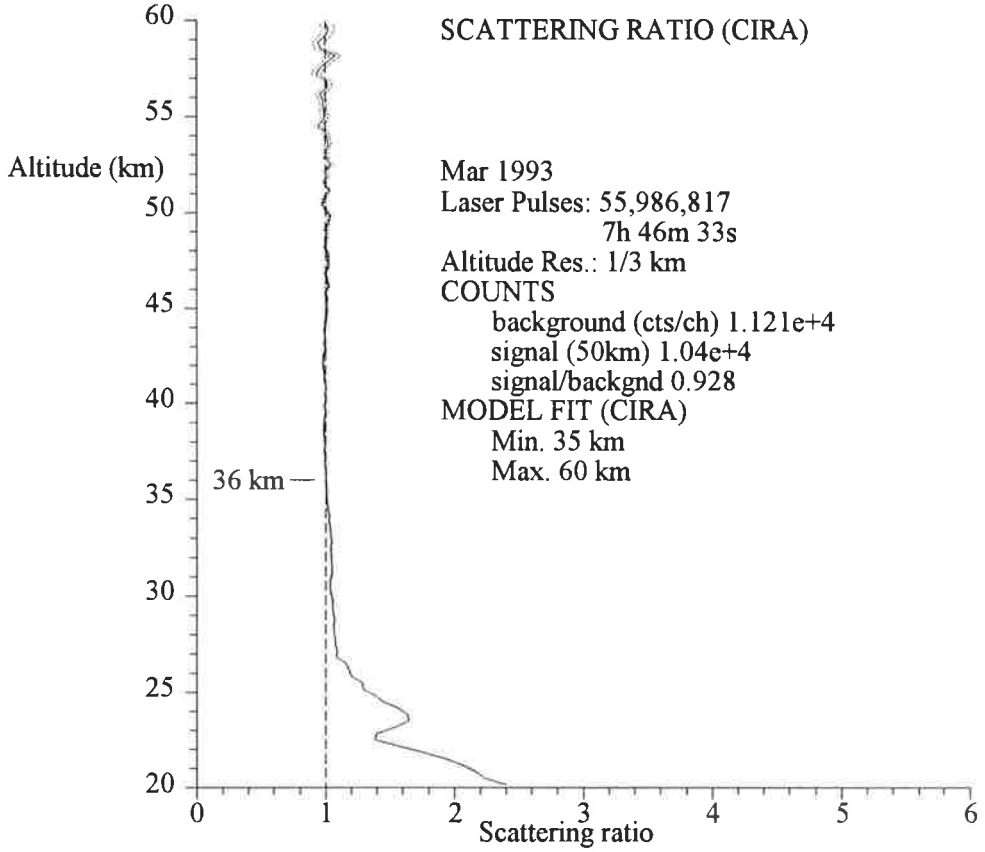
SCATTERING RATIO (CIRA)
Mar 1993
Laser Pulses: 55,986,817
7h 46m 33s
Altitude Res.: 1/3 km
COUNTS
background (cts/ch) 1.121e+4
signal (50km) 1.04e+4
signal/backgnd 0.928
MODEL FIT (CIRA)
Min. 35 km
Max. 60 km
36 km
Altitude (km)
Scattering ratio

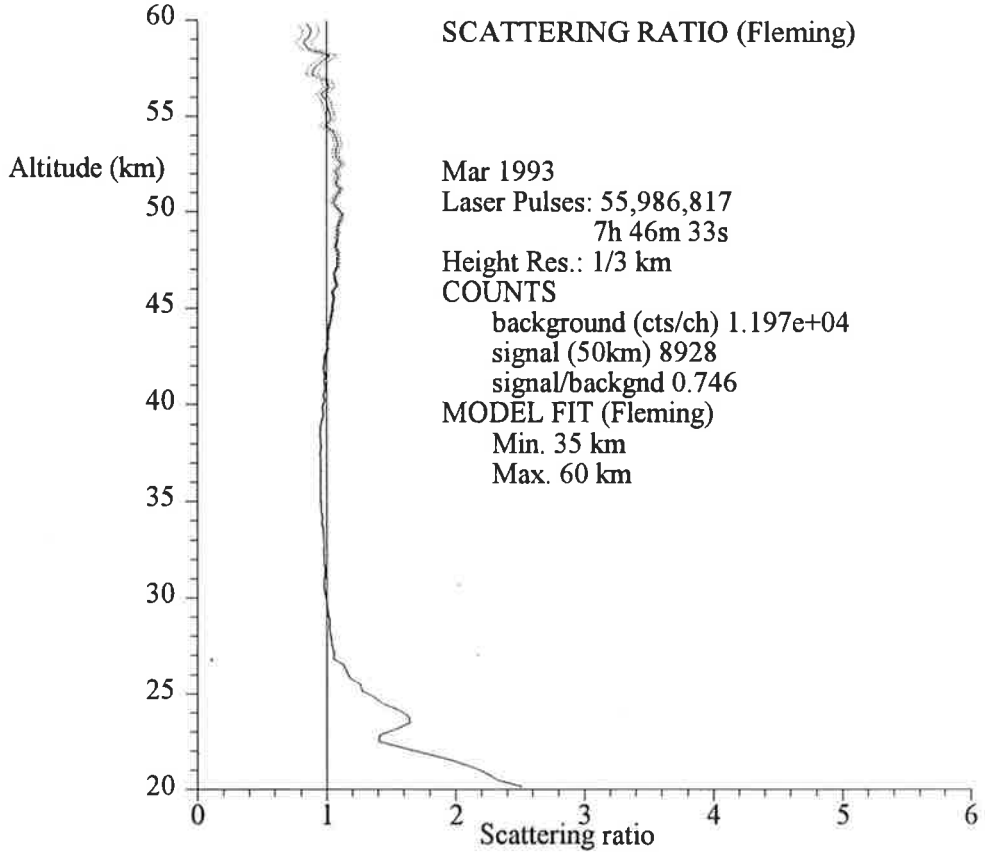
SCATTERING RATIO (Fleming)
Mar 1993
Laser Pulses: 55,986,817
7h 46m 33s
Height Res.: 1/3 km
COUNTS
background (cts/ch) 1.197e+04
signal (50km) 8928
signal/backgnd 0.746
MODEL FIT (Fleming)
Min. 35 km
Max. 60 km
Altitude (km)
Scattering ratio

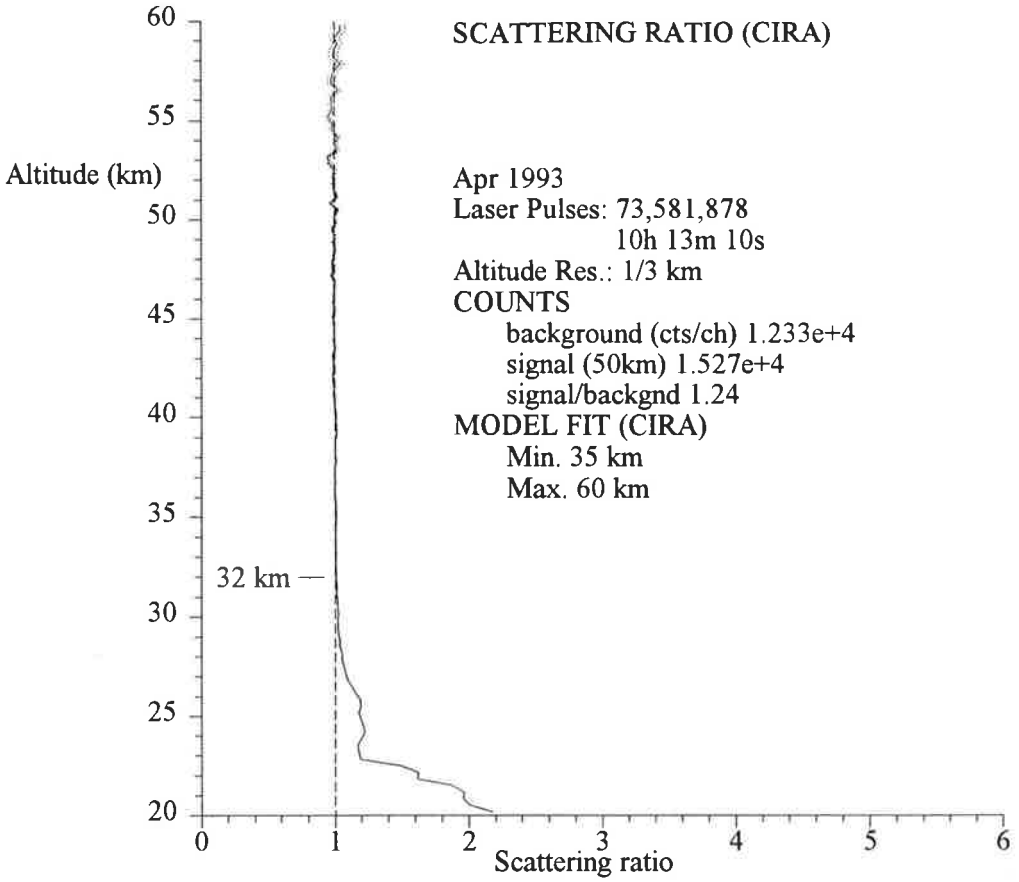
SCATTERING RATIO (CIRA)
Apr 1993
Laser Pulses: 73,581,878
10h 13m 10s
Altitude Res.: 1/3 km
COUNTS
background (cts/ch) 1.233e+4
signal (50km) 1.527e+4
signal/backgnd 1.24
MODEL FIT (CIRA)
Min. 35 km
Max. 60 km
Altitude (km)
32 km
Scattering ratio

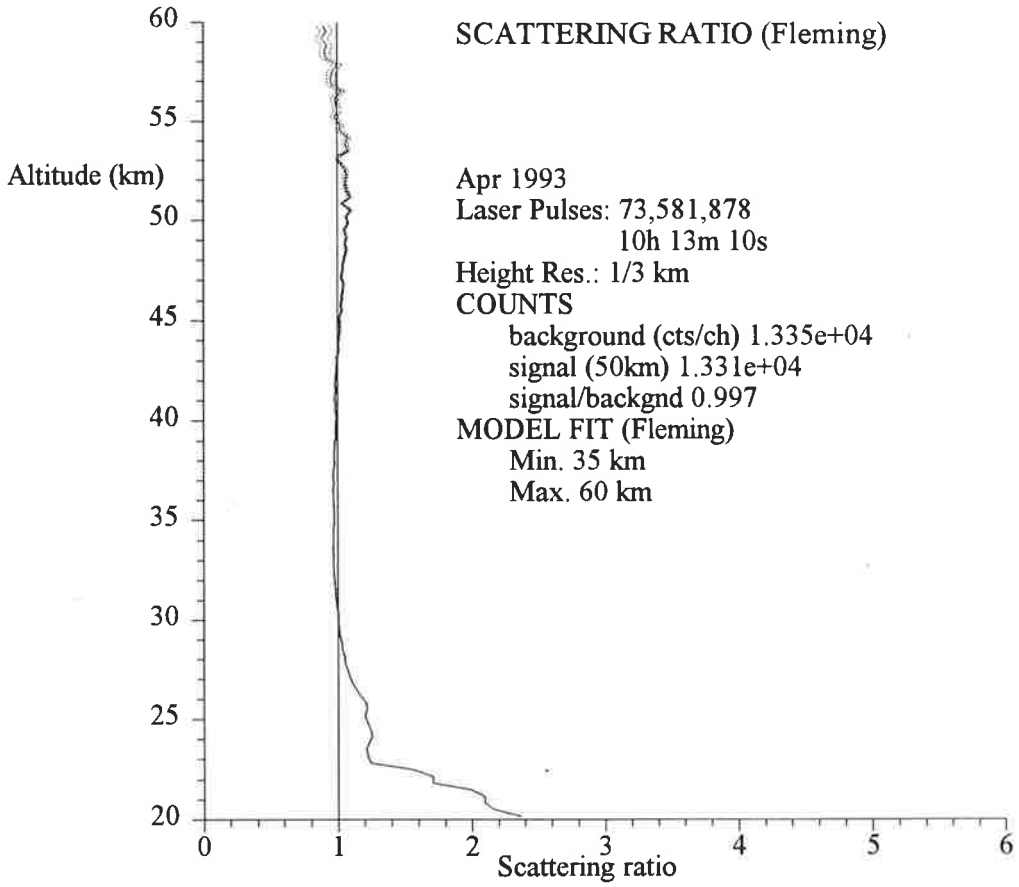
SCATTERING RATIO (Fleming)
Apr 1993
Laser Pulses: 73,581,878
10h 13m 10s
Height Res.: 1/3 km
COUNTS
background (cts/ch) 1.335e+04
signal (50km) 1.331e+04
signal/backgnd 0.997
MODEL FIT (Fleming)
Min. 35 km
Max. 60 km
Altitude (km)
Scattering ratio

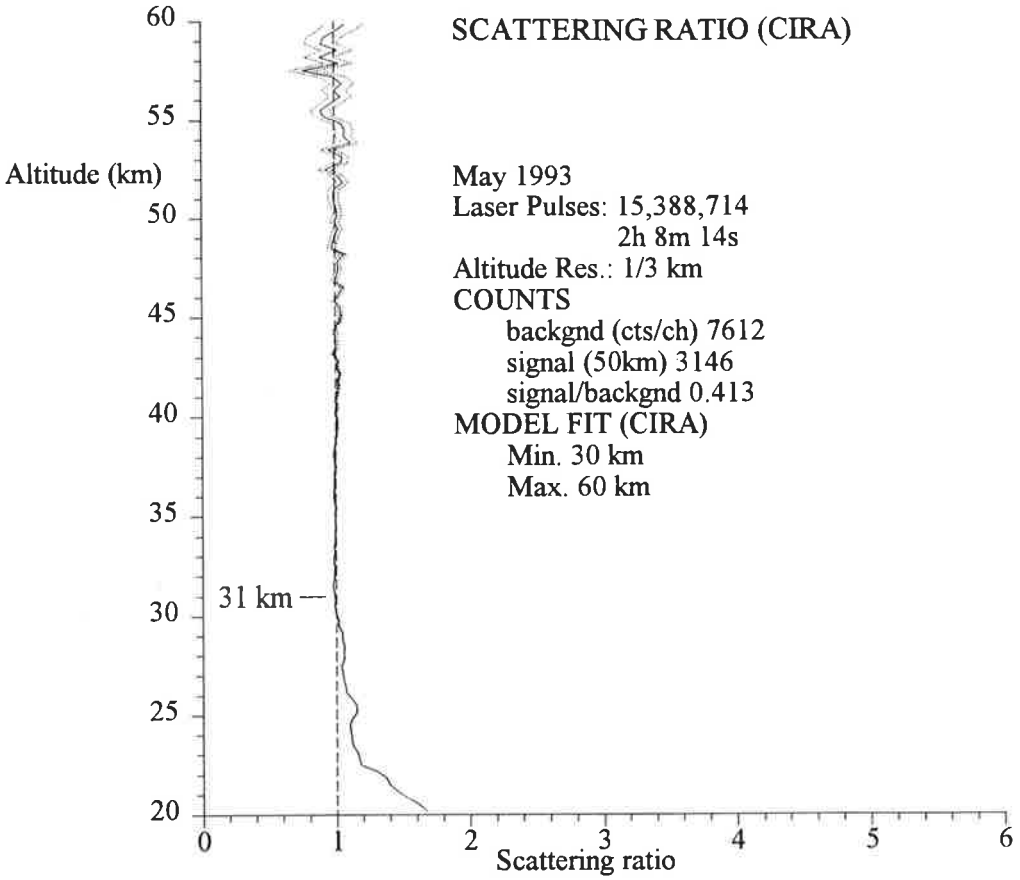
SCATTERING RATIO (CIRA)
May 1993
Laser Pulses: 15,388,714
2h 8m 14s
Altitude Res.: 1/3 km
COUNTS
backgnd (cts/ch) 7612
signal (50km) 3146
signal/backgnd 0.413
MODEL FIT (CIRA)
Min. 30 km
Max. 60 km
Altitude (km)
60
55
50
45
40
35
30
25
20
31 km
0
1
2
3
4
5
6
Scattering ratio

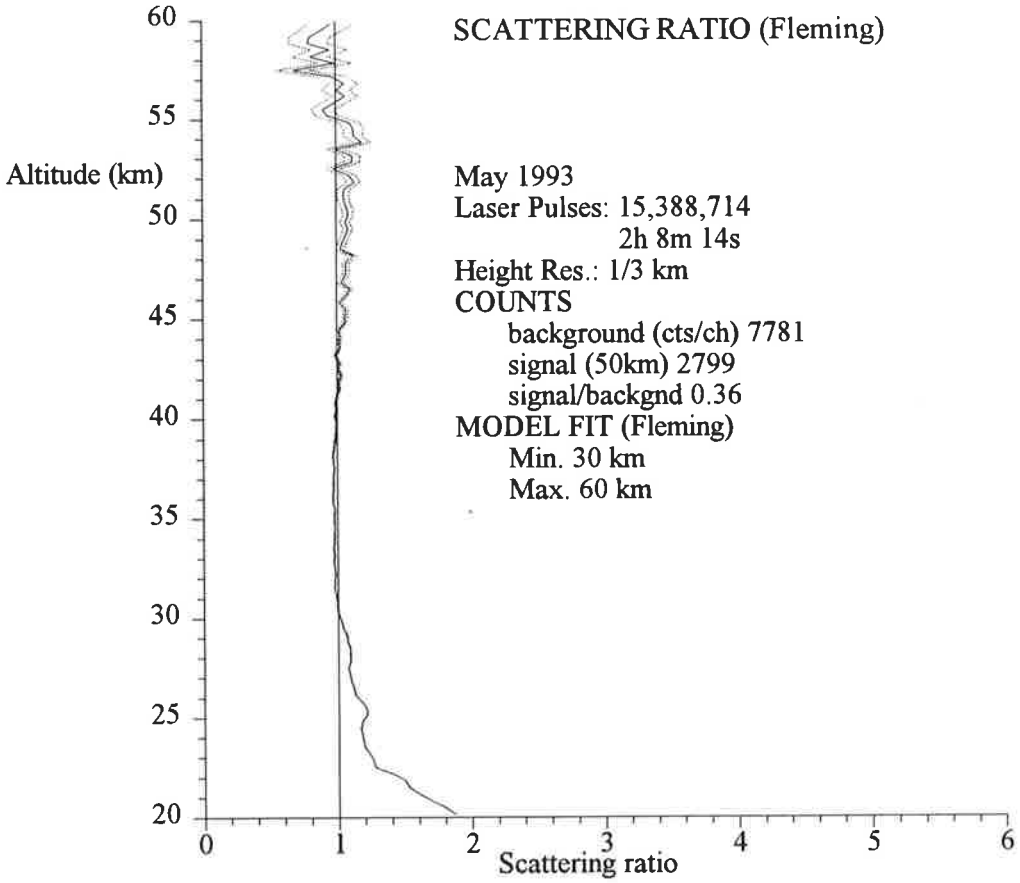
SCATTERING RATIO (Fleming)
May 1993
Laser Pulses: 15,388,714
2h 8m 14s
Height Res.: 1/3 km
COUNTS
background (cts/ch) 7781
signal (50km) 2799
signal/backgnd 0.36
MODEL FIT (Fleming)
Min. 30 km
Max. 60 km
Altitude (km)
60
55
50
45
40
35
30
25
20
0
1
2
3
4
5
6
Scattering ratio

Appendix D

Monthly Temperature Profiles

The temperature profiles presented below were calculated using all of the available data for each month. The method used to calculate the temperature profiles is given in chapter 7.

All temperature profile calculations were initiated at an altitude of 60 km and are presented below 55 km due to the dependence of the calculation on the model fitting in the first several kilometres, see chapter 7. Minimum altitudes for calculation are those given in appendix C.

The height resolution for each plot was selected in order to give reasonable uncertainties. For this same reason the plot for September 1992 starts at 50 km (calculations start at 60 km).

Each graph has the CIRA model Temperature (dashed line) for 35°S and the model of Fleming et al (dotted line) for 35°S plotted with the measured data (crosses) and the uncertainties in the measured values (error bars).

LIDAR Temperature Profile

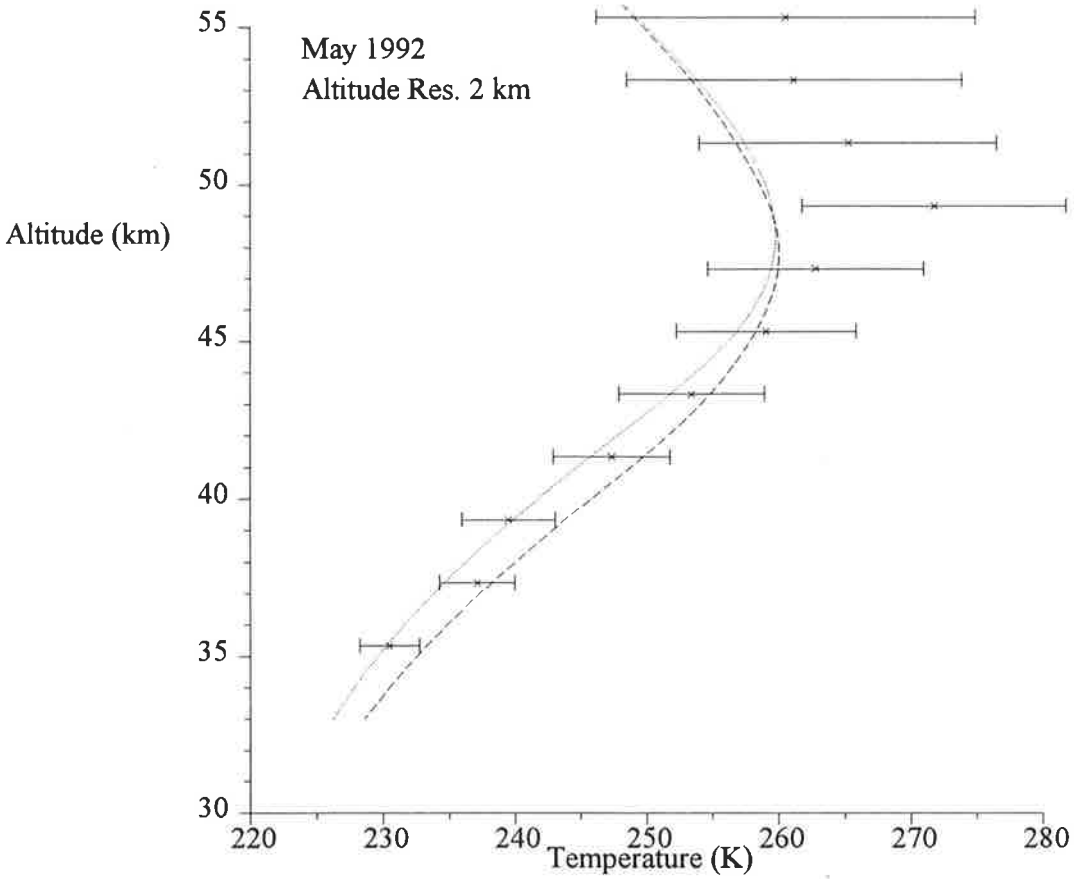

LIDAR Temperature Profile

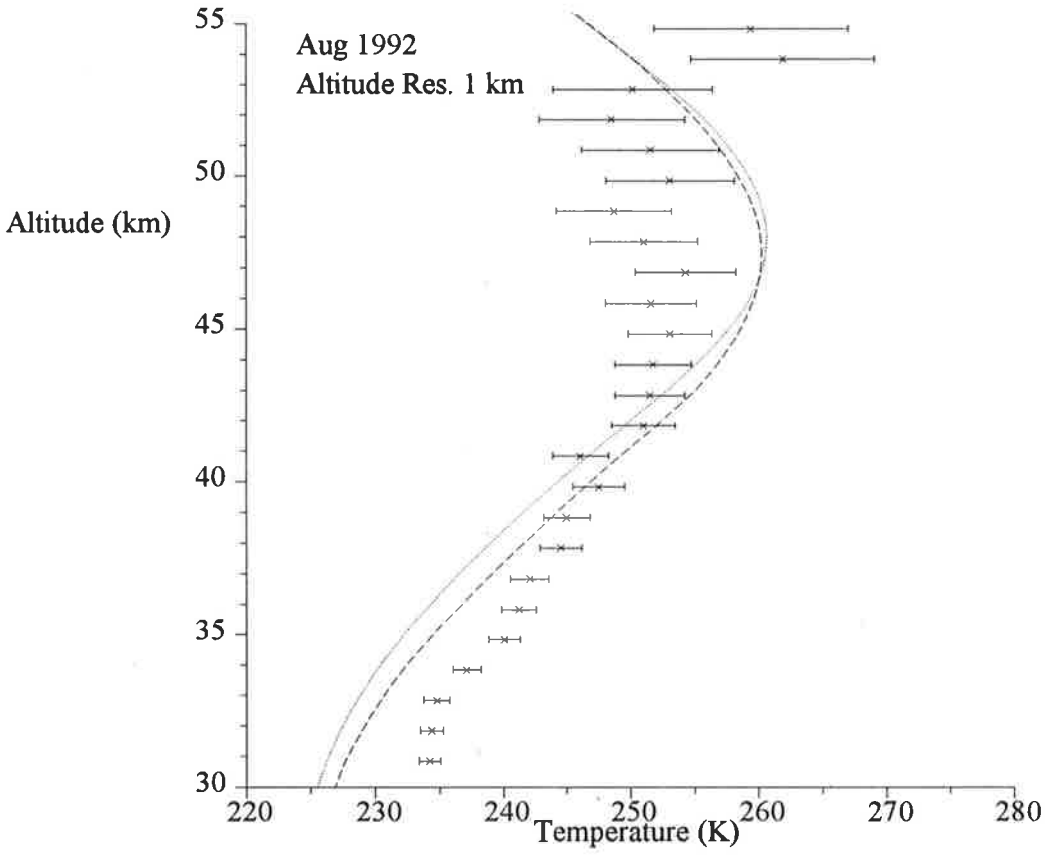

LIDAR Temperature Profile

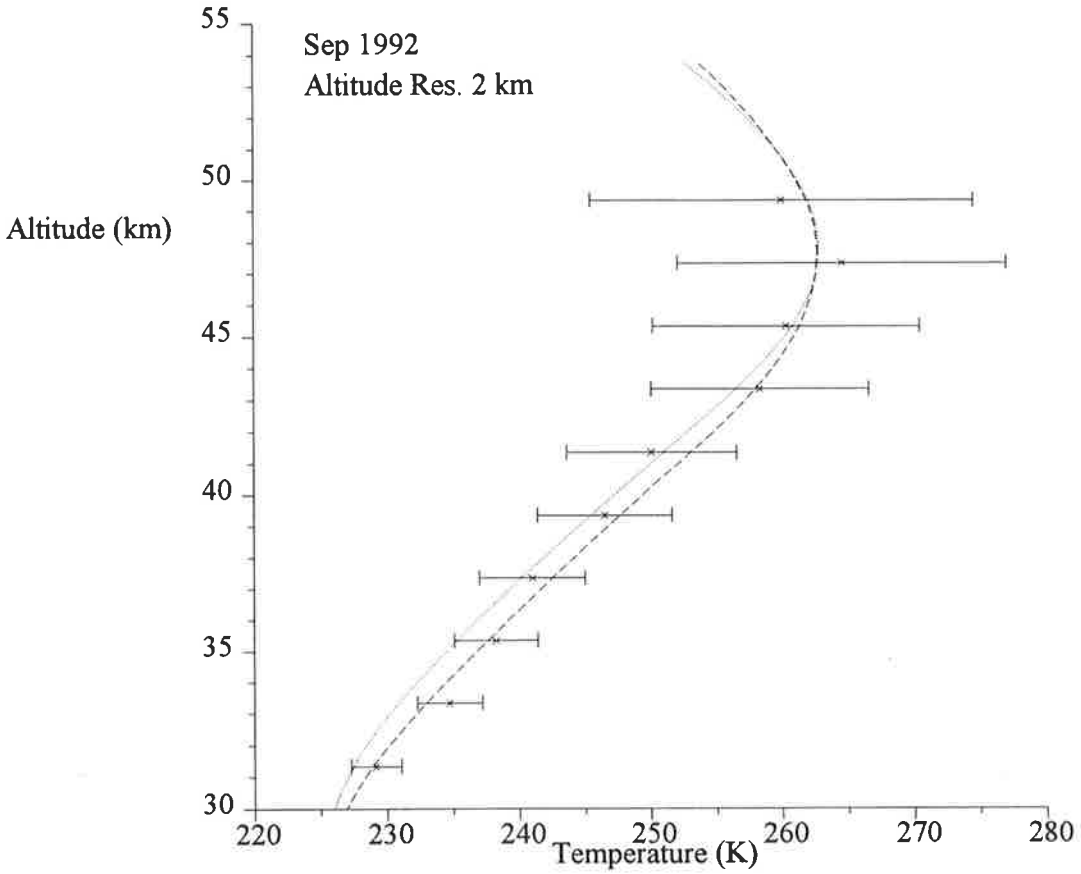

LIDAR Temperature Profile

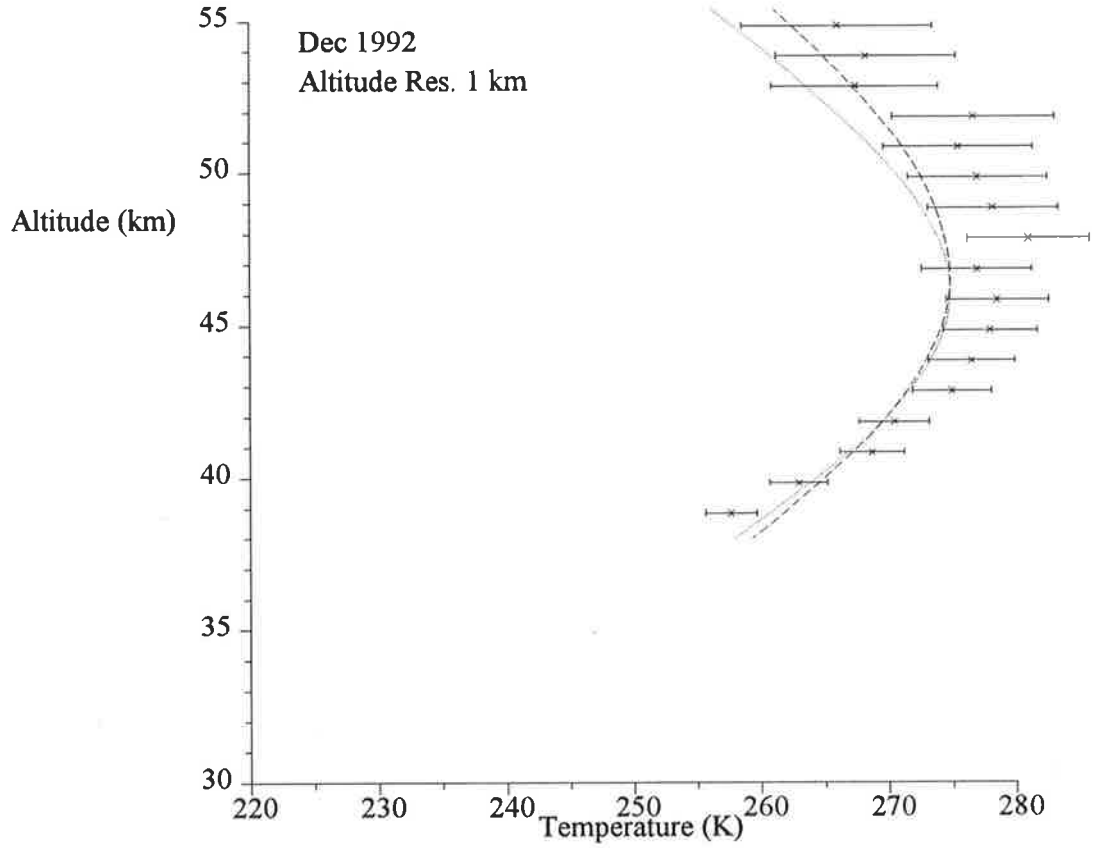

LIDAR Temperature Profile

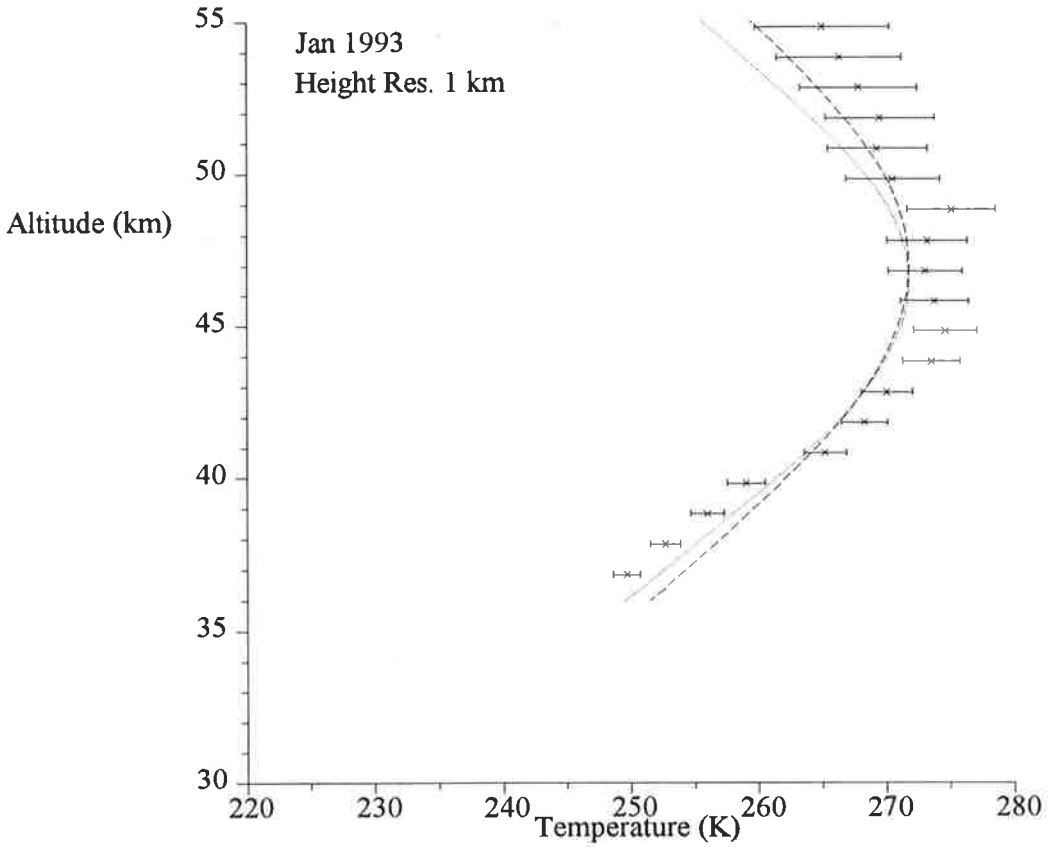

LIDAR Temperature Profile

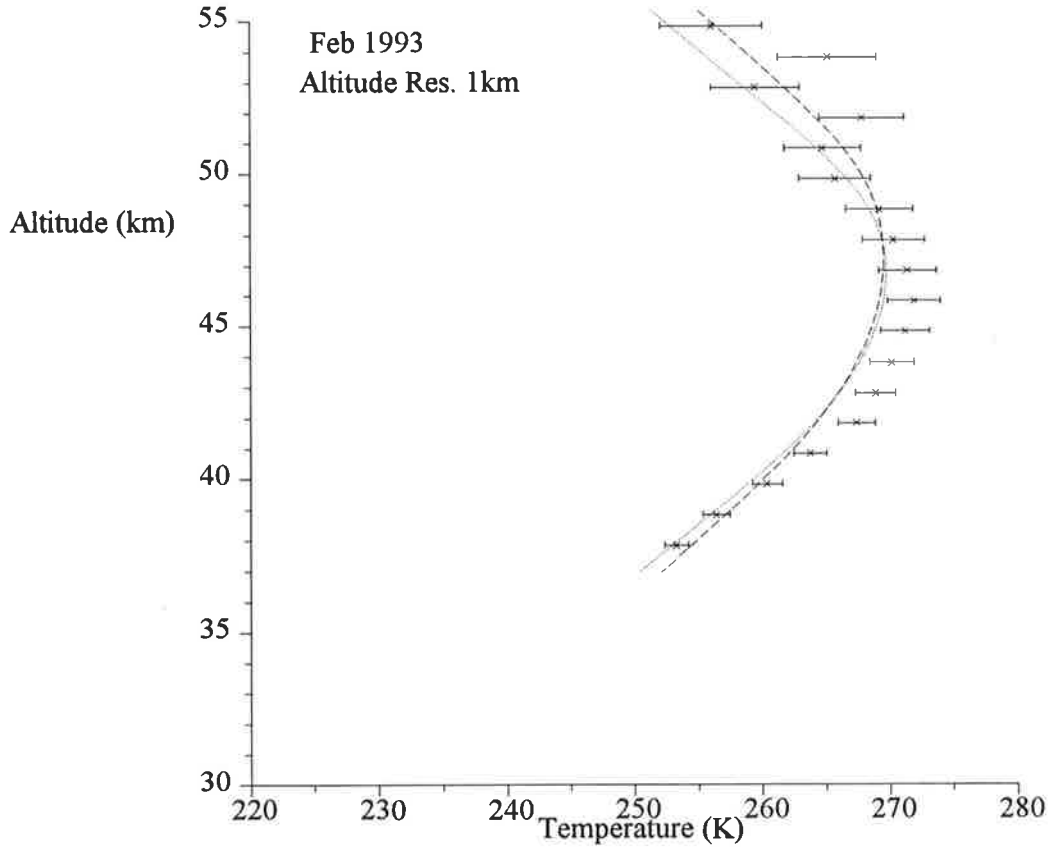

LIDAR Temperature Profile

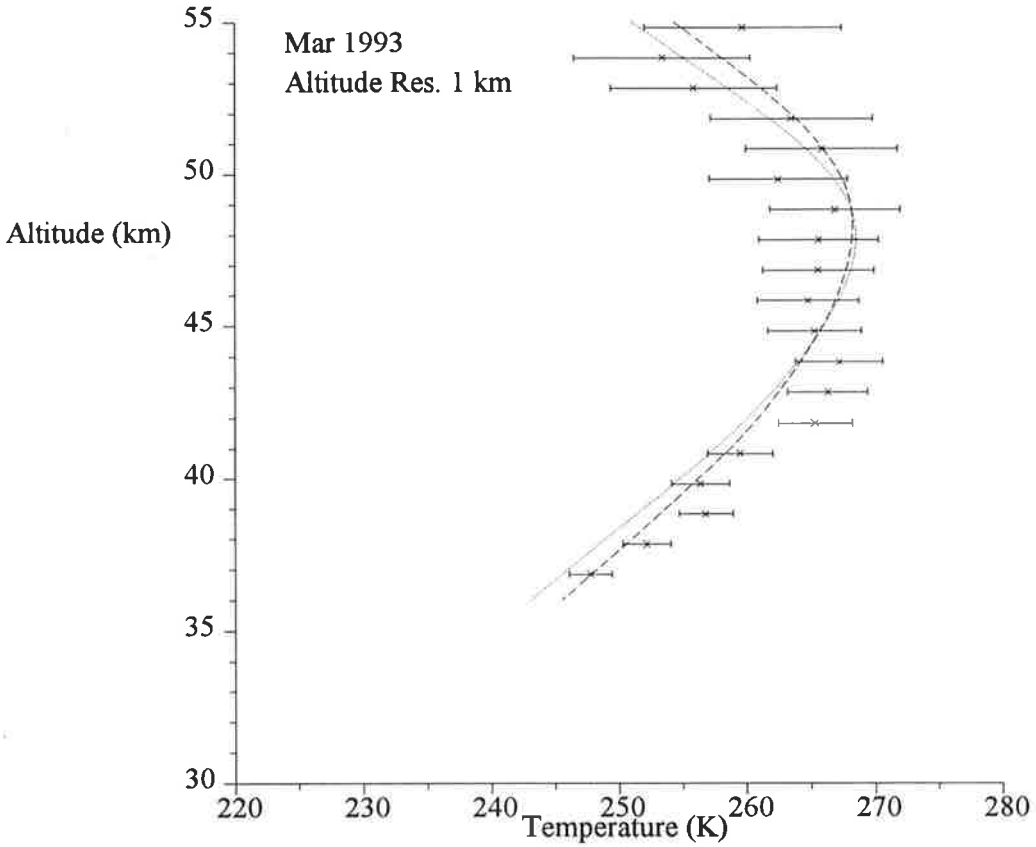

LIDAR Temperature Profile

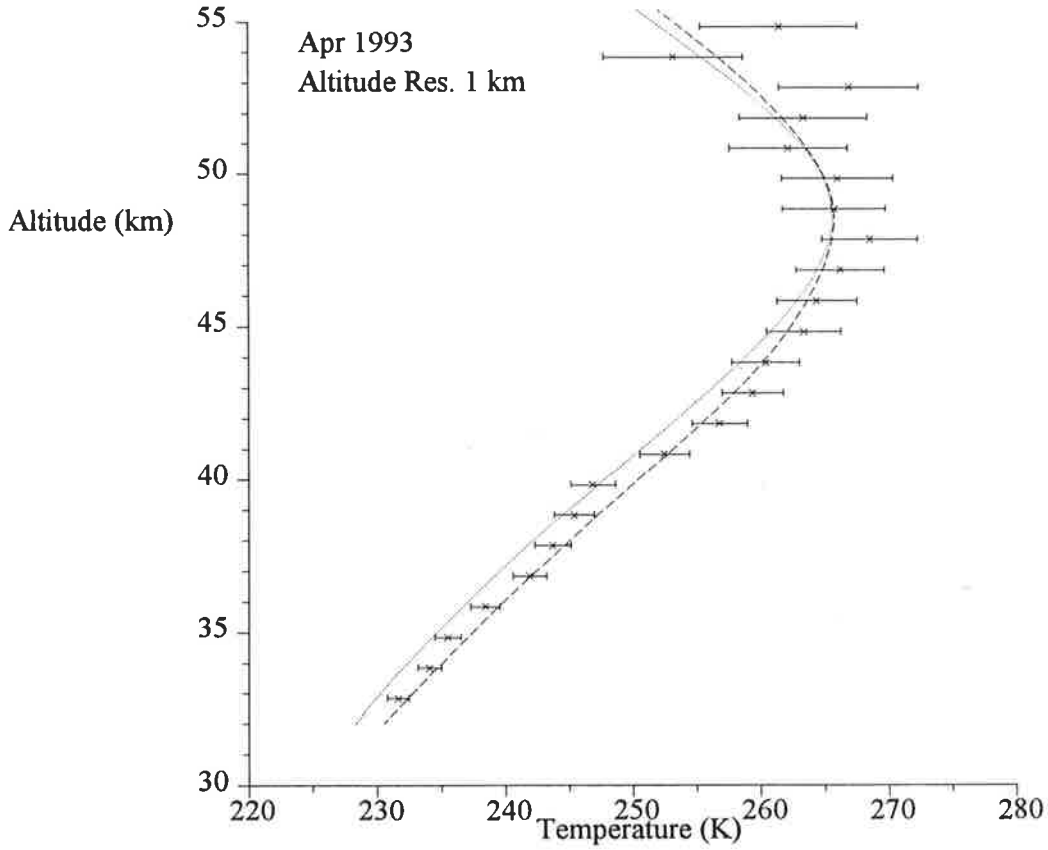

LIDAR Temperature Profile

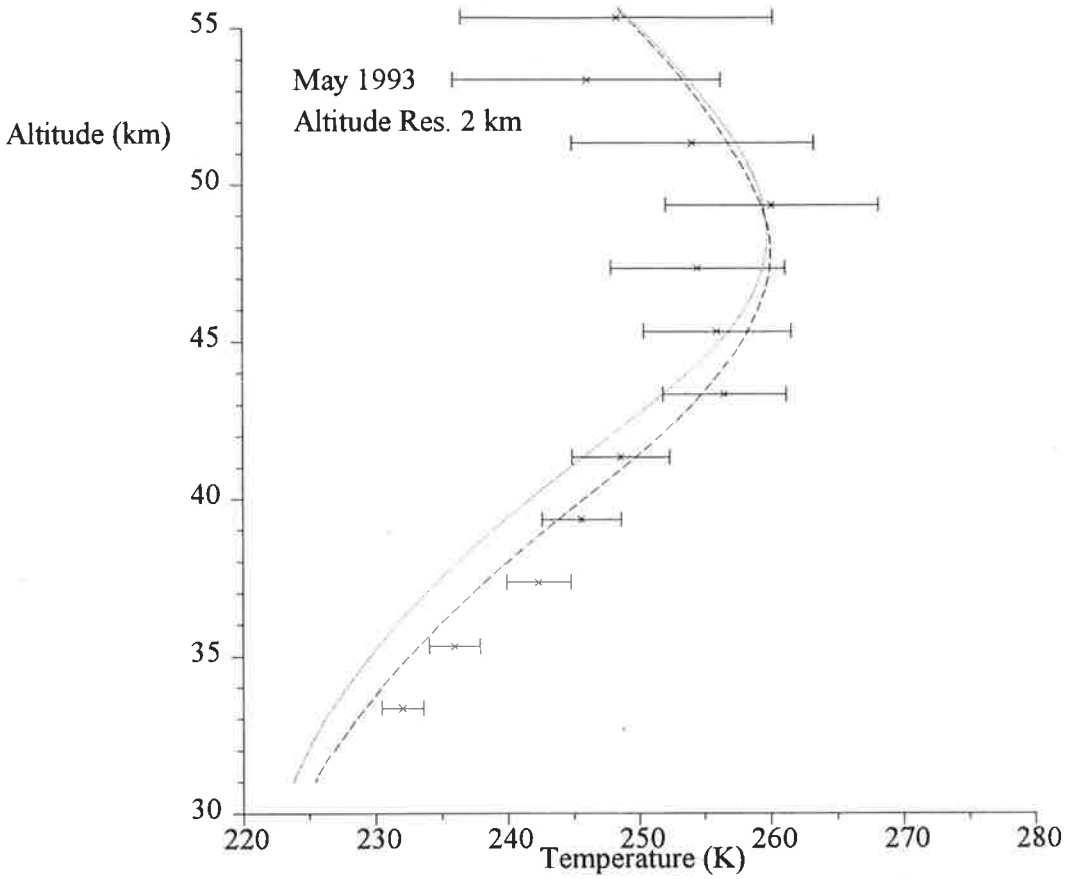

Appendix E

Nightly Temperature Profiles

The temperature profiles presented below were calculated using all of the available data for each night for which the data have sufficient signal to noise ratio to allow temperature calculation with reasonable uncertainties. The method used to calculate the temperature profiles is given in chapter 7.

All temperature profile calculations were initiated at an altitude of 60 km and are presented below 55 km due to the dependence of the calculation on the model fitting in the first several kilometres, see chapter 7.

The height resolution for each plot was selected in order to give reasonable uncertainties in the measure temperatures.

Each graph has the CIRA model Temperature (solid line) plotted with the measured data (crosses) and the uncertainties in the measured values (error bars).

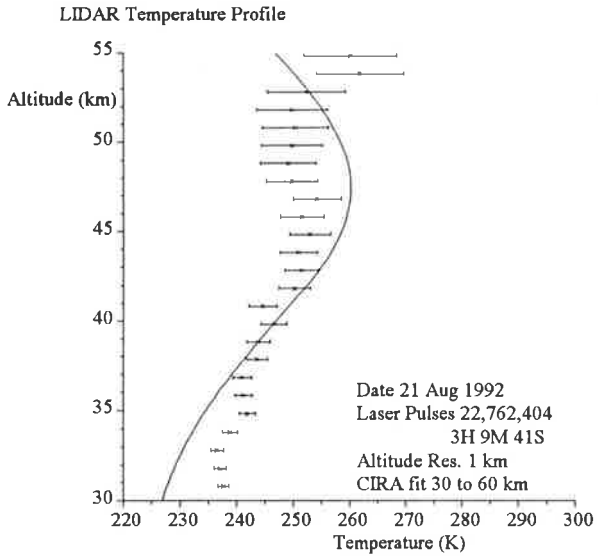
LIDAR Temperature Profile
Altitude (km)
55
50
45
40
35
30
220 230 240 250 260 270 280 290 300
Temperature (K)
Date 21 Aug 1992
Laser Pulses 22,762,404
3H 9M 41S
Altitude Res. 1 km
CIRA fit 30 to 60 km

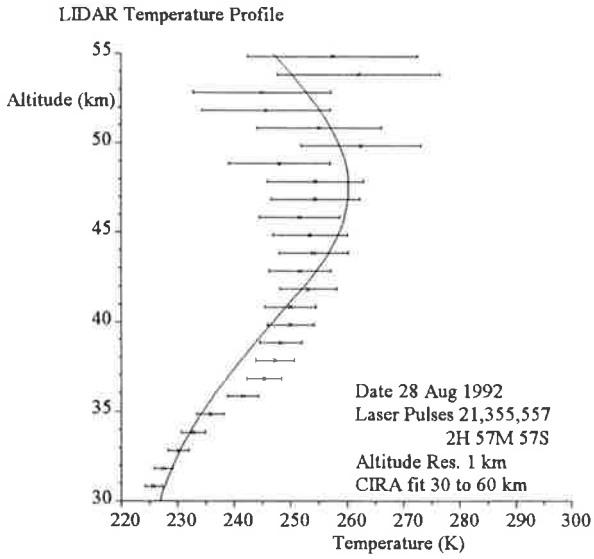
LIDAR Temperature Profile
Altitude (km)
55
50
45
40
35
30
220 230 240 250 260 270 280 290 300
Temperature (K)
Date 28 Aug 1992
Laser Pulses 21,355,557
2H 57M 57S
Altitude Res. 1 km
CIRA fit 30 to 60 km

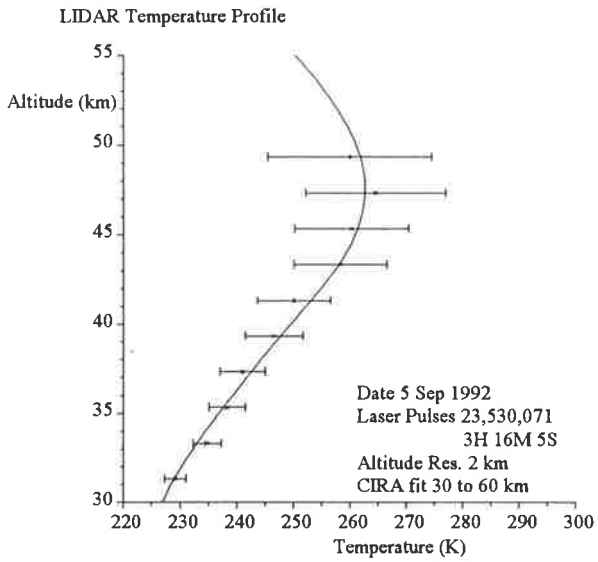
LIDAR Temperature Profile
Altitude (km)
55
50
45
40
35
30
220 230 240 250 260 270 280 290 300
Temperature (K)
Date 5 Sep 1992
Laser Pulses 23,530,071
3H 16M 5S
Altitude Res. 2 km
CIRA fit 30 to 60 km

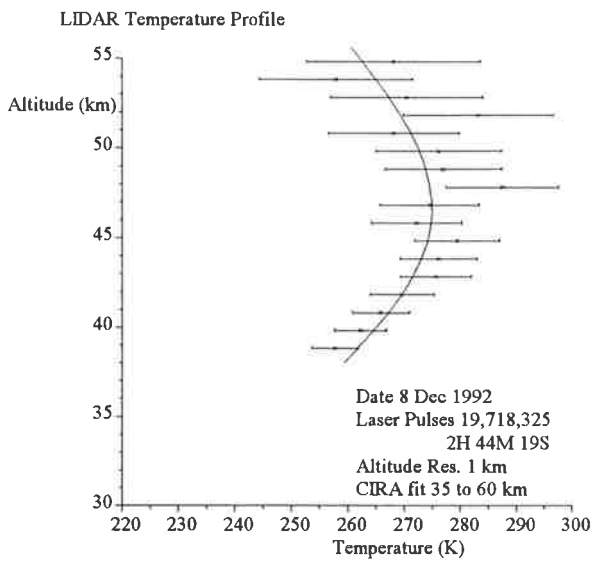
LIDAR Temperature Profile
Altitude (km)
55
50
45
40
35
30
220 230 240 250 260 270 280 290 300
Temperature (K)
Date 8 Dec 1992
Laser Pulses 19,718,325
2H 44M 19S
Altitude Res. 1 km
CIRA fit 35 to 60 km

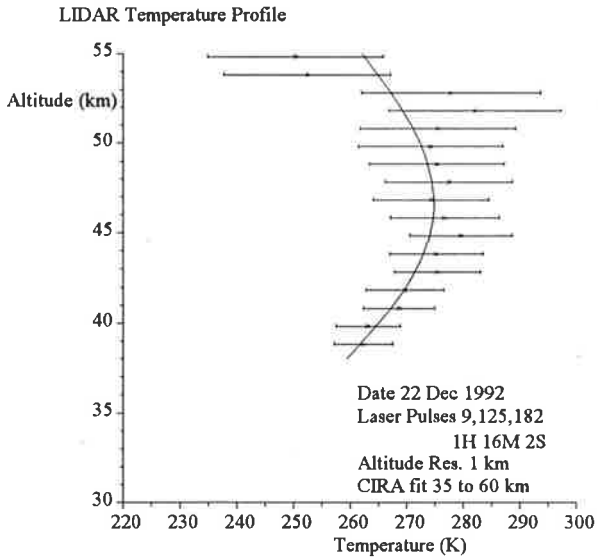
LIDAR Temperature Profile
Altitude (km)
55
50
45
40
35
30
220 230 240 250 260 270 280 290 300
Temperature (K)
Date 22 Dec 1992
Laser Pulses 9,125,182
1H 16M 2S
Altitude Res. 1 km
CIRA fit 35 to 60 km

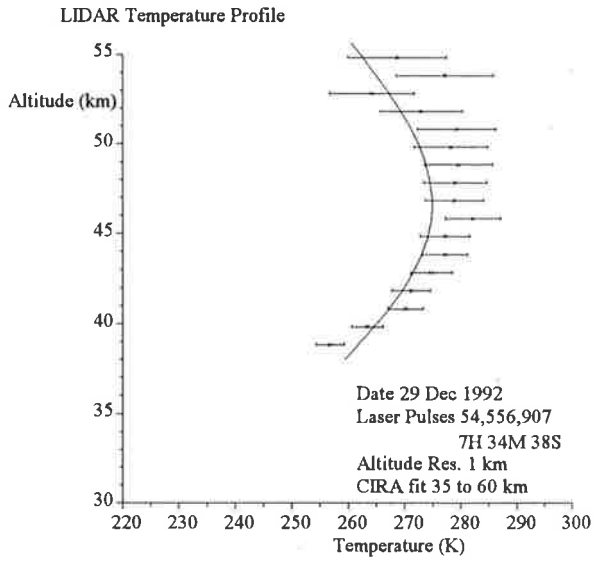
LIDAR Temperature Profile
Altitude (km)
55
50
45
40
35
30
220 230 240 250 260 270 280 290 300
Temperature (K)
Date 29 Dec 1992
Laser Pulses 54,556,907
7H 34M 38S
Altitude Res. 1 km
CIRA fit 35 to 60 km

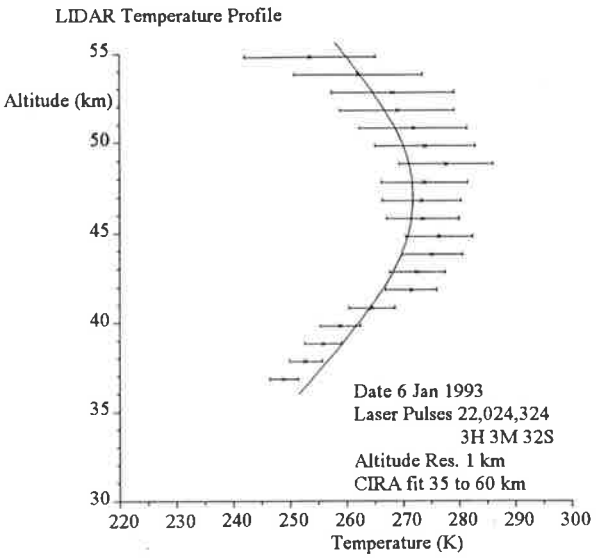
LIDAR Temperature Profile
Altitude (km)
55
50
45
40
35
30
220 230 240 250 260 270 280 290 300
Temperature (K)
Date 6 Jan 1993
Laser Pulses 22,024,324
3H 3M 32S
Altitude Res. 1 km
CIRA fit 35 to 60 km

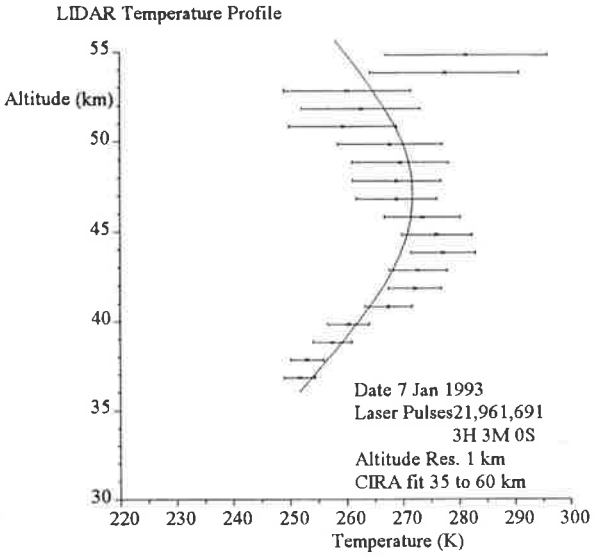
LIDAR Temperature Profile
Altitude (km)
55
50
45
40
35
30
220 230 240 250 260 270 280 290 300
Temperature (K)
Date 7 Jan 1993
Laser Pulses21,961,691
3H 3M 0S
Altitude Res. 1 km
CIRA fit 35 to 60 km

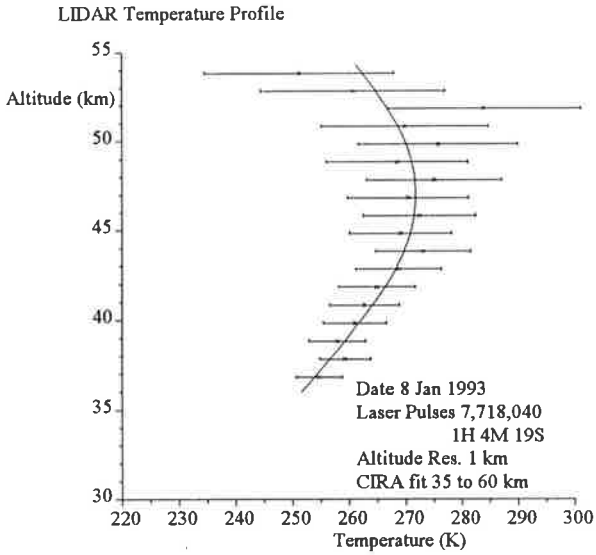
LIDAR Temperature Profile
Altitude (km)
55
50
45
40
35
30
220 230 240 250 260 270 280 290 300
Temperature (K)
Date 8 Jan 1993
Laser Pulses 7,718,040
1H 4M 19S
Altitude Res. 1 km
CIRA fit 35 to 60 km

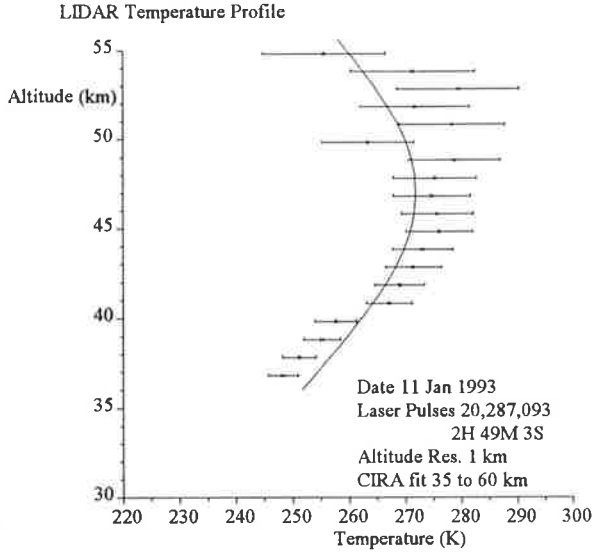
LIDAR Temperature Profile
Altitude (km)
55
50
45
40
35
30
220 230 240 250 260 270 280 290 300
Temperature (K)
Date 11 Jan 1993
Laser Pulses 20,287,093
2H 49M 3S
Altitude Res. 1 km
CIRA fit 35 to 60 km

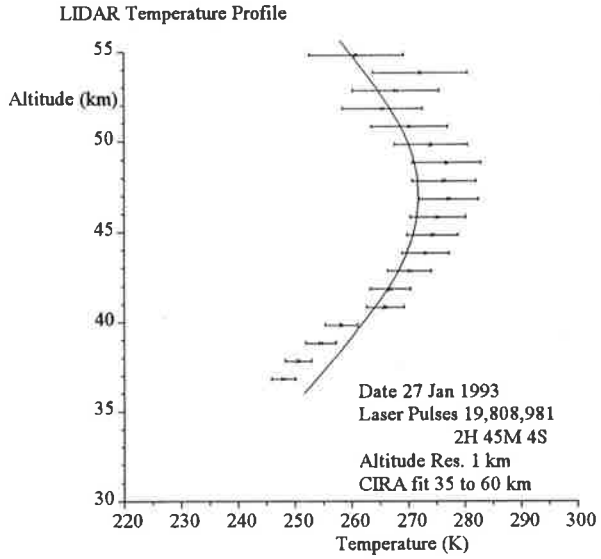
LIDAR Temperature Profile
Altitude (km)
55
50
45
40
35
30
220 230 240 250 260 270 280 290 300
Temperature (K)
Date 27 Jan 1993
Laser Pulses 19,808,981
2H 45M 4S
Altitude Res. 1 km
CIRA fit 35 to 60 km

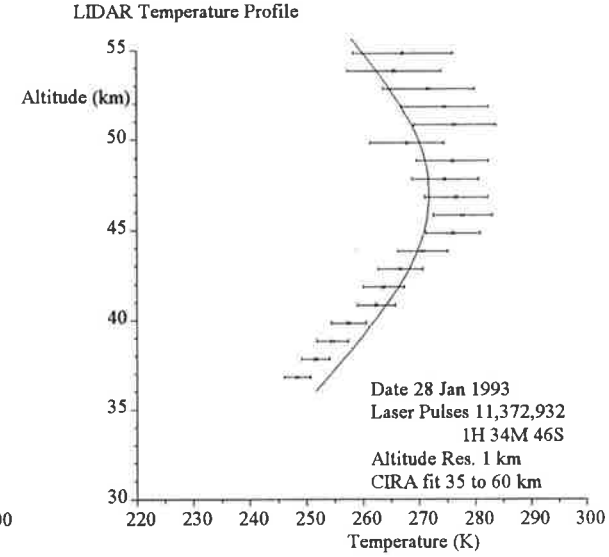
LIDAR Temperature Profile
Altitude (km)
55
50
45
40
35
30
220 230 240 250 260 270 280 290 300
Temperature (K)
Date 28 Jan 1993
Laser Pulses 11,372,932
1H 34M 46S
Altitude Res. 1 km
CIRA fit 35 to 60 km

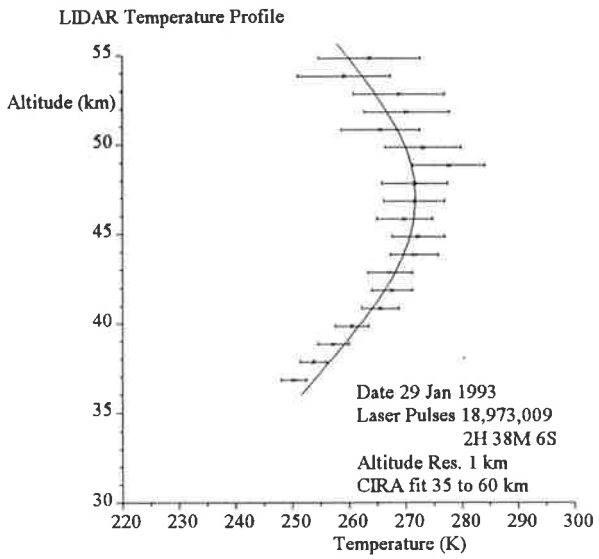
LIDAR Temperature Profile
Altitude (km)
55
50
45
40
35
30
220 230 240 250 260 270 280 290 300
Temperature (K)
Date 29 Jan 1993
Laser Pulses 18,973,009
2H 38M 6S
Altitude Res. 1 km
CIRA fit 35 to 60 km

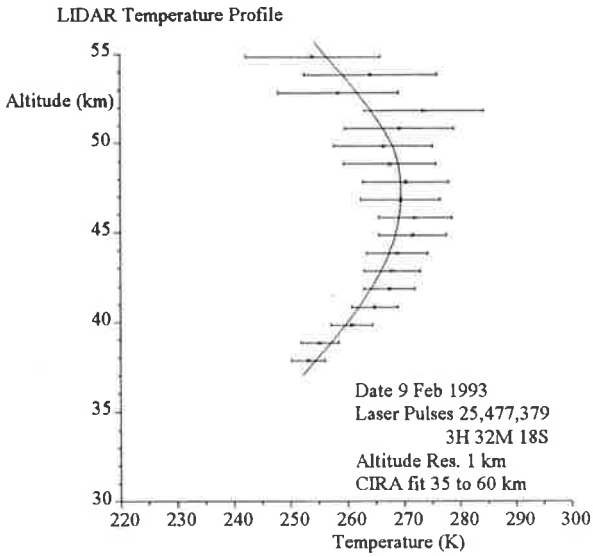
LIDAR Temperature Profile
Altitude (km)
55
50
45
40
35
30
220 230 240 250 260 270 280 290 300
Temperature (K)
Date 9 Feb 1993
Laser Pulses 25,477,379
3H 32M 18S
Altitude Res. 1 km
CIRA fit 35 to 60 km

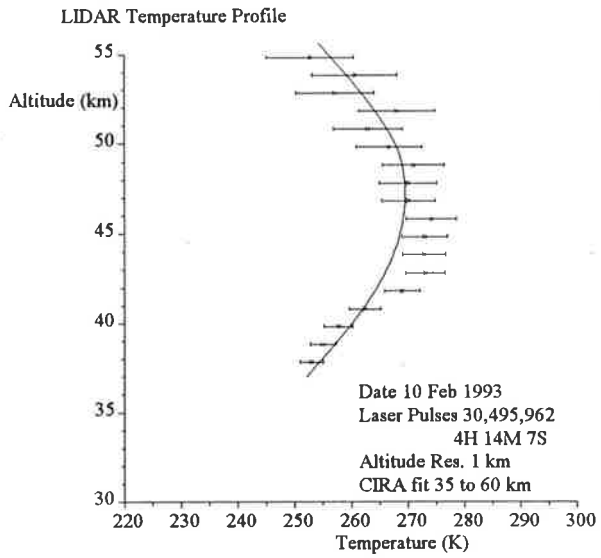
LIDAR Temperature Profile
Altitude (km)
55
50
45
40
35
30
220 230 240 250 260 270 280 290 300
Temperature (K)
Date 10 Feb 1993
Laser Pulses 30,495,962
4H 14M 7S
Altitude Res. 1 km
CIRA fit 35 to 60 km

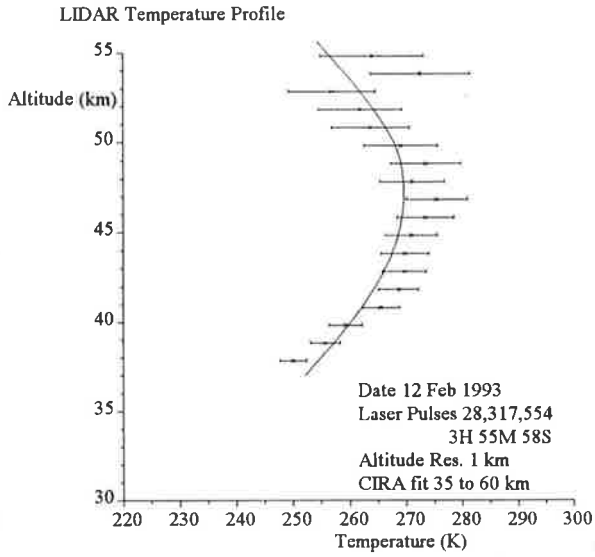
LIDAR Temperature Profile
Altitude (km)
55
50
45
40
35
30
220 230 240 250 260 270 280 290 300
Temperature (K)
Date 12 Feb 1993
Laser Pulses 28,317,554
3H 55M 58S
Altitude Res. 1 km
CIRA fit 35 to 60 km

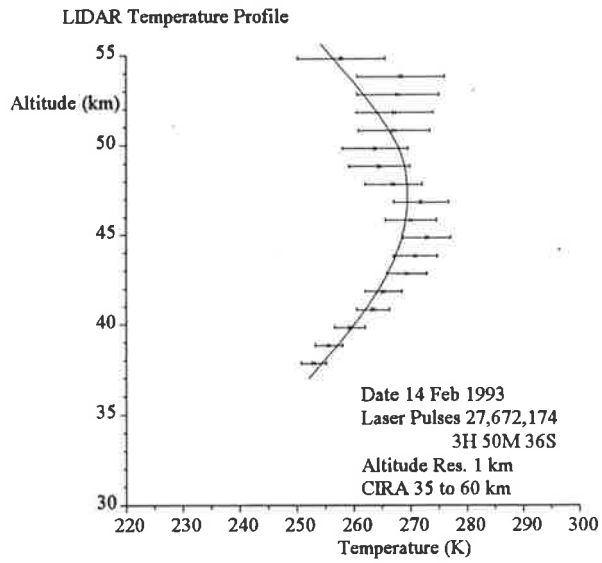
LIDAR Temperature Profile
Altitude (km)
55
50
45
40
35
30
220 230 240 250 260 270 280 290 300
Temperature (K)
Date 14 Feb 1993
Laser Pulses 27,672,174
3H 50M 36S
Altitude Res. 1 km
CIRA 35 to 60 km

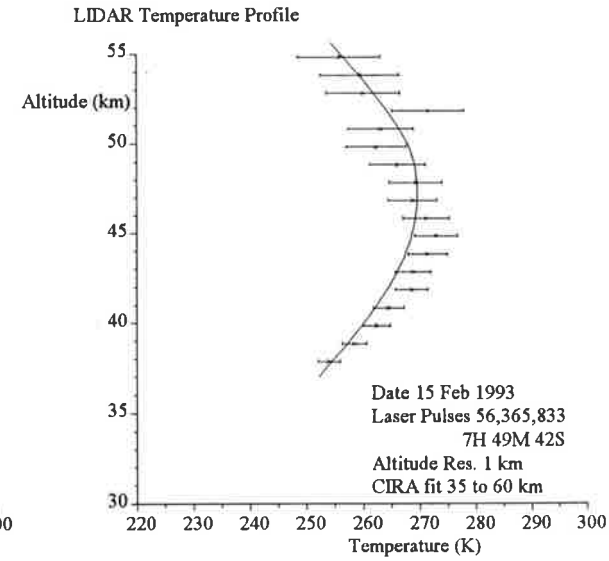
LIDAR Temperature Profile
Altitude (km)
55
50
45
40
35
30
220 230 240 250 260 270 280 290 300
Temperature (K)
Date 15 Feb 1993
Laser Pulses 56,365,833
7H 49M 42S
Altitude Res. 1 km
CIRA fit 35 to 60 km

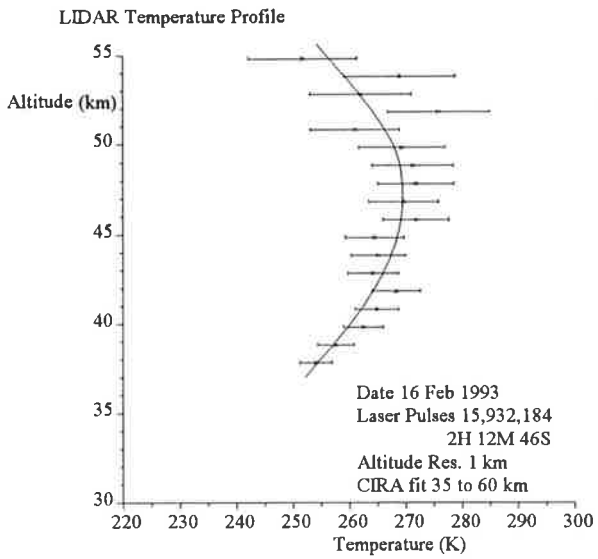
LIDAR Temperature Profile
Altitude (km)
55
50
45
40
35
30
220 230 240 250 260 270 280 290 300
Temperature (K)
Date 16 Feb 1993
Laser Pulses 15,932,184
2H 12M 46S
Altitude Res. 1 km
CIRA fit 35 to 60 km

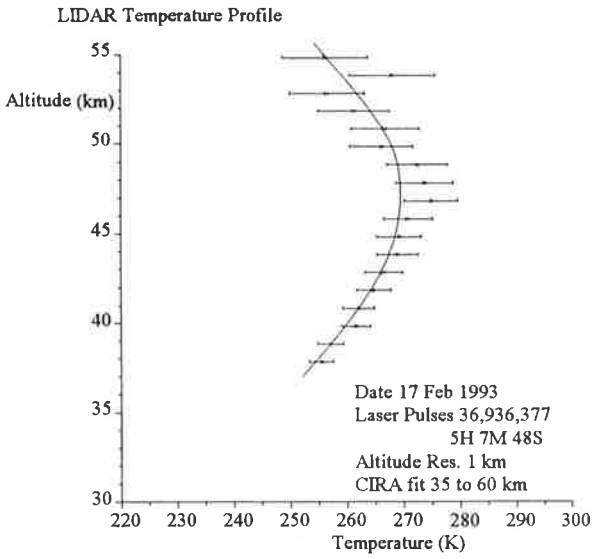
LIDAR Temperature Profile
Altitude (km)
55
50
45
40
35
30
220 230 240 250 260 270 280 290 300
Temperature (K)
Date 17 Feb 1993
Laser Pulses 36,936,377
5H 7M 48S
Altitude Res. 1 km
CIRA fit 35 to 60 km

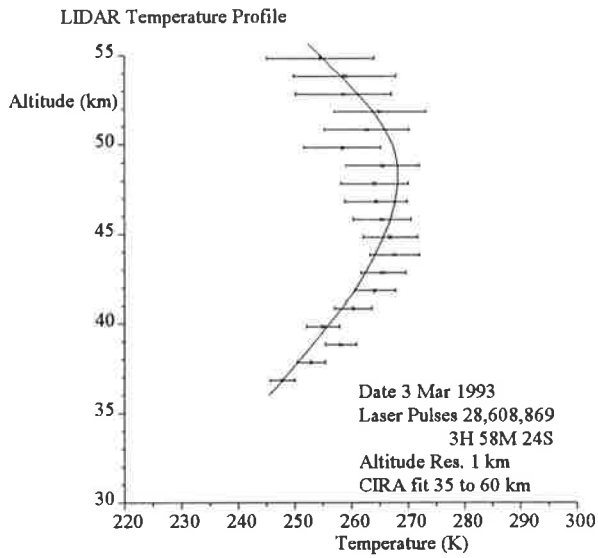
LIDAR Temperature Profile
Altitude (km)
55
50
45
40
35
30
220 230 240 250 260 270 280 290 300
Temperature (K)
Date 3 Mar 1993
Laser Pulses 28,608,869
3H 58M 24S
Altitude Res. 1 km
CIRA fit 35 to 60 km

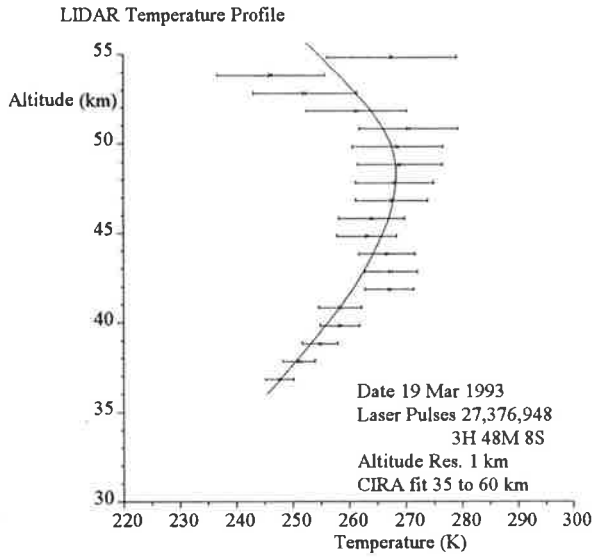
LIDAR Temperature Profile
Altitude (km)
55
50
45
40
35
30
220 230 240 250 260 270 280 290 300
Temperature (K)
Date 19 Mar 1993
Laser Pulses 27,376,948
3H 48M 8S
Altitude Res. 1 km
CIRA fit 35 to 60 km

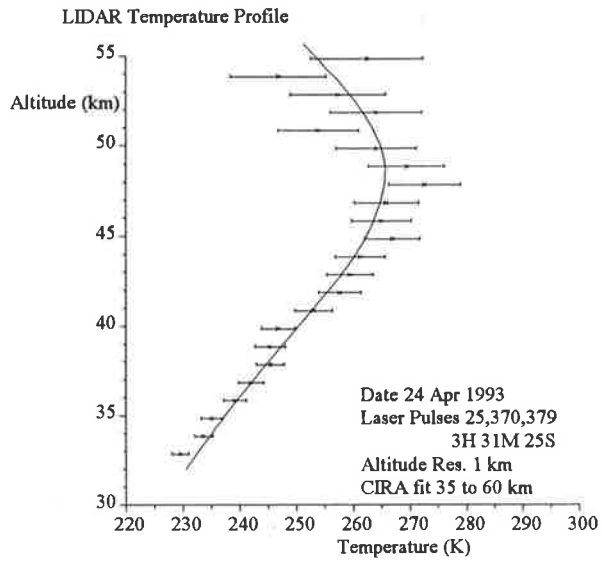
LIDAR Temperature Profile
Altitude (km)
55
50
45
40
35
30
220 230 240 250 260 270 280 290 300
Temperature (K)
Date 24 Apr 1993
Laser Pulses 25,370,379
3H 31M 25S
Altitude Res. 1 km
CIRA fit 35 to 60 km

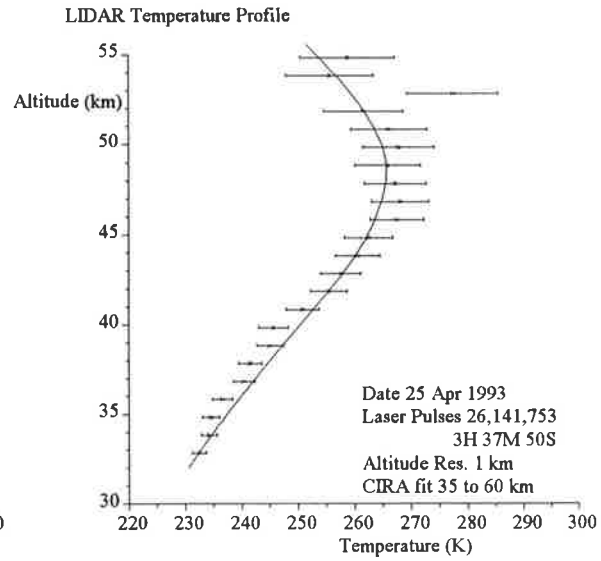
LIDAR Temperature Profile
Altitude (km)
55
50
45
40
35
30
220 230 240 250 260 270 280 290 300
Temperature (K)
Date 25 Apr 1993
Laser Pulses 26,141,753
3H 37M 50S
Altitude Res. 1 km
CIRA fit 35 to 60 km

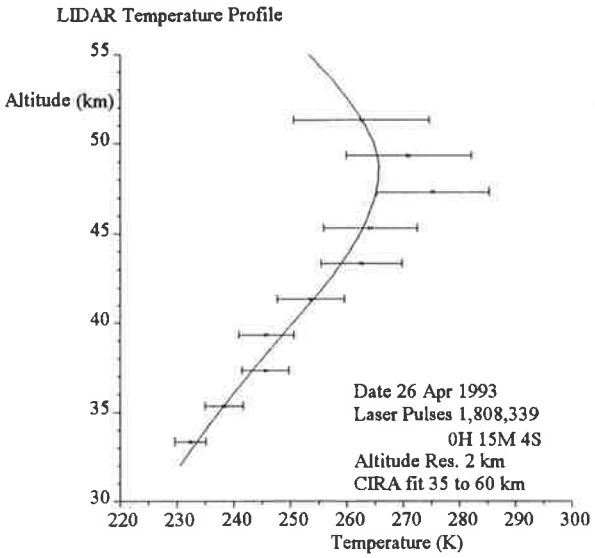
LIDAR Temperature Profile
Altitude (km)
55
50
45
40
35
30
220 230 240 250 260 270 280 290 300
Temperature (K)
Date 26 Apr 1993
Laser Pulses 1,808,339
0H 15M 4S
Altitude Res. 2 km
CIRA fit 35 to 60 km

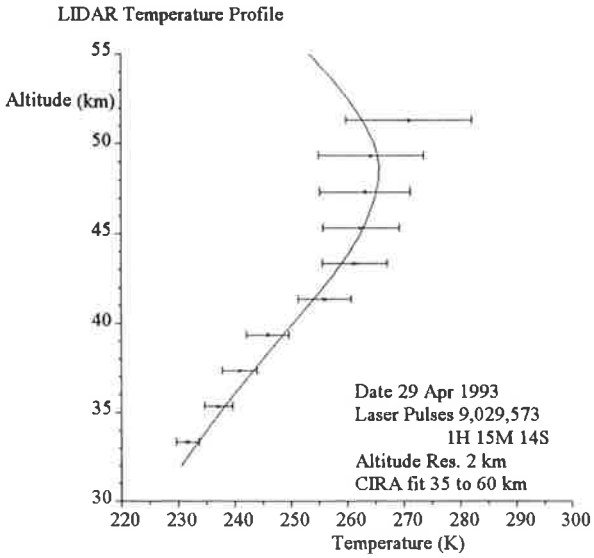
LIDAR Temperature Profile
Altitude (km)
55
50
45
40
35
30
220 230 240 250 260 270 280 290 300
Temperature (K)
Date 29 Apr 1993
Laser Pulses 9,029,573
1H 15M 14S
Altitude Res. 2 km
CIRA fit 35 to 60 km

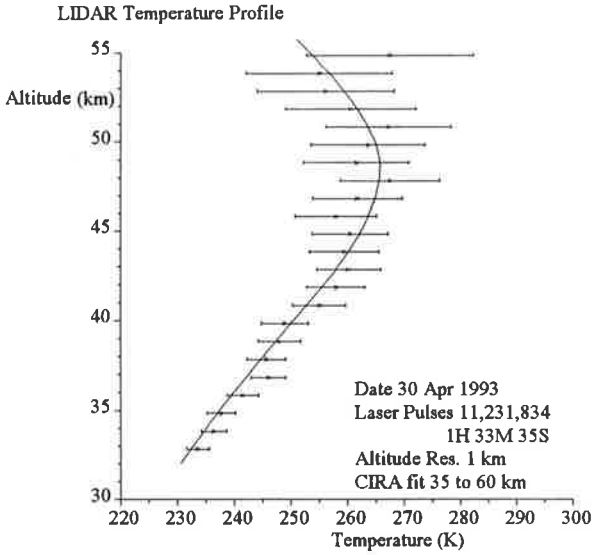
LIDAR Temperature Profile
Altitude (km)
55
50
45
40
35
30
220 230 240 250 260 270 280 290 300
Temperature (K)
Date 30 Apr 1993
Laser Pulses 11,231,834
1H 33M 35S
Altitude Res. 1 km
CIRA fit 35 to 60 km

References

Abreu V.J., J.E. Barnes, and P.B. Hays (1992) "Observations of winds with an incoherent lidar detector", *Appl. Opt.*, 31, pp 4509-4514.

Adriani A., G.P. Gobbi, F. Congeduti, and G. Di Donfrancesco (1991) "Lidar observations of stratospheric and mesospheric temperature: November 1988-November 1989", *Ann. Geophysicae* 9, pp 252-258.

Andrews D.G., J.R. Holton, and C.B. Leovy (1987) "Middle Atmosphere Dynamics" International Geophysics Series Vol. 40.Academic Press, London.

Arshinovo Yu.F., S.M. Bobrovnikov, V.E. Zuev, and M. Mitev (1983) "Atmospheric temperature measurement using a pure rotational Raman lidar", *Appl. Opt.*, 22, pp 2984-90.

Banwell C.N. (1983) "Fundamentals of Molecular Spectroscopy", Third Edition, McGraw-Hill, London.

Bayvel L.P., and A.R. Jones (1981) "Electromagnetic scattering and its applications", Applied Science Publishers, England.

Beatty T.J., C.A. Hostetler, and C.G. Gardner (1992) "Lidar Observations of Gravity Waves and Their Spectra near the Mesopause and Stratopause at Arecibo", *J. Atmos. Sci.*, 49,pp 477496.

Benedetti-Michelangelli G., F. Congeduti, and G. Fiocco (1972) "Measurement of Aerosol Motion and Wind Velocity in the Lower Troposphere by Doppler Optical Radar", *J. Atmos. Sci.*, 29, pp 906-910.

Benedetti-Michelangelli G., F. Congeduti, and G. Fiocco (1974) "Determination of Vertical Eddy Diffusion Parameters by Doppler Optical Radar", *Atmospheric Environment*, 8, pp 793-799.

Bevington P.R. (1969) "Data Reduction and Error Analysis for the Physical Sciences" McGraw-Hill, USA.

Bills R.E., and C.S. Gardner (1990) "LIDAR Observations of Mesospheric Fe and Sporadic Fe Layers at Urbana, Illinois", *Geophys. Res. Lett.*, 17, pp577-579.

Bills R.E., C.S. Gardner, and C.Y. She (1991) "Narrow-Band LIDAR Technique for Sodium Temperature and Doppler Wind Observationsof the Upper Atmosphere", *Opt. Eng.*, 30, pp 13-21.

Bohren C.E., and D.R. Huffman (1983) "Absorption and Scattering of Light by Small Particles", John Wiley & Sons, New York.

Boley C.D., R.C. Desai, and G. Tenti (1972) "Kinetic Models and Brillouin Scattering in a Molecular Gas", *Can. J. Phys.*, 50, pp 2158-2173.

Born M., and Wolf E. (1970) "Principles of Optics", Pergamon Press, Great Britian.

Bowman M.R., A.J. Gibson, and M.C.W. Sandford (1969) *Nature,* 221, pp 456-457.

Browell E.V. (1989) "Differential Absorption Lidar Sensing of Ozone", *Proc. IEEE.*, 77, pp 419-432.

Bureau R. (1946) Meteorologie (Paris), 3, pp 292.

Carswell A.I., S.R. Pal, W. Steinbrecht, J.A. Whiteway, A. Ulitsky and T.Y. Wang (1991) "Lidar Measurements of the Middle Atmosphere", *Can. J. Phys.*, 69, 1076.

Chamberlain J.W. (1961) "Physics of Aurora and Airglow", Academic Press, New York

Chamberlain J.W., and M. Hunten (1987) "Theory of Planetary Atmospheres: An Introduction to Their Physics and Chemistry" Academic Press, International Geophysics Series.

Chanin M.L., and A. Hauchecorne (1980) "Density and Temperature Profiles Obtained by Lidar between 35 and 70 km" *Geophys. Res. Lett.*,Vol 7, No 8, pp 565-568.

Chanin M.L., and A. Houchecorne (1981) "Lidar Observation Of Gravity And Tidal Waves In The Stratosphere And Mesosphere" *J. Geophys. Res.* Vol 86, No C10, pp 9715-9721.

Chanin M.L. (1984) "Review of Lidar contribution to the description and understanding of the middle atmosphere", *J. Atmos. Terr. Phys.*,Vol 46, No 11, pp 987-993.

Chanin M.L., and A. Houchecorne (1984) "Lidar Studies of Temperature and Density Using Rayleigh Scattering", *Handbook of MAP*, Vol 13, pp 87-98.

Chanin M.L., A. Houchecorne, and N. Smires (1985) "Contribution to the CIRA Model from Ground-Based Lidar", *Handbook of MAP*, Vol 16, pp 305-314.

Chanin M.L., N. Smires, and A. Houchecorne (1987) "Long Term Variation of the Temperature of the Middle Atmosphere at Mid-Lattitude:Dynamical and Radiative Causes", *J. Geophys. Res.*, Vol 92, No D9, pp 10,993-10,941.

Chanin M.L., A. Garnier, A. Hauchecorne, and J. Porteneuve (1989) "A Doppler Lidar for Measureing Winds in the Middle Atmosphere", *J. Geophys. Res.*Vol 16, No 11, pp 1273-1276.

CIRA (COSPAR International Refenence Atmosphere, 1986 Part II: Middle atmosphere Models), (1990), *Adv. Space Res.*, Vol 10, no 12. pp 1-519"

Cohen A., J.A. Cooney, and K.N. Geller, *Appl. Opt.*, 15, 2896.

Collis R.T.H., and P.B. Russell (1976) "Lidar Measurements of Particles and Gases by Elastic Backscatter and Differential Absorption." in *Laser Monitoring of the Atmosphere*, E.D. Hinkley Ed. Springer-Verlag.

Congeduti F., G. Fiocco, A. Adriani, and C. Guarrella (1981) "Vertical wind velocity measurements by a Dopler lidar and comparisons with a Doppler sodar", *Appl. Opt.*, 20, pp 2048-2054.

Cooney J.A. (1968) "MeasureMent of the Raman Component of Laser Atmospheric Backscatter", *Appl. Phys. Lett.*, 12, pp 40-42.

Cooney J.A. (1970) "Remote Measurement of Atmospheric Water Vapor Profiles using the Raman Component of Laser Backscatter", *J. Appl. Meteorol.*, 9, pp 182.

Cooney J.A. (1972a) "Measurement of Atmospheric Temperature Profiles by Raman Backscatter", *J. Appl. Meteorol.*, 11, pp 108-112.

Cooney J.A. (1972b) "Measurement of Stratospheric Water Vapor", *J. Geophys. Res.*, 77, pp 1078.

Cooney J.A., and M. Pina (1976) "Laser radar measurements of atmospheric temperature profiles by use of Raman rotational backscatter", *Appl. Opt.*, 15, pp 602

Cooney J.A., K. Petri, and A. Salik (1985) "Measurement of high resolution atmospheric water-vapor profiles by the use of a solar blind Raman Lidar", *Appl. Opt.*, 24, pp 104-108.

Czechowsky P., B. Inhester, J. Klostermeyer, R. Ruster, and G. schmidt (1990) "Simultaneous Radar and Lidar Observations During the DYNA-Campaign" ESA SP-317, pp 399-405.

Davies C.N. (1987) "Particles in the Atmosphere: A Review", *J. Aerosol Sci.*, 18, pp 469-477.

Duclaux (1936) *J de phys. et rad.*, 7, 361.

Elterman L. (1953) "A Series of Stratospheric Temperature Profiles obtained with the Searchlight Technique.", *J. Geophys. Res.*, 58, pp 519-530.

Elterman L. (1968) "UV, Visible and IR Attenuation for Altitudes to 50 km", *AFGRL-68-0153, Environmental Research Paper No. 285.*

Farlow N.H., V.R. Oberbeck, K.G. Snetsinger, G.V. Ferry, G. Polkowski, and D.M. Hays, (1981) *Science,* 211, pp 832-834.

Fiocco G., and L.D. Smullin (1963) "Detection of Scattering Layers in the Upper Atmosphere (60-140 km) by Optical Radar", *Nature Phys. Sci.*, 199, pp 1275-1276.

Fiocco G., and J.B. DeWolf (1968) "Frequency Spectrum of Laser Echoes from Atmospheric Constitutents and Determination of the Aerosol Content of Air" *J. Atmos. Sci.*, 25, pp 488-496.

Fiocco G., G. Benedetti-Michelangeli, K. Maischberger, and E. Madanna (1971) "Measurement of Temperature and Aerosol to Molecule Ratio in the Troposphere by Optical Radar", *Nature Phys. Sci.*, 229, pp 78-79.

Fiocco G. (1984) "Lidar systems for aerosol studies: an outline", in *Handbook for MAP*, 13, Ed R.A. Vincent, pp 56-68.

Fleming S., S. Chandra, M. Schoeberl, and J. Barnett "Monthly Mean Global Climatology of Temperature, Wind, Geopotential Height, and Pressure for 0 - 120 km", NASA Technical Memorandum, #NASA TM-100697.

Fricke K.H., and U. von Zahn (1985) "Mesopause temperatures derivedfrom probing the hyperfine structure of the D2 resonance line of sodium by lidar", *J. Atmos. Terr. Phys.*, 47, pp 499-512.

Friedland S.S., J. Katzenstein, and M.R. Zatzick (1956) "Pulsed Searchlighting the Atmosphere", *J. Geophys. Res.*, 61, pp 415-434.

Gardner C.S., D.G. Voelz, C.F. Sechrist,Jr., and A.C. Segal (1986) "Lidar Studied of the Nighttime Sodium Layer Over Urbana, Illinois 1. Seasonal and Nocturnal Variations", *J. Geophys. Res.*, 91, pp 13,659-673.

Gardner C.S., M.S. Miller, and C.H. Liu (1989) "Rayleigh Lidar Observations of Gravity Wave Activity in the Upper Stratosphere at Urbana, Illinois", *J. Atmos. Sci., 46,* pp 1838-1854.

Georgiyevskiy Yu.S., V.I. Ivanov, V.M. Kopeykin, and I.Ya. Sergeyev (1986) "On the Finely Dispersed Atmospheric Aerosol Fraction", *Izvestiya, Atmospheric and Oceanic Physics*, 22, pp 646-651.

Gill R., K. Geller, J. Farina., J. Cooney, and A. Cohen (1979) "Measurement of Atmospheric Temperature Profiles Using Raman Lidar", *Appl. Meteorol.*, 18, pp 225.

Gruner P. and H. Kleinert (1927) "Die dämmerungerscheinen", *Probl. Kosm. Phys.*, 10, pp 1-113.

Grund C,J. and E.W. Eloranta (1991) "University of Winsconsin High Spectral Resolution Lidar", *Opt. Engr.*, 30, pp 6-12.

Harris F.S. (1978) "Atmospheric aerosol measurement problems", *Proc. Soc. Photo-Opt. Instrum. Eng.*, 142, pp 38-44.

Hauchcourne A. and M.L. Chanin (1980) "Density and Temperature Profiles Obtained by Lidar between 35 and 70 km", *Geophys. Res. Lett.*, 7, pp 565-568.

Herzberg G. (1950) "Spectra of Diatomic Molecules Vol 1", Van Nostrand, Princeton.

Holton, J.R. (1975) "The Dynamic Meteorology of the stratosphere and mesosphere" Meteorol. Monogr. No 37, Am. Meteor. Soc., Boston, Massachusetts.

Holton J.R. (1992) "An Introduction to Dynamic Meteorology" Third Edition, Vol 48 Internaltional Geophysics Series, Academic Press, California.

Hyllerass E.A. (1970) "Mathematical & Theoretical Physics", John Wiley & Sons, New York.

Hulbert E.O. (1937) "Observations of a Searchlight Beam to an Altitude of 28 Kilometers.", *J. Opt. Soc. Am.*, 27, pp 377-382.

Inn E.C.Y., N.H. Farlow, PB. Russell, M.P. McCormick, and W.P. Chu (1982) in "The Stratospheric Aerosol Layer" Ed Whitten R.C., Springer-Verlag Berlin Heidelberg.

Jenkins D.B., D.P. Wareing, L. Thomas, and G. Vaughan (1987) "Upper stratospheric and mesospheric temperatures derived from lidar observations at Aberystwyth.", *J. Atmos. Terr. Phys.*, 49, pp 287298.

Junge C.E., C.W. Chagnon, and J.E. Manson (1961) "Stratospheric Aerosols", *J. Meteorol.*, 18, pp 81-108.

Kalshoven J.E., C.L. Korb, J. Milrod, H. Walden, and R.H. Kagann (1981) "Laser Remote Sensing of Atmospheric Temperature by Observing Resonant Absorption of Oxygen", *Appl. Opt.*, 20, pp 1967-1971.

Kay and Laby (1968) "Tables of Physical and Chemical Constants", Longmans, Green and Co. Ltd., London.

Kennard E.H. (1938) "Kinetic theory of gases", McGraw-Hill, New York.

Keckhut P., Chanin M.L., and A. Huachecorne (1990) "Stratosphere temperature measurement using Raman lidar", *Appl. Opt.*, 29, pp 5182-5186

Kent G.S., and R.W.H. Wright (1970) "A review of laser radar Measurements of atmospheric properties", *J. Atmos. Terr. Phys.*,32, pp 917-943.

Kerker M. (1969) "The scattering of light and other electromagnetic radiation", Academic Press, New York.

King L.V. (1923) "On the complex anisotropic molecule in relation to the dispersion and scattering of light", *Proc. Roy. Soc. London,* A104, pp 333-357.

Kirchhoff V.W.J.H., P.P. Batista, P.R. Clemeasha, and D.M. Simonich (1986) "The twilight sodium layer", *J. Geophys. Res.*, 91, pp 13,303-307.

Labitzke K, and B. Naujokat and J.J. Bernett (1990) "Interannual Variability", *Adv. Space Res.* Vol 10, no 12, pp 163-184.

Labitzke K., and H. van Loon (1992) "Some Influences Responsible for the Interannual Variations in the Stratosphere of the Northern Hemisphere",presented at NATO, ASI, The Role of the Stratosphere in Global Change, Carqueiranne, France, Sept. 1992.

Leonard D.A. (1967) "Observations of Raman Scattering from the Atmosphere Using a Pulsed Nitrogen Ultraviolet Laser", *Nature,* 216, pp 142-143.

Liou K.N. (1980) "An Introduction to Atmospheric Radiation", International Geophysics Series Vol. 40.Academic Press, New York.

McCartney E.J. (1976) "Optics of the Atmosphere", John Wiley & Sons, New York.

McClatchey R.A., R.W. Fenn, J.E.A. Selby, F.E. Volz, and J.S. Garing (1978) in "*Handbook of Optic*", Ed W.G. Driscoll, McGraw-Hill

McDermid I.S., S.M. Godin, and L.O. Lindqvist (1990a) "Ground-based laser Dial system for long-term measurements of stratospheric ozone", *Appl. Opt.*, 29, pp 3603-3612.

McDermid I.S., S.M. Godin, and T.D. Walsh (1990b) "Lidar Measurements of stratospheric ozone and inter-comparision and validation", *Appl. Opt.*, 29, pp 4914-4923.

McEwan M.J., and L.F. Phillips (1975) "Chemistry of the Atmosphere", Edward Arnold (Publishers), London.

McIntosh D.H., and A.S. Thom (1981) "Essentials of Meteorology", Taylor and Francis Ltd, London.

Measures R.M. (1984) "Laser Remote Sensing", John Wiley & Sons, New York.

Melfi S.H. (1972) "Remote Measurement of the Atmosphere using Raman Scattering", *Appl. Opt.*, 11, pp 1605.

Menyuk N., D.K. Killinger, and W.E. DeFoe (1983) "Remote Sensing of Hydrazine Compounds Using a Dual Mini-TEA CO2 Laser DIAL System", From "*Optical and Laser Remote Sensing*" ed. Killinger D.K. and A. Mooradian, Springer-Verlag, pp 17-24.

Midelton W.E.K. (1952) "Vision through the atmosphere", Univ. of Toronto Press, Toronto.

Mitchell N.J., L. Thomas, and A.K.P. Marsh (1990) "Lidar studies of stratospheric gravity waves: A comparison of analysis techniques", *Annales. Geophysicae,* 8, pp 705-712.

Nomura A., T. Kano, Y. Iwasaka, H. Fukunishi, T. Hirasawa, and S. Kawaguchi (1987) "Lidar observations of the Mesospheric Sodium Layer at Syowa Station, Antarctica", *Geophy. Res. Lett.*, 14, pp 700-703.

Pelon J., S. Godin, and G. Megie (1986) "Upper Stratospheric (30-50 km) Lidar Observations of the Ozone Vertical Distribution", *J. Geophys. Res.*, 91, pp 8667-8671.

Pendorf R. (1962) "Angular Mie Scattering", *J. Opt. Soc. Am.*, 52, pp 402-408.

Raman C.V. (1928) *Indian Journal of Physics,* 2, pp 387.

Rayleigh (J.W. Strutt) (1871a) "On the light from the sky, its polarisation and colour", *Phil. Mag.*, 41, pp 274-279.

Rayleigh (J.W. Strutt) (1871b) "On the scattering of light by small particles", *Phil. Mag.*, 41, pp 447-454.

Rayleigh (J.W. Strutt) (1881) *Phil. Mag.*, 12, pp 81.

Rayleigh (J.W. Strutt) (1899) "On the transmission of light through an atmosphere containing many small particles in suspension, and the origin of the blue sky", *Phil. Mag.*, 47, pp 375-384.

Reagan J.A., J.D. Spinhirne, and M.P. McCormick (1989) " Lidar Sensing of Aerosols and Clouds in the Troposphere and Stratosphere", *Proc. IEEE*, 77, pp 433-448.

Rees D., J.J. Barnett, and K. Labitzke (editors) (1990) "COSPAR International Reference Atmosphere: 1986, Part II: Middle Atmosphere Models", *Advances in Space Science*, vol 10, no 12.

Rothe K.W., U. Brinkmann, and H. Walther (1974) "Applications of Tunable Dye Lasers to Air Pollution Detection", *Appl. Phys.*, 3, pp 115.

Rothe K.W., H. Walther, and J. Werner (1983) "Differential-Absorption Measurements With Fixed-Frequency IR and UV Lasers", From "*Optical and Laser Remote Sensing*" ed. Killinger D.K. and A. Mooradian, Springer-Verlag, pp 10-16.

Rothschild M. (1993) "Optical Materials for Excimer Laser Application", *Optics and Photonics News,* vol 4, no 5, pp 9-15.

Sasano Y., and E.V. Browell (1989) "Light-Scattering Characteristics of Various Aerosol Types Derived from Multiple Wavelength Lidar Observations", *Appl. Opt.*, 28, pp 1670-1679.

Sassen K. (1991) " The Polarisation LIDAR Technique for Cloud Research - A Review and Current Assessment", *Bull. Am. Meteorol. Soc.*, 72, pp 1848-1866.

Scholand R.M. (1964) "The Determination of the Vertical Profile of Atmospheric Gases by means of a Ground Based Optical Radar." Proc. of the Third Symposium on Remote Sensing of the Environment. pp 215-224.

Schwemmer G.K., M. Dombrowski, C.L. Korb, J. Milrod, H. Walden, and R.H. Kagann (1987) "A Lidar System for Measuring Atmospheric Pressure and Temperature Profiles.", *Rev. Sci. Instrum.*, 58, pp 2226-2237.

Schwiesow R.L. and L. Lading (1981) "Temperature Profiling by Rayleigh-scatter lidar", *Appl. Opt.*, 20, pp 1972-79.

She C.Y., J.R. Yu, H Latifi, and R.E. Bills (1992) "High-spectral-resolution fluorescence light detection and ranging for mesospheric sodium temperature measurements", *Appl. Opt.*, 31, pp 2095-2106.

Shibata T., M. Kobuchi, and M. Maeda (1986a) "Measurements of temperature profiles in the middle atmosphere with a XeF lidar", *Appl. Opt.*, 25, pp 685-688.

Shibata T., T. Fukuda, and M. Maeda (1986b) "Density Fluctuations in the Middle Atmosphere over Fukuoka Observed by an XeF Rayleigh Lidar", *Geophys. Res. Lett.*, 13, pp 1121-1124.

Shibata T., S. Ichimori, T. Narikiyo, and M. Maeda (1988) "Spectral Analysis of Vertical Temperature Profiles Observed by Lidar in the Upper Stratosphere and the Lower Mesosphere",*J. Met. Soc Jap.*, 66, 6, pp 1001-1005

Shimizu H., S.A. Lee, and C.Y. She (1983) "High spectral resolution lidar system with atomic blocking filters for measuring atmospheric parameters", *Appl. Opt.*, 22, pp 1373-1381.

Shimizu H., K. Noguchi, and C.Y. She (1986) "Atmospheric Temperature Measurement by a high spectral resolution lidar", *Appl. Opt.*, 25, pp 1460-1466.

Shine K.P. (1992) "The Greenhouse Effect and Stratospheric Change", presented at NATO, ASI, The Role of the Stratosphere in Global Change, Carqueiranne, France, Sept. 1992.

Shipley S.T., D.H. Tracey, E.W. Eloranta, J.T. Trauger, J.T. Sroga, F.L. Roesler, and J.A. Weinman (1983) "High spectral resolution lidar to Measure optical scattering properties of atmospheric aerosols. 1: Theory and instrumentation", *Appl. Opt.*, 22, pp 3716-3724.

Sica R.J. (1992) Private communication.

Stefanutti F., F. Castagnoli, M. Del Guasta, M. Morandi, V.M. Sacco, V. Venturi, L. Zaccagnoli, J. Kolenda, H. Kneipp, P. Rairoux, B. Stein, D. Weidauer, and J.P. Wolf (1992) "A Four Wavelength Depolarization Backscatter LIDAR for Polar Stratospheric Cloud Monitoring", *Appl. Phy.*, B55, pp13-17

Stratton J.A. (1941) "Electromagnetic Theory", McGraw-Hill, New York.

Sugawara A., and S. Yip (1967) *Phys. Fluids*, 10, pp 1911.

Synge E.H. (1930) "A Method of Investigating the Higher Atmosphere.", *Phil. Mag.*, 9, pp 1014-1020.

Tenti G., C.D. Boley, and R.C. Desai (1974) "On the Kinetic Model Description of Rayleigh-Brillouin Scattering from Molecular Gases", *Can. J. Phys.*, 52, pp 285-290.

Thomas L. (1987) "Laser radar observations of the middle-atmosphere structure and composition", *Phil. Trans. R. Soc. Lond.*, Ser. A, 323, pp 597-609.

Toon O.B., and J.B. Pollack (1982) "Stratospheric Aerosols and Climate" in The Stratospheric Aerosol Layer, Ed Whitten R.C., Springer-Verlag Berlin Heidelberg.

Turco R.P., R.C. Whitten, and O.B. Toon (1982) "Stratospheric Aerosols: Observations and Theory", *Reviews of Geophysics and Space Physics*, 31, pp 223-279.

Turco R.P., K. Drdla, A. Tabazadeh, and P. Hamill (1992) "Heterogenous Chemistry of Polar Stratospheric Clouds and Volcanic Aerosols" presented at NATO, ASI, The Role of the Stratosphere in Global Change, Carqueiranne, France, Sept. 1992.

Uchino O., M.P. McCormick, and T.J. Swissler (1986) "Temperature retrievals by Rayleigh backscatter lidar signals", *Appl. Opt.*, Vol. 25, No.17, pp 2868-2870.

Uthe E.E. (1986) "Airborne CO2 DIAL measurement of atmospheric tracer gas concentration distributions", *Appl. Opt.*, 25, pp 2492-2498.

Van de Hulst H.C. (1951) "Light scattering by small Particles", John Wiley & Sons, New York.

von Zahn U., P. von der Gathen, and G. Hansen (1987) "Forced release of sodium from upper atmospheric dust particles", *Geophy. Res. Lett.*, 14, pp 76-79.

Warneck P.(1988) "Chemistry of the Natural Atmosphere" Academic Press, San Diego, California.

Welsh B.M., and C.S. Gardner (1989) "Bistatic imaging lidar technique for upper atmospheric studies", *Appl. Opt.*, 28, pp 82-88.

Werner J., K.W. Rothe, and H. Walther (1984) in Proc. 12th International Laser Radar Conference, France 1984, pp 225.

Whitten R.C., and P. Hamill (1982) in "The Stratospheric Aerosol Layer" Ed Whitten R.C., Springer-Verlag Berlin Heidelberg.

Williams F. (1966) in "Luminescence of Inorganic Solids", ed. P. Goldberg, Academic Press, New York.

Wilson R., A. Hauchecorne, and M.L. Chanin (1990) "Gravity Wave Spectra in the Middle Atmosphere as Observed by Rayleigh Lidar",*Geophy. Res. Lett.*, 17, 10, pp 1585-1588.

WMO (1992) "WMO and the Ozone Issue" WMO No. 778, World Meteorological organization, Geneva.

Yaskovich L.G. (1986) "Determination of the Atmospheric Aerosol Absorption Coefficients from the Absorption of Radiation by Aerosol samples", *Izvestiya, Atmos. Ocean. Phy.*, 22,pp 640-645.

Yip N., and M. Nelkin (1964) "Application of a Kinetic Model to TimeDependent Density Correlations in Fluids", *Phys. Rev.* 135, pp A1241-A1247.

Young A.T. (1980) "Revised depolarization corrections for atmospheric extinction", *Appl. Opt.*, 19, pp 3427-28.

Young A.T. (1981) "On the Rayleigh-Scattering Depth of the Atmosphere", *J. Appl. Meteorol.*, 20, pp 328-30.

Young A.T. (1982) "Rayleigh scattering", *Phys. Today,* 35, pp 42-48.

Zander R., E. Mahieu, and Ph. Demoulin (1992) "Monitoring of the Stratospheric Changes at the Jungfraujoch Station by High Resolution Infrared Solar Observation in Support of the Network for the Detection of Stratospheric Change (NDSC)", presented at NATO, ASI, The Role of the Stratosphere in Global Change, Carqueiranne, France, Sept. 1992.

Zanzottera E. (1990) "Differential Absorption LIDAR Techniques in the Determination of Trace Pollutants and Physical Parameters or the Atmosphere", *Critial Reviews in Analytical Chemistry*, 21, pp 279.